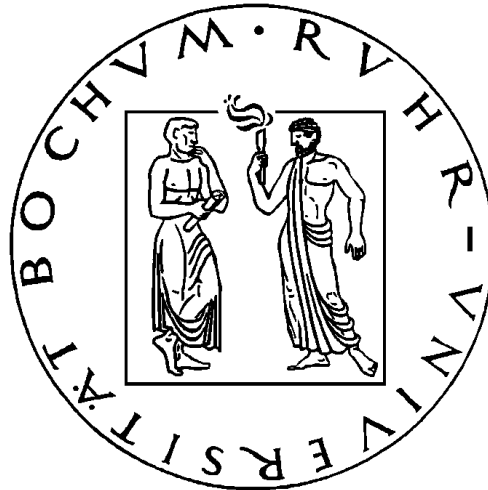


The Narrow-Line Region of Active Galaxies



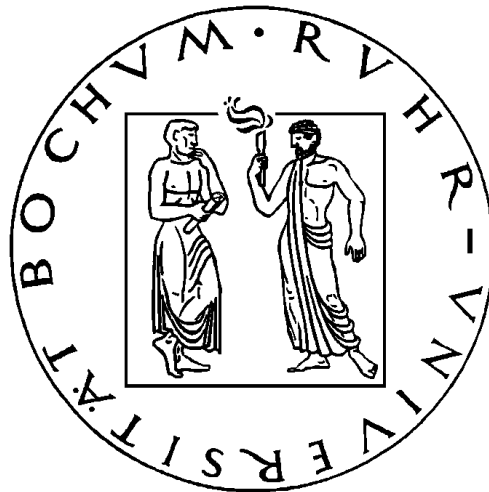
DISSERTATION

zur Erlangung des Grades
„Doktor der Naturwissenschaften“
der Fakultät für Physik und Astronomie
an der Ruhr-Universität Bochum

vorgelegt von
Nicola Bennert

Bochum 2005

The Narrow-Line Region of Active Galaxies



PHD THESIS

Faculty of Physics and Astronomy
Ruhr-University Bochum

Nicola Bennert

Bochum 2005

First referee: Prof. Dr. Rolf Chini
Second referee: Prof. Dr. Heino Falcke

Tag der mündlichen Prüfung: 17.10.2005

In memoriam Prof. Dr. Hartmut Schulz, deceased in August 2003.
I remember him gratefully for having been my "Doktorvater" in the truest sense of the word.
The astronomical community has lost a wonderful colleague and a truly independent mind.

Contents

1. Introduction	1
1.1 Global Picture	1
1.1.1 Broad-Line Region	6
1.1.2 Narrow-Line Region	6
1.2 Motivation	8
1.3 Layout of PhD Thesis	9
2. NLR Size and Luminosity: Observations	11
2.1 Introduction	11
2.2 Data	12
2.3 Results and Discussion	13
2.3.1 NLR Size and Luminosity	13
2.3.2 Consequences of the NLR Size-Luminosity Relation	19
2.3.3 BLR Size and NLR Size	24
2.3.4 Black Hole Mass	26
2.3.5 NLR Surface-Brightness Profiles	26
2.4 Conclusions	29
3. NLR Size and Luminosity: Modeling	31
3.1 Introduction	31
3.2 Model Description	31
3.2.1 Model Assumptions	31
3.2.2 Model Predictions	34
3.3 Receding-Torus Model and Modifications	40
3.4 Alternatives	43
3.5 Conclusions	44
4. Spatially-Resolved NLR Diagnostics	45
4.1 Introduction	45
4.2 Observations	46
4.2.1 VLT/FORS1	46
4.2.2 NTT/EMMI	49
4.3 Reduction and Analysis	50
4.3.1 Standard Reduction	50
4.3.2 Extraction	56

4.3.3	Stellar Population of Galactic Nuclei	56
4.3.4	Fe II Template	62
4.3.5	Emission-Line Fluxes and Reddening	62
4.4	Results and Discussion	67
4.4.1	Nuclear Spectra, Emission-Line Fluxes, and Temperature	71
4.4.2	Reddening Distributions	75
4.4.3	Diagnostic Diagrams	79
4.4.4	Photoionization Modeling and NLR size	82
4.4.5	Surface-Brightness Distributions	91
4.4.6	Electron-Density Distributions	93
4.4.7	Ionization-Parameter Distributions	99
4.4.8	Consequences for the NLR Size-Luminosity Relation	104
4.4.9	Velocities	105
4.4.10	Extended Broad Lines?	105
4.4.11	Differences between Type-1 and Type-2 Seyferts	118
4.4.12	Detailed Case Study of the Seyfert-2 Galaxy NGC 1386	124
4.4.13	Comments on Individual Objects	131
4.5	Conclusions	160
5.	Conclusions	163
5.1	Summary	163
5.2	Outlook	164
A.	Hubble Constant and World Model	165
B.	Observed Surface-Brightness Profiles	167
C.	Calculation of Physical Parameters	187
C.1	Reddening	187
C.2	Temperature	189
C.3	Electron Density	190
C.4	Ionization Parameter	190
C.5	FWHM	191
C.6	Mass	192
D.	Calculation of Errors	193
	Bibliography	195
	Acknowledgements	205
	Curriculum Vitae	207

List of Figures

1.1	Diagnostic line–ratio diagram; Unified scheme	5
2.1	NLR size–luminosity relation	14
2.2	Groundbased versus HST data; NLR size–luminosity relation (3σ limit)	14
2.3	NLR size–luminosity relation (50% luminosity); NLR–BLR relation	20
2.4	Gaussian to total luminosity versus total luminosity and linear scale	20
2.5	Surface–brightness profiles versus point–spread function	28
3.1	Geometrical model	32
3.2	Luminosity from ionization cone	34
3.3	Projected NLR radii for type–1 and type–2 AGNs	35
3.4	Theoretical NLR size–luminosity relations	41
4.1	Emission–line images (NGC 1386, NGC 3281, MCG –6–30–15, NGC 5643)	48
4.2	Emission–line images (Fairall 51, NGC 6860, Mrk 915, NGC 526a)	54
4.3	Emission–line images (MCG –05–13–017, IC 5063, NGC 7212, ESO 362–G008)	55
4.4	Reddening of stellar template	58
4.5	Template subtraction	60
4.6	Examples of Gaussian fits (Seyfert–2 galaxies)	64
4.7	Line–profile variations in NGC 5643 and IC 5063	65
4.8	Examples of Gaussian fits (Seyfert–1 galaxies)	66
4.9	Central spectra (NGC 1386, NGC 3281, NGC 5643, IC 5063)	68
4.10	Central spectra (NGC 7212, ESO 362–G008, MCG –6–30–15, Fairall 51)	69
4.11	Central spectra (NGC 6860, Mrk 915, NGC 526a, MCG –05–13–017)	70
4.12	Reddening distributions (NGC 1386, NGC 3281, NGC 5643)	76
4.13	Reddening distributions (IC 5063, NGC 7212, ESO 362–G008)	77
4.14	Reddening distributions (Seyfert–1 galaxies)	78
4.15	Diagnostic diagrams (NGC 1386, NGC 5643)	80
4.16	Diagnostic diagrams (NGC 6860, MCG –05–13–017)	81
4.17	NLR versus H II–region spectra	84
4.18	Diagnostic diagrams (NGC 3281, IC 5063, NGC 7212, ESO 362–G008, Fairall 51, Mrk 915, NGC 526a)	85
4.19	Spatially varying nitrogen and sulfur line–ratios (Seyfert–2 galaxies)	86
4.20	Spatially varying nitrogen and sulfur line–ratios (Seyfert–1 galaxies)	87
4.21	Spatially varying oxygen line–ratios (Seyfert–2 galaxies)	88

4.22	Spatially varying oxygen line-ratios (Seyfert-1 galaxies)	89
4.23	CLOUDY modeling results	92
4.24	Surface-brightness distributions (Seyfert-2 galaxies)	95
4.25	Surface-brightness distributions (Seyfert-1 galaxies)	96
4.26	Electron-density distributions (Seyfert-2 galaxies)	97
4.27	Electron-density distributions (Seyfert-1 galaxies)	98
4.28	Ionization-parameter distributions (Seyfert-2 galaxies)	101
4.29	Ionization-parameter distributions (Seyfert-1 galaxies)	102
4.30	Velocity fields (Seyfert-2 galaxies)	106
4.31	Velocity fields (Seyfert-1 galaxies)	107
4.32	Broad H α and H β emission in Fairall 51	109
4.33	Gaussian fits to broad H α emission in Fairall 51	110
4.34	Broad H α and H β emission in NGC 6860	111
4.35	Gaussian fits to broad H α emission in NGC 6860	112
4.36	Broad H α and H β emission in Mrk 915	113
4.37	Gaussian fits to broad H α emission in Mrk 915	114
4.38	Broad H α flux and comparison to narrow H α flux	116
4.39	Line-of-sight integration for type-1 and type-2 AGNs	122
4.40	H α -profile variations in NGC 5643	138
B.1	Observed surface-brightness profiles	168
C.1	Electron density and ionization parameter as function of line ratios	191

List of Tables

2.1	NLR size–luminosity relations and NLR–BLR relation	15
2.2	Comparison of HST and groundbased data	17
2.3	Observed NLR radius versus expected Strömgen radius	23
2.4	Distribution of surface–brightness profiles	28
3.1	Consequences of receding–torus model on NLR sizes	38
3.2	Theoretical NLR size–luminosity relations	40
4.1	Properties of the VLT sample	47
4.2	VLT observations	49
4.3	Properties of the NTT sample (Seyfert–1 galaxies)	51
4.4	Properties of the NTT sample (Seyfert–2 galaxies)	52
4.5	NTT observations	53
4.6	Template subtraction details	61
4.7	Emission–line intensity ratios relative to $H\beta$ (Seyfert–2 galaxies)	72
4.8	Emission–line intensity ratios relative to $H\beta$ (Seyfert–1 galaxies)	73
4.9	$H\beta$ luminosity and results from dereddened line ratios	74
4.10	Results from diagnostic diagrams	83
4.11	Fitting parameters of surface–brightness distributions	94
4.12	Fitting parameters of electron–density distribution	100
4.13	Fitting parameters of ionization–parameter distribution	103
4.14	Broad $H\beta$ and $H\alpha$ emission in Seyfert–1 galaxies	108
C.1	Central wavelengths of emission lines	188
C.2	Ionization potentials and critical densities	188
C.3	Reddening corrections	189
D.1	Error propagation	194

Abstract

This thesis presents an imaging and spectroscopic study of the narrow-line region (NLR) in active galaxies with the aim to explore the impact of the central engine onto the surrounding gas. The data basically comprise Hubble Space Telescope (HST) [O III] narrow-band images of 58 Seyfert galaxies and seven nearby quasars taken from literature as well as spatially resolved spectroscopy of 12 Seyfert galaxies observed with the New Technology Telescope (NTT) and the Very Large Telescope (VLT).

Based on the imaging study, we find striking correlations between the size and the luminosity of the NLR: For type-1 AGNs, the size scales with roughly the square root of [O III] luminosity, a behavior which can be explained if, on average, all AGNs have the same ionization parameter, density, and ionizing spectral energy distribution. Type-2 objects seem to follow a flatter slope of 0.33, expected for gas distributed in a Strömgren sphere, valid only in the case of constant density. While at first sight different slopes for type-1 and type-2 AGNs seem to contradict the unified model for AGNs, we show that the influence of the observers viewing angle with respect to the NLR cone axis as well as the effects of a receding torus can explain the observed relations, with the intrinsic NLR size scaling with the square root of the AGN luminosity. We find a correlation between NLR sizes and those of the BLR derived from reverberation mapping which can be useful to estimate black hole masses directly from the NLR sizes. We create NLR surface-brightness profiles to investigate the gas distribution.

From the high-sensitivity long-slit spectra, we analyze the radial properties of the NLR gas, such as reddening, electron density, ionization parameter, and velocity field, with unprecedented detail. We develop and improve methods to derive pure emission-line spectra and use the resulting absorption-line free ratios for spatially resolved spectral diagnostics. For four objects, we find a clear transition between the AGN-excited NLR and the surrounding star-forming areas. This approach allows for the first time to determine the NLR size independent of stellar contamination. We find a decreasing electron density and ionization parameter, indicating that the NLR is photoionized by the central source only. The decrease in electron density rules out a Strömgren-like behavior of the NLR gas, in agreement with our theoretical model.

The excellent data allow us to gain important insights into size, luminosity, and physical parameters of the NLR. Our results show the success of the methods developed here and may trigger further studies, in particular of the recently discovered type-2 quasars.

Introduction

The study of “active galactic nuclei” (AGNs) is a fascinating and rapidly evolving field of astrophysical research today. The term AGN refers to the existence of energetic phenomena in the nucleus of a galaxy which cannot be explained by a simple mixture of stars and interstellar medium (ISM) as in “normal galaxies”: The luminosity radiated from a central region smaller than a cubic parsec, as required from short-term variations, can exceed that of large galaxies by factors of ten to a thousand. In addition, it emits a characteristic spectrum with strong contributions of high-energy photons (UV, X-rays, and sometimes γ -rays). The fundamental question about AGNs is how this energy can be generated on that small scales.

In the following, we describe the generally accepted global picture on how AGNs work and briefly introduce the different phenomena related to AGNs, focussing on those which are of special interest for our study (Section 1.1)¹. We motivate the presented research (Section 1.2) and give a layout of this thesis (Section 1.3).

1.1 Global Picture

In the current paradigm, the primary energy source of AGNs is believed to be gravitational accretion of matter by a **supermassive black hole** (BH).

Techniques used to estimate the central BH mass in active and non-active galaxies rely on primary methods such as measuring the stellar velocities near the BH in the Galactic Center [e.g. Eckart & Genzel (1996); Ghez et al. (1998)], tracing the H₂O megamaser emission in central disks as in NGC 4258 (Greenhill et al., 1995; Myoshi et al., 1995), measuring stellar dynamics which lead to the discovery of the $M_{\text{BH}} - \sigma^2$ (Ferrarese & Merrit, 2000), and reverberation mapping to determine the radius of the broad line region (BLR) using the line widths as indicator of the corresponding velocities [e.g. Peterson (1993); Wandel et al. (1999); Kaspi et al. (2000)]. These techniques revealed a range of BH masses from $\sim 10^6 - 10^9 M_{\odot}$ with the most massive ones presumably residing in the most luminous AGNs. The lower limit of BH masses is given by the spatial and spectral resolution of current instruments which do not allow to dynamically detect BHs

¹ We basically refer to the book “An introduction to Active Galactic Nuclei” by Bradley M. Peterson (2003). For further background information, we refer the interested reader to this or other textbooks on AGNs.

² σ = stellar velocity dispersion relation

in the mass range $10^4 - 10^6$ (corresponding to velocity dispersions below 60 km s^{-1}) in galaxy centers (Bart, 2004). A secondary method used to estimate BH masses of AGNs is an empirical relation between the radius of the BLR and the continuum luminosity [e.g. Kaspi et al. (2000)].

Driven by its gravitational pull, matter spirals towards the black hole when losing its angular momentum. Its potential energy is converted into radiation via viscous dissipation in an **accretion disk** surrounding the BH. As in stars, the fundamental process at work is the conversion of mass to energy with an efficiency η ($E = \eta mc^2$). The efficiency is, however, with $\eta \sim 0.1$ much higher than that for fusion of hydrogen to helium ($\eta = 0.007$).³ To fuel luminous AGNs ($L \sim 10^{46} \text{ erg s}^{-1}$), a mass accretion rate of $2 M_{\odot}$ per year is sufficient. Thus, the main problem of AGN fueling is not the energy requirements but the angular momentum considerations: The infalling gas must lose enough angular momentum before reaching the accretion disk where further angular momentum transfer can occur through viscosity.

Among the mechanisms that have been proposed for angular momentum transfer, the principle ones are interactions between galaxies [e.g. Hernquist & Mihos (1995); Taniguchi & Wada (1996)], bars [e.g. Simkin et al. (1980); Shlosman et al. (1990)], and nuclear spirals [e.g. Regan & Mulchaey (1999)]. However, recent studies indicate that Seyfert galaxies do not have more close companions than normal galaxies [e.g. Schmitt (2004)]. Furthermore, a substantial fraction of Seyfert galaxies show no evidence of recent mergers [e.g. De Robertis et al. (1998)]. Also, there is no clear observational correlation between bars and nuclear activity [e.g. Mulchaey & Regan (1997)] which may be explained by self-destruction of fueling bars (Combes, 2004). However, one has to keep in mind that both the spatial scales and time scales of the involved phenomena differ: The fueling leading to the high energy radiation in an accretion disk is restricted to $\sim 0.01 \text{ pc}$ close to the central BH while bars are medium or large scale structures (several 100 pc to kpc). The central activity and formation of large scale bars or any other feeding process can be recurrent processes and may not be observed simultaneously (Emsellem, 2004; Combes, 2004).

Gas in the surroundings of the BH is photoionized by the central engine, leading to the so-called **broad-line region** (BLR) close to the BH and the **narrow-line region** (NLR) further out. The BLR and NLR exhibit optical emission lines, kinematically broadened with typical widths of $10^{3-4} \text{ km s}^{-1}$ and $10^{2-3} \text{ km s}^{-1}$, respectively. The most prominent optical emission lines of the NLR are the narrow permitted Balmer lines $H\alpha$ and $H\beta$ and narrow forbidden lines of e.g. $[\text{O III}] \lambda 5007 \text{ \AA}$ and $[\text{N II}] \lambda \lambda 6548, 6584 \text{ \AA}$. The BLR reveals only broad permitted lines of several elements, among those the strong Balmer series from hydrogen. These two regions are described in detail in the following Sections (1.1.1 and 1.1.2).

Another phenomenon connected with the AGN is the so-called **radio jet**. Jets are extended linear structures seen in radio wavelengths due to synchrotron emission of high-velocity electrons in magnetic fields. Jets may be important for shaping and ionizing the gas in quasars and Seyferts: Often, in objects with an axisymmetric NLR morphology and extended radio emission, the two axes coincide [e.g. Capetti et al. (1996); Falcke et al. (1998); Nagar et al. (1999)]. This alignment implies an interaction between the thermal NLR gas and the non-thermal plasma.

³ If the accretion process is radiatively inefficient as theoretically predicted in the context of advection dominated accretion flows (ADAFs), η can be much smaller [$\eta \ll 1$, e.g. $\eta \sim 10^{-4}$; Ho et al. (2003)].

In some sources, the radio morphology shows clear evidence for **shock** fronts at the interface between the radio-emitting plasma and the interstellar medium of the host galaxy [e.g. Falcke et al. (1998)]. It seems that the outflowing plasma which is responsible for the radio emission creates bow shocks, emission-line strands, bended radio jets or limb-brightened radio lobes as it collides with the ambient NLR gas. If the shock speed is high enough, the post-shock temperatures can lead to shock-ionization of the gas that goes through the shock front [e.g. Dopita & Sutherland (1996)].

A large variety of AGN properties has been observed. The two largest subclasses of AGNs are **Seyfert galaxies** and **quasars**. While quasars form the most luminous subclass of AGNs, Seyfert galaxies (short: Seyferts) are assumed to be their less luminous counterparts. Carl Seyfert realized that the spectra of several similar galaxies reveal strong high ionization nuclear emission lines and thus form a distinct group (Seyfert, 1943). The term QSO (“Quasi-Stellar Object”) is historically motivated: In 1963, Maarten Schmidt had identified an object which looked like a star on images rather than like a galaxy with a large recession velocity, i.e. at a large distance according to Hubble’s law. At this large distance, only the star-like nuclear source was seen on photographic plates, outshining the light from the surrounding host galaxy. Only 5–10% of QSOs are quasars (“quasi-stellar radio source”), i.e. strong radio sources (“radio-loud”).⁴ Morphological studies indicate that most radio-quiet quasars and Seyferts occur in spiral galaxies while radio-loud quasars rather have elliptical host galaxies [e.g. Malkan et al. (1984); Smith et al. (1986); Hutchings et al. (1989)]. In their catalog of quasars, Véron-Cetty & Véron (2001b) distinguish quasars from Seyferts according to their absolute B magnitude: Objects brighter than $M_B = -23^m$ are called quasars⁵. Seyferts and radio-quiet quasars seem to form a continuous sequence in luminosity and are probably the same phenomenon with physical differences depending on the luminosity of the source.

Khachikian & Weedman (1974) were the first to distinguish Seyfert galaxies by the presence or absence of broad emission lines. Seyferts of **type 1** (Sy1s) show both broad and narrow emission-lines with only permitted lines being broad, having narrow lines superimposed. In addition to these strong emission lines, weak absorption lines from starlight and a featureless continuum of the AGN component are opposed. Spectra from Seyferts of **type 2** (Sy2s) reveal only narrow emission-lines. The AGN continuum is usually weak and difficult to isolate from the stellar continuum.

The classification of two type of Seyferts, Seyfert-1 galaxies and Seyfert-2 galaxies, may be further subdivided according to the Balmer emission-line profiles: Seyfert galaxies in which both a broad component and a superimposed narrow component can be easily recognized are generally classified as Seyfert 1.5 galaxies (Sy1.5s). Seyferts with very weak but still visible broad components and strong narrow components in both $H\alpha$ and $H\beta$ are called Seyfert 1.8 galaxies (Sy1.8s), if the broad component is only visible in $H\alpha$ but not in $H\beta$, the galaxy is classified as Sy1.9 [e.g. Osterbrock (1989)].

Another peculiar subclass of Seyfert galaxies are the so-called **narrow-line Seyfert-1 galaxies** (NLS1s), defined by their optical line properties: The $H\beta$ FWHM does not exceed 2000 km s^{-1} , i.e. it is only slightly broader than the FWHM of the forbidden lines, the $[O III]/H\beta$ ratio is less than 3, and the UV-visual spectrum shows high-ionization

⁴ Throughout the thesis, only the term quasar will be used, referring to both radio-loud and radio-quiet objects.

⁵ The most recent catalog of quasars and AGNs, the 11th edition, is Véron-Cetty & Véron (2003), containing nearly 50 000 quasars and over 15 000 AGNs.

lines and strong Fe II emission multiplets (Osterbrock & Pogge, 1985). Moreover, NLS1s have a steep soft X-ray slope compared to that typical for Seyfert-1 galaxies, and show rapid and large soft X-ray variability (Boller et al., 1996). NLS1s seem to have relatively high accretion rates (Pounds et al., 1995) or small black hole masses, as suggested by Boller et al. (1996): If the gravitational force of the central black hole (BH) is the main cause of the motion of the BLR clouds, narrower optical emission lines will result from smaller BH masses ($\sim 10^{6-7} M_{\odot}$), as long as the BLR distance from the central source does not change strongly with the BH mass.

While in the local universe, Seyfert-2 galaxies outnumber Seyfert-1 galaxies, type-2 quasars, the luminous analogs of type-2 (narrow emission line) Seyfert galaxies, were unknown for a long time. With the advent of large surveys, such as the Sloan Digital Sky Survey (SDSS), a sample of 291 type-2 AGNs has recently been found, half of it with large [O III] values comparable to those of luminous quasars (Zakamska et al., 2003). These objects are called type-2 quasar candidates ($0.3 < z < 0.83$).

Two other groups related to the AGN phenomena are the so-called **LINERs** and **starburst galaxies** (short: starbursts). LINERs (Low Ionization Nuclear Emission-line Region galaxies) were identified by Heckman (1980) and resemble Seyfert-2 galaxies but with strong low ionization lines such as [O I] $\lambda\lambda$ 6300,6363 Å and [O II] $\lambda\lambda$ 3726,3728 Å but weak high ionization lines such as [O III] $\lambda\lambda$ 4959,5007 Å emission. LINERs may simply be very low-luminosity Seyferts or objects in which starburst-driven winds or shock-heated gas play a major role in ionizing the gas (Heckman et al., 1987; Filippenko & Terlevich, 1992). Starbursts are galaxies which show signatures of recent large-scale star formation activity: They have relatively blue colours with strong H II-region type emission-lines due to a large number of A and B stars. Often, the H II emission is confined to the unresolved region at the galactic center and looks like an AGN. The relationship between AGNs and nuclear starbursts is still a matter of debate: Do AGNs trigger star formation by e.g. shocks from jets? Are starbursts and AGNs processes competing for the available interstellar gas? Or is the apparent relationship a pure coincidence as both occur independent of each other in the nuclei of galaxies?

LINERs, Seyferts, and H II region spectra cannot be distinguished from one another on the basis of single flux ratios of a pair of lines. But the relative strengths of various lines are a function of the shape of the ionizing continuum and can be used to distinguish between the power law ionizing spectrum characteristic for AGNs and a black body spectrum typical for stars. Baldwin et al. (1981) were the first to use **diagnostic line-ratio diagrams** to distinguish between LINERs, Seyferts and H II regions (Fig. 1.1, *left panel*).

Radio galaxies form another distinct subclass of AGNs. They are classified from their strong radio emission which can exceed that of normal galaxies by a factor of 10^6 (e.g. in the case of the prototypical radio galaxy Cyg A). Host galaxies are giant ellipticals or of type S0. The optical spectra are similar to that of Seyfert galaxies: **Broad-line radio galaxies** (BLRGs) show broad and narrow emission lines, while **narrow-line radio galaxies** (NLRGs) only reveal narrow emission lines. Thus, they can be considered as radio-loud counterparts of Seyfert galaxies (although Seyferts appear in spirals rather than elliptical galaxies).

Several attempts have been made to explain the observed diversity of AGNs by a combination of real differences in physical parameters and apparent, observer-dependent ones. Optical **unification schemes** try to explain the two types of Seyfert galaxies,

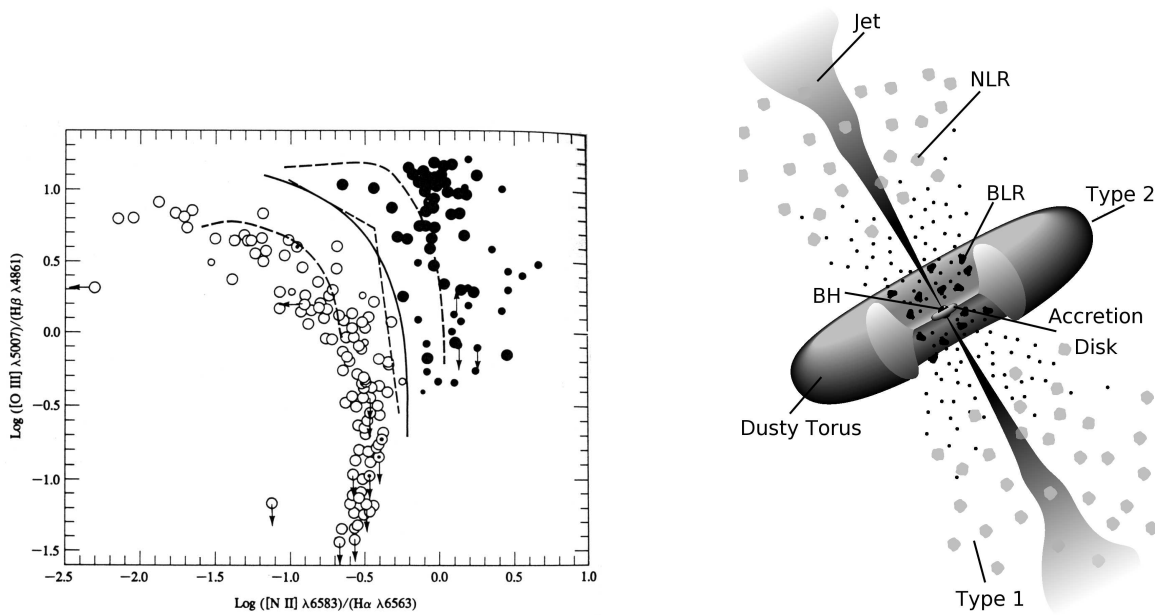


Figure 1.1: *Left panel:* $[\text{O III}]/\text{H}\beta$ versus $[\text{N II}]/\text{H}\alpha$ diagnostic diagram from emission-line galaxies [Osterbrock (1989), page 346]. The filled circles are (narrow-line) AGNs, the open circles H II-region like objects. The solid line is the dividing line between both types. The dashed lines represent several photoionization models. *Right panel:* Schematic illustration of the unified model for AGNs [adopted from Urry & Padovani (1995)].

type 1 and type 2, by an inclination dependent view of intrinsically the same object. In the generally accepted unified model of AGNs, an optically thick obscuring dust torus is envisioned to encircle the accretion disk (Antonucci, 1993) (Fig. 1.1, *right panel*). If this torus is viewed edge-on, the dust absorbs the emitted photons and hides the nucleus as well as the BLR from observers view: Only narrow emission-lines from the NLR further out can be detected in the spectra, resulting in a type-2 Seyfert classification. For a face-on view, both BLR and NLR can be seen and the Seyfert is classified as type 1. The anisotropic escape of ionizing photons can lead to a so-called “ionization cone” (Schulz, 1988; Pogge, 1988, 1989; Storchi-Bergmann et al., 1992a). Indeed, more than a dozen of Seyfert-2 galaxies are known with NLRs resembling a cone-like structure [e.g. Pogge (1988); Tadhunter & Tsvetanov (1989); Wilson & Tsvetanov (1994)].

A major success for the unified model was the detection of broad lines in polarized light in NGC 1068 (Antonucci & Miller, 1985) and other Seyfert-2 galaxies [e.g. Miller & Goodrich (1990); Tran et al. (1992)]. These broad polarized lines can be explained by photons, originating from the BLR hidden from direct view, which are scattered into the observers line-of-sight by electrons or dust above and below the plane of obscuration, e.g. in the NLR. It indicates that at least some of the type-2 AGNs are in fact partially obscured type 1s, the key element of the unification scheme.

However, some Seyfert-2 galaxies do not seem to contain a hidden Seyfert-1 nucleus, at least spectroscopic studies do not show any signs of polarized broad lines [e.g. Tran (2003)]. Two populations of Seyfert-2 galaxies may exist: one with a genuine type-1 nucleus hidden from view and one without a BLR. This interpretation is not unambiguous as e.g. the detection limit of polarized lines may play a role. Also, the nature of the obscuring/scattering medium may influence the detection of hidden BLRs. A thorough

discussion on possible alternative explanations for the existence of Seyfert–2 galaxies without hidden BLR can be found in Tran (2003).

Only recently, several type–2 quasars have been found [e.g. Zakamska et al. (2003)]. It is still under debate whether the simple, inclination based unified scheme can be extended to quasars.

Nevertheless, the unified model is now supported by several lines of evidence and widely accepted by the AGN community as broadly, if not universally, applicable.

1.1.1 Broad–Line Region

The BLR is important due to its proximity to the central source ($r < 0.1$ pc). The gas is photoionized by the continuum UV radiation and its motion seems to be determined by the BH mass.

The BLR shows strong recombination lines such as the Balmer series from optically permitted transitions, i.e. those with non–zero electric dipole moment. Typical widths are ~ 15 – 150 Å which cannot be explained by the natural line width: The occupation time in the excited upper level is low and these transitions are fast (10^8 s $^{-1}$), yielding a small intrinsic line width (using Heisenbergs uncertainty relation). Instead, the observed profiles can be explained by Doppler broadening due to velocities of 10^{3-4} km s $^{-1}$ of the emitting atoms. It results in a Doppler (also called Gaussian) profile.

Forbidden lines are not observed in the BLR, indicating that they are collisionally suppressed in a high density medium ($n_e > 10^8$ cm $^{-3}$). Thus, no simple temperature and density diagnostics exists as in the NLR.

The BLR is too compact to derive its size and structure directly (typically smaller than 0.01 pc). However, broad emission lines show intensity variations with time responding to continuum variations. The response is delayed by light–travel time effects in the BLR and can be used to measure the size of the BLR by the so–called reverberation mapping technique [e.g. Peterson (1993); Wandel et al. (1999); Kaspi et al. (2000)]. Knowing the BLR size and assuming Keplerian motions, the central black hole mass can be estimated: $M_{\text{BH}} = \alpha \frac{v_{\text{BLR}}^2 R_{\text{BLR}}}{G}$ (with the proportionality factor α depending on the geometry of the BLR). Reverberation mapping results have shown a stratification of the BLR with lines from ions with higher ionization potential coming from the inner part.

1.1.2 Narrow–Line Region

The NLR has the advantage of being extended enough (typically 100 – 1000 pc) to resolve it spatially with current instruments for many (nearby) galaxies. The main resource of knowledge comes from the narrow emission lines produced by recombination in the ionized medium (e.g. Balmer lines) as well as by forbidden transitions. Their widths are in the order of 10^{2-3} km s $^{-1}$ (i.e. again significantly larger than the intrinsic line width), probably reflecting the gravitational field of stars in the host galaxy with additional components from shocks and outflows in the inner region.

Forbidden lines have zero electric dipole moments and arise from magnetic dipole or electric quadrupole transitions with low transition probability (occupation time ~ 1 s). The excited levels are called metastable. Forbidden line cooling is the most important cooling mechanism: The atoms are photoionized but the resulting ions are excited by collisions with hot electrons and re–radiate the energy subsequently. This radiation can

leave the NLR without further absorption. The observed forbidden lines of the NLR are indicative of a low density and are very useful to measure several physical parameters of the region such as temperature and electron density: The derived temperatures range from $T = 10000$ to 25000 K and the measured densities from $n_e = 10^2 - 10^4 \text{ cm}^{-3}$.

While the details of ionization mechanisms are still a matter of debate, it is generally accepted that the gas is photoionized by UV and X-ray emission from the central source. This is confirmed by the wide variety of ionization states: Both low and high ionization lines are present in many NLR spectra (e.g. [O I] and [O III]). Sometimes even iron “coronal lines” such as $[\text{Fe X}]\lambda 6375 \text{ \AA}$ can be seen which have an ionization potential of $\sim 250 \text{ eV}$ (Appendix C, Table C.2). A stratification of the NLR with either density or ionization level is still being questioned.

The NLR of many Seyfert-2 galaxies is clearly illuminated in a non-spherical way and reveals an ionization-cone structure [e.g. Pogge (1988); Tadhunter & Tsvetanov (1989); Wilson & Tsvetanov (1994)] in agreement with the unified model. The ionization cones have sharp edges in excitation maps showing that they are defined by collimation of light from the nuclear source. However, it is unclear whether the dust torus leads to the collimation of the light or if the hole in the torus has been caused by nuclear radiation, collimated already at the very center. Most of the infrared (IR) emission appears to arise on spatial scales larger than the dust sublimation radius which may provide a natural border between BLR and NLR. Thus, the role of dust cannot be neglected in the NLR and indeed, the NLR often exhibits significant amounts of dust.

NLR variability is not expected. Only long term continuum changes would show up due to the long light-travel time, but emission-line variations are damped out by the long recombination times.

The close correlation between the radio jet and the emission-line morphology indicates a close jet/NLR interaction which strongly influences the excitation and morphology of the NLR [e.g. Falcke et al. (1998)]. While the heating and ionization of the NLRs in radio-quiet AGNs seem to be dominated by photoionization, jets and winds are nevertheless important for the dynamics. Unlike the BLR, NLR emission-line profiles often do not resemble a simple Gaussian profile. They reveal a broader base and often a blueward asymmetry, possibly indicating an outflowing component on the near side of the AGN [e.g. Whittle (1985); Veilleux et al. (1990); Leipski & Bennert (2005)].

Kinematical measurements have shown that two regions of the NLR can be distinguished: While the inner part is often heavily affected by radio jets and outflows [e.g. Crenshaw et al. (2000)], the outer part reveals a velocity field characteristic of normal galactic rotation where the FWHM drops below 45 km s^{-1} [e.g. Unger et al. (1987)]. Unger et al. (1987) have proposed the new terminology “extended narrow-line region” (ENLR) to identify the outer parts of the extended ionized gas which could be attributed to interstellar gas at kiloparsec scales in the host galaxies. Photoionization by the AGN seems to be the main mechanism producing the observed emission (Morse et al., 1996; Evans et al., 1999). Often, the spectral resolution does not allow to derive kinematical properties to distinguish between NLR and ENLR. However, recent works [e.g. Crenshaw et al. (2000) and Ruiz et al. (2001)] suggest an extent of the ‘classical’ NLR of $\sim 300 \text{ pc}$.

Emission-line diagnostics provide a powerful tool to study size, structure, and dynamics of the NLR. However, the detailed structure and dynamics of the NLR as well as the nature and the origin of the gas is still unknown.

1.2 Motivation

Understanding AGNs is an important issue of contemporary astrophysics. AGNs are bright and can be used to probe the farthest reaches of the universe. The earliest AGNs may even have contributed to the re-ionization of the universe at $z \geq 6-20$ [e.g. Ricotti & Ostriker (2003)]. The most luminous and distant AGNs are associated with the formation and early evolution of galaxies. It is suspected that at least the most luminous quasars in elliptical host galaxies are triggered by the mergers of galaxies. However, this cannot apply to the less luminous AGNs: Seyferts clearly did not have such a violent past and it could be that every spiral galaxy undergoes phases of Seyfert-like activity. This is strengthened by the fact that massive BHs are not only believed to exist in the centers of active galaxies but also in nearby inactive “normal” galaxies [e.g. Kormendy & Richstone (1995), van der Marel (1999)]. Indeed, one of the most convincing evidence for a BH of more than two million solar masses has been found in the center of our Milky Way Galaxy [e.g. Eckart & Genzel (1996); Ghez et al. (1998)]. The formation of black holes and the evolution and formation of stars and galaxies seem to be closely linked as indicated by the relation between black hole mass and bulge velocity dispersion [e.g. Gebhardt et al. (2000), Merritt & Ferrarese (2001)].

Given the ubiquity of nuclear BHs in hosts with significant bulges [e.g. Gebhardt et al. (2000)], it is surprising that only 20% of today's galaxies are active. However, the detectability of AGNs seems to depend strongly on the morphological type. Ho et al. (2001) report that AGNs are very common in nearby galaxies and at least 40% of all galaxies brighter than $B_T = 12.5$ mag emit AGN-like spectra. They find an AGN rate of 50%–75% in ellipticals, lenticulars, and bulge-dominated spirals while it drops to $\leq 20\%$ in galaxies classified as Sc or later.

Defining characteristics of AGNs as used in essentially all optical surveys to find them are their broad and narrow emission lines. Thus, with the increasing interest in the population and evolution of low- and high- z AGNs in major surveys, it is essential to understand the physics and nature of the innermost emission-line regions of these active galaxies. Until today, even very basic issues remain open: For example, what determines the size and structure of these emission-line regions? Do they grow with luminosity, and if so, how? What are the physical conditions such as electron density and ionization parameter and do they vary with distance from the nucleus?

While the BLR is of great interest due to its proximity to the BH, it is too small to measure its size and structure directly with current instruments. Time-consuming observations are needed to derive the BLR size indirectly via the reverberation mapping techniques [e.g. Peterson (1993); Wandel et al. (1999); Kaspi et al. (2000)]. In addition, due to the lack of forbidden lines, its physical parameters such as temperature and electron density are not easy to derive.

In contrast, the NLR has the advantages of being sufficiently extended to be visible irrespective of aspect angle and to be directly accessible with current instruments in most galaxies. Furthermore, it provides the necessary forbidden emission-lines for diagnostic. Since the NLR and its size measurement will be affected by various parameters such as the energy input from the central engine, the presence or absence of a nuclear torus, jets, star formation or tidal interactions, it is suited to investigate a number of key elements of AGN physics.

1.3 Layout of PhD Thesis

The PhD thesis is organized as follows:

In **Chapter 2**, we use literature data to perform statistics of a large data set of Seyferts and quasars and compare sizes and luminosities of BLR and NLR. We focus on whether there is a difference of the NLR size–luminosity relation between type–1 and type–2 objects. We address a relation between BLR and NLR sizes and show how it can be used to estimate BH masses. In addition, we derive the surface–brightness profiles of the NLR to gain insights into the NLR gas distribution.

In **Chapter 3**, the previous results on the size–luminosity relation are discussed in the context of the unified scheme and the so–called receding–torus concept. We develop a model to explain the different slopes for type–1 and type–2 AGNs.

Chapter 4 summarizes the results from long–slit spectroscopic observations performed at the VLT and the NTT of the NLR of 12 Seyfert galaxies. We subtract the stellar template determined from the galaxy itself and use diagnostic line–ratio diagrams to determine the size of the NLR. CLOUDY modeling is used to discuss these observational results. We derive physical parameters of the NLR such as reddening, surface brightness, electron density, and ionization parameter as a function of distance from the nucleus. The stellar and gaseous velocity curves are compared. The results are discussed in the framework of the unified model and we address the consequences for the size–luminosity relation.

Finally, we shortly summarize our results in the concluding **Chapter 5** and end with an outlook.

In **Appendix A**, we describe the world model and the adopted Hubble constant used throughout this thesis.

Appendix B shows the surface–brightness profiles of a sample of 58 Seyfert galaxies and seven quasars imaged with the HST.

Appendix C summarizes the calculations carried out to derive several physical parameters of the NLR such as reddening, temperature, electron density, ionization parameter, and mass.

Appendix D details the uncertainty estimations making use of the error propagation equation.

NLR Size and Luminosity: Observations

In this Chapter, we address the questions of what determines the size of the NLR and how it grows with luminosity. A literature study and comparison of Seyfert and quasar data from groundbased and HST observations is performed. We additionally investigate the NLR–BLR relation and the consequences for black–hole mass estimations. Surface–brightness profiles of the [O III] emission of type–1 and type–2 AGNs are compared to find clues to the gas distribution. A short summary of a part of this Chapter was published in Bennert et al. (2004b).

2.1 Introduction

The NLR size and its dependency on luminosity plays a key role in NLR physics. First, it gives a geometric estimate to AGN lifetimes (t_{AGN}), one of the most fundamental quantities for understanding BH accretion history and AGN evolution: Measuring AGN lifetimes will answer the question whether quasars are a common stage of galaxy evolution (t_{AGN} short) or a rare one (t_{AGN} long). If the NLR is ionization bounded, the size of the ionized region sets a lower limit to the lifetime of the ionizing source (Martini & Schneider, 2003a). Second, a relation between size and luminosity would provide insights into the nature of the photoionizing mechanism. Third, a size–luminosity relation may provide an independent measure of the central black hole mass.

A size–luminosity relation has been found for the BLR of 17 Seyferts and 17 quasars from reverberation mapping (Kaspi et al., 2000). However, the slope is discussed controversially: While Kaspi et al. (2000) report a relation of $R_{\text{BLR}} \propto L^{0.7}$, McLure & Jarvis (2002) find $R_{\text{BLR}} \propto L^{0.5}$. They rely on the same observational data but use different methods to derive the BLR sizes. The discrepancy in slope reflects the difficulty to use time lags as BLR size estimators and caution must be exercised as there are various assumptions involved (Kaspi et al., 2000).

We recently performed an HST imaging survey in the [O III] line using linear–ramp filters (LRFs) of a complete sample of the seven brightest [in [O III]; Boroson & Green (1992)] radio–quiet Palomar Green (PG) quasars from the Bright Quasar Survey (Schmidt & Green, 1983; Kellermann et al., 1989) with $z < 0.5$ and, for the first time, investigated the NLR size–luminosity relation (Bennert et al., 2002).

We found a relation $R_{\text{NLR}} \propto L_{[\text{O III}]}^{0.5}$ when including a sample of seven Seyfert–2 galaxies observed in a very similar fashion (Falcke et al., 1998). This result suggests a self-regulating mechanisms which determines the size to scale with the ionization parameter. It is not clear whether this new NLR size–luminosity relation will hold at all luminosities and redshifts. If, for example, the luminosity–scaled size of the NLR becomes larger than the size of the galaxy, the relation may flatten as the emission lines fade out and disappear (Netzer et al., 2004). This may be evident already in some spectral line studies of Two Degree Field (2dF) quasars (Croom et al., 2002).

Another issue concerns possibly different scalings for Seyferts and quasars. In response to the Bennert et al. (2002) results, Schmitt et al. (2003b) report a NLR size–luminosity relation which follows $R_{\text{NLR}} \propto L_{[\text{O III}]}^{0.33}$. While a slope of 0.33 as found for the Seyfert sample corresponds to that expected for a simple Strömngren law (valid only in the case of constant density), a slope of 0.5 has been explained by a constant ionization parameter (Bennert et al., 2002).

What causes the apparent different slopes for our quasar–dominated sample and their Seyfert sample: simple statistical uncertainty or selection effects? Are the NLRs of Seyferts and quasars intrinsically different? Given the fact that Seyferts seem to be lower luminosity cousins of quasars, this explanation seems to be very unlikely. Or is there a difference in the NLR size–luminosity relation between type–1 and type–2 objects?

Here, we address these questions: We describe the HST and groundbased data for the BLR and the NLR taken from literature (Section 2.2), and discuss the NLR size–luminosity relation, the BLR–NLR size relation, as well as the NLR surface–brightness profiles (Section 2.3). The Chapter ends with our conclusions (Section 2.4).

2.2 Data

We use data of the most extensive narrow–band imaging studies of the morphologies and sizes of Seyfert and quasar NLRs.

The HST Seyfert NLR data from Schmitt et al. (2003a) comprise a snapshot survey of the extended [O III] emission of 60 nearby Seyfert galaxies (22 Seyfert 1’s and 38 Seyfert 2’s) selected based on their far infrared properties (Kinney et al., 2000) and measured using mainly LRFs. Henrique Schmitt kindly provided us with the reduced and continuum–subtracted [O III] images of a sample of 58 Seyfert galaxies from Schmitt et al. (2003a). Additionally, 2 Seyfert 2’s from Falcke et al. (1998) as well as seven radio–quiet PG quasars ([O III] flux $> 6 \cdot 10^{-14}$ erg s $^{-1}$ cm 2 ; $z \leq 0.5$) observed in a very similar fashion with the HST using LRFs (Bennert et al., 2002) were included.

To compare these HST data with NLR groundbased data, we used the sample of Mulchaey et al. (1996a) consisting of 56 Seyfert galaxies observed in [O III]. From this sample, we excluded four objects with unknown or controversial Seyfert type.

The NLR sizes were compared to those of the BLR. The BLR radii were measured by Wandel et al. (1999) and Kaspi et al. (2000) via reverberation mapping using a spectrophotometrically monitored sample of 17 Seyfert–1 galaxies and 17 PG quasars ($z \leq 0.5$). To increase the number of objects with known BLR *and* NLR sizes, we additionally included the NLR sizes of three objects (Schmitt & Kinney, 1996) to the BLR–NLR size comparison, measured with the HST in the [O III] line–emission.

All sizes and luminosities were re–calculated according to the world model used throughout this PhD thesis (Appendix A).

2.3 Results and Discussion

2.3.1 NLR Size and Luminosity

HST data

We compared the NLR size with the [O III] luminosity of the HST sample of 62 Seyferts and seven PG quasars (Fig. 2.1, *left panel*). Although such a comparison was already presented by Schmitt et al. (2003b), we applied a fit to all type-1 AGNs and type 2s separately. This is missing in Schmitt et al. (2003b), but may give a crucial hint to why Bennert et al. (2002) and Schmitt et al. (2003b) observed different slopes in the size-luminosity relation (Chapter 1, Section 2.1). The results of the different fits are summarized in Table 2.1. As pointed out by Schmitt et al. (2003b), the uncertainty in the measurement of R_{NLR} is smaller than 10%, so the data were fit using uniform weighting of the points. While a fit to all objects yields a $R_{\text{NLR}} \propto L_{[\text{OIII}]}^{0.44 \pm 0.03}$ relation, type-1 objects seem to follow the relation $R_{\text{NLR},1} \propto L_{[\text{OIII}]}^{0.55 \pm 0.05}$, and type-2 objects are fit with approximately a Strömgen-law ($R_{\text{NLR},2} \propto L_{[\text{OIII}]}^{0.32 \pm 0.05}$).

This result indeed explains the different slopes found by the two groups: In the Bennert et al. (2002) sample, basically type-1 quasars define the slope resulting in a value of 0.5, whereas the slope of the Schmitt et al. (2003a) sample is dominated by Seyfert-2 galaxies which outnumber the Seyfert-1 galaxies by a factor of 1.4, simulating a slope of 0.33.

Note, however, that the observational data show a large scatter, especially for Seyfert-1 galaxies. One has to keep in mind that all Sy1s, Sy1.2s and Sy1.5s were included in the type-1 group, while all Sy1.8s, Sy1.9s and Sy2s were combined in the type-2 group. Also, morphological peculiarities (e.g. presence of dust clouds) will produce scatter.

Groundbased data

Additionally, we compared NLR sizes and [O III] luminosities from groundbased data of 52 Seyferts (Mulchaey et al. (1996a); Fig. 2.1, *right panel*) and find similar relations: Fitting all Seyferts yields a slope of 0.38 ± 0.04 . Calculating a fit to type-1 and type-2 separately, the type dependency of the slope of the NLR size-luminosity relation persists: While type-1 AGNs follow a relation $R_{\text{NLR},1} \propto L_{[\text{OIII}]}^{0.46 \pm 0.06}$, type 2s are fit with $R_{\text{NLR},2} \propto L_{[\text{OIII}]}^{0.34 \pm 0.06}$ (Table 2.1).

HST versus groundbased data

When comparing the Mulchaey et al. (1996a) and Schmitt et al. (2003a) NLR size and luminosity measurements for those Seyferts included in both samples, we find a large discrepancy of the NLR size measurements: The groundbased NLR sizes are on average six times larger. A serious drawback of the Schmitt et al. (2003a) HST snapshot survey is the 15 to 20 times lower sensitivity which may explain their much smaller NLR sizes. Another limitation of the HST data is the field-of-view of the linear-ramp filter ($\sim 13''$).

Table 2.2 give the radii along the semi-major axis and the [O III] luminosities for the nine galaxies common to both samples.

The ratio between the NLR sizes obtained in the two surveys varies between 2.5 and 10.6; on average, Mulchaey et al. (1996a) find 5.9 ± 0.9 times larger NLRs.

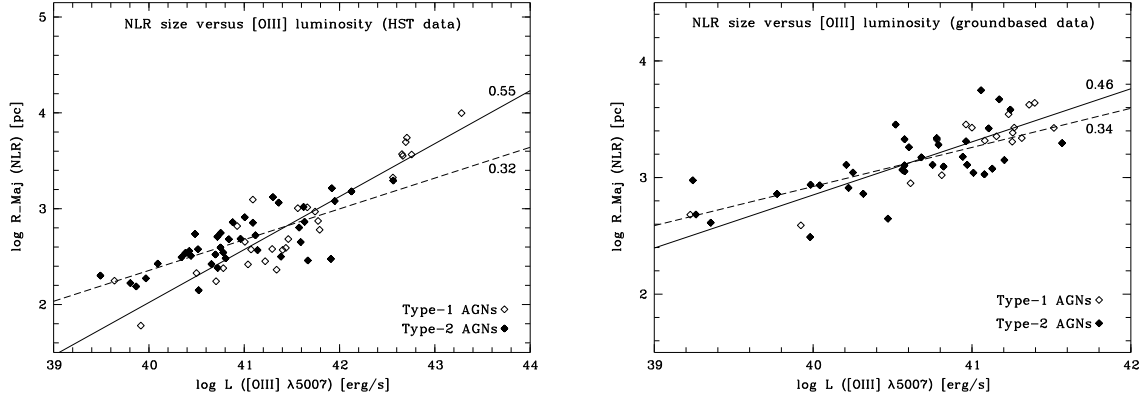


Figure 2.1: *Left panel:* Radius of the NLR versus the emission-line luminosity in [O III] on logarithmic scales (from HST data). The open symbols are type-1 AGNs, the filled ones type-2. While the solid line represents the fit to type-1 AGNs ($R_{\text{Maj}}(\text{NLR}) \propto L_{[\text{OIII}]}^{0.55 \pm 0.05}$), the dashed line corresponds to the fit to type-2 AGNs ($R_{\text{Maj}}(\text{NLR}) \propto L_{[\text{OIII}]}^{0.32 \pm 0.05}$). *Right panel:* The same as in the *left panel* for groundbased data. While the solid line represents the fit to type-1 AGNs ($R_{\text{Maj}}(\text{NLR}) \propto L_{[\text{OIII}]}^{0.46 \pm 0.06}$), the dashed line corresponds to the fit to type-2 AGNs ($R_{\text{Maj}}(\text{NLR}) \propto L_{[\text{OIII}]}^{0.34 \pm 0.06}$).

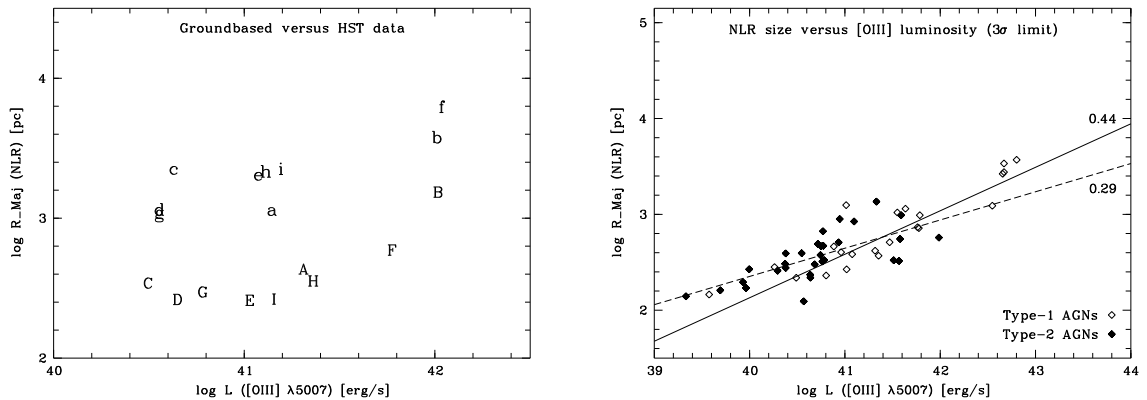


Figure 2.2: *Left panel:* Comparison of NLR size and [O III] luminosity for nine galaxies from groundbased data (Mulchaey et al., 1996a) (small letters) and HST data (Schmitt et al., 2003a) (capital letters). The corresponding galaxies are marked with the same letters (see Table 2.2 to attribute the letters to the galaxies). *Right panel:* The same as in Figure 2.1 for HST data with the same sensitivity. While the solid line represents the fit to type-1 AGNs ($R_{\text{Maj}}(\text{NLR}) \propto L_{[\text{OIII}]}^{0.44 \pm 0.04}$), the dashed line corresponds to the fit to type-2 AGNs ($R_{\text{Maj}}(\text{NLR}) \propto L_{[\text{OIII}]}^{0.29 \pm 0.06}$).

Table 2.1: NLR size–luminosity relations and NLR–BLR relation

x	y	Data	Data Points	m	k	cc
$\log L_{[\text{OIII}]}$	$\log R_{\text{Maj}}$ (NLR)	HST ^a	All (69)	0.44 ± 0.03	-15.2 ± 1.3	0.85
			Type 1 (29)	0.55 ± 0.05	-20.1 ± 1.9	0.73
			Type 2 (40)	0.32 ± 0.05	-10.5 ± 1.8	0.76
$\log L_{[\text{OIII}]}$	$\log R_{\text{Maj}}$ (NLR)	Groundbased ^b	All (52)	0.38 ± 0.04	-12.3 ± 1.8	0.77
			Type 1 (17)	0.46 ± 0.06	-15.4 ± 2.6	0.88
			Type 2 (35)	0.34 ± 0.06	-10.5 ± 2.5	0.68
$\log L_{[\text{OIII}]}$	$\log R_{\text{Maj}}$ (NLR)	HST, 3σ limit ^c	All (52)	0.38 ± 0.03	-12.8 ± 1.3	0.86
			Type 1 (22)	0.44 ± 0.04	-15.2 ± 1.9	0.91
			Type 2 (40)	0.29 ± 0.06	-9.4 ± 2.3	0.69
$\log L_{[\text{OIII}]}$	$\log R_{\text{Maj}}$ (NLR)	HST, 50% ^d	All (50)	0.29 ± 0.05	-9.9 ± 2.2	0.61
			Type 1 (18)	0.42 ± 0.09	-15.2 ± 3.6	0.76
			Type 2 (32)	0.27 ± 0.08	-9.0 ± 3.2	0.53
$\log R_{\text{Maj}}$ (NLR)	$\log R$ (BLR)	HST ^e	Type 1 (11)	0.88 ± 0.10	-4.1 ± 0.3	0.86

Note. – Units of R and L are parsec and erg s^{-1} , respectively. We give the slope m and the y-axis intercept k of the linear fits ($y = mx + k$) as well as the correlation coefficient cc. The fits were applied to either all data points, type-1 AGNs or type-2 AGNs only, with the number of objects included given in brackets.

^a Comparing HST data of Schmitt et al. (2003a) and Bennert et al. (2002)

^d Taken from Mulchaey et al. (1996a)

^c HST data with the same surface-brightness limit

^d Radius in which 50% of total [O III] luminosity is included

^e BLR sizes from reverberation mapping (Wandel et al., 1999; Kaspi et al., 2000)

While the difference in measured sizes is large possibly due to different sensitivities, the deviations in luminosity are small and the ratios scatter around 1 (on average $L_{[\text{OIII}]}$ (groundbased/HST) $\sim 1.01 \pm 0.13$). One would expect that the larger NLR sizes of Mulchaey et al. (1996a) derived with higher sensitivity should result in higher luminosities. This is not the case for four out of nine objects, probably due to photometric errors such as different continuum subtraction.

In Figure 2.2 (*left panel*), we compare these nine galaxies in the size–luminosity diagram individually: While the luminosity difference is small and scatters around 1, there is a clear shift towards larger sizes measured from the groundbased data.

The comparison between groundbased and HST data indicates that most of the flux is included in the central region and that the extended flux does not contribute much to the total flux. The fact that different sensitivities result in different sizes shows that “size” is not a well defined quantity.

HST data to the same surface–brightness limit

One major problem indicated by the different results above is the definition of the size of the NLR. The comparison of groundbased and HST data shows that it depends on the sensitivity limit used. The NLR size–luminosity relation for groundbased data is “self consistent”: Mulchaey et al. (1996a) used values corresponding to the same surface–brightness limit. To first order, the HST data of Schmitt et al. (2003a) and Bennert et al. (2002) are also comparable in terms of surface–brightness limits, as they were taken with the same telescope, instrument configuration and approximately the same integration time (see their Table 2 in both publications). However, the 3σ values used as reference to determine the size and luminosity by Schmitt et al. (2003a) show a scatter of 2 to $14 \cdot 10^{-17} \text{ erg s}^{-1} \text{ cm}^{-2} \text{ pix}^{-1}$. Therefore, we re-analyzed both the Schmitt et al. (2003a) data and the Bennert et al. (2002) data and determined size and luminosity to the same surface brightness level $\sigma_{\text{all}} = 6 \cdot 10^{-17} \text{ erg s}^{-1} \text{ cm}^{-2} \text{ pix}^{-1}$. We used this limit to not exclude too much of faint extended emission and to include as many objects as possible. We had to exclude 13 Seyfert galaxies from the Schmitt et al. (2003a) sample and 2 quasars. (Note that the two Seyferts from Falcke et al. (1998) were not re-analyzed.)

To take into account the cosmological dimming, we calculated $\sigma_z = \frac{\sigma_{\text{all}}}{(1+z)^4}$. We repeated the same procedure as carried out by Schmitt et al. (2003a), i.e. plotted each galaxy to the corresponding $3\sigma_z$ [O III] contour and measured the major radius R_{Maj} directly. The flux was integrated along this contour. Both pixel radius and flux were calculated to radius in pc and luminosity in erg s^{-1} (Appendix A). The NLR size–luminosity relation is shown in Figure 2.2 (*right panel*). Again, there is a difference in slope between type–1 and type–2 objects: While type 2s can be fitted with $R_{\text{Maj}}(\text{NLR}) \propto L_{[\text{OIII}]}^{0.29 \pm 0.06}$, type 1s follow a steeper slope of 0.44 ± 0.04 . Both slopes flatten in comparison with the previous results (Table 2.1).

However, also the “ 3σ size” definition may not measure the “real” NLR size as it depends on the sensitivity of the survey.

NLR size at 50% of total luminosity

Here, we use an alternative NLR size definition: We determine the radius at which 50% of the total integrated [O III] luminosity is included, to be less dependent on sensitivity and the detection of extended emission.

Table 2.2: Comparison of HST and groundbased data

Seyfert galaxy	R_{Maj} (gb)	R_{Maj} (HST)	R_{Maj} (gb/HST)	$L_{[\text{O III}]}$ (gb)	$L_{[\text{O III}]}$ (HST)	$L_{[\text{O III}]}$ (gb/HST)
Mrk 348 (A/a)	1152	434	2.7	14.03	20.64	0.7
Mrk 573 (B/b)	3791	1535	2.5	102.49	103.80	1.0
Mrk 607 (C/c)	2265	343	6.6	4.26	3.13	1.4
ESO 33-G02 (D/d)	<1155	263	<4.4	3.60	4.46	0.8
MCG -05-13-017 (E/e)	2056	259	7.9	11.82	10.68	1.1
Mrk 6 (F/f)	6261	592	10.6	109.37	59.63	1.8
Mrk 622 (G/g)	<1105	297	<3.7	3.58	6.06	0.6
Mrk 705 (H/h)	2161	356	6.1	13.03	23.08	0.6
NGC 4253 (I/i)	2258	264	8.6	15.65	14.36	1.1

Note. – Unit of R and L are parsec and erg s^{-1} , respectively. For nine Seyfert galaxies (in brackets, we give the corresponding letter used in Fig. 2.2), the NLR radii and [O III] luminosities from groundbased images (gb) (Mulchaey et al., 1996a) are compared with those from HST images (Schmitt et al., 2003a).

As total integrated [O III] luminosity we used the values from Schmitt et al. (2003a) and Bennert et al. (2002). Aperture photometry using IRAF was performed to determine the radius at which 50% of the total flux is included.

To use only those objects for which the corresponding central region is resolved, we compared the results with the instrumental point–spread function (PSF) of an unresolved source. For this purpose, we determined the PSF of a star imaged with the HST on the WF and PC chips using linear–ramp filters. [These stars were included in the calibration process of the quasar images of Bennert et al. (2002).]

The PSF can be approximated with a Gaussian profile defined as (a = peak height; c = FWHM):

$$\text{Gauss}(x; a, c) = a \cdot \exp \left[-\ln 2 \left(\frac{2x}{c} \right)^2 \right] . \quad (2.1)$$

The corresponding FWHM is $0''.2$ for the WF chip and $0''.065$ for the PC chip.

To derive the flux in a three dimensional Gaussian of this form, we calculated the rotational integral by rotating the Gaussian around the y –axis:

$$I(\text{Gauss}_{3D}) = \pi \int_0^a x^2 dy \quad (2.2)$$

$$= \pi \int_0^a \frac{-c^2}{4 \ln 2} \cdot (\ln y - \ln a) dy \quad (2.3)$$

$$= \frac{\pi}{4 \ln 2} \cdot ac^2 . \quad (2.4)$$

We inserted the measured central peak of the [O III] emission as a and used the FWHM of the star for c .

Now, we compared the luminosity included in an unresolved Gaussian profile centered at the peak emission of each object with the total integrated luminosity by building the ratio $L_{\text{Gauss}}/L_{\text{tot}}$. If this ratio is smaller than 0.5, it implies that the central region emitting 50% of the total [O III] emission is resolved. Only these objects were included in calculating the size–luminosity relation at 50% total luminosity (Table 2.1; Fig 2.3, *left panel*). In total, we excluded 15 objects (23%) which emit more than 50% of their total luminosity in an unresolved central source. The resulting fit shows that again type–1 AGNs follow a steeper slope of 0.42 compared to that of type 2s (0.27).

The majority of objects with unresolved central emission are type 1s (36% versus 11% of Sy2s).

When comparing the ratios for 25% of luminosity, the same general difference between type–1 and type–2 AGNs persists: 86% of type–1 objects emit more than 25% of their total luminosity in an unresolved central source while only 50% of Seyfert 2s emit the same amount from an unresolved source.

However, apart from this general trend, comparing the ratio $L_{\text{Gauss}}/L_{\text{tot}}$ with the total amount of emitted [O III] luminosity does not show a significant relation. The objects scatter individually between 1% and 90% of total luminosity emitted from an unresolved central source (Fig. 2.4, *left panel*).

Considering the quasars alone, all seven quasars emit more than 25% of their total luminosity in an unresolved central source, which is, given their distances, not surprising (a FWHM of $0''.2$ corresponds to on average 635 pc).

The observational bias involved when comparing objects at different distances is already visible when comparing the Seyfert galaxies alone (Fig. 2.4, *right panel*), at least for Seyfert 2s: In general, in distant galaxies, more luminosity is emitted from an unresolved central source. However, the individual scatter is rather large. For Seyfert–1 galaxies, this trend is not that obvious: There are nearby type–1 objects which already emit most of their luminosity from an unresolved central source.

When comparing the radius, at which 50% of the luminosity is emitted, to the major NLR radius of the total integrated luminosity determined by Schmitt et al. (2003a) and Bennert et al. (2002), the different types are remarkably similar: Seyfert–1 galaxies, Seyfert–2 galaxies, and quasars have on average 1.3 ± 0.1 times larger 3σ radii than the radii at which 50% of the total luminosity is emitted.

Generally, the [O III] emission has been considered as largely orientation–independent measure of the intrinsic luminosity of AGNs [e.g. Mulchaey et al. (1994); Falcke et al. (1995)]. However, the question arises whether the [O III] emission from the central part may be obscured in type–2 AGNs resulting in an underestimation of the total [O III] luminosity. On the contrary, type–1 AGNs may be subject to a larger obscurational effect if the torus absorbs [O III] emission from the counter cone (see also our discussion in Chapter 3).

Apart from the dust torus, one needs to take into account the different line–of–sight integrations, when comparing type–1 and type–2 AGNs under the assumption that the unified model is valid: For type 1s, the integrational path at a viewing angle near 0° is long in the center where we sum up all the line flux emitted along the line–of–sight. (Note that [O III] is emitting optically thin.) For type 2s observed nearly perpendicular to the ionization cone, the integrational path through the ionized gas at the apex of the cone is rather short and increases with distance from the center. Thus, from line–of sight arguments alone, it is evident that we possibly miss extended [O III] emission in Seyfert–1 galaxies due to the small line–of–sight integration through a putative ionization cone at the edge of the NLR (whereas in type–2 objects, we integrate over a large volume of emitting gas). We expect to see more centrally concentrated flux for type–1 AGNs than type 2s, in agreement with our observations. We will come back to the viewing angle dependency of radial distributions in Chapter 4 (Section 4.4.11).

However, from the observations and the comparisons presented above, we estimate that the [O III] luminosity in both objects is comparable within a factor of 2.

2.3.2 Consequences of the NLR Size–Luminosity Relation

In general, the NLR size–luminosity relation predicts an increase of the NLR size with luminosity, but seems to have different slopes for type–1 and type–2 objects. Is this further evidence for a deviation from the simple unified scheme or can it be made consistent with projection effects? One has to keep in mind that the size determination is only straightforward in type–2 AGNs, but more difficult in type 1s, due to the foreshortening of the latter. Alternatively, does the opening angle of the obscuring torus increase with luminosity and thus changes the measured NLR size towards higher luminosity? While we develop a model to explore these issues in Chapter 3, we here discuss possible physical interpretations of the relation.

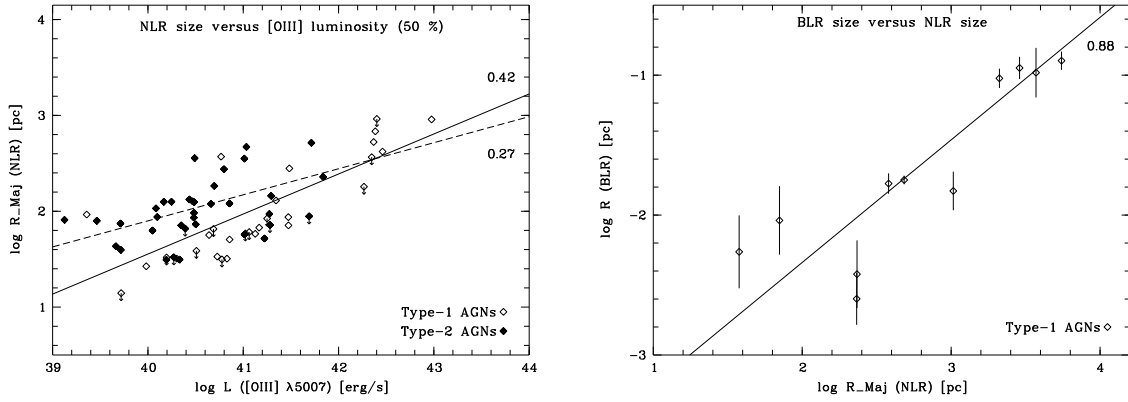


Figure 2.3: *Left panel:* The same as in Figure 2.1 for HST data with the NLR radius determined at 50% of total luminosity. Only objects for which 50% of the luminosity comes from a resolved central source were included in the fit (the others are marked by down arrows). While the solid line represents the fit to type-1 AGNs ($R_{\text{Maj}} \text{ (NLR)} \propto L_{[\text{OIII}]}^{0.42 \pm 0.09}$), the dashed line corresponds to the fit to type-2 AGNs ($R_{\text{Maj}} \text{ (NLR)} \propto L_{[\text{OIII}]}^{0.27 \pm 0.08}$). *Right panel:* Distribution of NLR and BLR radii on logarithmic scales. The error bars indicate the uncertainty in defining the BLR radius. The solid line represents the fit corresponding to $R \text{ (BLR)} \propto R_{\text{Maj}} \text{ (NLR)}^{0.88 \pm 0.1}$.

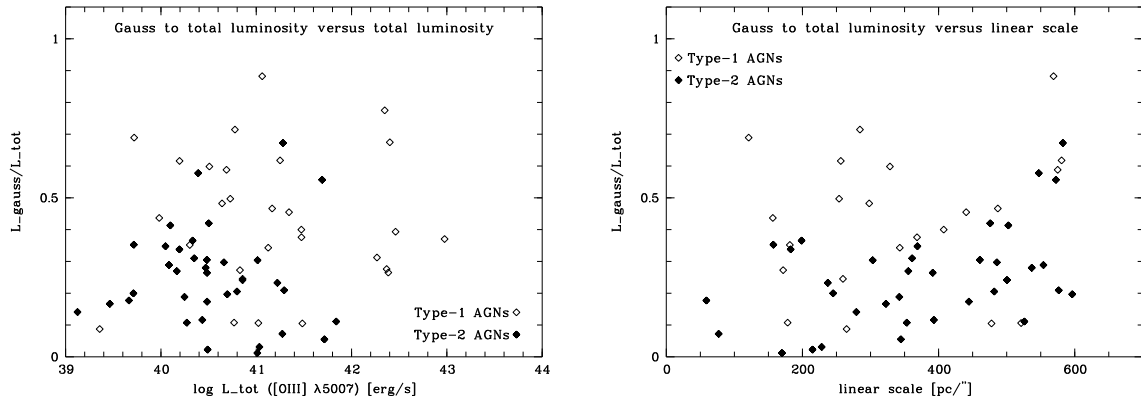


Figure 2.4: Ratio of luminosity included in an unresolved Gaussian profile (centered at the peak emission of each object) to total integrated [O III] luminosity. In the *left panel*, we compare this ratio to the total integrated [O III] luminosity. Apart from Seyfert-1 galaxies showing on average a larger fraction of luminosity emitted in a central unresolved source, no general trend is seen. In the *right panel*, the ratio of Gaussian to total luminosity is compared to the distance of the galaxy, given as linear scale in $\text{pc}/''$. Although the galaxies show a large scatter, the observational bias can be seen, especially for type-2 objects, which results in more distant galaxies to emit more luminosity from an unresolved source.

To compare the slopes of the NLR size–luminosity relation for type–1 and type–2 AGNs, we averaged the slopes derived with different methods and data sets (HST data, HST data to the same surface–brightness limit, HST data with radius at 50% luminosity, groundbased data). As all methods and data sets have their intrinsic errors, we decided to use the averaged value instead of referring to one specific result. We get a slope of 0.31 ± 0.02 for type–2 AGNs and a slope of 0.47 ± 0.03 for type–1 AGNs. While a slope of 0.5 is expected for a constant ionization parameter, a slope of 0.33 is suggestive of a Strömrgren relation.

Constant ionization parameter

The slope of 0.47 for the type–1 AGNs is close to a slope of 0.5 found by Bennert et al. (2002) and can be explained in terms of a constant ionization parameter. We here briefly summarize their argumentation: Considering a recombination line like H β , rather than [O III], the ionization parameter is given by $U = Q/(4\pi cn_e R_u^2)$ (Q = rate of H–ionizing photons, R_u = distance between photoionizing source and emission–line clouds). To infer the number of ionizing photons produced per seconds from the H β luminosity, we use the relation $\omega Q = \alpha_B/(\alpha_{H\beta} h\nu_{H\beta}) L_{H\beta} = 3.1 \cdot 10^{12} L_{H\beta}$ (cgs units; ω is the covering factor and the recombination coefficients $\alpha_B = 2.59 \cdot 10^{-13} \text{ cm}^3 \text{ s}^{-1}$ and $\alpha_{H\beta} = 2.04 \cdot 10^{-14} \text{ cm}^3 \text{ s}^{-1}$ are taken from Osterbrock (1989) for $T = 10^4$ K, pages 19, 79).¹ This relation between Q and $L_{H\beta}$ yields a relation $R_u \propto L_{H\beta}^{0.5}$ for given U , n_e and constant ω . Bennert et al. (2002) show that such a relation is indeed derived for the size versus the luminosity in H β . If most of the [O III] emission originates from ionization–bounded clouds as suggested by the fairly uniform value of the ratio of [O III] flux to narrow H β flux, the relation $R \propto L_{H\beta}^{0.5}$ can be replaced by $R \propto L_{[\text{O III}]}^{0.5}$ (Netzer et al., 2004). At the outskirts of the NLR, $n_e \sim 10^{2-3} \text{ cm}^{-3}$, $U \sim 10^{-(2-3)}$, so that efficient [O III] emission comes from regions with $Un_e \approx 1$, corresponding to an ionizing flux $Q/(4\pi R_u^2) = 3 \cdot 10^{10}$ photons/(s cm²).

For nearly three decades now, the similarity of the narrow–line spectrum in low and high luminosity AGNs has suggested a common effective value of U as well. Basically three models have been proposed to explain the apparent uniformity in ionization conditions: (a) a model that includes strong action of a quasar wind on the NLR clouds (Schiano, 1986); (b) models that involve drastic effects of radiation pressure on dusty NLR clouds (Dopita et al., 2002); (c) models that take into account a wide range of cloud properties, which has an overall smoothing effect, and which describe remaining observational spread mainly by a slight variation of the ionizing continuum (Komossa & Schulz, 1997).

A slope of 0.5 is comparable to the slope of the BLR size–luminosity relation, indicating that both the BLR and the NLR gas are photoionized by a the central source which has an ionizing spectral energy distribution which is roughly independent of luminosity.

To conclude, such a slope can be explained if, on average, all AGNs have the same ionization parameter, density, and ionizing spectral energy distribution (Netzer, 1990; Netzer et al., 2004).

¹ Using this formula, we make the assumption that we have ionization equilibrium, i.e. the number of ionizing photons produced by the central source is equal to the total number of recombinations over the ionized volume; see also Peterson (2003) for a detailed discussion.

Strömgren law

A slope of 0.31 found for type-2 AGNs seems to follow a simple Strömgren law (0.33) and was reported by Schmitt et al. (2003b) for their Seyfert sample. Although the geometry of an AGN, with the NLR being distributed in a sphere, is in principle consistent with this picture, it is valid only in the case of constant density. Furthermore, the exponent of 0.33 defines only the slope and does not take into account the proportionality factors. A direct comparison between the measured radius and the one expected for a Strömgren sphere is in principle possible. Again, this can be done for a recombination line like H β : The Strömgren radius is given as $R_s = \left(\frac{3Q}{4\pi\alpha_B}\right)^{0.33} \cdot n_H^{-0.66}$. As above, Q is the rate of H-ionizing photons ($Q = 3.1 \cdot 10^{12} L_{H\beta}$ in cgs units for $T = 10^4$ K) and α_B the recombination coefficient. Using these values, individual Strömgren radii can be calculated from $R_s \simeq 142 \cdot 10^6 \cdot L_{H\beta}^{0.33} \cdot n_H^{-0.66}$, if the H β luminosity is known.

In the optical spectroscopic atlas of low-redshift AGNs of Marziani et al. (2003b), we found H β /[O III] ratios for six Seyfert-1 galaxies. Multiplying this ratio by the measured [O III] luminosities from Schmitt et al. (2003a), we calculated the H β luminosities and therewith the expected Strömgren radius. Note that for Seyfert-2 galaxies, these ratios are generally too low, as the broad H β is hidden by the dust torus. Boroson & Green (1992) found for example that only $\sim 3\%$ of the total H β flux is visible as the narrow-line component. Therefore, the observed H β flux is not a good tracer of the total AGN luminosity for Seyfert-2 galaxies. (Although also for Seyfert-1 galaxies, extended narrow H β flux may have been missed in these spectroscopic measurements, this flux is negligible compared to the total H β flux for the same reasons.) We used the typical density range for NLRs ($100 \text{ cm}^{-3} \leq n_e \leq 10000 \text{ cm}^{-3}$) and compared the Strömgren radius calculated this way with the measured NLR size in [O III].

The results are summarized in Table 2.3: The observed radii are 1.3 to 100 times larger than those expected for a Strömgren sphere, depending on the assumed (constant) electron density.

An assumption involved in this comparison is that the NLR size measured from the H β recombination line is similar to the size traced by the [O III] emission line, originating from a collisionally excited level. For example, Falcke et al. (1998) and Ferruit et al. (2000) showed that the H α and [O III] images of Seyfert galaxies have similar structures and extents (excluding Balmer emission from surrounding H II regions). Thus, in a first approximation, the assumption that the measured radius in [O III] is comparable to the one in H β should be valid.

In Fraquelli et al. (2003), the density in the nuclei of 18 Seyfert-2 galaxies ranges from 300–1000 cm^{-3} with an average density of 440 cm^{-3} . Using this average density, the measured NLR radii are five times larger than the radii expected for gas distributed in a Strömgren sphere. A possible explanation for this discrepancy is that the density is not constant but decreasing with distance from the nucleus. Indeed, several authors observe a decreasing density with distance from the nucleus [e.g. Storchi-Bergmann et al. (1992a), Fraquelli et al. (2000), Fraquelli et al. (2003)]. We will come back to this issue in Chapter 4 when discussing the results of our long-slit spectroscopic measurements (Section 4.4.8).

However, the comparison of the Strömgren sphere with the observed NLR size may not be straightforward and simply applicable, even if the electron density is constant.

Table 2.3: Observed NLR radius versus expected Strömgen radius

Seyfert galaxy	R_{NLR}	$R_{\text{s}}(100)$	$R_{\text{s}}(10000)$	$R_{\text{NLR}}/R_{\text{s}}(100)$	$R_{\text{NLR}}/R_{\text{s}}(10000)$
Mrk 590	385	222	10	1.72	33
Mrk 705	350	184	9	1.92	50
NGC 3783	175	134	6	1.30	25
Mrk 766	255	81	4	3.10	100
NGC 4593	150	98	5	1.52	33
NGC 5548	450	177	8	2.56	50

Note. – Unit of R is parsec. R_{NLR} is the major NLR radius given in Schmitt et al. (2003a). R_{s} is the expected Strömgen radius calculated with electron densities $n_e = 100 \text{ cm}^{-3}$ and $n_e = 10000 \text{ cm}^{-3}$, respectively.

First, if the gas is distributed in a sphere, there is an ionization cone determining the shape of the NLR emission. In that case, the NLR size corresponds to the size of a Strömgen sphere only for a viewing angle close to the cone axis. For other viewing angles, the measured projected NLR size is a function of viewing angle and opening angle of the torus (see Chapter 3). Second, the NLR gas needs not to be distributed in a sphere but can as well be distributed in e.g. a disk.

Disappearing narrow–line region

Independent of the slope, the NLR size–luminosity relation implies an increasing NLR size with luminosity. Extrapolating the correlation to very high luminosities predicts an NLR size of galactic scale dimensions and, in principle, even in excess of the host galaxy. The effect of very high luminosities on the NLR size was already pointed out by Croom et al. (2002) who report a decrease in the equivalent width of several narrow lines with source luminosity. They suggest that at least part of this effect is due to the increase in NLR size with source luminosity, leading to galactic scale dimensions in the most luminous objects. Such NLRs are likely to escape the system, leading to AGNs with weak or no NLR emission.

To investigate this effect, Netzer et al. (2004) study near–infrared long–slit spectra of 29 high–luminosity quasars with $2 < z < 3$: Approximately 1/3 of their sources lack any sign of [O III] while 2/3 are still very strong [O III] emitters. For both classes, luminous (broad) H β emission was found. They propose a scenario in which two distinct populations of quasars exist at high redshift: For one population, the scaling of the known NLR size–luminosity relations continues to high luminosities. But combining the measured FWHMs with the escape velocities at these large radii yields an NLR that is dynamically unbound and likely to leave the galaxy. This results in short–lived, enormous NLRs following the size–luminosity relation but which cannot be maintained for long periods. The NLR gas will disappear, resulting in a quasar which will show basically no nuclear narrow emission lines during most of its life. The other population shows very prominent nuclear [O III] emission that, in contrast to the first population, argues for unusual dense NLR environments, capable of producing high emission–line luminosities in small volumes.

If such a scenario can be confirmed it implies a major evolution of quasar emission-line regions. The change in NLR density, and thus covered volume, will result in the flattening of the size–luminosity relation at high luminosities. Moreover, a disappearing NLR will have serious implications for searches of luminous type–2 quasars which simply may not have luminous narrow emission line regions.

We cannot answer these open questions at present. Observations of high– z quasars are needed to probe whether their NLR properties are different to today's NLRs and whether indeed different quasar populations do exist. The NLR size–luminosity relation seems to be valid at least up to redshifts of $z \sim 0.5$ but it still needs to be verified for AGNs at higher redshifts.

2.3.3 BLR Size and NLR Size

Here, we compare the scaling of NLR and BLR sizes. Given that for type–1 objects, both NLR and BLR size scale with roughly the square root of luminosity, an approximately linear correlation of BLR–NLR sizes is expected. To prove this, we collected all BLR sizes measured so far (only type–1 objects) and their corresponding NLR sizes. Unfortunately, the overlap is rather poor and leaves us with 11 objects (Fig. 2.3; *right panel*). As the uncertainty in estimating the BLR size can be quite high, we applied a weighted linear least–squares fit (weight = σ^{-2} , where σ is the standard error in $\log R_{\text{BLR}}$) and tentatively find, that the sizes of NLR and BLR are proportional: $R_{\text{BLR}} \propto R_{\text{NLR},1}^{0.88 \pm 0.1}$ (Table 2.1).

While the NLR size seems to be determined by a lack of ionizing photons, dust sublimation theory may provide a natural explanation of the BLR limit:

Consider a (spherical symmetric) dust particle with radius r located at a distance R of a central source with luminosity L_{UV} . (The UV luminosity mostly provides heating and photoevaporation of dust). The particle absorbs the emission with πr^2 and re–emits with $4\pi r^2$. Assuming that the particle emits like a black body, its temperature can be derived from (with σ = Stefan–Boltzmann constant)

$$L_{\text{dust}} = 4\pi\sigma r^2 \cdot T_{\text{eff,dust}}^4 . \quad (2.5)$$

Furthermore, we assume that the dust particle is in thermodynamic equilibrium

$$\frac{dE_{\text{abs}}}{dt} = \frac{dE_{\text{em}}}{dt} . \quad (2.6)$$

Combining these relations yields

$$\frac{L_{\text{UV}}}{4\pi R^2} \cdot \pi r^2 = 4\pi\sigma r^2 \cdot T_{\text{eff,dust}}^4 \quad (2.7)$$

$$\Leftrightarrow \frac{L_{\text{UV}}}{R^2} \propto T_{\text{eff,dust}}^4 . \quad (2.8)$$

The dust sublimation temperature T_{sub} at which dust evaporates has a constant value for a given dust particle, but it strongly varies from one element to the other (for Si it is ~ 1300 K, for C ~ 100 K).

Thus, we get the relation

$$R_{\text{dust}} \propto L_{\text{UV}}^{0.5}, \quad (2.9)$$

i.e. the more luminous the central AGN, the larger is the region in which no dust can survive as its temperature would exceed the dust sublimation temperature. (Deriving this relation, it is assumed that the dust composition does not change with AGN luminosity.)

Note that the proportionality factor given by this strongly simplified model will change when taking into account the optical properties of dust particles as they do not emit and absorb as a black body. Corrections include a dependency on the size of the grain and change the dependency on the evaporation (or better, condensation) temperature. A review on interstellar dust grains is given by Draine (2003).

The dust sublimation radius as natural, parameter-free explanation for the outer boundary of the BLR seems to be consistent with observations: Oknyanskij & Horne (2001) present an observational study for a sample of 10 AGNs measuring reverberation radii of dust holes and find that the dust-hole radius indeed does increase with the square root of UV luminosity. Moreover, it is in agreement with the slope of the the BLR size–luminosity relation $R_{\text{BLR}} \propto L^{0.5}$ which, according to McLure & Jarvis (2002), seems to be valid for the BLR sizes measured so far.

But how does the dust sublimation radius R_{sub} limit the BLR size? First of all, dust absorbs the emission lines and competes with the gas in absorbing the ionizing photons and can thus strongly suppress line emission [e.g. Netzer & Laor (1993), Laor (2003)].

Second, dust can be important due to the radiation pressure acting on it: Beyond R_{sub} , dust can survive and radiation pressure is acting as a driving force more effectively than on gas. The electrically charged grains lock the motion of the dust to that of the ionized gas. Thus, both dust and gas are swept away leaving a hole in the zone between the BLR and NLR, the so-called intermediate-line region (ILR), with a lack of significant line emission. The ILR reveals few blueshifted coronal lines which are interpreted as net inflow motion by Netzer & Laor (1993) but may also be indicative of shocks and clouds drifting *outwards*. When dust and gas are swept up, the NLR starts which often shows significant dust amounts. Dopita et al. (2002) have investigated dusty, radiation dominated photoionization models for the NLR in detail.

Thus, there is both theoretical and observational evidence for a BLR size–luminosity relation. Under the assumption that both BLR and NLR have a common ionization source, BLR and NLR size are expected to correlate. We indeed find, for a small sample of 11 type-1 AGNs, that NLR and BLR sizes are related following $R_{\text{BLR}} \propto R_{\text{NLR},1}^{0.88 \pm 0.1}$.

However, there are some caveats: For one, we have a very limited number of sources available. Second, the individual scatter is relatively large. Third, especially estimating the BLR size using time lags is very uncertain as there are various assumptions and complications involved (Kaspi et al., 2000).

Nevertheless, our results are consistent with the assumption of a common ionization source for BLR and NLR, thus minimizing the needed number of hypotheses. The BLR size seems to be determined by the dust sublimation radius and is proportional to the NLR size. This correlation is of interest as it can in principle be used to estimate black hole masses.

2.3.4 Black Hole Mass

As deriving BLR sizes via reverberation mapping is very time consuming, relationships with luminosity or NLR size can be extremely useful for measuring BH masses. Given the NLR size (either directly measured or derived from the [O III] luminosity), the BLR size can be estimated, which, assuming Keplerian motions, yields M_{BH} :

$$M_{\text{BH}} = (10^{5.22} M_{\odot}) \cdot v_{3000}^2 \cdot R_{\text{NLR},1}^{0.88} , \quad (2.10)$$

$$M_{\text{BH}} = (10^{8.83} M_{\odot}) \cdot v_{3000}^2 \cdot L_{44, [\text{OIII}]}^{0.48} , \quad (2.11)$$

where $v_{3000} = \text{FWHM}(\text{H}\beta) / 3000 \text{ km s}^{-1}$, $R_{\text{NLR},1}$ in parsec, and $L_{44, [\text{OIII}]} = [\text{O III}]$ luminosity / $10^{44} \text{ erg s}^{-1}$: The latter equation is very similar to the correlation of M_{BH} and continuum luminosity at 5100 \AA (Shields et al., 2003).

2.3.5 NLR Surface–Brightness Profiles

The [O III] surface–brightness profiles (SBP) of the NLRs can be directly drawn from the [O III] images. However, this additional information is seldom used and not often presented in literature, although it can in principle be very useful:

For one, a comparison of the SBPs of several galaxies reveals whether the NLR gas in different galaxies is distributed similarly. If the SBPs of several galaxies are similar, this yields an explanation for the persisting size–luminosity relation for different size measurements due to different sensitivities as found in Section 2.3.1. Second, the SBPs give hints to the gas density distribution. They can be directly compared to the one expected e.g. in the simplest case of a Strömgen sphere.

The SBPs were created using IRAF². Three vectorplots along the major axis of the NLR emission $\pm 1^\circ$, starting at the central [O III] emission, were averaged [using the position angles given by Schmitt et al. (2003a) in their Table 3]. The pixel scale was transformed to arcseconds according to the chip used (PC chip $\sim 0''.0455 \text{ pixel}^{-1}$, WF chip $\sim 0''.0996 \text{ pixel}^{-1}$) and then to parsec according to the world model (Appendix A). The luminosity per pixel was derived from the flux per pixel using the same world model. In order to allow a comparison among all galaxies of the sample, we divided the luminosity per pixel by the corresponding area in square parsecs at the galaxy. The resulting SBPs for the 58 Seyfert galaxies from Schmitt et al. (2003a) and the seven quasars from Bennert et al. (2002) are shown in Appendix B.

The SBPs are similar and centrally peaked with most flux included in the central ~ 5 – 20 data points for the Seyfert galaxies, corresponding to $0''.5$ – $2''$ (most objects were imaged with the WF chip and a resolution of $\sim 0''.1/\text{pix}$). Depending on the distance of the object, that corresponds on average to 200 – 700 pc . The SBP of the PG quasars are centrally peaked with most flux included in the central ~ 4 – 6 data points, corresponding to $0''.4$ – $0''.6$, and, on average, to 1500 – 6500 pc . Thus, the different distance scale has to be taken into account when comparing the SBPs, as substructure may more easily be missed in the distant quasars.

The central SBPs closely resemble a Gaussian profile in most objects. We created the “SBP of a star”, i.e. the instrumental PSF, from stars taken with the linear–ramp

² “Image Reduction and Analysis Facility” provided by “National Optical Astronomy Observatories”

filter imaged on the PC and WF chips. The resulting instrumental FWHM is $\sim 0''.2$ (WF chip) and $0''.065$ (PC chip), respectively. Comparing this PSF with the central SBP of all objects shows that 50 out of 65 (77%) have central profiles broader than the PSF. Examples of both resolved and unresolved in Seyfert–1 and Seyfert–2 galaxies are shown in Fig 2.5.

Comparing the distribution of type–1 and type–2 objects, 36% of type 1s have an unresolved central source while only for 11% of type 2s the central emission is unresolved. (These results are comparable to the percentage of objects which emit more than 50% of their total luminosity in an unresolved central source).

Thus, for nearly 25% of the whole sample, especially type 1s, the major part of [O III] emission comes from a central source which is even with the high spatial resolution of the HST not resolved [assuming that the continuum distribution was subtracted correctly in the calibration process by Schmitt et al. (2003a) and Bennert et al. (2002)].

The fact that a broader central SBP with respect to the PSF is observed in many Seyfert–2 galaxies can be interpreted as integration over two peaks of [O III] emission originating from both sides of the (hidden) nucleus. Such a scenario is in agreement within the unified model: The [O III] emission comes from gas within the ionization cone and reaches its maximum on both sides close to the center due to a combination of line–of–sight integration and decreasing flux with distance from the center (see Chapter 4, Section 4.4.11 for a detailed discussion on the effects of line–of–sight integration). Due to the limited spatial resolution, the two peaks on either side of the nucleus are smoothed out to a broader profile.

Some galaxies, especially Seyfert–2 galaxies, show a secondary or a tertiary peak on one or both sides of the central peak, indicating substructure in the extended [O III] emission. This substructure is already visible in the two dimensional images from Schmitt et al. (2003a) and pronounced in these SBP plots, as the vectorplots were calculated along the major axis of the NLR emission, i.e. along extended substructure. However, the profiles are all centrally peaked indicating that the extended emission is negligible in its contribution to the total luminosity. On the other hand, the extended emission has great influence on the measured NLR size: With increasing sensitivity, more extended emission can be seen, increasing the NLR size without changing the measured integrated flux significantly. This explains the results of the comparison of groundbased and HST data (summarized in Table 2.2).

For a detailed comparison, we divided the observed SBPs into four groups:

- 0: SBP with central peak only
- (0): SBP with faint blobs or asymmetries on either side of the central peak but with a maximum height $< 10\%$ of the central peak height
- 1: SBP with a secondary peak or more on one side of the central peak with a height $> 10\%$ of the central peak height
- 2: SBP with secondary or more peaks on both sides of the central peak with a height $> 10\%$ of the central peak height.

In addition, we took into account the AGN type (1 or 2). The results of this statistical comparison are summarized in Table 2.4.

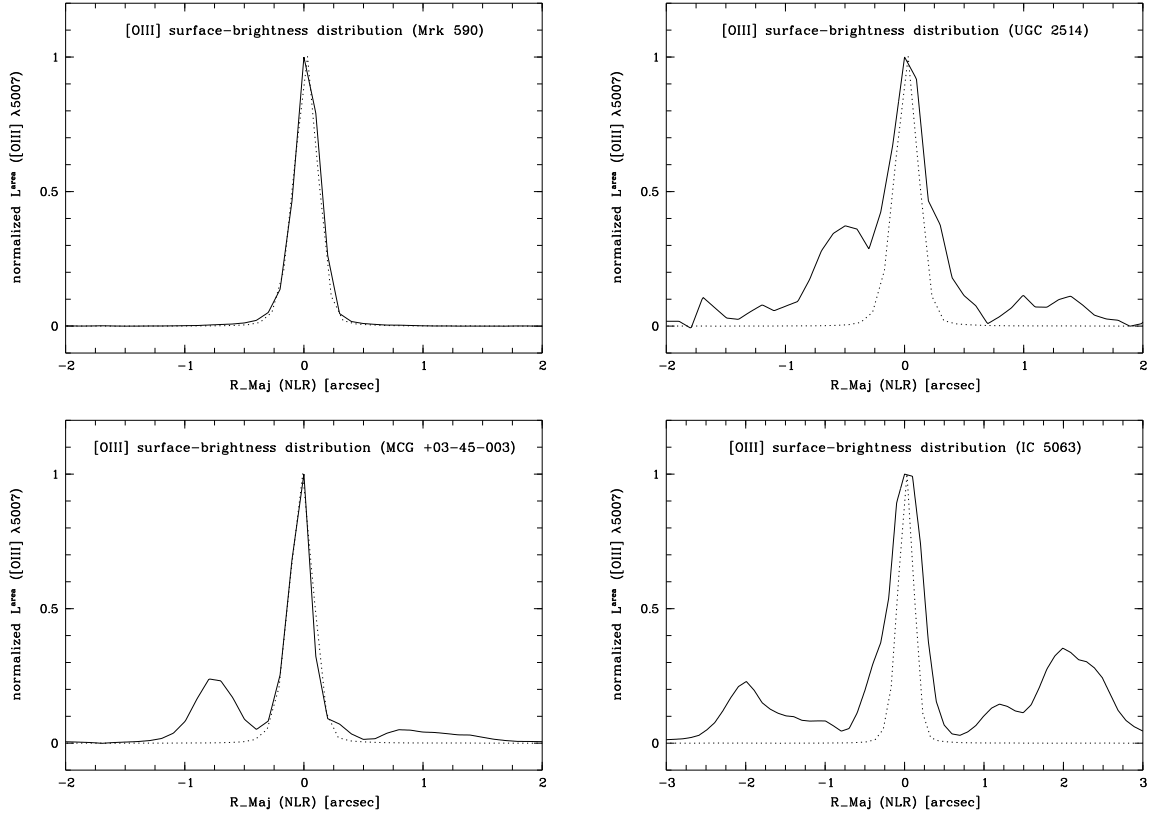


Figure 2.5: *Upper panels:* Observed surface-brightness profile of the Seyfert-1 galaxies Mrk 590 (*left*; solid line) and UGC 2514 (*right*; solid line) with the PSF of a star overlaid as dotted line. *Lower panels:* The same for the Seyfert-2 galaxies MCG +03-45-003 (*left*) and IC 5063 (*right*). The objects on the left hand show unresolved central emission while in the right panels, the central surface-brightness profile is larger than the PSF.

Table 2.4: Distribution of surface-brightness profiles

Type	0	(0)	1	2
All (65)	30	20	10	5
Seyferts (58)	24	19	10	5
Quasars (7)	6	1	0	0
Type-1 AGNs (28)	20	6	2	0
Type-2 AGNs (37)	10	14	8	5

Note. – The AGN type is given with, in brackets, the total number of objects included in our sample. We summarize the number of objects with SBP classified as 0, (0), 1, and 2, respectively.

It is remarkable that 50 of 65 objects (77 %) have SBPs classified as “0” or “(0)”, i.e. without significant extended [O III] emission with respect to the central flux.

There are differences between the SBPs of type–1 and type–2 objects: Out of 28 type–1 AGNs, only two ($\sim 7\%$) have SBPs with extended emission above the 10% level. In contrary, 13 out of 37 type–2 AGNs (35%) have SBPs with extended emission above the 10% level. While the majority (71%) of type–1 AGNs have SBPs classified as “0”, the majority (73 %) of SBPs of type 2s are of “(0), 1” or “2” type, i.e. with at least some extended emission.

The statistical distribution of SBPs is in agreement with the unified model, i.e. most type–1 objects show no extended [O III] emission, indicating a halo–like structure while the majority of type 2s reveal at least some extended emission. Our results are comparable to the results of Schmitt et al. (2003b) who find that Seyfert–1 NLRs are more circular and concentrated than Seyfert 2s, due to foreshortening of the former.

The observed central profiles are all convex and not concave as expected for gas distributed in a Strömngren sphere, i.e. NLR gas distributed with constant density in a sphere. One caveat is of course the limited resolution of the observations: We cannot rule out that the central NLR gas which is unresolved in most of our objects (but contribute up to 50% to the total luminosity) is indeed distributed in a sphere. The convex shape of the surface–brightness profiles often reflects the instrumental PSF, i.e. a Gaussian profile, of an unresolved central source.

Moreover, the different observed profile shape than a Strömngren one may not be surprising: While the gas itself may be distributed in a sphere, the intersection with the photoionizing AGN continuum is thought to result in NLR emitting gas in an ionization cone in the framework of the unified model. In that case, the observed SBPs depend on the line–of–sight through this ionization cone. Also, there is several observational evidence hinting that the NLR gas is not distributed with constant density but rather that the density is decreasing with distance from the nucleus. Finally, if the gas is instead distributed in a disk, one additionally has to take into account the intersection of the disk and the ionization cone.

2.4 Conclusions

Comparing NLR sizes and luminosities of 62 Seyfert galaxies and seven quasars imaged with the HST, we find that type–2 AGNs follow a relation $R_{\text{NLR},2} \propto L_{[\text{OIII}]}^{0.32 \pm 0.05}$, while type–1 objects are fit with a steeper slope of 0.55 ± 0.05 . Using a fixed surface–brightness limit, the slopes flattens ($R_{\text{NLR},2} \propto L_{[\text{OIII}]}^{0.29 \pm 0.06}$, $R_{\text{NLR},1} \propto L_{[\text{OIII}]}^{0.44 \pm 0.04}$). An alternative definition of the NLR size was applied by using the size at which 50% of the total luminosity was included: The slope of the NLR size–luminosity relation for both types flatten slightly (type–1 AGNs: 0.42 ± 0.09 , type–2 AGNs: 0.27 ± 0.08). Similar relations persist using groundbased data of a sample of 52 Seyfert galaxies: Type–2 AGNs follow the relation $R_{\text{NLR},2} \propto L_{[\text{OIII}]}^{0.34 \pm 0.06}$, while type–1 objects are fit with a steeper slope of 0.46 ± 0.06 .

On average, the slopes derived with different methods and data sets (HST data, HST data to the same surface–brightness limit, HST data with radius at 50% luminosity, groundbased data) are 0.31 ± 0.02 for type–2 AGNs and 0.47 ± 0.03 for type–1 AGNs.

Our results explain the different slopes for the NLR size–luminosity relation found by Bennert et al. (2002) (slope $\simeq 0.5$) and Schmitt et al. (2003b) (slope $\simeq 0.33$) by (intrinsic or apparent) differences in the NLR size or luminosity between type–1 and type–2 AGNs.

In Chapter 3, we investigate why type–1 and type–2 objects scale differently and whether it can be explained by projection effects on the basis of the unified model.

We discuss the physical reason for the size–luminosity relation in terms of a Strömgen law or a constant ionization parameter. A calculation of the expected Strömgen radius for six objects indicates that the observed radii are larger and thus, that the density is not constant but decreasing with radius.

In Chapter 4, we study the electron density and ionization parameter as a function of distance from the nucleus and discuss this issue again.

For a small sample of 11 type–1 AGNs, we find that NLR and BLR sizes are related following $R_{\text{BLR}} \propto R_{\text{NLR},1}^{0.88 \pm 0.1}$. While the edge of the NLR seems to be determined by a lack of ionizing photons, the dust sublimation radius provides a natural boundary for the BLR size. The NLR–BLR size relation can be used to estimate BH masses.

The surface–brightness profiles of 58 Seyfert galaxies and seven quasars as imaged with the HST are similar and centrally peaked. They indicate that the extended emission is negligible in its contribution to the total luminosity. Thus, the critical factor of the NLR size–luminosity relation seems to be the size rather than the luminosity. The central emission, contributing the major part to the total [O III] emission is often unresolved, especially for type–1 AGNs. The statistical distribution of the shape of the observed surface–brightness profiles is in agreement with the unified model: The majority of type–1 AGNs have surface–brightness profiles without extended emission, suggesting halo–like NLR gas distributions while most type 2s show at least some extended [O III] emission. The observed surface–brightness profiles are a by–product of the [O III] images and can be very useful for future NLR studies, e.g. for comparison with theoretical surface–brightness profiles expected for different NLR gas distributions.

NLR Size and Luminosity: Modeling

Here, we develop a model on the basis of the unified scheme and the receding-torus concept to explain the different slopes of the NLR size-luminosity relation for type-1 and type-2 AGNs.

3.1 Introduction

In Chapter 2 (Section 2.3.1), we found different slopes of the NLR size-luminosity relation for type-1 and type-2 AGNs. Can we understand these different slopes on the basis of the unified model and projection effects, resulting in different size measurements for type 1 and type 2s? Or does the opening angle of the ionization cone increase with luminosity due to dust sublimation of the obscuring torus and thus, the measured NLR sizes change towards higher luminosity?

To investigate these issues, we here develop a model taking into account the NLR size dependency on viewing angle and luminosity. We describe how the NLR size-luminosity relations for both type-1 and type-2 AGNs can be understood in the framework of the unified scheme and the so-called receding-torus model which assumes that the opening angle of the ionization cone increases with luminosity.

We describe the model with the involved assumptions as well as the predictions (Section 3.2). We discuss the receding-torus model, possible modifications (Section 3.3), and alternatives (Section 3.4), and end with our conclusions (Section 3.5).

3.2 Model Description

The model is shown in Figure 3.1 as “edge-on profile”, consisting of an optically thick obscuring torus (height b , distance Δr of the ionizing source) which leads to an anisotropic radiation along the ionization cone (radius h , half-opening angle β).

3.2.1 Model Assumptions

To probe a relation between NLR size and luminosity on a theoretical basis, we assume that the NLR is ionization bounded rather than matter bounded. Moreover, we assume that all NLRs have common properties such as density and volume-filling factor.

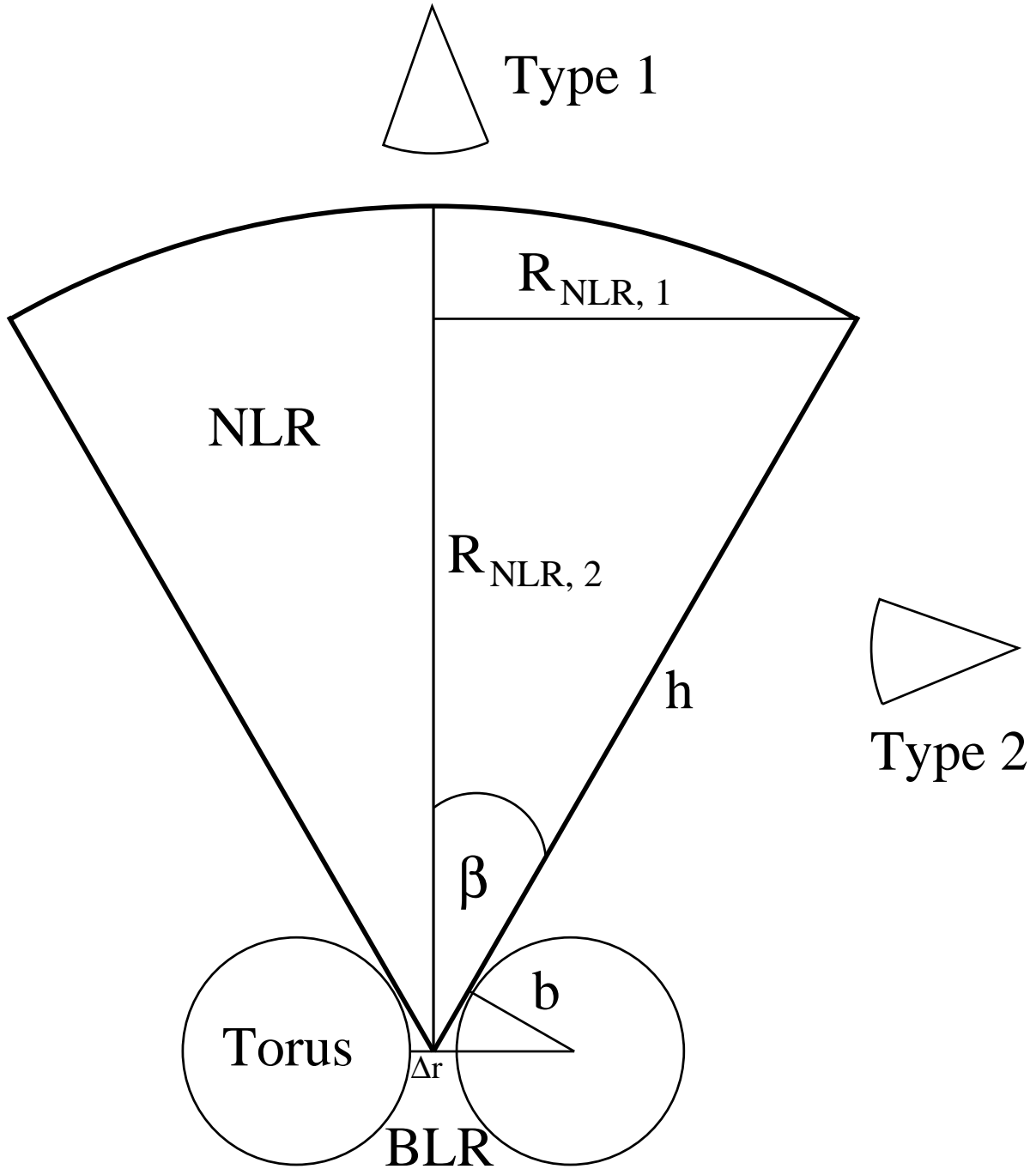


Figure 3.1: Illustration of the model. Schematic profile of an AGN seen “edge on”: dust torus with height b leading to the ionization cone with half-opening angle β (here $\beta = 30^\circ$). The radius of the ionization cone is h . The [O III] emission is considered to originate from this cone. $R_{\text{NLR},1}$ and $R_{\text{NLR},2}$ are the projected NLR radii measured for type-1 objects ($\iota = 0^\circ$) and type-2 objects ($\iota = 90^\circ$), respectively. (Note that the projected NLR radii shown here are only valid for these two extreme viewing angles; see Figure 3.3 for more general viewing angles.)

Additionally, we make the following assumptions:

- (i) Radius of the ionization cone h increases with square root of L_{UV} : $h \propto L_{\text{UV}}^{0.5}$;
- (ii) torus height b independent of L_{UV} : $b = \text{constant}$;
- (iii) inner radius of torus Δr proportional to dust sublimation radius R_{sub} , $R_{\text{sub}} \propto L_{\text{UV}}^{0.5}$:
 $\Delta r \propto L_{\text{UV}}^{0.5}$;
- (iv) $L_{[\text{O III}]}$ $\propto L_{\text{UV}} \cdot (1 - \cos \beta)$;
- (v) torus dimensions small against NLR size.

A slope of 0.5 assumed in **(i)** is expected if on average, all AGNs have the same ionization parameter, density, and ionizing spectral energy distribution (see Chapter 2, Section 2.3.2). However, we will also discuss relations derived with the alternative assumption of $h \propto L_{\text{UV}}^{0.33}$, expected in the case of a Strömgen sphere.

Assumptions **(ii)** and **(iii)** are known as the receding-torus model proposed by Lawrence (1991) and Hill et al. (1996): The obscuring region has a constant physical thickness, i.e. the torus height b does not depend on luminosity **(ii)**, but its inner edge (Δr) is determined by the radius until which dust sublimates (R_{sub}) and thus scales as $L_{\text{UV}}^{0.5}$ **(iii)**. There are several observations supporting at least assumption **(iii)**: For example, Oknyanskij & Horne (2001) present an observational study for a sample of 10 AGNs using reverberation radii of dust holes and find that the dust-hole radius indeed increases as the square root of UV luminosity. For the Seyfert-1 galaxy NGC 4151, Minezaki et al. (2004) interpret the observed time lag between the optical and near-infrared light curves as thermal dust reverberation and a torus with inner radius corresponding to $\Delta r \propto L_{\text{UV}}^{0.5}$.

Note that the dust distribution we assume is in fact a torus, i.e. the height b above the midplane is the same in all directions (Fig. 3.1). From VLT interferometry, there is observational evidence for such an assumption for the closest and brightest (in the IR) Seyfert-2 galaxy NGC 1068 (Röttgering et al., 2005). However, it is also possible that the dust is distributed in an extended disk.

We used **(iv)** $L_{[\text{O III}]} \propto L_{\text{UV}} \cdot (1 - \cos \beta)$, an assumption derived from the ratio between photons emitted by the AGN which are in principle able to ionize oxygen (L_{UV}) and the photons in the ionization cone which do in fact ionize oxygen, leading to the observed [O III] emission (from collisionally excited levels). Some of the UV photons emitted by the AGN are absorbed by the dust torus and do not contribute to the observed [O III] emission. The fraction of photons absorbed by the torus depends on the half-opening angle β of the ionization cone. The UV photons fill the whole volume of a sphere around the AGN with

$$V_0 = \frac{4}{3}\pi h^3 . \quad (3.1)$$

The UV photons ionizing oxygen atoms to O^{++} leading to the observed [O III] emission are limited to the ionization cone which is a section of this sphere, on both sides of the torus, depending on β (see Fig. 3.2 for details):

$$V_\beta = 2 \cdot \frac{2}{3}\pi h^2 a = \frac{4}{3}\pi h^2 \cdot (h - h \cos \beta) = V_0 \cdot (1 - \cos \beta) . \quad (3.2)$$

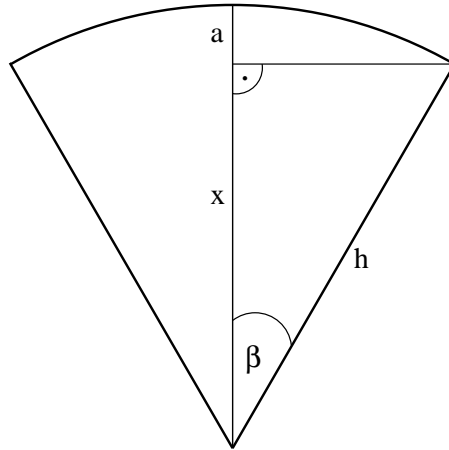


Figure 3.2: Half-ionization cone to calculate the dependency of [O III] luminosity on AGN luminosity L_{UV} : While UV photons escape into the whole sphere, only part of them create the ionization cone due to the dust torus. The fraction depends on the half-opening angle β and is given by $L_{[\text{O III}]} \propto L_{\text{UV}} \cdot (1 - \cos \beta)$. (Note that $a = h - x$ with $x = h \cos \beta$.)

This corresponds to $L_{[\text{O III}]} \propto L_{\text{UV}} \cdot (1 - \cos \beta)$.¹ While we measure $L_{[\text{O III}]}$, L_{UV} is responsible for ionizing oxygen and for the increase of β (assumptions ii and iii). We thus take into account the obscuring effect of the torus for the UV photons, resulting in an ionization cone. Note that in the inner region of the size Δr , UV photons can in principle ionize oxygen in the whole sphere. However, the density is too high to observe the forbidden [O III] line (the excited level is instead collisionally de-excited).

We assume that the torus dimensions are small against the NLR size (assumption v), to neglect the obscuring effect of the torus on the [O III] emission itself for both AGN types. Such an assumption is difficult to probe directly. Using high resolution adaptive optics, Canalizo et al. (2004) propose a projected diameter of the dust torus in Cygnus A of ~ 600 pc, a value which is indeed comparable to some NLR sizes. However, Cygnus A may be an exceptional case with a large torus; it is also possible that the observed dust emission does not arise from the obscuring torus which limits the AGN ionization field but originates from dust in the galactic disk. Nevertheless, the [O III] emission is often considered as largely orientation-independent measure of the intrinsic luminosity of AGNs [e.g. Mulchaey et al. (1994); Falcke et al. (1995)]. Our results from Chapter 2 (Section 2.3.5) suggests that this is the case at least within a factor of 2.

3.2.2 Model Predictions

Projected NLR radii

First, we calculate the projected (observed) NLR radii for type-1 ($\iota < \beta$) and type-2 objects ($\iota > \beta$).

¹ This relation can also be derived using the solid angle of a cone, given as $\Omega = 2\pi(1 - \cos \beta)$, with $L_{[\text{O III}]} \propto L_{\text{UV}} \cdot \frac{2\Omega}{4\pi}$.

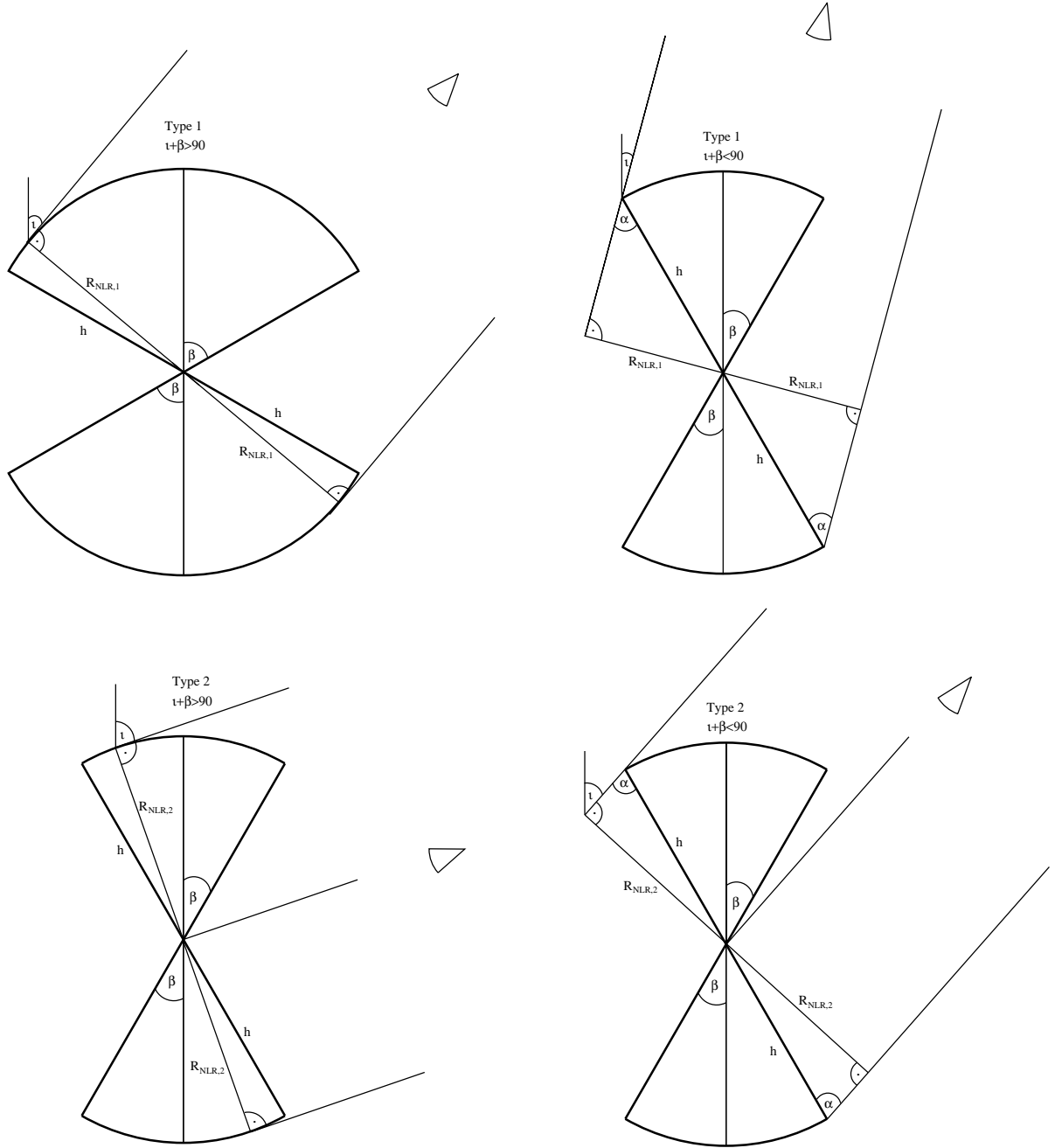


Figure 3.3: *Upper panels:* Projected NLR radius for type-1 AGNs ($\iota < \beta$). *Left panel:* $(\iota + \beta) > 90^\circ \Rightarrow R_{\text{NLR},1} = h$ (here $\iota = 40^\circ$, $\beta = 60^\circ$). *Right panel:* $(\iota + \beta) < 90^\circ \Rightarrow R_{\text{NLR},1} = h \sin \alpha = h \sin(\beta + \iota)$ (here $\iota = 20^\circ$, $\beta = 30^\circ$). *Lower panels:* Projected NLR radius for type-2 AGNs ($\iota > \beta$). *Left panel:* $(\iota + \beta) > 90^\circ \Rightarrow R_{\text{NLR},2} = h$ (here $\iota = 70^\circ$, $\beta = 30^\circ$). *Right panel:* $(\iota + \beta) < 90^\circ \Rightarrow R_{\text{NLR},2} = h \sin \alpha = h \sin(\beta + \iota)$ (here $\iota = 40^\circ$, $\beta = 30^\circ$).

We define the radius as the maximum distance between the center and the edge of the observed [O III] emission, although the emission-line region will in most cases not be circular. While the dust torus included in the model limits the ionization to the cone, we neglect the obscuring effect on both luminosity and size measurements (assumption v), i.e. we assume that we see [O III] emission of the cone and the counter cone independent of viewing angle. In Figure 3.3, we show the projected NLR radii and their derivation.

The formulae for the projected radii are the same for type-1 and type-2 AGNs and depend on the value of $\iota + \beta$: As long as $(\iota + \beta) \geq 90^\circ$, the radius corresponds directly to the radius of the ionized zone h . For $(\iota + \beta) < 90^\circ$, the radius is projected according to $h \sin(\beta + \iota)$:

$$R_{\text{NLR},1}(\iota < \beta) = h \quad \text{if } (\iota + \beta) \geq 90^\circ \quad (3.3)$$

$$= h \sin(\beta + \iota) \quad \text{if } (\iota + \beta) < 90^\circ ; \quad (3.4)$$

$$R_{\text{NLR},2}(\iota > \beta) = h \quad \text{if } (\iota + \beta) \geq 90^\circ \quad (3.5)$$

$$= h \sin(\beta + \iota) \quad \text{if } (\iota + \beta) < 90^\circ . \quad (3.6)$$

For $\beta < 45^\circ$, all measured type-1 NLR radii are shortened according to Equation 3.4. On the contrary, if $\beta \geq 45^\circ$, all measured type-2 NLR radii directly correspond to h (Eq. 3.5).

From these projections, averaged NLR radii can be calculated, weighted by $\sin \iota$. For type-1 AGNs, for example, a viewing angle of $\iota = 0^\circ$ is much less probable than $\iota = \beta$.

$$\langle R_{\text{NLR},1} \rangle = \frac{\int_0^\beta R_{\text{NLR},1}(\iota) \cdot \sin \iota \cdot d\iota}{\int_0^\beta \sin \iota \cdot d\iota} = \frac{\int_0^\beta R_{\text{NLR},1}(\iota) \cdot \sin \iota \cdot d\iota}{1 - \cos \beta} ; \quad (3.7)$$

$$\langle R_{\text{NLR},2} \rangle = \frac{\int_\beta^{\pi/2} R_{\text{NLR},2}(\iota) \cdot \sin \iota \cdot d\iota}{\int_\beta^{\pi/2} \sin \iota \cdot d\iota} = \frac{\int_\beta^{\pi/2} R_{\text{NLR},2}(\iota) \cdot \sin \iota \cdot d\iota}{\cos \beta} . \quad (3.8)$$

For Seyfert-1 galaxies:

a) if $\beta < 45^\circ$, all objects are shortened:

$$\langle R_{\text{NLR},1} \rangle = \frac{h \cdot \int_0^\beta \sin(\iota + \beta) \cdot \sin \iota \cdot d\iota}{1 - \cos \beta} = h \cdot \frac{2\beta \cdot \cos \beta + \sin \beta - \sin(3 \cdot \beta)}{4 \cdot (1 - \cos \beta)} ; \quad (3.9)$$

b) if $\beta \geq 45^\circ$, only objects with $i \leq 90^\circ - \beta$ are shortened:

$$\langle R_{\text{NLR},1} \rangle = \frac{h \cdot \int_{\pi/2-\beta}^\beta \sin \iota \cdot d\iota + h \cdot \int_0^{\pi/2-\beta} \sin(\iota + \beta) \cdot \sin \iota \cdot d\iota}{1 - \cos \beta} \quad (3.10)$$

$$= h \cdot \frac{\sin \beta - (1 - \pi/4 + \beta/2) \cdot \cos \beta}{1 - \cos \beta} . \quad (3.11)$$

For Seyfert–2 galaxies:

a) if $\beta < 45^\circ$, objects with $i \leq 90^\circ - \beta$ are shortened:

$$\langle R_{\text{NLR},2} \rangle = \frac{h \cdot \int_{\pi/2-\beta}^{\pi/2} \sin \iota \cdot d\iota + h \cdot \int_{\beta}^{\pi/2-\beta} \sin(\iota + \beta) \cdot \sin \iota \cdot d\iota}{\cos \beta} \quad (3.12)$$

$$= h \cdot \frac{(\pi/4 - \beta) \cdot \cos \beta + (1/2) \cdot \sin \beta \cdot \cos(2 \cdot \beta) + \sin \beta}{\cos \beta} ; \quad (3.13)$$

b) if $\beta \geq 45^\circ$, no objects are shortened:

$$\langle R_{\text{NLR},2} \rangle = h . \quad (3.14)$$

Half–opening angle β

Now, we use the receding–torus model to calculate the relation between different β and AGN luminosities L_{UV} (assumptions ii and iii: b independent of L and $\Delta r \propto L_{\text{UV}}^{0.5}$):

$$\cos \beta = \frac{b}{\Delta r + b} \quad (3.15)$$

$$\Leftrightarrow \frac{1}{\cos \beta} - 1 = \frac{\Delta r}{b} \quad (3.16)$$

$$\Leftrightarrow \frac{1}{\cos \beta} - 1 = \frac{f}{b} \cdot L_{\text{UV}}^{0.5} . \quad (3.17)$$

Here, we use a proportionality constant f for the relation $\Delta r \propto L_{\text{UV}}^{0.5}$. f basically depends on the dust evaporation temperature and thus, the dust composition (see also our discussion in Chapter 2, Section 2.3.3).

In the next step, we calculate the ratio of two luminosities. Thus, f as well as the constant torus height b (assumption ii) simply cancel out. For a luminosity $L_{\text{UV},0}$, we have a half–opening angle β_0 and for $L_{\text{UV},1}$ the angle is β_1 :

$$\left(\frac{1}{\cos \beta_1} - 1 \right) \cdot \left(\frac{1}{\cos \beta_0} - 1 \right)^{-1} = \left(\frac{L_{\text{UV},1}}{L_{\text{UV},0}} \right)^{0.5} \quad (3.18)$$

$$\Leftrightarrow \frac{1}{\cos \beta_1} - 1 = \left(\frac{L_{\text{UV},1}}{L_{\text{UV},0}} \right)^{0.5} \cdot \left(\frac{1}{\cos \beta_0} - 1 \right) \quad (3.19)$$

$$\Leftrightarrow \cos \beta_1 = \left[1 + \left(\frac{L_{\text{UV},1}}{L_{\text{UV},0}} \right)^{0.5} \cdot \left(\frac{1}{\cos \beta_0} - 1 \right) \right]^{-1} . \quad (3.20)$$

Assuming that $\beta_0 = 15^\circ$ for $L_{\text{UV},0}$, the opening angle β_1 for increased luminosity $L_{\text{UV},1}$ can be calculated and used to estimate the NLR sizes for type–1 and type–2 AGNs at the corresponding luminosity (Table 3.1).

Table 3.1: Consequences of receding–torus model on NLR sizes

$\frac{L_{UV,1}}{L_{UV,0}}$	10	100	1000	10000	100000
β_1	26°	42°	62°	77°	85°
$R_{NLR,1} (\iota = 0^\circ)$	0.44	0.67	0.88	0.98	1
$\langle R_{NLR,1} \rangle$	0.68	0.93	0.99	1	1
$R_{NLR} (\iota = \beta)$	0.79	0.99	1	1	1
$\langle R_{NLR,2} \rangle$	0.97	1	1	1	1
$R_{NLR,2} (\iota = 90^\circ)$	1	1	1	1	1

Note. – Calculation of half–opening angle β_1 from luminosity ratio $\frac{L_{UV,1}}{L_{UV,0}}$ assuming the receding–torus model (Eq. 3.20, $\beta_0 = 15^\circ$). The NLR sizes are given in units of h .

[O III] luminosities

To estimate the [O III] luminosity, we take into account that [O III] is a forbidden line and thus emitting optically thin². The observed luminosity corresponds to the integrated emission–line flux of the total emitting region (i.e. the ionization cone). We assume that the integration is the same for type–1 and type–2 AGNs, i.e. that no significant amount of [O III] is absorbed by the central obscuring medium (assumption v). If this is the case, the observed [O III] luminosity is the same for both types and proportional to the AGN luminosity times $(1 - \cos \beta)$.

To estimate the proportionality factor, we use Equation 7 from Falcke et al. (1995):

$$\log L_{\text{disk}} = (-0.4 \cdot M_{[\text{O III}]} + 34.45 \pm 0.08) \pm 0.44 . \quad (3.21)$$

Falcke et al. (1995) refer with L_{disk} to the dominant UV bump luminosity of the accretion disk. Thus, this equation can be converted to a relation between $L_{UV} \propto L_{[\text{O III}]}$, taking into account the dependency on β :

$$L_{[\text{O III}]} \simeq 0.1 \cdot L_{UV} \cdot (1 - \cos \beta) . \quad (3.22)$$

Starting values

The equations given above are used to calculate a theoretical size–luminosity relation. The starting values β_0 and h_0 at $L_{UV,0} = 10^{40} \text{ erg s}^{-1}$ are chosen such that the covered range of NLR sizes in the observed [O III] luminosity range ($10^{39-44} \text{ erg s}^{-1}$) is comparable to the sizes measured from the HST data, for comparison with observations (Chapter 2).

While the choice of the starting value h_0 has no influence on the derived slopes but results in a y–axis shift, the choice of β is more critical: It can change the slopes of the NLR size–luminosity relations, especially for type–2 objects as well as the intersection between both slopes: A value of $\beta_0 = 5^\circ$ results in a slope for type–1 AGNs of 0.45 and a slope of 0.36 for type–2 AGNs, intersecting at $\log L_{[\text{O III}]} = 43.3$.

² In the NLR, also the Balmer lines can be considered as optically thin, as flux ratios are typical of the so–called “case B” recombination, implying that only the Lyman series is optically thick. In “case A”, all lines are emitting optically thin (Peterson, 2003).

Increasing β_0 to 25° results in a steeper slope for type–2 AGNs (0.4) while for type–1 objects, it remains roughly the same (0.44). The intersection occurs at $\log L_{[\text{OIII}]} = 40.3$.

So far, no direct observations of the intrinsic opening angle at different luminosities exist. The opening angles of the ionization cone estimated from images reflect only the projected angle but not the true one. In principle, assuming the receding–torus model, β can be estimated from dust sublimation theory as discussed above. However, as it strongly depends on the assumed dust composition as well as the height of the torus, such an estimation is difficult. Thus, our choice of β_0 remains somewhat arbitrary. On the contrary, by fitting the predicted slopes to the observed ones, our model can be used to predict β_0 at $L_{\text{UV},0}$.

We start with $\beta_0 = 15^\circ$ and calculate the increased β_1 at $L_{\text{UV},1} = (1, 2.3, 5, 10, 23, 50, 100, 230 \dots 100000) \cdot L_{\text{UV},0}$ with $L_{\text{UV},0} = 10^{40} \text{ erg s}^{-1}$. The radius of the ionization cone h increases with luminosity $L_{\text{UV},1}$ according to assumption (i), $h_1 = h_0 \cdot L_{\text{UV},1}^{0.5}$, starting with $h_0 = 25 \text{ pc}$ ($L_{\text{UV},1}$ in units of $10^{40} \text{ erg s}^{-1}$).

These values correspond to [O III] luminosities of $\log L_{[\text{OIII}]} \simeq 37.5 - 44$ as well as $\beta = 26^\circ$ and $h \simeq 80 \text{ pc}$ at $L_{[\text{OIII}]} = 10^{39} \text{ erg s}^{-1}$.

To calculate the corresponding NLR radii, we insert the values h_1 and β_1 into Equations 3.3–3.6, using different viewing angles. Radii are calculated for $\iota = 0 \dots 90^\circ$ in steps of 5° . For type–1 AGNs, only those data points for which $\iota < \beta_1$ are plotted, for type–2 AGNs, only data points with $\iota > \beta_1$. Linear fits are applied to the averaged NLR radii calculated from Equations 3.9–3.14.

The [O III] luminosities are calculated from Equation 3.22, corresponding to the increased $L_{\text{UV},1}$ and β_1 .

Size–luminosity relation: Theory versus observation

From these values, the theoretical NLR size–luminosity relation is derived. It is shown in Figure 3.4 (*upper panel*).

A fit to type–1 AGNs gives a slope of 0.44 ± 0.01 . For type–2 objects, the slope flattens: Applying a linear fit to the data points in the low luminosity regime which are covered by the observations of type–2 Seyferts ($39 \leq \log L_{[\text{OIII}]} \leq 42$) results in a slope of $\sim 0.37 \pm 0.01$. The slopes intersect at $\log L_{[\text{OIII}]} \simeq 41.4$ and $\log R \simeq 2.8$. The details of the fits are summarized in Table 3.2.

To compare our model to observations, we refer to the results from the HST data using the same 3σ limit to have a homogeneous sample. Although the comparison with groundbased data in Chapter 2 has shown that the HST data suffer from low sensitivity, the HST data cover a larger luminosity range due to the quasar data. In the model, the lower sensitivity limit is indirectly taken into account by using a starting value of h_0 resulting in comparable measured NLR sizes. The observed slopes of the NLR size–luminosity relation are 0.29 ± 0.06 for type–2 AGNs and 0.44 ± 0.04 for type–1 AGNs with the intersection at $\log L_{[\text{OIII}]} \simeq 41.4$ and $\log R \simeq 2.8$ (Chapter 2, Table 2.1).

Thus, observed and theoretical slopes intersect at the same point. Moreover, the theoretically predicted slope for type–1 AGNs is quasi identical to the observed one. The difference between observed and predicted slopes for type–2 objects is larger, but the slopes are still comparable within the errors. [Note that for example the slope for type–2 AGNs measured from groundbased data is with 0.34 much closer to what our model predicts (0.37).]

Table 3.2: Theoretical NLR size–luminosity relations

Assumption	β_0	$h \propto$	intersection $\log L_{[\text{O III}]} / \log R$	m_{type1}	k_{type1}	m_{type2}	k_{type2}
HST, 3σ limit	—	—	41.4/2.8	0.44	−15.2	0.29	−9.4
r.t.	15°	$L_{\text{UV}}^{0.5}$	41.4/2.8	0.44	−15.3	0.37	−12.6
r.t.	15°	$L_{\text{UV}}^{0.33}$	43.1/2.9	0.30	−10.0	0.27	−8.9
mod. r.t.	15°	$L_{\text{UV}}^{0.5}$	43.5/3.9	0.47	−16.5	0.42	−14.4
mod. r.t.	15°	$L_{\text{UV}}^{0.33}$	43.8/3.1	0.33	−11.1	0.28	−9.15
$\beta = \text{constant}$	25°	$L_{\text{UV}}^{0.5}$	—	0.50	−17.8	0.50	−17.6
$\beta = \text{constant}$	25°	$L_{\text{UV}}^{0.33}$	—	0.33	−11.3	0.33	−11.1

Note. – NLR size–luminosity relation of the form $\log R$ (NLR) = $m \log L_{[\text{O III}]} + k$ with $[\text{O III}]$ luminosities in the range of $10^{39-44} \text{ erg s}^{-1}$. Units of R and L are parsec and erg s^{-1} , respectively. For the theoretical relations, the assumptions involved are either the receding–torus model (r.t.; $b \propto L_{\text{UV}}^{0.5}$), a modified receding–torus model (mod. r.t.; $b \propto L_{\text{UV}}^{0.25}$) or $\beta = \text{constant}$. The intrinsic relation between size of the ionization cone and AGN luminosity was either $h = h_0 \cdot L_{\text{UV}}^{0.5}$ or $h = h_0 \cdot L_{\text{UV}}^{0.33}$ with $h_0 = 25 \text{ pc}$ at $L_{\text{UV},0} = 10^{40} \text{ erg s}^{-1}$. For type–2 AGNs, the fit was only applied to $L_{[\text{O III}]} < 10^{42} \text{ erg s}^{-1}$ for comparison with observations. Note that for calculation of the intersection, we used the original m and k values and not the rounded ones given in this Table. The error bars for m and k of the theoretical fits are $< \pm 0.01$ and $< \pm 0.5$, respectively, the correlation coefficient is > 95 .

One has to keep in mind that the observational scatter is rather large and more data are needed, especially at high luminosities: Our model predicts that the curve of the size–luminosity relation for type–2 AGNs approaches the steeper slope followed by type–1 AGNs, but no observations of the NLR size of high–luminosity type–2 AGNs (i.e. type–2 quasars) exist to probe this effect.

While we assumed an intrinsic relation of the size of the ionization cone and the UV luminosity with a slope of 0.5, the predicted slopes for both AGN types flatten when taking into account projection of sizes and a receding torus.

Using a relation expected for gas distributed in a Strömgren sphere as alternative assumption ($h \propto L_{\text{UV}}^{0.33}$), the resulting slopes are significantly flatter for both type–1 and type–2 AGNs (Table 3.2) and do not get as close to the observed ones. Moreover, the predicted intersection occurs at too high $[\text{O III}]$ luminosities.

Thus, our model confirms an intrinsic scaling with a constant ionization parameter as suggested by Bennert et al. (2002), expected if, on average, all AGNs have the same ionization parameter, density, and ionizing spectral energy distribution.

3.3 Receding–Torus Model and Modifications

It seems that using the simple model on the basis of the unified scheme and the receding–torus concept can indeed explain the different observed slopes of the NLR size–luminosity relation for type–1 and type–2 AGNs.

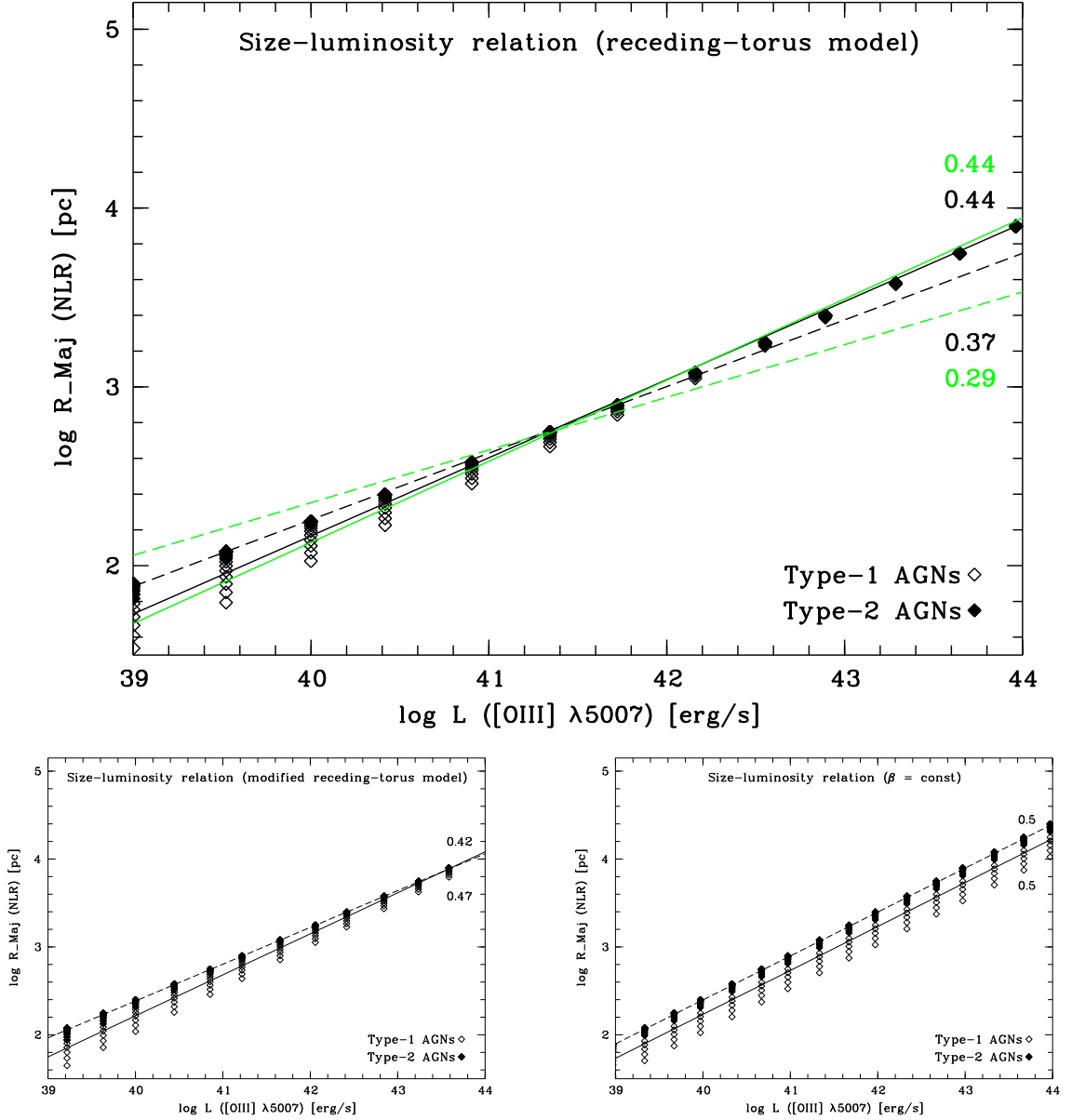


Figure 3.4: Theoretical NLR size–luminosity relations on the basis of the unified scheme. The open symbols are type–1 AGNs, the filled ones type–2. An intrinsic relation of $h = h_0 L_{\text{UV}}^{0.5}$ was assumed with $h_0 = 25 \text{ pc}$ at $L_{\text{UV},0} = 10^{40} \text{ erg s}^{-1}$. For all fits, the averaged NLR radii were used (Eqs. 3.9–3.14). Note that the scatter of projected NLR radii for different viewing angles is larger for type–1 AGNs and that the average radii are closer to those of $\iota = \beta$ than $\iota = 0^\circ$ (smallest projected NLR radii for a given luminosity), due to the weighting by $\sin \iota$.

Upper panel: Receding–torus model ($b = \text{constant}$, $\Delta r \propto L_{\text{UV}}^{0.5}$): The solid line represents the fit to type–1 AGNs, resulting in a relation $R_{\text{Maj}} \text{ (NLR)} \propto L_{[\text{OIII}]}^{0.44 \pm 0.01}$. The dashed line corresponds to the fit to type–2 AGNs $R_{\text{Maj}} \text{ (NLR)} \propto L_{[\text{OIII}]}^{0.37 \pm 0.01}$, including only data points in the low luminosity regime ($\log L_{[\text{OIII}]} < 42$) for comparison with observations. The grey lines correspond to the fits to the HST data from Chapter 2 (3σ limit) with a slope of 0.44 ± 0.04 for type–1 AGNs and 0.29 ± 0.06 for Seyfert–2 galaxies.

Lower left panel: Modified receding–torus model ($b \propto L_{\text{UV}}^{0.25}$, $\Delta r \propto L_{\text{UV}}^{0.5}$): The solid line represents the fit to type–1 AGNs, resulting in a relation $R_{\text{Maj}} \text{ (NLR)} \propto L_{[\text{OIII}]}^{0.47 \pm 0.01}$. The dashed line corresponds to the fit to type–2 AGNs, $R_{\text{Maj}} \text{ (NLR)} \propto L_{[\text{OIII}]}^{0.42 \pm 0.01}$.

Lower right panel: $\beta = \text{constant} = 25^\circ$: Both type–1 and type–2 AGNs follow the same (assumed) slope of 0.5 ± 0.01 .

While there are several studies supporting the receding-torus model [e.g. Hill et al. (1996); Simpson (1998); Simpson et al. (1999); Willott et al. (2000); Grimes et al. (2004)], it is not generally accepted. Especially, it is not clear if it holds for all luminosities.

While assumption (iii), i.e. that the inner radius increases with the square root of luminosity, is physically motivated by the dust sublimation radius and supported by observations [see e.g. Netzer & Laor (1993), Oknyanskij & Horne (2001), and our discussion in Chapter 2], the constant torus scale height (assumption ii) is more critical. It is possible that the torus height b increases with AGN luminosity: For one, the more luminous AGNs are, the more fueling material is needed which may be provided through the torus. Second, the star formation rate may grow with AGN luminosity and supernovae will blow up the torus (Haas et al., 2004).

If both the torus height (b) and the inner radius (Δr) increase with luminosity, the opening angle may stay constant with luminosity.

Haas et al. (2004) argue that in case of an increasing opening angle, the covering angle of the dust decreases, resulting in a decreasing IR luminosity with AGN luminosity. For the high luminous sources in their sample, such a trend is not observed, speaking against the simple version of the receding-torus model. Also Cao (2005) suggests that the torus height b increases with AGN luminosity when comparing infrared and bolometric luminosities of PG quasars ($b \propto L_{\text{bol}}^{0.37 \pm 0.05}$). Using AGNs from the Sloan Digital Sky Survey, Simpson et al. (2005) find that the fraction of type-1 AGNs increases with [O III] luminosity, in general agreement with the receding-torus model but with a shallower slope than predicted for a constant scale height. He proposes a modification in which the height of the torus increases slowly with AGN luminosity ($b \propto L_{\text{UV}}^{0.23}$). From the luminosity-dependent variations of QSO fractions, Arshakian (2005) estimates a range of $b \propto L_{\text{UV}}^{0.1-0.2}$.

Here, we use the modification $b \propto L_{\text{UV}}^{0.25}$ to calculate the theoretical NLR size-luminosity relation for the modified receding-torus model (Fig. 3.4, *lower left panel*). We use similar equations as above (Eqs. 3.15–3.19) which lead to

$$\cos \beta_1 = \left[1 + \left(\frac{L_{\text{UV},1}}{L_{\text{UV},0}} \right)^{0.25} \cdot \left(\frac{1}{\cos \beta_0} - 1 \right) \right]^{-1}. \quad (3.23)$$

While the resulting NLR size-luminosity relation for type-1 AGNs has with 0.47 a slope close to the assumed relation $h \propto L_{\text{UV}}^{0.5}$, a fit to all type-2 data points gives a slope of 0.42 (Table 3.2). These fits do not correspond to the observed ones as closely as those derived using the “normal” receding-torus model with $b = \text{constant}$. Moreover, the intersection of both fits at $\log R \simeq 3.9$ and $\log L_{[\text{OIII}]} \simeq 43.5$ occurs at too high values compared to the observed one.

As previously for the “normal” receding-torus model, we here again start with a different assumption than (i), using $h \propto L_{\text{UV}}^{0.33}$ instead: Both slopes flatten while the intersection takes place at $\log R \simeq 3.5$, $\log L_{[\text{OIII}]} \simeq 44.4$, i.e. again at too high luminosities and radii compared to the observed intersection (Table 3.2).

It seems that the modified receding-torus model is not able to reproduce the observed relations as closely as the “normal” one with $h \propto L_{\text{UV}}^{0.5}$.

3.4 Alternatives

Due to the controversy on the validity of the receding-torus model, we looked for alternatives explaining different slopes of the NLR size-luminosity relation for type-1 and type-2 AGNs based on the unified model.

In Figure 3.4 (*lower right panel*), we show the predicted size-luminosity relation without assuming the receding-torus model, i.e. with $\beta = \text{constant}$ (25°). The relations for type-1 and type-2 AGNs are parallel following both the (assumed) slope of 0.5, with $R_{\text{NLR},1} < R_{\text{NLR},2}$. (Likewise, parallel slopes of 0.33 can be achieved when assuming $h \propto L_{\text{UV}}^{0.33}$ instead of $h \propto L_{\text{UV}}^{0.5}$; Table 3.2.) It implies that projection effects of the measured NLR size alone cannot explain different slopes of the NLR size-luminosity relation. When excluding the dependency of β on luminosity, another assumption is needed to derive different slopes.

One possibility is that the observed [O III] luminosity does not depend only on L_{UV} and the half-opening angle β , but also on viewing angle and thus, varies for both types: We may not measure the same [O III] luminosities for type-1 and type-2 AGNs even if they are intrinsically the same (the contrary to what is assumed under v). Such a behavior can be introduced by the obscuring effect of the dust torus. The amount of obscuration depends on several factors such as the viewing angle, the torus dimensions as well as the NLR gas distribution.

However, in the framework of the unified scheme, the torus cannot obscure more than half of the intrinsic [O III] luminosity for type-1 objects (the counter cone). For type-2 objects, the obscuration effect is probably even smaller as in the central (obscured) part, the density is too high for [O III] emission. The comparison of the observations presented in Chapter 2 gives similar estimations, i.e. that the [O III] luminosities of type-1 and type-2 AGNs differ at most by a factor of 2. If the torus obscures a fraction of the NLR, it may also result in a decrease of the measured NLR size by up to a factor of 2. However, a difference of up to 2 does not have a great influence on the size-luminosity relation which extends over four orders of magnitudes in luminosity and two orders of magnitudes in size. Moreover, including a factor alone between the observed [O III] luminosity or the measured NLR radii for type-1 and type-2 objects results only in a parallel shift and not in different observed slopes of the NLR size-luminosity relation.

Thus, the different observed slopes for type-1 and type-2 AGNs support the receding-torus concept which may at least be valid for low-luminosity AGNs.

However, some issues were not taken into account but may alter the observed slopes: a possible disk NLR gas distribution as well as the effects of a decreasing NLR gas density. For the moment, the model assumes a spherical distribution of NLR gas which is ionized in a cone-like structure, but the NLR gas can also be distributed in a disk [see e.g. Mulchaey et al. (1996b)]. In that case, the calculations get more difficult and have to take into account the intersection of the ionization cone and the disk. We assumed that the NLR is ionization bounded, i.e. that the size is limited by the ionizing photon flux from the AGN. In case of a disk distribution, it is likely that the NLR is instead matter bounded and that many photons escape, depending on the orientation of the disk towards the ionizing field. For statistical reasons, disk and ionization-cone axis will be aligned only in few cases. Moreover, it is possible that the obscuring torus and the disk are aligned, for reasons of e.g. angular momentum conservation or the feeding of the torus via gas and dust from the disk.

Schmitt (1998) propose that the NLR sizes in Seyfert–1 galaxies are (intrinsically) smaller than those of type 2s: If the torus axis of Seyfert–1 galaxies is more likely to be aligned with the galaxy plane, but has random orientations in Seyfert–2 galaxies, there is a smaller number of ionization–bounded clouds in Seyfert–1 galaxies.

To estimate the effects of both a diskly NLR distribution and a decreasing gas density on the NLR size–luminosity relation, numerical simulations are needed. In close cooperation with Dr. Bruno Jungwiert, such simulations have already been started and will be presented in detail elsewhere. These simulations will also enable us to study the effect of the obscuring torus on the observed [O III] emission for different viewing angles and gas distributions.

3.5 Conclusions

We present a model based on the unified scheme and the receding–torus concept, taking into account the NLR size dependency on viewing angle and luminosity. Starting with the assumption that the radius of the ionization cone increases with the square root of the UV luminosity, the model predicts a slope of 0.44 for the NLR size–luminosity relation for type–1 AGNs. For type–2 AGNs, it yields a slope of 0.37. Both slopes are approximately in agreement with the observed ones, taking into account the observational scatter.

Independent of the exact values of the slopes, the model predicts different slopes for type–1 and type–2 AGNs with a flatter slope for type–2 objects, implying that the observations are qualitatively compatible with the receding–torus model which may be valid at least for low–luminosity AGNs. The scaling of the intrinsic size of the ionization cone with the square root of the UV luminosity is expected if, on average, all AGNs have the same ionization parameter, density, and ionizing spectral energy distribution. Our model shows that the observed slopes cannot be explained by gas distributed in a Strömngren sphere. It seems that under reasonable assumptions, we are able to explain the observed slopes of the NLR size–luminosity relation which extends over four orders of magnitudes in luminosity and two orders of magnitude in size.

In the observed luminosity range, linear fits to the calculated projected NLR radii and [O III] luminosities introduce an apparent intersection between the two slopes for type–1 and type–2 AGNs while the “real” curve for type 2s predicted by the model approaches that of type 1s at high luminosities. Unfortunately, no NLR measurements are available for high–luminosity type–2 AGNs.

Observations of the recently discovered type–2 quasars will provide a crucial probe of the model. Indeed, we planned and applied for the first 3D spectroscopy of type–2 quasars, using the new 3D spectroscopic techniques with the VLT/VIMOS³. Time has been granted and the observations will be carried out in March 2006⁴. Apart from measuring the NLR size and luminosity to add data points to the relation in the high–luminosity regime, we are able to probe whether a bi–cone with a large opening angle, as predicted from the receding–torus model, indeed exists in these high–luminosity type–2 AGNs.

³ VISIBLE MultiObject Spectrograph

⁴ PI: Marcus Albrecht, 076.B-0770, 12 h service mode (A priority)

Spatially-Resolved NLR Diagnostics

In this Chapter, we describe the results of high-sensitivity spatially-resolved spectroscopy of 12 Seyfert galaxies obtained at the VLT¹ and the NTT². We probe the AGN-photoionization of the NLR and thus, its “real” size. We derive physical properties of the NLR such as reddening, ionization parameter, electron density, and velocity and discuss their variations with distance from the nucleus.

4.1 Introduction

While [O III] narrow-band imaging is commonly used to study the NLRs of active galaxies, this emission can be contaminated by contributions from starbursts, shock-ionized gas or tidal tails, resulting in an apparent increase of the NLR. AGNs are known to often have circumnuclear starbursts; whether they occur as decoupled or competitive phenomena also dependent on gas fueling or play a key role in AGN physics is still a matter of debate [e.g. Terlevich et al. (1992); Hernquist & Mihos (1995); Cid Fernandes et al. (2001)]. In addition, AGNs, especially high-luminosity sources, i.e. quasars, are sometimes related to interacting systems [e.g. Heckman et al. (1984); Canalizo & Stockton (2001)], and we may see tidal tails and bridges ionized by the central source, resulting in an apparent increase of the NLR size. Finally, shocks from jets may also play a role in ionization of interstellar gas.

These considerations and the fact that different sensitivities lead to different size measurements found in Chapter 2 immediately question the definition of the “NLR size”. It shows that narrow-band imaging alone may not be a conclusive method to find the real edge of the NLR. Long-slit spectroscopy is a valuable alternative approach as it can directly probe the size in terms of AGN photoionization and discriminate the stellar or shock-ionized contribution. In addition, several physical parameters of the NLR such as reddening, ionization parameter, electron density, and velocity can be directly accessed and analyzed as a function of distance from the nucleus.

We applied for observing time at the VLT and the NTT: One night, respectively four nights, in visitor mode were granted and carried out in February and September 2004³. We obtained high-sensitivity long-slit spectra of 12 Seyfert galaxies.

¹ Very Large Telescope, ESO, Cerro Paranal, Chile

² New Technology Telescope, ESO, La Silla, Chile

³ PI: Nicola Bennert, 072.B-0144, 073.B-0013

Here, we describe the observations (Section 4.2), reduction, and analysis (Section 4.3), discuss the results (Section 4.4), and end with a concluding summary (Section 4.5).

4.2 Observations

The spectra were taken in the wavelength range $\sim\lambda 3700\text{--}7000\text{ \AA}$ to cover the emission lines suited for specific diagnoses: $\text{H}\alpha$ and $\text{H}\beta$ (normalizer, reddening indicator, counter of ionizing photons); $[\text{O II}]\lambda 3727\text{ \AA}/[\text{O III}]\lambda 5007\text{ \AA}$ (ionization parameter); $[\text{O III}]\lambda\lambda 4363, 5007\text{ \AA}$ (temperature sensitive); $[\text{O I}]\lambda 6363\text{ \AA}$, $[\text{N II}]\lambda 6583\text{ \AA}$, $[\text{S II}]\lambda\lambda 6716, 6731\text{ \AA}$ (AGN classifier); $[\text{S II}]\lambda 6716\text{ \AA}/[\text{S II}]\lambda 6731\text{ \AA}$ (density).

The wavelength of the most important emission lines visible in the spectra as well as the abbreviations used throughout this thesis are given in Appendix C (Table C.1).

4.2.1 VLT/FORS1

The high signal-to-noise ratio (S/N) long-slit spectra of four Seyfert galaxies (3 Sy2s, 1 Sy1.2) described here were obtained using FORS1⁴ attached to the Cassegrain focus of UT1 at the VLT on the 25th of February 2004. The FORS1 detector is a 2048×2048 pixels Tektronix CCD⁵ with a pixel size of $24\text{ }\mu\text{m} \times 24\text{ }\mu\text{m}$. Single readout mode (A), 1×1 binning and high ADU⁶ level settings were used. The spatial resolution element is $0''.2\text{ pix}^{-1}$. Observations were made in the spectral range $3050\text{--}8300\text{ \AA}$ through the nucleus of each galaxy with exposure times of 1800 s (to study the emission lines far from the nucleus) and 30 s (to gain the central emission lines which may be saturated in the 1800 s exposure) with a typical seeing of $\sim 1\text{--}2''$.

The slit width was chosen according to the seeing corresponding to $0''.7\text{--}1''.3$ on the sky. These slit widths project to a spectral resolution of $\sim 8\text{--}14\text{ \AA}$ ($\sim 450\text{--}770\text{ km s}^{-1}$) as is confirmed by the full-width-at-half-maximum (FWHM) of wavelength calibration lines as well as of the $[\text{O I}]\lambda 5577\text{ \AA}$ night-sky line. The long slit used corresponds to $6''.8$ on the sky. The slit was orientated along the position angle (p.a.) of the maximum extent of the high excitation gas observed in narrow-band images centered on $[\text{O III}]$ from Schmitt et al. (2003a) in the cases of NGC 1386, NGC 3281, and MCG $-6\text{--}30\text{--}15$. For NGC 5643, the p.a. from the HST $[\text{O III}]$ image of Simpson et al. (1997) was planned to be used. However, by mistake, the observed p.a. differ by 24° to the p.a. of the major $[\text{O III}]$ extension (66° instead of 90°). Fortunately, Christian Leipski observed this galaxy at a p.a. of 90° in a different observing run at the NTT and provided us with these data (see next Section for details). We nevertheless used the high S/N VLT data to derive the stellar template of the galaxy itself and apply it to the NTT data. The HST $[\text{O III}]$ images with the slit position overlaid are shown in Figure 4.1. As UT1 (FORS1) is equipped with an atmospheric dispersion corrector (ADC), there was no need to consider the effects of atmospheric diffraction. The average projected linear scale is $140\text{ pc}/''$, ranging from $52\text{ pc}/''$ (NGC 1386) to $236\text{ pc}/''$ (NGC 3281). Relevant information on the sample and the observations is presented in Tables 4.1 and 4.2.

⁴ FOcal Reducer/low dispersion Spectrograph

⁵ Charge Coupled Device

⁶ Analog-Digital-Unit

Table 4.1: Properties of the VLT sample

	NGC 1386	NGC 3281	NGC 5643	MCG -6-30-15
Alternative Name	ESO 385-G035	ESO 375-G055	ESO 272-G016	ESO 383-G035
α (J2000)	03 ^h 36 ^m 46 ^s .2	10 ^h 31 ^m 52 ^s .1	14 ^h 32 ^m 40 ^s .8	13 ^h 35 ^m 53 ^s .8
δ (J2000)	-35°59'57"	-34°51'13"	-44°10'29"	-34°17'44"
Inclination ($^{\circ}$) ^a	77	66	31	57
Major Axis ($^{\circ}$) ^b	25	140	128	116
V_{hel} (km s ⁻¹)	868±5	3200±22	1199±5	2323±15
$V_{3\text{k}}$ (km s ⁻¹) ^c	774	3523	1400	2595
Distance (Mpc) ^d	11	50	20	37
Linear Scale (pc/'') ^e	52	236	95	175
Morphology	SB(s)0+	SAB(rs+)a	SAB(rs)c	E-S0
AGN Type	Sy2	Sy2	Sy2	Sy1.2
$E(B - V)_G$ (mag) ^f	0.012	0.096	0.169	0.062
M_B (mag)	12.09	12.7	10.74	13.7

Note. – If not stated otherwise, the properties were taken from the NASA/IPAC Extragalactic Database (NED).

^a Inclination angle from face-on (RC3)

^b Position angle of host galaxy major axis (RC3); for NGC 5643, it was taken from Morris et al. (1985) as it is not given in RC3.

^c Velocity relative to the 3K background using the NED velocity calculator

^d Distance D in Mpc, using $v_{3\text{K}}$ and the world model from Appendix A

^e Linear scale d using distance D and $d = 4.848 \cdot 10^{-6} \cdot D$

^f Foreground Milkyway reddening (NED) used for correction

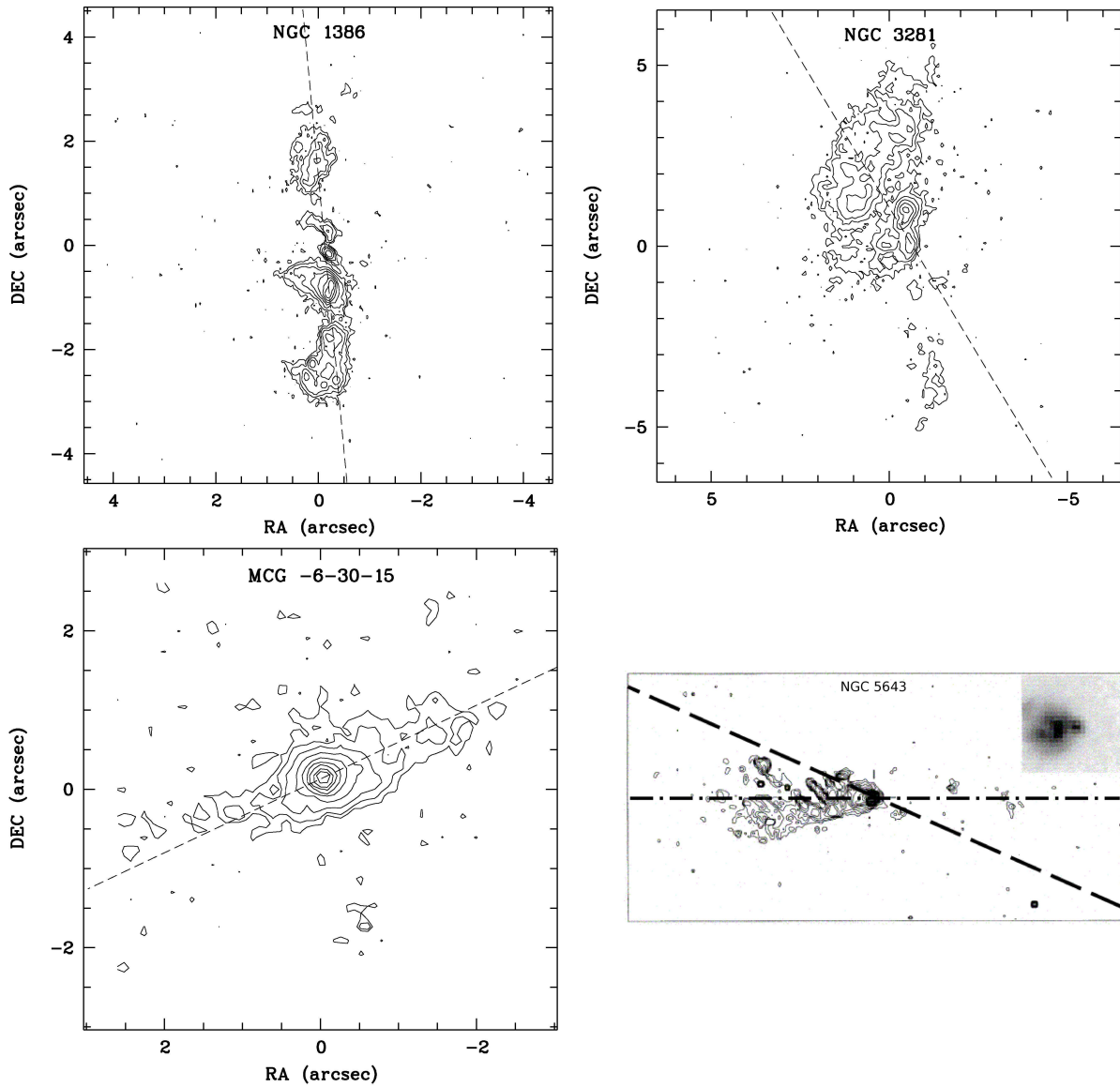


Figure 4.1: HST [O III] images of NGC 1386 (Sy2), NGC 3281 (Sy2), and MCG -6-30-15 (Sy1.2) from Schmitt et al. (2003a). Only NGC 1386 was imaged with the PC chip and its higher resolution of $\sim 0''.05 \text{ pix}^{-1}$, the other objects were imaged with the WF chip ($\sim 0''.1 \text{ pix}^{-1}$). The contours start at the 3σ level above the background (Schmitt et al. (2003a), their Table 2) and increase in powers of 2 times 3σ ($3\sigma \times 2^n$). The position of the long slit is shown as dashed line. The HST [O III] image of NGC 5643 (Sy2, *lower right panel*) was taken from Simpson et al. (1997) and has the dimensions $30'' \times 15''$. The inset shows the central $1'' \times 1''$. The direction of the long slit used in our VLT observations is presented by the long-dashed black line while the p.a. of the long slit used in the NTT observations by Christian Leipski is indicated by the dashed-dotted black line. North is up, east to the left.

Table 4.2: VLT observations

	NGC 1386	NGC 3281	NGC 5643	MCG –6–30–15
Date (beg.)	25-Feb-04	25-Feb-04	25-Feb-04	25-Feb-04
Exposure Time (s) ^a	1800	1800	1800	1800
Seeing	~1''	~1''.5	~2''	~1''.5
Slit Width	0''.7	0''.7	1''.3	1''
FWHM _{instr} (km s ⁻¹)	460	460	770	590
PA (°) ^b	5	31	66	115
Hel. Corr. (km s ⁻¹) ^c	-29	-4	+11	+12
Average (pixel) ^d	5	7	9	7
Scale ^e	1'' × 0''.7	1''.4 × 0''.7	1''.8 × 1''.3	1''.4 × 1''

Note. –

^a Total integration time

^b Position angle of the slit

^c This heliocentric correction was added to the measured radial velocities.

^d Number of pixel rows which were averaged

^e Formal spatial resolution of final extracted spectral rows

4.2.2 NTT/EMMI

High S/N long-slit spectra of another eight Seyfert galaxies (3 Sy2s, 2 Sy1.5s, 3 Sy1s) were obtained using EMMI⁷ attached to the Nasmyth B focus of the NTT on 4 subsequent nights from the 14th to the 18th of September 2004. Medium dispersion spectroscopy was performed in the observing modes REMD⁸ and BLMD⁹ in the red and blue wavelength range, respectively. In the red, two CCD chips are read in a mosaic of four output modes via four separate amplifiers. For spectroscopic modes, only amplifier B is used (MIT/LL CCD). The image size is 2048 × 4096 pixels with pixel sizes of 15 μm × 15 μm. The BLMD detector is a 1024 × 1024 pixels Tektronix CCD with a pixel size of 24 μm × 24 μm. Single binning was used in the blue and double binning in the red, respectively, both in slow CCD readout mode for the lowest readout noise. The spatial resolution element is 0''.37 pix⁻¹ in the blue and 0''.33 pix⁻¹ in the red. Observations were made in the spectral range 3650–5350 Å (blue) and 4540–7060 Å (red) through the nucleus of each galaxy. All four nights were photometric with a typical seeing of ~0.5–1''. Thus, for all objects a slit width of 1'' was chosen. It projects to a spectral resolution of ~4 Å (~250 km s⁻¹ at [O III]) as is confirmed by the FWHM of wavelength calibration lines as well as of the [O I] λ5577 Å night-sky line. The long slit used corresponds to 5'.5 on the sky. The slit was orientated along the p.a. of the maximum extent of the [O III] emission taken from Mulchaey et al. (1996a) for NGC 526a and ESO 362–G008, and from Schmitt et al. (2003a) for the remaining six objects. In Figures 4.2 and 4.3, we show the corresponding [O III] images and the long-slit position overlaid as dashed line. The average scale is 335 pc'', ranging from 220 pc'' (IC 5063) to 504 pc'' (NGC 7212). Relevant information on the sample and observations is summarized in Tables 4.3, 4.4, and 4.5.

⁷ ESO Multi-Mode Instrument

⁸ REd Medium Dispersion spectroscopy

⁹ BLue Medium Dispersion spectroscopy

For Mrk915, the spectra taken in the blue wavelength range were corrupted due to instrumental problems.

NGC 5643 was observed with EMMI at the NTT in REMD mode (spatial resolution $\sim 0''.33 \text{ pix}^{-1}$) on April 21st 2004 by Christian Leipski. The seeing was $\sim 1''$ and the slit corresponds to $0''.7$. NGC 5643 was observed at a low airmass (< 1.1) with a total integration time of 3600 s in both the blue (4650–5450 Å) and the red wavelength range (6500–7250 Å). While the spectral resolution is high ($\sim 1.5 \text{ Å} \simeq 90 \text{ km s}^{-1}$ at [O III]), the spectral range does not cover the [O II] and the [O I] lines. Therefore, we can neither derive the ionization parameter from the ratio [O II]/[O III] nor the second diagnostic diagrams which involves the [O I] line.

At the NTT, no ADC is available. As we aimed to observe along the major extension of the [O III] emission, we could not observe along the parallactic angle. Thus, several precautions were taken: (i) The galaxies were centered using the red slit camera in the red wavelength range, and on the contrary, a blue filter was used to center the objects for observations in the blue wavelength range. (ii) All objects were observed at airmasses higher than 1.3 in which case the atmospheric differential refraction is smaller than the slit width in both the blue and red wavelength range (Filippenko, 1982).

4.3 Reduction and Analysis

4.3.1 Standard Reduction

Standard reduction including bias subtraction, flat-field correction, and cosmic ray rejection was performed using the ESO MIDAS¹⁰ software (version Nov. 99). Night-sky spectra “above” and “below” any notable galaxy emission were interpolated in the region of the galactic spectrum and subtracted in each case. Wavelength calibration was achieved by rebinning the spectra to a scale of 2.65 Å pix^{-1} during wavelength calibration for the VLT spectra. For the NTT data, a scale of 1.84 Å pix^{-1} for the blue and 1.58 Å pix^{-1} for the red wavelength range was obtained. For NGC 5643, the spectra taken by Christian Leipski have a higher resolution, corresponding to a scale of 0.4 Å pix^{-1} . The curve of Tüg (1997) was used to correct for atmospheric extinction. The spectra were flux calibrated using the standard star CD-32°9927 in case of the VLT data and LTT 7379 for the NTT data (with the exception of NGC 5643 for which LTT 3684 was used as standard star). At the NTT, we observed several standard stars during the night to independently probe the quality of the flux calibration. We applied the instrumental response function derived from LTT 7379 to the observed spectra of the other standard stars and compared the resulting flux calibrated standard star spectra with literature values: In all nights, a very good agreement was found. Foreground Milky Way reddening was corrected using values from Schlegel et al. (1998), as listed in NED, and the extinction law from Savage et al. (1979). Forbidden-line wavelengths were taken from Bowen (1960). Heliocentric corrections as given in Tables 4.2 and 4.5 were added to the observed velocities.

¹⁰ Munich Image Data Analysis System, trade-mark of the ESO

Table 4.3: Properties of the NTT sample (Seyfert–1 galaxies)

	Fairall 51	NGC 6860	Mrk 915	NGC 526a	MCG –05–13–017
Alternative Name	ESO 140–G043	ESO 143–G009	MCG –02–57–023	MCG –06–04–019	ESO 362–G018
α (J2000)	18 ^h 44 ^m 54 ^s .0	20 ^h 08 ^m 46 ^s .9	22 ^h 36 ^m 46 ^s .5	01 ^h 23 ^m 54 ^s .4	05 ^h 19 ^m 35 ^s .8
δ (J2000)	–62°21′53″	–61°06′01″	–12°32′43″	–35°03′56″	–32°39′28″
Inclination (°) ^a	64	61	80	55	54
Major Axis (°) ^b	162	34	166	112	160
V_{hel} (km s ^{–1})	4255±10	4462±24	7228±2	5725±39	3790±30
$V_{3\text{k}}$ (km s ^{–1}) ^c	4228	4377	6863	5446	3620
Distance (Mpc) ^d	60	62	98	78	52
Linear Scale (pc/″) ^e	283	293	454	362	243
Morphology	(R’_2)SB(rs)b	(R’)SB(r)ab	Sb	S0pec?	S0/a
AGN Type	Sy1	Sy1	Sy1	Sy1.5	Sy1.5
$E(B - V)_G$ (mag) ^f	0.108	0.041	0.063	0.028	0.017
M_B (mag)	14.7	13.68	14.82	14.5	12.5

Note. – If not stated otherwise, the properties were taken from NED. For three Seyfert–1 galaxies, we derive a different AGN classification from our spectra than the one given in NED: We classify both NGC 6860 and Mrk 915 as Sy1.5 instead of Sy1 [in agreement with Cid Fernandes et al. (1998); Lípari et al. (1993)], and MCG –05–13–017 as Sy1.9 instead of Sy1.5 [in agreement with Winkler (1992); see also Section 4.4.13].

^a Inclination angle from face–on (RC3)

^b Position angle of host galaxy major axis (RC3)

^c Velocity relative to the 3K background using the NED velocity calculator

^d Distance D in Mpc, using $v_{3\text{K}}$ and the world model from Appendix A

^e Linear scale d using distance D and $d = 4.848 \cdot 10^{-6} \cdot D$

^f Foreground Milkyway reddening (NED) used for correction

Table 4.4: Properties of the NTT sample (Seyfert-2 galaxies)

	IC 5063	NGC 7212	ESO 362-G008
Alternative Name	ESO 187-G023	MCG +02-56-011	MCG -06-12-009
α (J2000)	20 ^h 52 ^m 02 ^s .3	22 ^h 07 ^m 01 ^s .3	05 ^h 11 ^m 09 ^s .1
δ (J2000)	-57°04'08"	+10°13'52"	-34°23'36"
Inclination (°) ^a	51	66	70
Major Axis (°) ^b	116	42	167
V_{hel} (km s ⁻¹)	3402±6	7984±21	4785±24
$V_{3\text{k}}$ (km s ⁻¹) ^c	3276	7638	4809
Distance (Mpc) ^d	47	110	67
Linear Scale (pc/'') ^e	220	504	321
Morphology	SA(s)0+:	Sab	Sa
AGN Type	Sy2	Sy2	Sy2
$E(B - V)_G$ (mag) ^f	0.061	0.072	0.032
M_B (mag)	12.89	14.8	13.6

Note. – If not stated otherwise, the properties were taken from NED.

^a Inclination angle from face-on (RC3)

^b Position angle of host galaxy major axis (RC3)

^c Velocity relative to the 3K background using the NED velocity calculator

^d Distance D in Mpc, using $v_{3\text{K}}$ and the world model from Appendix A

^e Linear scale d using distance D and $d = 4.848 \cdot 10^{-6} \cdot D$

^f Foreground Milkyway reddening (NED) used for correction

Table 4.5: NTT observations

	Fairall 51	NGC 6860	Mrk 915	NGC 526a	MCG -05-13-017
Date (beg.)	14/15-Sep-04	15/16-Sep-04	14/15-Sep-04	16-Sep-04	17-Sep-04
Exposure Time Blue (s) ^a	3000	6000	–	3000	3600
Exposure Time Red (s) ^a	3600	3600	3000	2400	3000
Seeing	< 1''	< 1''	< 1''	< 1''	< 1''
Slit Width	1''	1''	1''	1''	1''
FWHM _{instr} (km s ⁻¹)	250	250	250	250	250
PA (°) ^b	160	85	5	123	140
Hel. Corr. (km s ⁻¹) ^c	-2	0	-4	+17	+29
Average (pixel) ^d	3	3	3	3	3
Scale ^e	1''.1 × 1''	1''.1 × 1''	1''.1 × 1''	1''.1 × 1''	1''.1 × 1''
	IC 5063	NGC 7212	ESO 362-G008	NGC 5643	
Date (beg.)	15/16-Sep-04	17-Sep-04	14/15/16-Sep-04	21-Apr-04	
Exposure Time Blue (s) ^a	6000	2732	5400	3600	
Exposure Time Red (s) ^a	3600	1800	5400	3600	
Seeing	< 1''	< 1''	< 1''	1''	
Slit Width	1''	1''	1''	0''.7	
FWHM _{instr} (km s ⁻¹)	250	250	250	90	
PA (deg) ^b	115	170	163	90	
Hel. Corr. (km s ⁻¹) ^c	0	-12	+29	-9	
Average (pixel) ^d	3	3	3	3	
Scale ^e	1''.1 × 1''	1''.1 × 1''	1''.1 × 1''	1''.1 × 1''	

Note. –

^a Total integration time

^b Position angle of the slit

^c This heliocentric correction was added to the measured radial velocities.

^d Number of pixel rows which were averaged

^e Formal spatial resolution of final extracted spectral rows

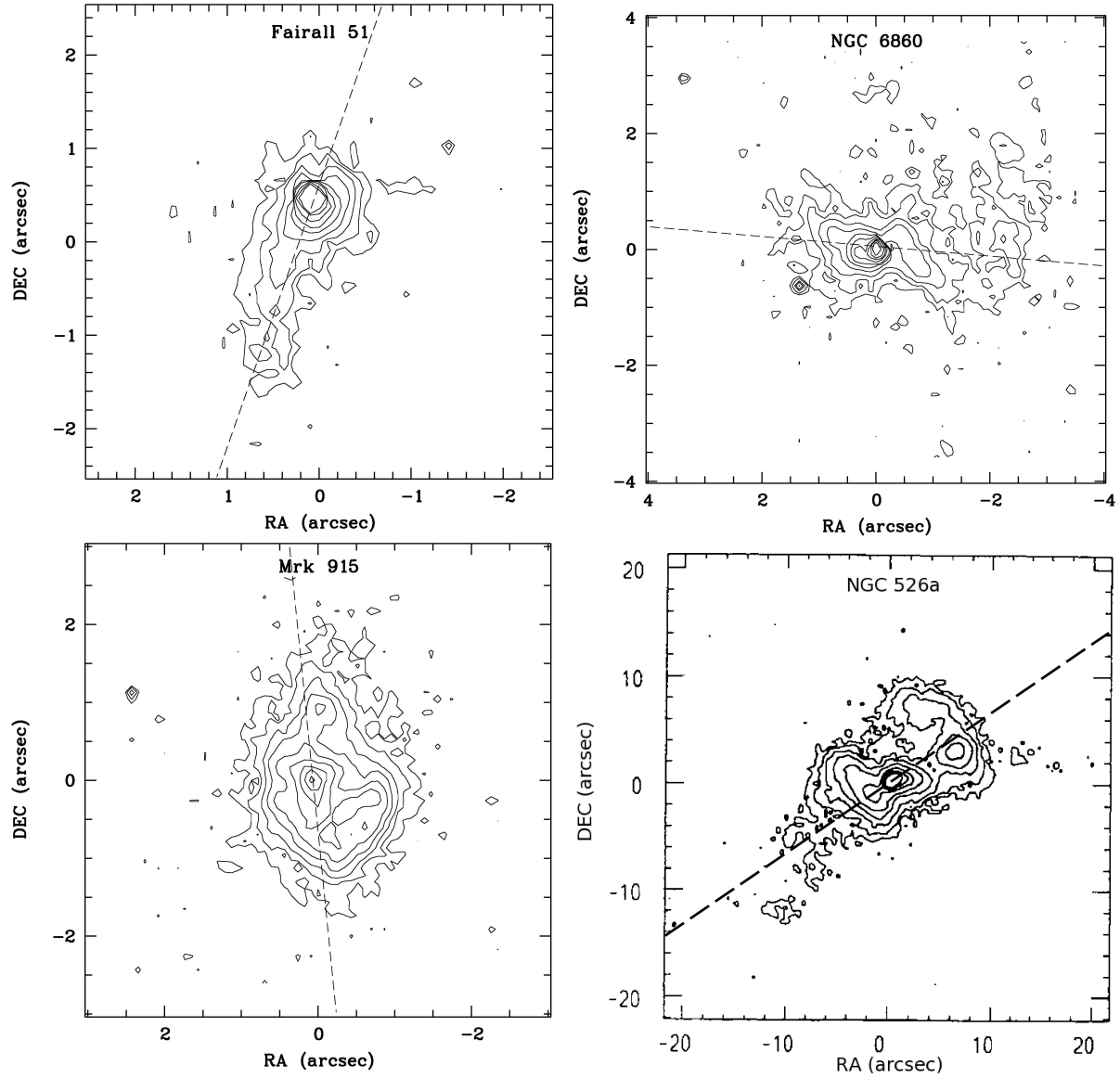


Figure 4.2: HST [O III] images of Fairall 51 (Sy1), NGC 6860 (Sy1), and Mrk 915 (Sy1) taken from Schmitt et al. (2003a), imaged with the WF chip ($\sim 0''.1 \text{ pix}^{-1}$). The contours start at the 3σ level above the background (Schmitt et al. (2003a), their Table 2) and increase in powers of 2 times 3σ ($3\sigma \times 2^n$). The groundbased [O III] image of NGC 526a (Sy1.5) was taken from Mulchaey et al. (1996a). The position of the long slit is shown as dashed line. North is up, east to the left.

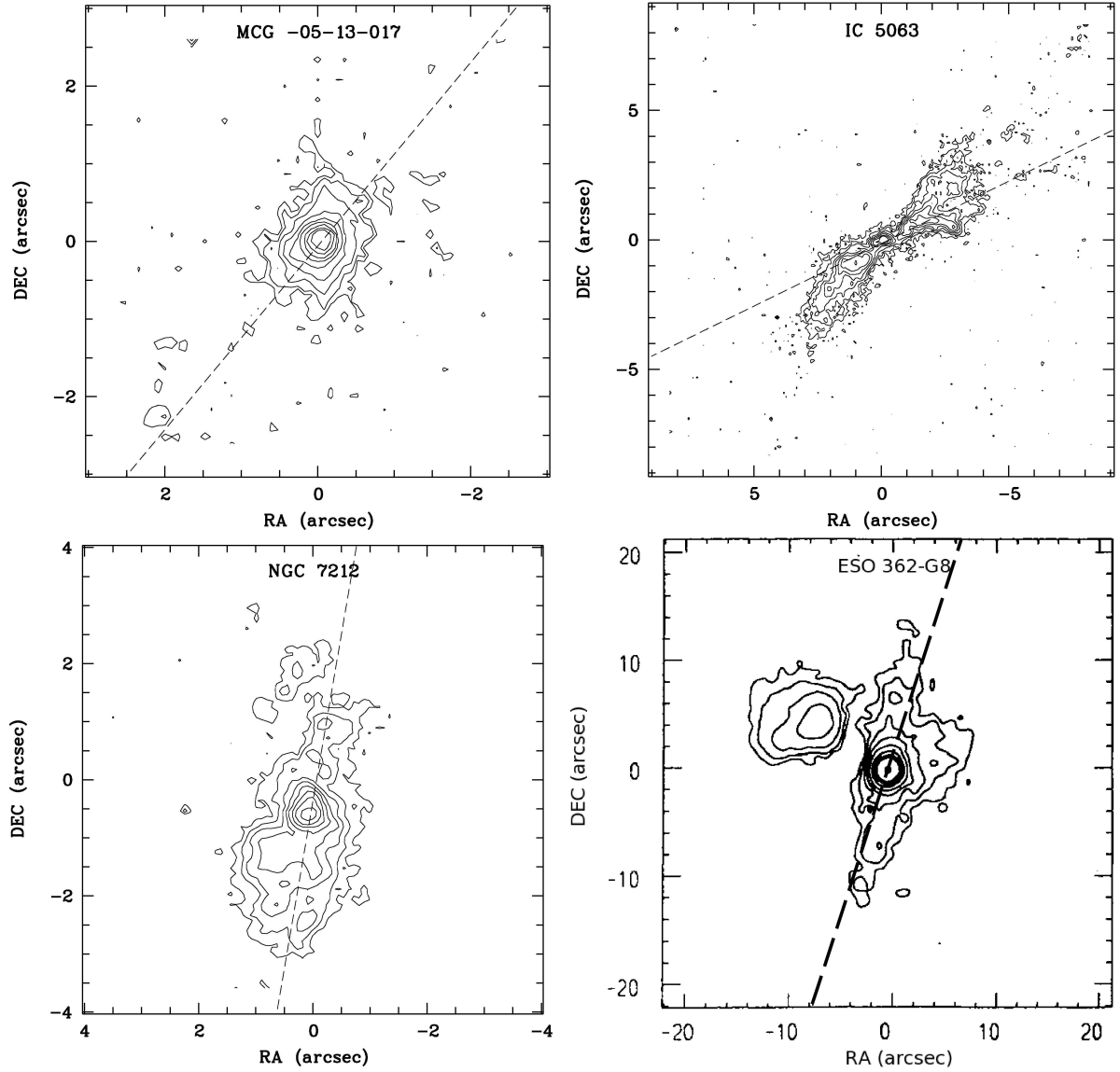


Figure 4.3: HST [O III] images of MCG -05-13-017 (Sy1.5), IC 5063 (Sy2), and NGC 7212 (Sy2) taken from Schmitt et al. (2003a), imaged with the WF chip ($\sim 0''.1 \text{ pix}^{-1}$). The contours start at the 3σ level above the background (Schmitt et al. (2003a), their Table 2) and increase in powers of 2 times 3σ ($3\sigma \times 2^n$). The groundbased [O III] image of ESO 362-G008 (Sy2) was taken from Mulchaey et al. (1996a). The position of the long slit is shown as dashed line. North is up, east to the left.

4.3.2 Extraction

Single rows were extracted from the frames cleaned in this way. In the case of the FORS1 spectra, each pixel row corresponds to $0''.2$ and $1\text{--}2''$ along and perpendicular to the slit direction, respectively. In the case of the EMMI spectra, the spectra taken with the red chip and its slightly higher spatial resolution ($0''.33 \text{ pix}^{-1}$ compared to $0''.37 \text{ pix}^{-1}$ in the blue) were rebinned to the resolution of the blue chip. Thus, each pixel row corresponds to $0''.37$ and $1''$ along and perpendicular to the slit direction, respectively. Along the “spatial axis” of the CCD, we identified the “photometrical center” (that we choose as “zero” on the spatial scale) with that spectral row of the CCD where continuum and intensities of $\text{H}\alpha$ and $[\text{O III}]$ are at maximum (“central row”). (Note that this optical nucleus needs not necessarily coincide with the position of the AGN, which may be hidden by dust.) In the case of the FORS1 spectra, three to nine pixel rows were averaged according to the seeing to enhance the S/N without losing any spatial information (see Table 4.2 for a detailed information on each galaxy). We averaged 3 pixel rows of all NTT spectra, corresponding to $1''.1$. Thus, line intensities and ratios refer to windows of $1\text{--}2$ square arcsec size. On average, $[\text{O III}]$ emission at a $\text{S/N} > 3$ out to $r \sim 13''$ distance from the nucleus were measured, ranging from a spatial coverage of $4''$ (ESO 362-G008) to $20''$ (IC 5063), plus extended H II regions in some galaxies [e.g. in NGC 5643 out to $75''$ ($\sim 7125 \text{ pc}$) from the center]. Line ratios at a $\text{S/N} > 3$ were measured out to an average distance of $r \sim 8''$.

The angular distances were transformed to linear distances at the galaxies (Tables 4.1, 4.3, and 4.4). As the linear distances are projected distances and strongly depend on the (uncertain) distance to the galaxy as well as the adopted Hubble constant, we instead use in our figures the angular scale on the x-axis and give as bar a measure of the corresponding linear scale.

The observations of each galaxy with EMMI at the NTT were split over several nights and divided into two spectral ranges, covering the red and blue range, respectively. The same long-slit p.a. was used and we centered in each case on the bright nucleus. To probe that all spectra taken in subsequent nights cover the same galactic region in an object, we compared the positions of stellar spectra visible in our images. We chose only those 3D spectra that show the same stars at the same distance to the brightest row in continuum, identified as the center of the galactic emission: Observing at the same p.a. and finding the same stars at a certain distance to the center of the galaxy indicates that we cover the same region within each galaxy. The blue and red spectra as well as the spectra of different nights were matched on the photometrical center.

4.3.3 Stellar Population of Galactic Nuclei

Starlight constitutes a substantial fraction of light gathered in the optical spectra of AGNs, particularly in low-luminosity objects such as LINERs and Seyfert galaxies. The emission-line fluxes are affected by underlying absorption lines which can be large especially in the case of $\text{H}\beta$. As a consequence, starlight can have a great influence on the determination of the reddening value $\text{H}\alpha/\text{H}\beta$, the reddening correction, and the AGN diagnostic line ratio $\text{H}\beta/[\text{O III}]$. Thus, removing the contribution of the stellar population is one of the first and most critical steps in the analysis of AGN emission-line spectra.

The most widely used technique for starlight subtraction makes use of an appropriately chosen spectrum of a normal galaxy as a template for the stellar component.

However, the stellar populations in the inner regions of AGNs present a variety of characteristics (Cid Fernandes et al., 1998), giving rise to the need of a library with a large diversity of stellar populations.

Alternatively, the shape and strength of the starlight component can be estimated by means of stellar population synthesis techniques, following the work pioneered by Bica (1988). The classification refers to the library of synthetic spectra of Bica (1988), i.e. templates composed of different percentages of star cluster spectra of several ages and metallicities. An S3 template, for example, contains only the contribution of stars older than 10 Gyr. In S4, 95% of the light at 5870 Å comes from old stars and 5% from young and intermediate age ones. In S5, the contribution is 85% from old stars and 15% from young and intermediate age ones, etc. Thus, a low number “Sx” indicates a rather old stellar population, a high number a young one. This method, however, involves several assumptions of stellar modeling and does not necessarily yield an unambiguous solution.

The galaxy itself as stellar template

Here, we applied the straightforward approach of using the galaxy *itself* as starlight template which should give the best representation of the stellar population.

However, this method has some caveats: First, one implicitly assumes that the stellar population does not vary much in the inner few arcseconds, i.e. the bulge. This assumption can be probed: The close match of the stellar template and the absorption lines in all studied rows in most of our spectra justifies this assumption. Second, one needs high sensitivity data to gain spectra of the host galaxy far away from the NLR emission which is possible in our case. Third, the contribution of the AGN featureless continuum must be negligible to not overestimate the underlying absorption lines by scaling the template to the continuum of the NLR spectra. The latter assumption seems to be justified at least for type-2 AGNs: For most of the 20 Seyfert 2s in their sample, including e.g. NGC 1386, Cid Fernandes et al. (1998) find little or no dilution of the stellar lines by an underlying featureless continuum.

The available high-sensitivity spectra allow us to use several rows with good S/N ratios in the outer part of the galaxy spectrum as template. These rows were averaged and median filtered along the spectral axis over three pixels to increase the S/N.

The template was scaled to each row of the NLR spectrum by normalization in the red ($\sim 5400\text{--}5700$ Å), justified by the fact that the slope at $\lambda \geq 5400$ Å does not change significantly for different stellar populations (Bica & Alloin, 1986). (Note that we also chose this range as it does not cover any strong NLR emission lines.) To allow for a possible reddening difference of the template and each row of the NLR spectra due to different dust amounts in different galactic regions (or e.g. dust intrinsic to the NLR), we applied a reddening correction to the template by fitting the continuum slope of the template to the spectra of the NLR [MIDAS command “extinct/long” with extinction-law from Savage et al. (1979)]. This procedure was often necessary to avoid a template continuum exceeding that of the NLR continuum at some wavelength after normalization.

In Figure 4.4, we show an example of a stellar template with and without reddening correction with respect to the nucleus of NGC 1386.

The reddening correction of the stellar template gives us an independent reddening measurement from the one using emission-line ratios. However, we cannot calibrate this “slope reddening” as we do not know the reddening of our stellar template.

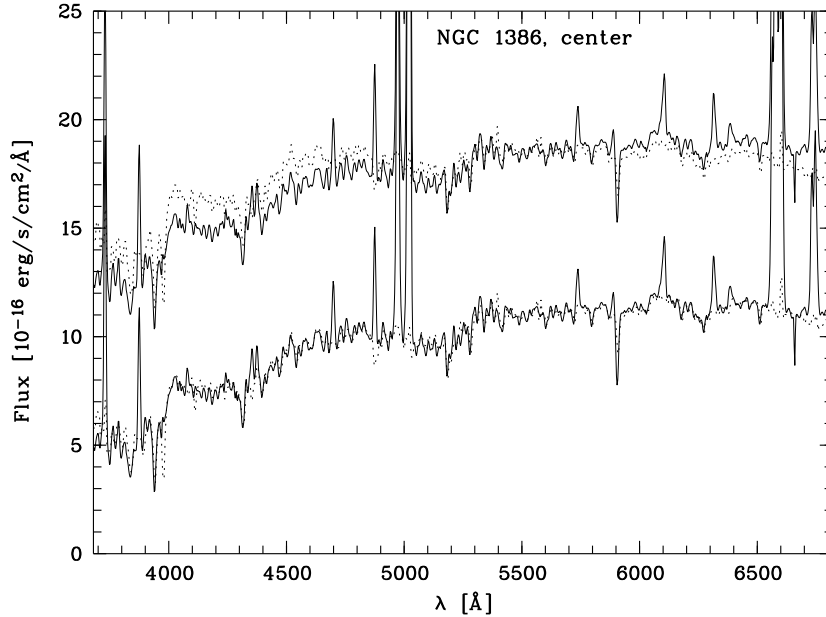


Figure 4.4: Central spectra of NGC 1386 with stellar template overlaid as dotted line. In the upper spectra which were shifted by an arbitrary amount for comparison, the reddening of the NLR spectra with respect to the template can be clearly seen. In the lower spectra, a reddening correction of $E_{(B-V)} = 0.12$ mag was applied to the template to improve the match of the template and the continuum of the NLR spectrum.

Moreover, the reddening observed for the stellar population needs not necessarily be connected to the reddening of the NLR as the stars can suffer a different dust extinction. In Section 4.4.2, we show the reddening distributions derived by both methods and discuss the differences.

The scaled (de-)reddened template was subtracted from each row of the NLR spectrum. Finally, any remaining continuum contribution was fit manually and subtracted to gain the pure emission-line spectra ready for fitting.

The details of the template subtraction procedure for both type-1 and type-2 objects are given in Table 4.6. The templates compared to the emission-line spectra are shown in Figure 4.5.

Seyfert-2 galaxies

For all type-2 objects, this procedure was generally applied (see Table 4.6 and Figure 4.5) with the exception of NGC 7212 as no stellar absorption lines were seen in the spectra.

To probe the quality of the match between the stellar template and each row of the observed NLR, we concentrated on stellar absorption lines which were not contaminated by emission throughout the NLR. Two strong lines suited for this purpose are Ca II K and Na I D. While the residuum of Ca II K absorption in the resulting spectrum after subtraction of the stellar template is within the noise levels, Na I D absorption remains in some objects (e.g. NGC 1386, NGC 3281, IC 5063; Figure 4.9). However, at least part of the Na I D absorption line may originate from interstellar absorption.

The lack of significant other stellar absorption lines after subtraction of the template confirms our approach and the assumption that the stellar population does not change much throughout the NLR in the observed objects.

The exception, however, is ESO 362–G008. Here, the stellar population seems to change very rapidly in the innermost regions and the equivalent widths (EW) of the underlying stellar absorption lines get significantly larger towards the center. It implies the existence of a very young stellar population close to the AGN. It was not possible to derive a template spectrum neither from the outer part of the galaxy which fit the stellar absorption lines throughout the NLR nor from the inner part due to the “contamination” by emission lines. Close to the center, the Balmer emission lines start to fill the underlying absorption trough making it impossible to correct for the stellar absorption. Thus, we decided to use an outer template as first approach. Our results for this object have to be taken with some caution. They indicate that in the cases of $H\beta$ and $H\alpha$, the correction was not sufficient.

For one object (IC 5063), the velocity gradient across the NLR was large compared to our resolution ($\sim 500 \text{ km s}^{-1}$ compared to $\text{FWHM}_{\text{instr}} \sim 250 \text{ km s}^{-1}$). Therefore, we rebinned the chosen stellar template (velocity measured by fitting a Gaussian to the absorption profile of Ca II K) to the velocity of each individual row (as measured by fitting a Gaussian to the [O III] profile). For the other objects, the velocity gradient is significantly smaller than our spectral resolution and we did not apply such a correction.

Note that for NGC 5643, the high S/N VLT spectra was used to derive a stellar template. No reddening correction was applied during the fitting of the stellar template due to the low S/N of the EMMI spectra.

Seyfert–1 galaxies

For the type–1 objects, the procedure is more difficult. The AGN featureless continuum can be very strong, especially in the central parts where the broad emission lines are seen. Thus, a stellar template cannot be simply scaled to the continuum value in these regions as the contribution of the underlying stellar population would be overestimated. However, the AGN continuum and the broad and narrow emission lines often completely dominate the spectrum. We did not find signs of strong underlying Balmer absorption lines. In some cases, faint absorption is visible in Ca II H&K and in Na I D. Some of the Na I D absorption may be of interstellar origin. We consider the underlying stellar absorption as negligible compared to the central emission line fluxes. Moreover, it was difficult to derive a suited template without contaminating emission lines and at a high S/N.

Only for MCG –6–30–15, we were able to gain a suited template free of contaminating emission lines. Thus, a correction of underlying stellar absorption lines in the Seyfert–1 galaxies were applied only to MCG –6–30–15. We scaled the template to the continuum as we do not know the contribution of a featureless continuum. As a consequence, the reddening measure using the continuum slope variation relative to the stellar template was, among the Seyfert–1 galaxies, only determined for MCG –6–30–15.

To conclude, the results for the Seyfert–1 galaxies suffer from a larger uncertainty in the emission–line fluxes of the narrow Balmer lines compared to the Seyfert 2s, due to both possibly remaining underlying absorption and the contribution of the BLR.

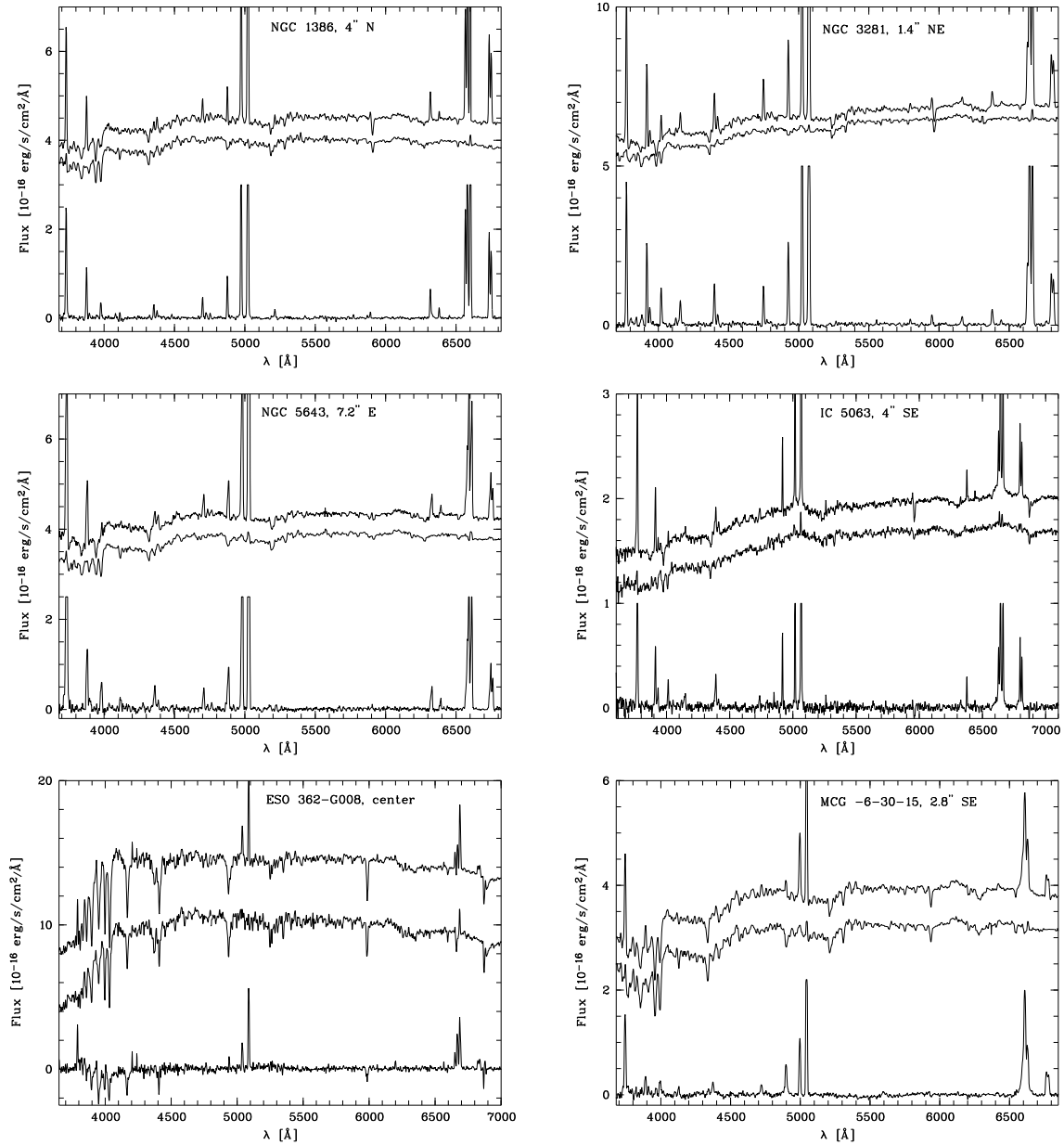


Figure 4.5: Template subtraction for NGC 1386 (Sy2), NGC 3281 (Sy2), NGC 5643 (Sy2), IC 5063 (Sy2), ESO 362-G008 (Sy2), and MCG -6-15-30 (Sy1). The observed spectra (upper), the template spectra (middle) and the template-subtracted spectra (lower spectrum) are shown. For comparison, both upper spectra are shifted vertically by an arbitrary amount. Strong emission lines are truncated in the difference spectrum. The template matches the stellar absorption lines seen in the NLR spectrum fairly well, with the exception of ESO 362-G008 for which strong Balmer absorption lines remain.

Table 4.6: Template subtraction details

Galaxy	Distance	Size
NGC 1386	18" (N)	3"
NGC 3281	11" (SW)	1".5
NGC 5643 ^a	26" (SW)	2"
IC 5063 ^b	23" (NW)	7"
ESO 362–G008	6" (SE)	1"
MCG –6–30–15	12" (NW)	2"

Note. – The template distance from the nucleus is given with the direction in brackets as well as the size (diameter) of the region that was averaged to gain the template. The spectra were median-filtered over three pixel to increase the S/N.

^a Template taken from VLT spectra (p.a. 66°); no reddening correction applied.

^b Velocity correction applied

Influence of stellar template

Although we developed the method of using the galaxy itself as stellar template independently from literature, it has been applied by several authors [e.g. Weaver et al. (1991); Reynolds et al. (1997); Fraquelli et al. (2000); Schmid et al. (2001)]. Often, the stellar template consists not only of stellar absorption lines but also of some emission due to H II regions: For all objects where we used a template to subtract the stellar absorption lines, faint emission lines in [O II], [O III], [N II], and [S II] are seen in the template spectrum.

Some authors [e.g. Weaver et al. (1991); Schmid et al. (2001)] clip this emission to get the stellar absorption lines only. However, this clipping procedure has to be taken with some caution. First, by clipping the visible emission only, one most probably artificially changes the ratios between e.g. [O III]/H β or [N II]/H α as the forbidden lines are in emission only and easy to be clipped but the corresponding H β and H α emission are missed due to the underlying absorption trough. That means that the H β and H α absorption is underestimated. Second, depending on the distribution of a young stellar population and its H II-region emission, this emission may be a real contribution to the observed NLR emission lines and thus, it is a good approach to really subtract it. This is for example the case, if the H II regions are homogeneously distributed and lie in the line-of-sight in front of the NLR. In general, starbursts occur where the dense gas is present, i.e. towards the stellar disk, and often form a ring around the center [see e.g. review by Buta & Combes (1996)]. Circumnuclear starbursts are known to occur in AGNs [e.g. Terlevich et al. (1992); Hernquist & Mihos (1995); Cid Fernandes et al. (2001)] and will thus contribute to the observed NLR emission.

For a quantitative approach, we exemplarily clip the emission lines visible in the stellar template of NGC 1386 (Section 4.4.12). The difference in the results using such a template compared to the “normal” one is within the errors. To conclude, we tried to avoid to use regions with H II regions as stellar template and used only those rows as template where the spectra is dominated by absorption lines. Any remaining faint emission were not clipped but subtracted.

4.3.4 Fe II Template

When studying optical spectra of type-1 AGNs, another issue that needs to be taken into account is the contribution of broad Fe II emission. While the Fe II origin is still being questioned, it is possible that it arises from the BLR or the accretion disk. (For type-2 AGNs it is thus not visible as it is absorbed by the torus, in the framework of the unified model.) The Fe II emission consists of several lines, and, depending on the spectral resolution (which was rather low in our observations), it is smeared out to a whole underlying band of Fe II emission in the $H\beta$ to [O III] regime.

To probe the contribution of Fe II to the observed type-1 spectra, we used the Fe II template of Véron-Cetty et al. (2004). It was rebinned to the same resolution and shifted to the object's redshift. We used several scaling factors and subtracted the template. The residual continuum was searched for signs of remaining Fe II emission. However, in all our type-1 objects, the contribution of Fe II seems to be negligible and for most scalings, we artificially induced “Fe II absorption lines”, indicating that the scaling was too high. Thus, no Fe II template was finally subtracted as we believe that the Fe II contribution is negligible in our Seyfert-1 galaxies.

4.3.5 Emission-Line Fluxes and Reddening

The fluxes of the pure emission-line spectra were measured as a function of distance from the nucleus by integrating along a Gaussian fit to the line profile. The fit routine “fit/spec” (Rousset, 1992) was used for this purpose. For pairs of lines ([O III] $\lambda\lambda 4959, 5007 \text{ \AA}$, [O I] $\lambda\lambda 6363, 6300 \text{ \AA}$, and [N II] $\lambda\lambda 6548, 6583 \text{ \AA}$) with a fixed line ratio [$\sim 1:3$; Osterbrock (1989), his Tables 3.8 and 3.9], this line ratio was used to constrain the fit. Due to our low spectral resolution, [Fe X] $\lambda 6375 \text{ \AA}$ is blended with the [O I] $\lambda 6363 \text{ \AA}$ line. Thus, to estimate the contribution of [Fe X] $\lambda 6375 \text{ \AA}$, we fit two Gaussians to [O I] $\lambda 6300, 6363 \text{ \AA}$ with line fluxes fixed to the ratio of 1:3 and a third one to fit any remaining flux of [Fe X] $\lambda 6375 \text{ \AA}$.

The wavelengths of the most important emission lines visible in the spectra are given in Appendix C (Table C.1). In the following, we simply use the abbreviations without the corresponding wavelengths as long as it is unambiguous.

In addition to the emission lines, Ca II K $\lambda 3933 \text{ \AA}$ and Na I D are sometimes seen in absorption and used to fit the stellar velocity curve. However, some of the Na I D may also arise from interstellar absorption.

In one case (NGC 1386), the strongest emission lines were saturated in the three central rows (center $\pm 1''$) in the 1800 s exposure. We therefore derived all fluxes in the center from the 30 s nuclear exposure instead.

The derivation of physical parameters from emission-line ratios such as temperature, reddening, density, and ionization parameter is summarized in Appendix C.

The uncertainties in deriving the fluxes were mostly caused by uncertainties in the placement of the continuum and were thus estimated as the product of the FWHM of the line and the root-mean square deviation of the continuum flux in a spectral region without emission or absorption lines. The error propagation equation was used to calculate the errors of subsequent parameters (Appendix D, Eq. D.2). The resulting errors are in the range of ~ 1 –15%. Note that we did not take into account uncertainties introduced by the stellar absorption correction and the quality of the Gaussian fits which was very good given the low spectral resolution of our data.

The spectra were dereddened using the recombination value for the intensity ratio $H\alpha/H\beta = 2.87$ (a typical value for AGNs for $T = 10000$ K) and an average reddening curve [Osterbrock (1989), Table 7.2; see Appendix C for details]. Note that in the following, only those spectral rows are used which have emission-line fluxes exceeding the S/N value of 3.

Seyfert-2 galaxies

For most of the type-2 objects in our sample, a simple Gaussian was sufficient to fit the observed narrow-line profiles. Examples of the Gaussian fits to the blended, and thus more complicated to fit, $H\alpha + [N\text{II}]$ as well as $[S\text{II}]$ emission lines are presented in Figure 4.6.

In the cases of NGC 5643 and IC 5063, the profiles revealed substructure such as blue- or redshifted subpeaks and shoulders. This is not unusual for AGNs and commonly interpreted as outflow [e.g. Whittle (1985); Veilleux et al. (1990)]. The pronounced substructure was limited to the central arcseconds ($22''$ for NGC 5643 and $9''$ for IC 5063) and we used three Gaussians (a central one as well as a blueshifted and a redshifted one) to fit the narrow emission lines with the strengths varying spatially to closely approximate the total line flux (Fig. 4.7). For NGC 5643, we were able to study the profiles and their spatial variation in greater detail, given the high resolution of these spectra (Section 4.4.13).

Seyfert-1 galaxies

For type-1 objects, the fitting procedure is more difficult due to the additional broad lines of the BLR underlying all permitted emission of the NLR. Broad $H\alpha$ lines are observed in the central spectra of all our type-1 objects (according to their classification as Sy1, Sy1.2 or Sy1.5). Broad $H\beta$ emission is seen in all type 1s with the exception of NGC 526a, classifying it as Sy1.9 (see also Section 4.4.13).

In three exceptional cases (Fairall 51, NGC 6860, and Mrk 915), we observe broad $H\alpha$ emission extending much further (up to $r \sim 4-6'' \simeq 1.2-1.8$ kpc from the center) than what can be explained by scattering due to the very good seeing ($< 1''$). Instrumental effects can also be excluded. A possible explanation is scattering within the AGN. We discuss these observations in detail in Section 4.4.10.

A common approach to disentangle the narrow and broad permitted lines is to use the profile of the forbidden narrow lines such as $[O\text{III}]$ as template for the permitted narrow line, scaled to the appropriate height. A second Gaussian (a broad one) is additionally used to fit the permitted broad line profile.

During the fitting procedure, we found that the use of two Gaussians, a broad and a narrow one, was in most cases not suited to fit the broad wings. Thus, for all lines with underlying broad emission, we additionally added a third Gaussian: We fitted a narrow Gaussian, one with an intermediate width, and a broad one for an optimal total fit to the observed emission-line profiles. Three Gaussians have already been used by other authors to fit the $H\alpha$ and $H\beta$ lines in Seyfert-1 galaxies [e.g. Reynolds et al. (1997)].

One has to keep in mind that emission-line profiles represent line-of-sight integrations of several kinematical components and even for “narrow” lines, considerable profile structure is measured at sufficient resolution [e.g. Vrtilik & Carleton (1985); Whittle (1985); Schulz & Henkel (2003)].

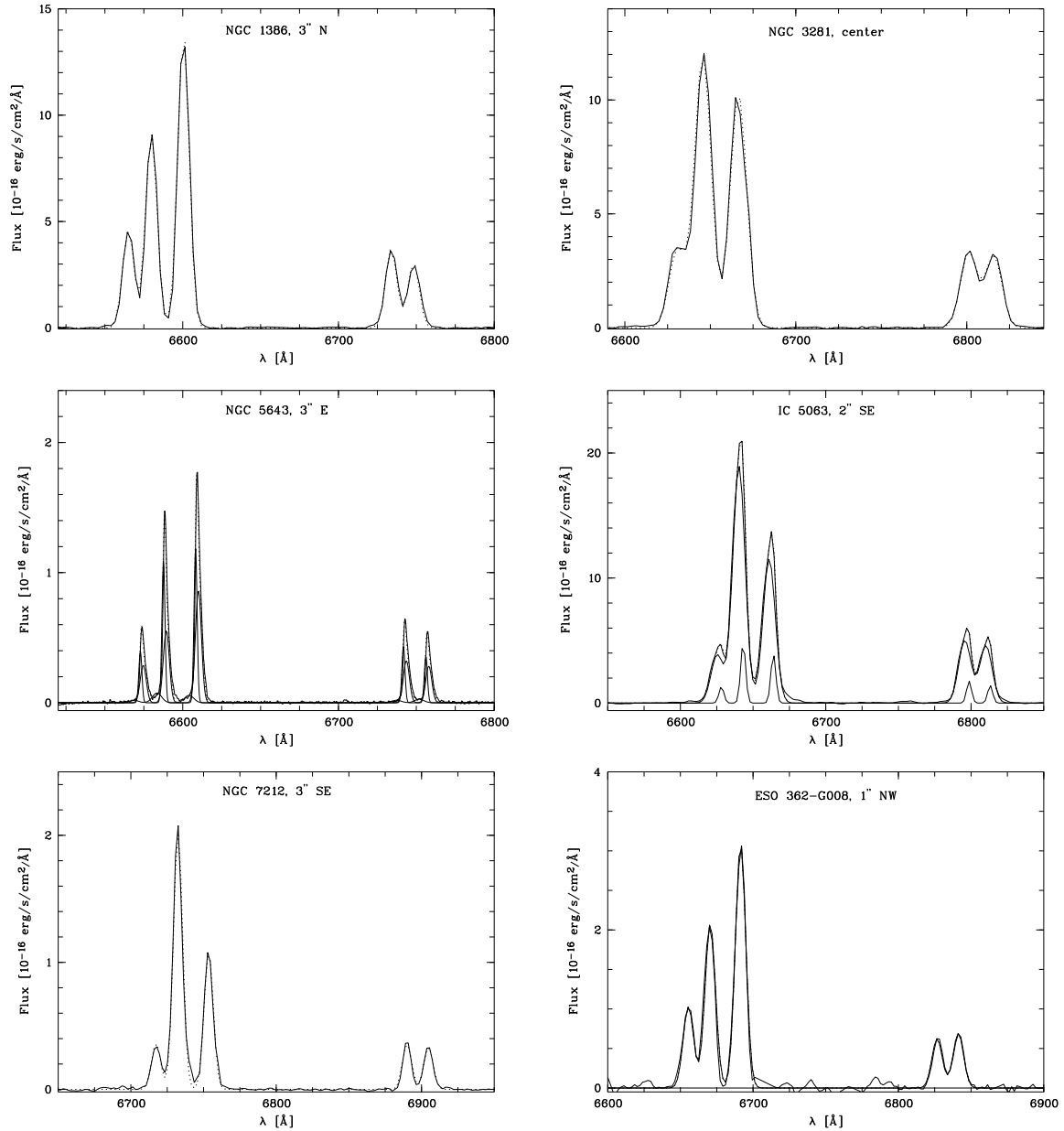


Figure 4.6: Single Gaussians fit to the $H\alpha$ + $[N\text{II}]$ as well as the $[S\text{II}]$ emission lines in representative NLR spectra of the Seyfert-2 galaxies NGC 1386, NGC 3281, NGC 5643, IC 5063, NGC 7212, and ESO 362-G008. The total fit is shown as dashed line and matches the observed emission lines very closely. Only for IC 5063 and NGC 5643, several components were fit and the individual components are shown as solid lines.

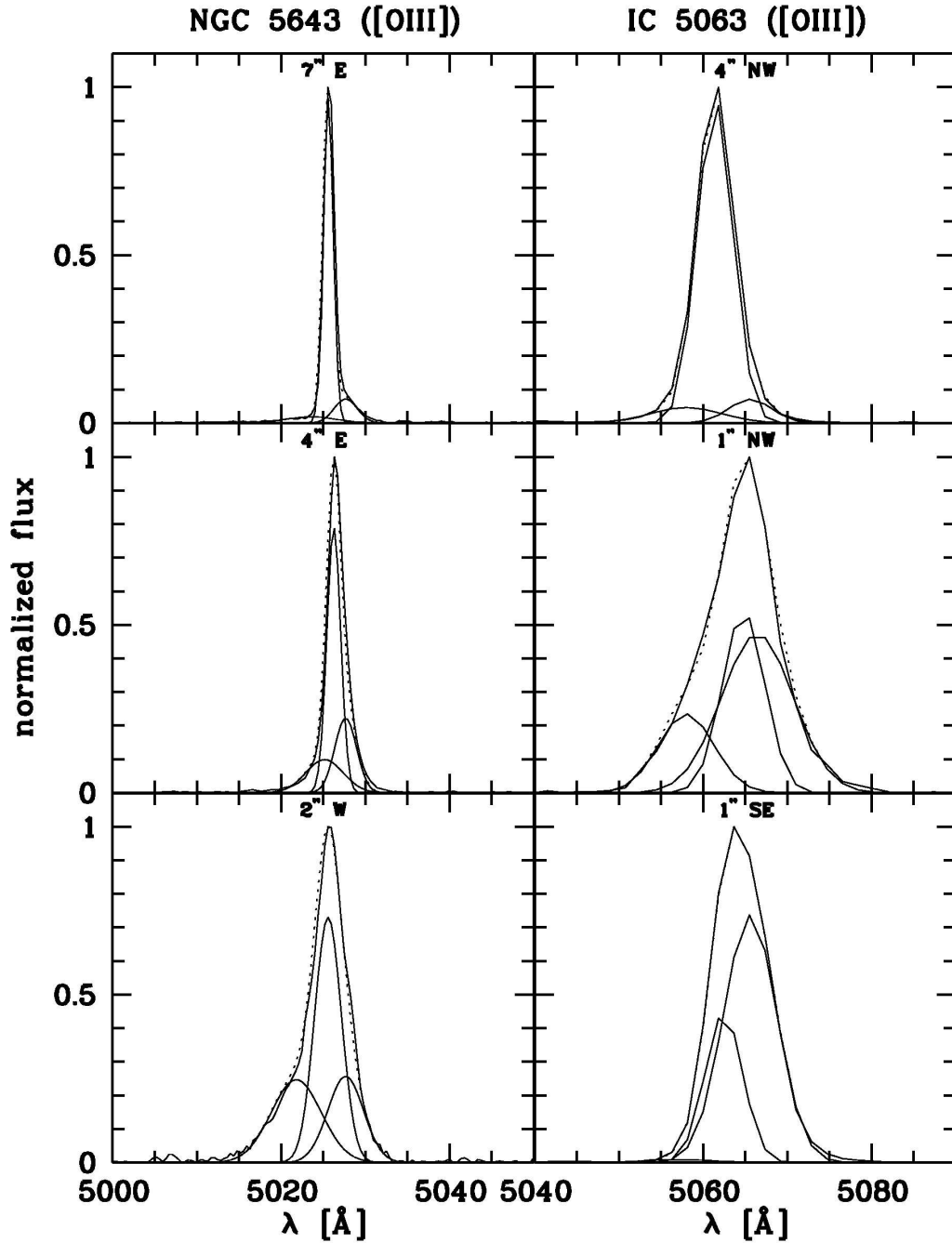


Figure 4.7: [O III] profile variation in the Seyfert-2 galaxies NGC 5643 (*left panel*) and IC 5063 (*right panel*). The peak fluxes were normalized to 1, for comparison. The individual components are shown as solid lines, the total resulting fit as dashed line.

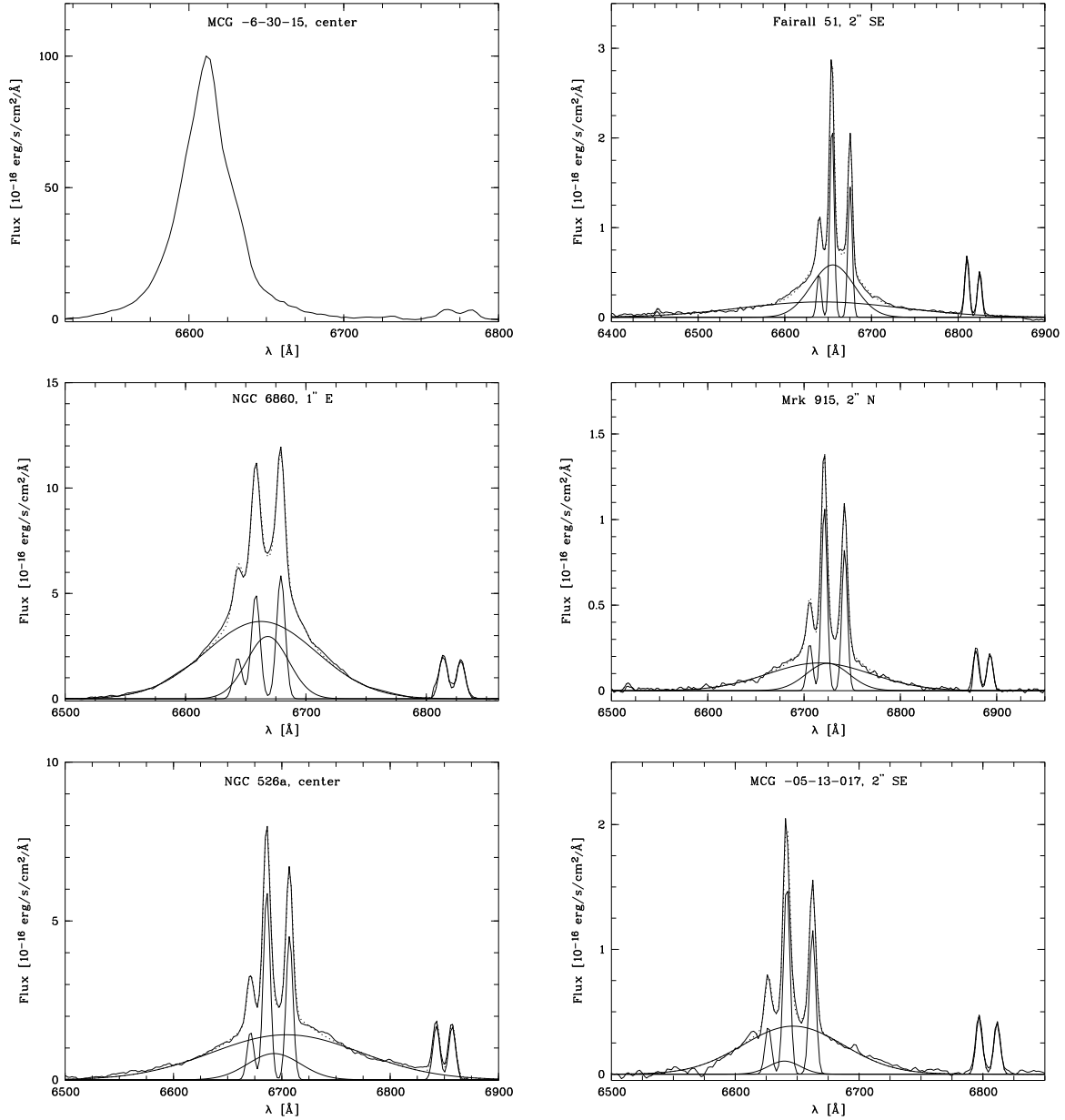


Figure 4.8: Single Gaussians fit to the $H\alpha$ + $[N\text{ II}]$ as well as the $[S\text{ II}]$ emission lines in representative NLR spectra of the Seyfert-1 galaxies MCG-6-30-15, Fairall 51, NGC 6860, Mrk 915, NGC 526a, and MCG-05-13-017. In addition to a narrow Gaussian comparable to the one fit to $[O\text{ III}]$, an intermediate and a broad Gaussian were fit to the $H\alpha$ emission line. The individual components are shown as solid lines. The total resulting fit is shown as dashed line and matches the observed emission lines very closely. The exception is MCG-6-30-15 (*upper left panel*), where we cannot separate the $H\alpha$ from the $[N\text{ II}]$ lines. Thus, no fit was applied.

Gaussian fits or Lorentz fits are commonly used when single component fits fail. Whittle (1985) already describe the non-Gaussian nature of observed [O III] line profiles “which revealed a stronger base relative to the core than Gaussians”. A Lorentz profile with has broader wings compared to a Gaussian seems to be better suited as has been shown by Véron-Cetty et al. (2001a) for the broad emission lines in narrow-line Seyfert-1 galaxies and by Schulz & Henkel (2003) for narrow emission lines in Seyfert-2 galaxies. Bennert et al. (2004a) suggest the use of d -Lorentzians which allow to fit both permitted and forbidden lines by adjusting an additional parameter d .

Unfortunately, the “fit/spec” routine does not include other functions than Gaussians to fit the profiles. However, using single Gaussians to fit the narrow lines and three Gaussians to fit narrow lines with underlying broad emission yields a very good result, taking into account the low resolution of our spectra.

The individual components as well as the resulting total fit to the blended emission lines $H\alpha + [N II]$ and $[S II]$ are shown in Figure 4.8. In all but one case (MCG-6-30-15), the permitted profiles show a clear separation between broad underlying emission and a narrow “peak”. Thus, for most Seyfert-1 galaxies, we were able to distinguish between the broad and narrow emission using three Gaussians with one resembling the shape of forbidden narrow lines.

For MCG-6-30-15 (Fig. 4.8, *upper left panel*), the only type-1 observed with the lower resolution of VLT/FORS1, the profile fitting to the permitted Balmer lines could not successfully disentangle the broad and narrow line. Thus, we applied a Gaussian fit to forbidden lines only (except for the $[N II]$ lines which are blended by $H\alpha$). In the central rows, the broad emission of $H\beta$ and $H\alpha$ even affect the adjacent $[O III]$ and $[S II]$ lines. In that cases, we subtracted the broad underlying wing by extrapolation. As a consequence, the only emission-line ratio we were able to derive directly is that of the two forbidden sulfur lines to measure the electron density. The narrow $H\alpha$ and $H\beta$ emission-line fluxes are needed to plot diagnostic line-ratio diagrams, thus we cannot present these results for MCG-6-30-15. Moreover, the ionization parameter strongly depends on the reddening value. As we cannot estimate it from the narrow $H\alpha/H\beta$ ratio, we used as first guess the reddening slope determined by matching the stellar template to the NLR spectra. The estimated ionization parameter and its spatial variation has to be taken with some caution.

4.4 Results and Discussion

We here present the nuclear spectra with emission-line fluxes and temperature (4.4.1), reddening distributions (4.4.2), diagnostic line-ratio diagrams (4.4.3), surface-brightness distributions (4.4.5), electron-density distributions (4.4.6), ionization-parameter distributions (4.4.7), and velocity fields (4.4.9) of the six Seyfert-2 and the six Seyfert-1 galaxies. We show results of CLOUDY photoionization modeling and compare them to the results of the spatially-resolved diagnostics (4.4.4). The consequences of our results for the NLR size-luminosity relation are discussed (4.4.8). We describe observations of extended broad Balmer emission lines in several Seyfert-1 galaxies (4.4.10). We compare the general trends for type-1 and type-2 AGNs (4.4.11) and discuss them on the basis of the unified scheme. The results of the nearby Seyfert-2 galaxy NGC 1386 are discussed in detail (4.4.12) before referring to the remaining 11 objects on an object-by-object basis (4.4.13).

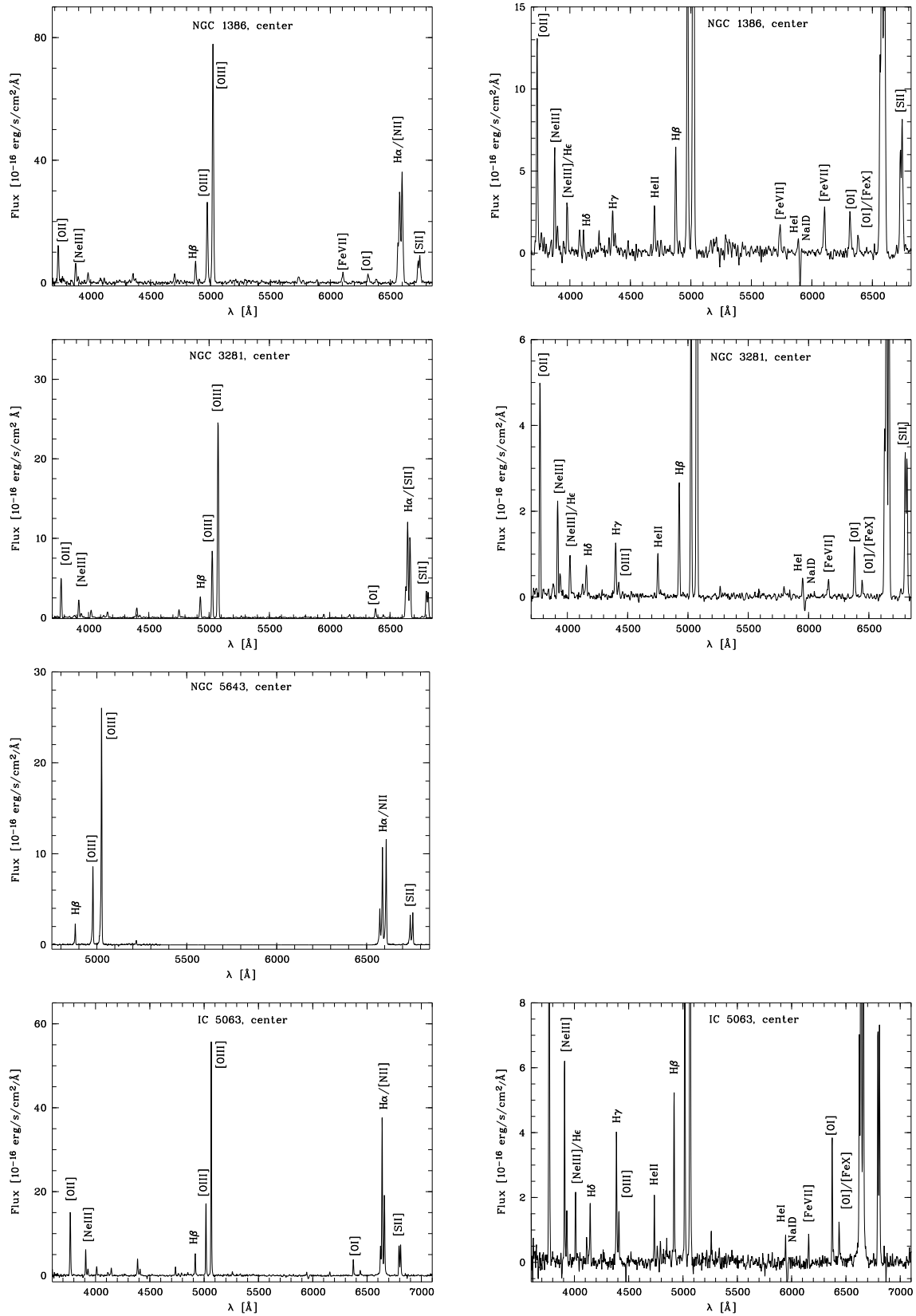


Figure 4.9: *Left panel:* Spectra of the type-2 nuclei of NGC 1386, NGC 3281, NGC 5643, and IC 5063 (from top to bottom) showing all the strong oxygen and Balmer emission lines. *Right panel:* Same spectra but with a different flux scale showing faint high-excitation lines.

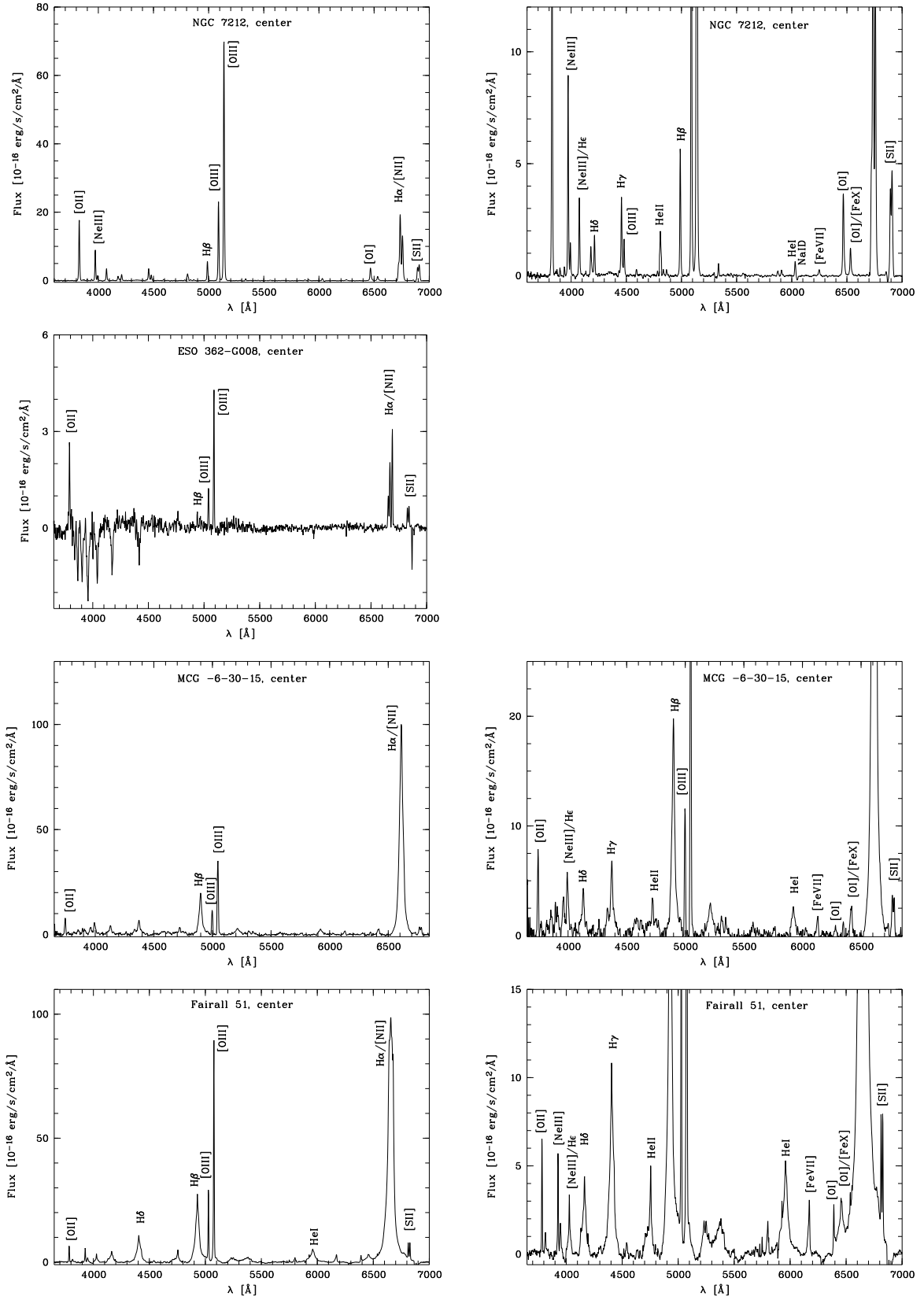


Figure 4.10: The same as in Figure 4.9 for the type-2 nuclei of NGC 7212, ESO 362-G008, as well as the type-1 nuclei of MCG -6-30-15 and Fairall 51.

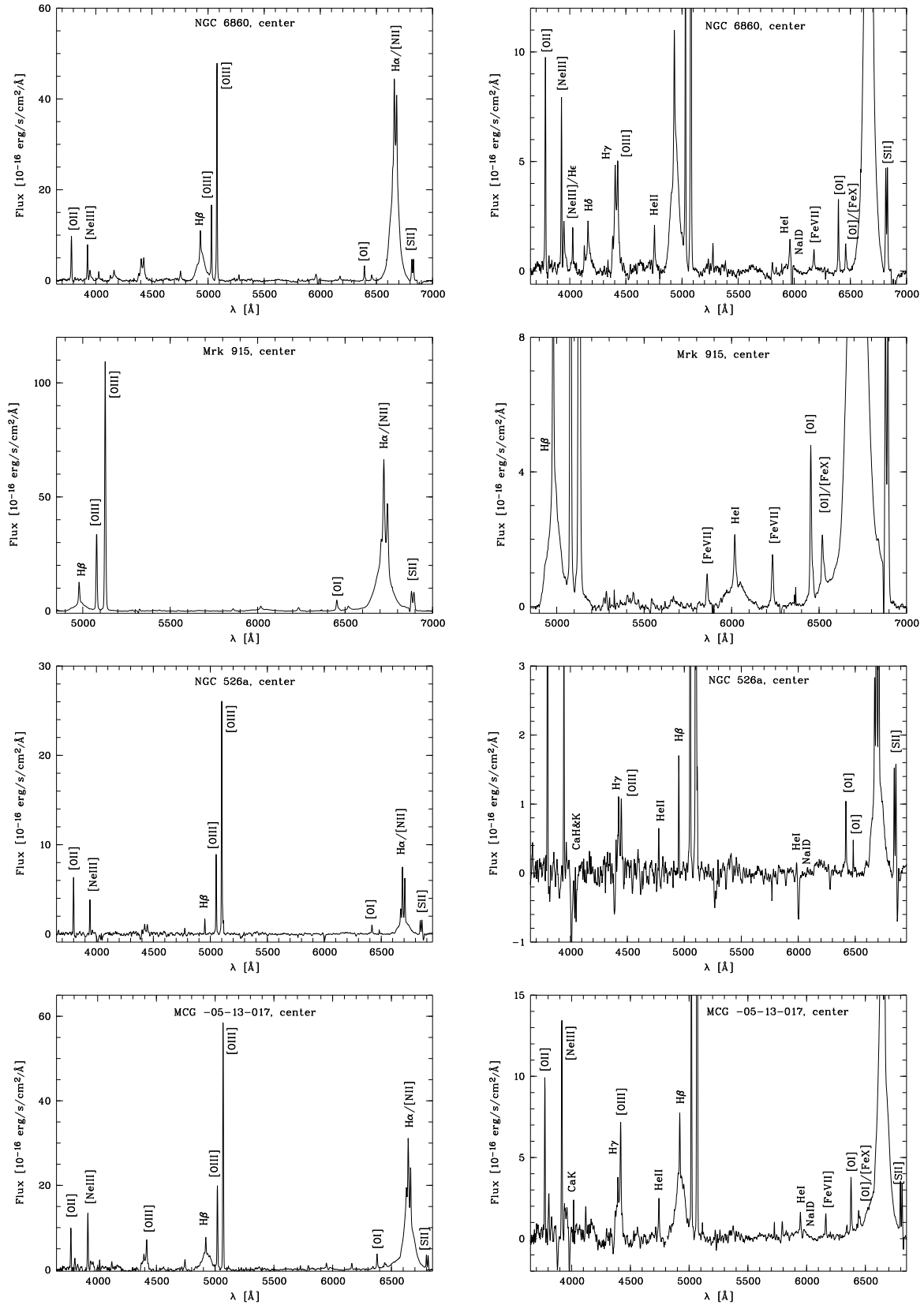


Figure 4.11: The same as in Figure 4.9 for the Seyfert-1 galaxies NGC 6860, Mrk 915, NGC 526a, and MCG -05-13-017.

4.4.1 Nuclear Spectra, Emission–Line Fluxes, and Temperature

In Figures 4.9–4.11, we present the central spectra of all objects with the most important emission lines indicated.

The strongest lines which can be traced throughout the NLR are [O II] $\lambda 3727 \text{ \AA}$, H β , [O III] $\lambda\lambda 4959, 5007 \text{ \AA}$, [O I] $\lambda 6300 \text{ \AA}$, H α , [N II] $\lambda\lambda 6548, 6583 \text{ \AA}$, and [S II] $\lambda\lambda 6716, 6731 \text{ \AA}$.

In addition, emission lines of Ne⁺⁺ ([Ne III] $\lambda\lambda 3869, 3967 \text{ \AA}$), higher order Balmer lines, the [O III] $\lambda 4363 \text{ \AA}$ line as well as emission lines of both ionized and neutral Helium can be seen (He II $\lambda 4686 \text{ \AA}$, He I $\lambda 5876 \text{ \AA}$).

In most objects, high–excitation iron lines ([Fe VII] $\lambda\lambda 5721, 6087 \text{ \AA}$ and [Fe X] $\lambda 6375 \text{ \AA}$) are clearly seen in the central NLR spectra ($\sim 1\text{--}2''$). These lines are characteristic of a subclass of Seyfert 2s called “high–excitation Seyfert–2 galaxies” (Ferland & Osterbrock, 1986). They indicate the existence of a powerful and hard ionization source in the center (the lower ionization potential of Fe⁶⁺ is 99.1 eV; Appendix C, Table C.2) and are also referred to as coronal lines.

In Tables 4.7 and 4.8, we give both the observed and reddening–corrected line–intensities relative to H β (uncorrected for slit losses) from the narrow emission lines in the nuclear spectra for all Seyfert–2 and Seyfert–1 galaxies in our sample. For pairs of lines ([O III], [O I], and [N II]) with a fixed line ratio ($\sim 1:3$), only the brighter line is listed. Estimated errors of line ratios lie in the range of $\sim 1\text{--}15\%$. (Note that we refer in the following only to the narrow emission lines if not stated otherwise.)

The line ratios are in general similar in all objects. There are no significant differences between type–1 and type–2 galaxies with the exception of the emission lines of oxygen and iron which are on average higher in the Seyfert–1 galaxies: [O III] $\lambda 4363 \text{ \AA}/\text{H}\beta \sim 0.82 \pm 0.3$ (4 Sy1s) versus 0.19 ± 0.02 (4 Sy2s); [O III] $\lambda 5007 \text{ \AA}/\text{H}\beta \sim 13.4 \pm 1.4$ (5 Sy1s) versus 10.3 ± 0.6 (6 Sy2s); [Fe VII] $\lambda 5721 \text{ \AA}/\text{H}\beta \sim 0.19 \pm 0.05$ (5 Sy1s) versus 0.14 ± 0.1 (2 Sy2s); [Fe VII] $\lambda 6087 \text{ \AA}/\text{H}\beta \sim 0.24 \pm 0.07$ (5 Sy1s) versus 0.14 ± 0.06 (4 Sy2s); [Fe X] $\lambda 6375 \text{ \AA}/\text{H}\beta \sim 0.17 \pm 0.07$ (5 Sy1s) versus 0.03 ± 0.01 (4 Sy2s).

In Table 4.9, we give the reddening–corrected H β luminosity and summarize the results from dereddened line ratios such as the electron temperature T_e , the reddening value E_{B-V} , the electron density n_e , and the ionization parameter U for the nuclear spectra of all objects (see Appendix C for details on the derivation of these parameters). Clearly, the parameters represent some average over the central several hundred parsecs.

The temperature was, in most objects, only determined for the nuclear spectrum due to the faintness of the involved [O III] $\lambda 4363 \text{ \AA}$ emission line in the outer rows in most cases. In some objects, we were able to derive the electron temperature in the inner few arcseconds (NGC 1386, NGC 3281, NGC 7212, IC 5063, NGC 526a, MCG –05–13–017) where it stays roughly constant within the errors or scatters without showing a clear dependency on radius. The central temperature was used to apply a correction to the electron density. In those cases in which no temperature was measured we used $T = 10000 \text{ K}$ or an average temperature derived from the other galaxies instead.

Comparing the results for the central spectra of type–1 and type–2 Seyferts shows that higher temperatures occur in type–1 objects ($T_{e,\text{ave},4\text{Sy}1\text{s}} \sim 33600 \pm 7100 \text{ K}$ versus $T_{e,\text{ave},4\text{Sy}2\text{s}} \sim 14465 \pm 445 \text{ K}$). The reddening is on average higher in the Seyfert 2s in our sample ($E_{B-V,\text{ave},6\text{Sy}2\text{s}} \sim 0.61 \pm 0.09 \text{ mag}$ versus $E_{B-V,\text{ave},6\text{Sy}1\text{s}} \sim 0.46 \pm 0.07 \text{ mag}$).

The electron densities are comparable in both objects within the errors ($n_{e,\text{ave},6\text{Sy}2\text{s}} \sim 1070 \pm 180 \text{ cm}^{-3}$ versus $n_{e,\text{ave},6\text{Sy}1\text{s}} \sim 1100 \pm 315 \text{ cm}^{-3}$).

Table 4.7: Observed and reddening-corrected line intensity ratios relative to H β for Seyfert-2 galaxies

Line	NGC 1386		NGC 3281		NGC 5643		IC 5063		NGC 7212		ESO 362-G008	
	F_{obs}	F_{dered}	F_{obs}	F_{dered}	F_{obs}	F_{dered}	F_{obs}	F_{dered}	F_{obs}	F_{dered}	F_{obs}	F_{dered}
[O II] $\lambda 3727 \text{ \AA}$	1.81	2.63	1.80	2.62	— ^a	— ^a	1.48	2.96	2.03	2.63	1.48	2.61
[Ne III] $\lambda 3869 \text{ \AA}$	0.77	1.07	0.73	1.01	— ^a	— ^a	0.47	0.86	0.98	1.22	— ^b	— ^b
[Ne III] $\lambda 3967 \text{ \AA}$	0.48	0.64	0.26	0.35	— ^a	— ^a	0.18	0.31	0.4	0.49	— ^b	— ^b
[O III] $\lambda 4363 \text{ \AA}$	0.19	0.23	0.12	0.14	— ^a	— ^a	0.11	0.15	0.20	0.23	— ^b	— ^b
He II $\lambda 4686 \text{ \AA}$	0.46	0.48	0.36	0.38	— ^a	— ^a	0.14	0.15	0.23	0.24	— ^b	— ^b
[O III] $\lambda 5007 \text{ \AA}$	11.34	10.73	9.21	8.72	12.38	11.40	8.88	8.03	12.52	12.06	11.57	10.65
[Fe VII] $\lambda 5721 \text{ \AA}$	0.29	0.22	0.08	0.06	— ^a	— ^a	—	—	—	—	—	—
[Fe VII] $\lambda 6087 \text{ \AA}$	0.44	0.31	0.17	0.12	— ^a	— ^a	0.14	0.07	0.06	0.04	—	—
[O I] $\lambda 6300 \text{ \AA}$	0.46	0.30	0.46	0.30	— ^a	— ^a	0.71	0.32	0.76	0.56	0.44	0.23
[Fe X] $\lambda 6375 \text{ \AA}$	0.07	0.05	0.02	0.01	— ^a	— ^a	0.04	0.02	0.04	0.03	—	—
H α	4.70	2.87	4.71	2.87	6.03	2.87	7.10	2.87	4.04	2.87	6.06	2.87
[N II] $\lambda 6583 \text{ \AA}$	5.60	3.41	4.02	2.44	6.30	2.98	4.27	1.71	2.82	1.99	6.78	3.18
[S II] $\lambda 6716 \text{ \AA}$	1.04	0.62	1.31	0.78	1.74	0.80	1.51	0.58	0.80	0.56	1.19	0.54
[S II] $\lambda 6731 \text{ \AA}$	1.29	0.77	1.24	0.74	1.94	0.89	1.49	0.57	0.98	0.63	1.53	0.70

Note. – All narrow emission line ratios were derived from the nuclear spectra. After reddening correction, other Balmer line-ratios such as H γ /H β and H δ /H β are consistent with the recombination values within the errors.

^a Not covered by wavelength range

^b Underlying absorption lines

Table 4.8: Observed and reddening-corrected line intensity ratios relative to $H\beta$ for Seyfert-1 galaxies

Line	Fairall 51		NGC 6860		Mrk 915		NGC 526a		MCG -05-13-017	
	F_{obs}	F_{dered}	F_{obs}	F_{dered}	F_{obs}	F_{dered}	F_{obs}	F_{dered}	F_{obs}	F_{dered}
[O II] $\lambda 3727 \text{ \AA}$	1.33	2.21	1.60	2.04	— ^a	— ^a	3.20	4.20	1.84	2.62
[Ne III] $\lambda 3869 \text{ \AA}$	0.86	1.32	1.18	1.45	— ^a	— ^a	1.80	2.27	2.54	3.43
[Ne III] $\lambda 3967 \text{ \AA}$	0.08	0.11	0.24	0.29	— ^a	— ^a	— ^b	— ^b	0.28	0.37
[O III] $\lambda 4363 \text{ \AA}$	0.40	0.49	0.53	0.59	— ^a	— ^a	0.65	0.73	1.26	1.46
He II $\lambda 4686 \text{ \AA}$	0.41	0.44	0.29	0.30	— ^a	— ^a	0.33	0.34	0.48	0.50
[O III] $\lambda 5007 \text{ \AA}$	15.58	14.47	8.84	8.53	12.72	11.82	16.35	15.71	17.15	16.29
[Fe VII] $\lambda 5721 \text{ \AA}$	0.49	0.34	0.14	0.12	0.15	0.11	0.11	0.09	0.37	0.29
[Fe VII] $\lambda 6087 \text{ \AA}$	0.83	0.49	0.20	0.16	0.27	0.16	0.09	0.07	0.47	0.33
[O I] $\lambda 6300 \text{ \AA}$	0.92	0.51	0.71	0.53	0.81	0.45	0.74	0.54	1.19	0.79
[Fe X] $\lambda 6375 \text{ \AA}$	0.81	0.43	0.08	0.06	0.17	0.09	0.06	0.04	0.38	0.25
H α	5.60	2.87	3.95	2.87	5.60	2.87	4.11	2.87	4.57	2.87
[N II] $\lambda 6583 \text{ \AA}$	5.57	2.84	3.38	2.44	3.70	1.88	3.14	2.18	3.02	1.89
[S II] $\lambda 6716 \text{ \AA}$	1.47	0.73	1.28	0.92	1.29	0.64	1.18	0.81	1.01	0.62
[S II] $\lambda 6731 \text{ \AA}$	1.68	0.84	1.15	0.82	1.31	0.65	1.16	0.80	1.19	0.73

Note. – All narrow emission line ratios were derived from the nuclear spectra. After reddening correction, other Balmer line-ratios such as $H\gamma/H\beta$ and $H\delta/H\beta$ are consistent with the recombination values within the errors. No ratios are given for the Seyfert-1 galaxy MCG -6-30-15 as we were not able to disentangle the broad and narrow Balmer lines in the central spectra.

^a Not covered by wavelength range

^b Underlying absorption lines

Table 4.9: Reddening-corrected $H\beta$ luminosity and results from dereddened line ratios

Seyfert-2 galaxies						
	NGC 1386	NGC 3281	NGC 5643	IC 5063	NGC 7212	ESO 362-G008
$L_{H\beta}$ (10^{39} erg s $^{-1}$)	14.2 \pm 1	107 \pm 4	4.8 \pm 0.3	140 \pm 3	169 \pm 5	65 \pm 9
T (K)	15650 \pm 1500	13715 \pm 440	— ^a	13865 \pm 1800	14635 \pm 1500	— ^b
E_{B-V} (mag)	0.48 \pm 0.02	0.49 \pm 0.01	0.73 \pm 0.02	0.89 \pm 0.01	0.33 \pm 0.01	0.73 \pm 0.05
n_e (cm $^{-3}$)	1545 \pm 50	540 \pm 40	860 (1035) \pm 30 ^c	635 \pm 30	1420 \pm 50 ^d	1420 (1710) \pm 70 ^c
$U_{\log(n_e)=3}$ (10^{-3})	2.83 \pm 0.01	2.3 \pm 0.02	— ^a	2.15 \pm 0.01	3.27 \pm 0.02	2.76 \pm 0.1

Seyfert-1 galaxies						
	MCG -6-30-15	Fairall 51	NGC 6860	Mrk 915	NGC 526a	MCG -05-13-017
$L_{H\beta}$ (10^{39} erg s $^{-1}$)	— ^e	93 \pm 9	37 \pm 2	416 \pm 30	18 \pm 1	25 \pm 2
T (K)	— ^e	22200 \pm 400	36325 \pm 250	— ^a	23330 \pm 1700	52500 \pm 3000
E_{B-V} (mag)	0.3 \pm 0.02 ^f	0.65 \pm 0.03	0.31 \pm 0.02	0.66 \pm 0.02	0.35 \pm 0.03	0.46 \pm 0.03
n_e (cm $^{-3}$)	300 (550) \pm 40 ^g	1430 \pm 40	1015 \pm 50	570 (1045) \pm 35 ^{d,g}	835 \pm 70 ^h	2460 \pm 55
$U_{\log(n_e)=3}$ (10^{-3})	2.95 \pm 0.04	9.25 \pm 0.9	2.73 \pm 0.04	— ^a	2.89 \pm 0.05	4.28 \pm 0.1

Note. – All values refer to the nuclear spectra.

^a Not covered by wavelength range

^b Underlying absorption lines

^c Using $T_e = 10000$ K and, in brackets, $T_{e,ave,4Sy2s} \sim 14465$, respectively

^d [S II] $\lambda 6716$ Å is slightly truncated by telluric absorption bands.

^e No deconvolution of underlying broad Balmer lines possible

^f Determined from reddening of continuum slope relative to template

^g Using $T_e = 10000$ K and, in brackets, $T_{e,ave,4Sy1s} \sim 33600$, respectively

^h [S II] $\lambda 6731$ Å is slightly truncated by telluric absorption bands.

This does not change when using the average electron temperature determined for Seyfert–1 galaxies and Seyfert–2 galaxies as correction for those objects for which we could not measure the central temperature directly ($n_{e,\text{ave},6\text{Sy}2\text{s}} \sim 1150 \pm 200 \text{ cm}^{-3}$ versus $n_{e,\text{ave},6\text{Sy}1\text{s}} \sim 1220 \pm 270 \text{ cm}^{-3}$).

The ionization parameter is higher in Seyfert–1 galaxies [$U_{\log(n_e)=3\text{ave},5\text{Sy}1\text{s}} \sim (4.42 \pm 1.2) \cdot 10^{-3}$ versus $U_{\log(n_e)=3\text{ave},5\text{Sy}2\text{s}} \sim (2.66 \pm 0.2) \cdot 10^{-3}$], also when excluding the exceptional high value of U seen in Fairall 51 [$U_{\log(n_e)=3\text{ave},4\text{Sy}1\text{s}} \sim (3.21 \pm 0.4) \cdot 10^{-3}$].

4.4.2 Reddening Distributions

Two different measures of the reddening distribution were derived: (i) the reddening of the continuum slope in the central parts with respect to the template derived in the outer parts of the galaxy; (ii) the reddening distribution obtained from the recombination value for the (narrow–line) intensity ratio $\text{H}\alpha/\text{H}\beta$ (Appendix C). (Note that the reddening of the BLR derived from the broad Balmer decrement for type–1 objects is given when discussing the objects individually.) The first reddening value was only derived for those objects for which a stellar template correction was applied (Section 4.3.3). The reddening distributions are shown in Figures 4.12, 4.13, and 4.14.

As the match between the absorption lines of the stellar template and those seen in the spectra is quite close for all rows, we believe that reddening by dust is the cause of the spatially varying continuum slope and not an intrinsically redder stellar population in the central part.

We cannot compare the absolute values of $E_{(B-V)}$ directly as the reddening determined from the continuum slope is a value relative to the reddening of the outer regions in the galaxy, i.e. the template (that is why “negative” $E_{(B-V)}$ values can occur). The dispersion $\Delta E_{(B-V)}$ is significantly smaller than that obtained from the Balmer decrement. This can be due to extinction by foreground dust in e.g. the host galaxy which affects both the template and the central spectra and thus do not reflect in the relative reddening value. However, often both reddening values are distributed differently indicating that the stellar population and the NLR are suffering different dust extinctions. The most probable explanation is dust intrinsic to the NLR clouds which varies locally. The two alternatives are (i) high density leading to an additional collisional contribution to the observed $\text{H}\alpha/\text{H}\beta$ ratio independent of dust. However, extremely high densities are needed to explain the large ratios and there is no observational evidence for such high densities. (ii) Patchy dust clouds beyond the NLR may absorb the emission lines along the line–of–sight of the NLR clouds. As both alternatives are rather unlikely, we favor the scenario of locally varying dust within the NLR clouds.

We decided to use the reddening distribution determined from the narrow $\text{H}\alpha/\text{H}\beta$ emission–line ratio to correct for the intrinsic reddening of the NLR itself as these lines originate in the NLR and thus give a better estimate for the reddening within the NLR than the one determined from the continuum slope.

In some cases (e.g. NGC 5643, IC 5063), the reddening is highest in the center and decreases with distance from the nucleus. But more often, the distributions show deviations from such a general trend. There are no clear differences between the two Seyfert types.

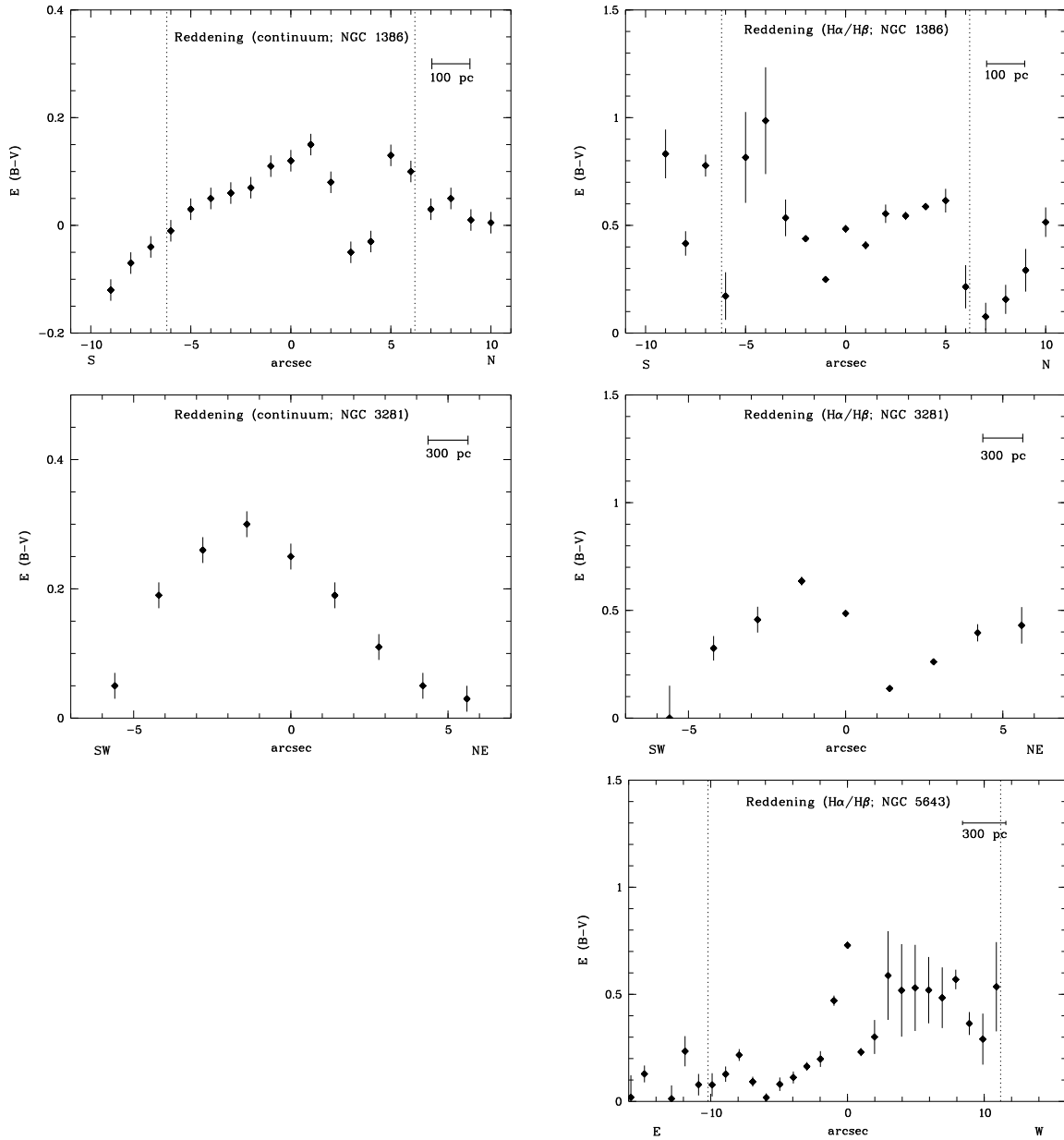


Figure 4.12: Reddening distributions of the Seyfert-2 galaxies NGC 1386, NGC 3281, and NGC 5643. *Left panel:* Reddening distribution of the continuum slope with respect to the stellar template. *Right panel:* Reddening distribution derived from the recombination value of the narrow $H\alpha/H\beta$ emission-line ratio. The edge of the NLR as determined from the diagnostic diagrams is indicated by dotted lines (NGC 1386 and NGC 5643). For NGC 5643, no reddening correction was applied during stellar template fitting due to the low S/N. Thus, no reddening distribution of the continuum slope is determined.

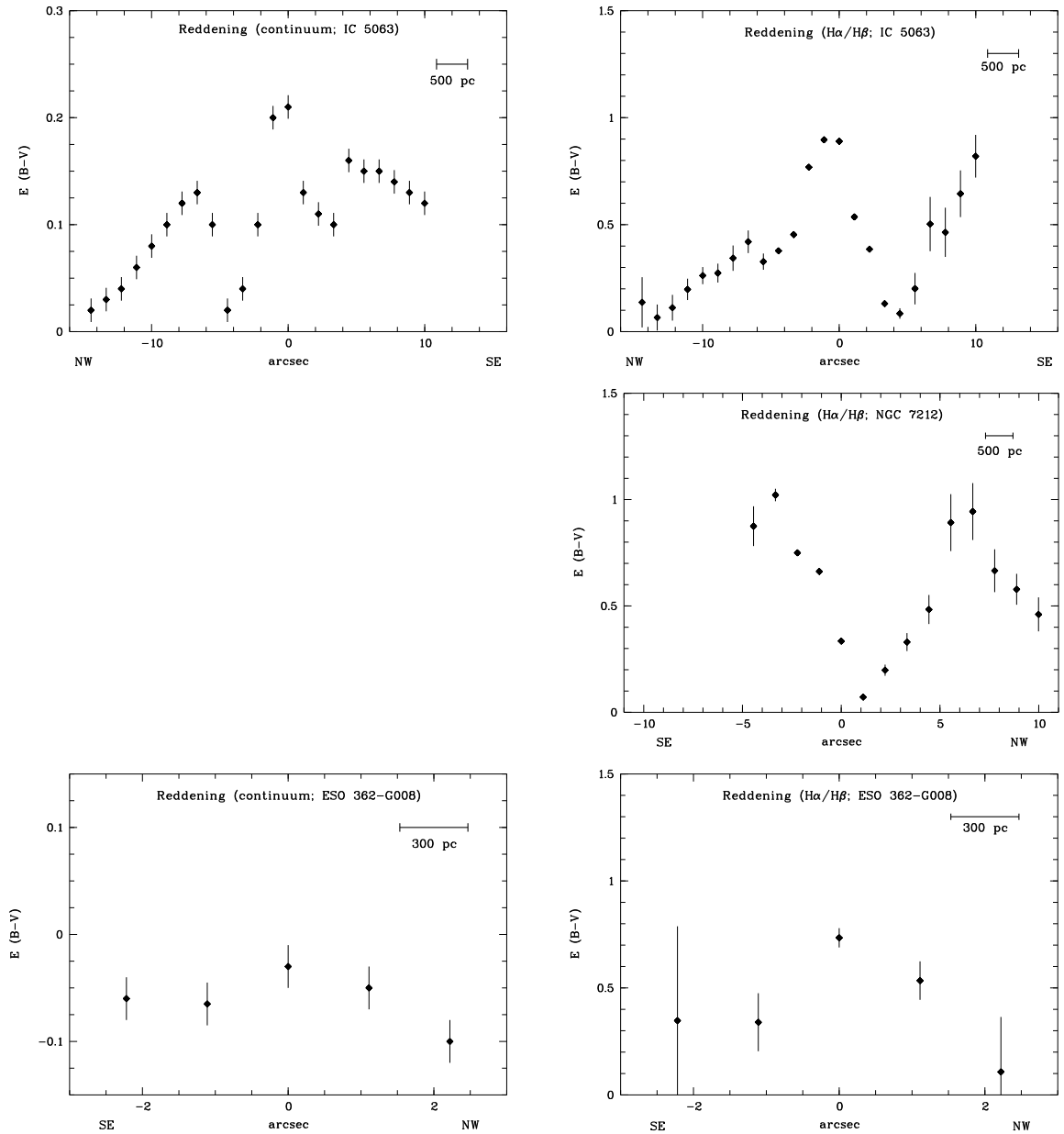


Figure 4.13: The same as in Figure 4.12 for the Seyfert-2 galaxies IC 5063, NGC 7212, and ESO 362-G008. No stellar template was fit to NGC 7212 and thus no continuum slope reddening was determined.

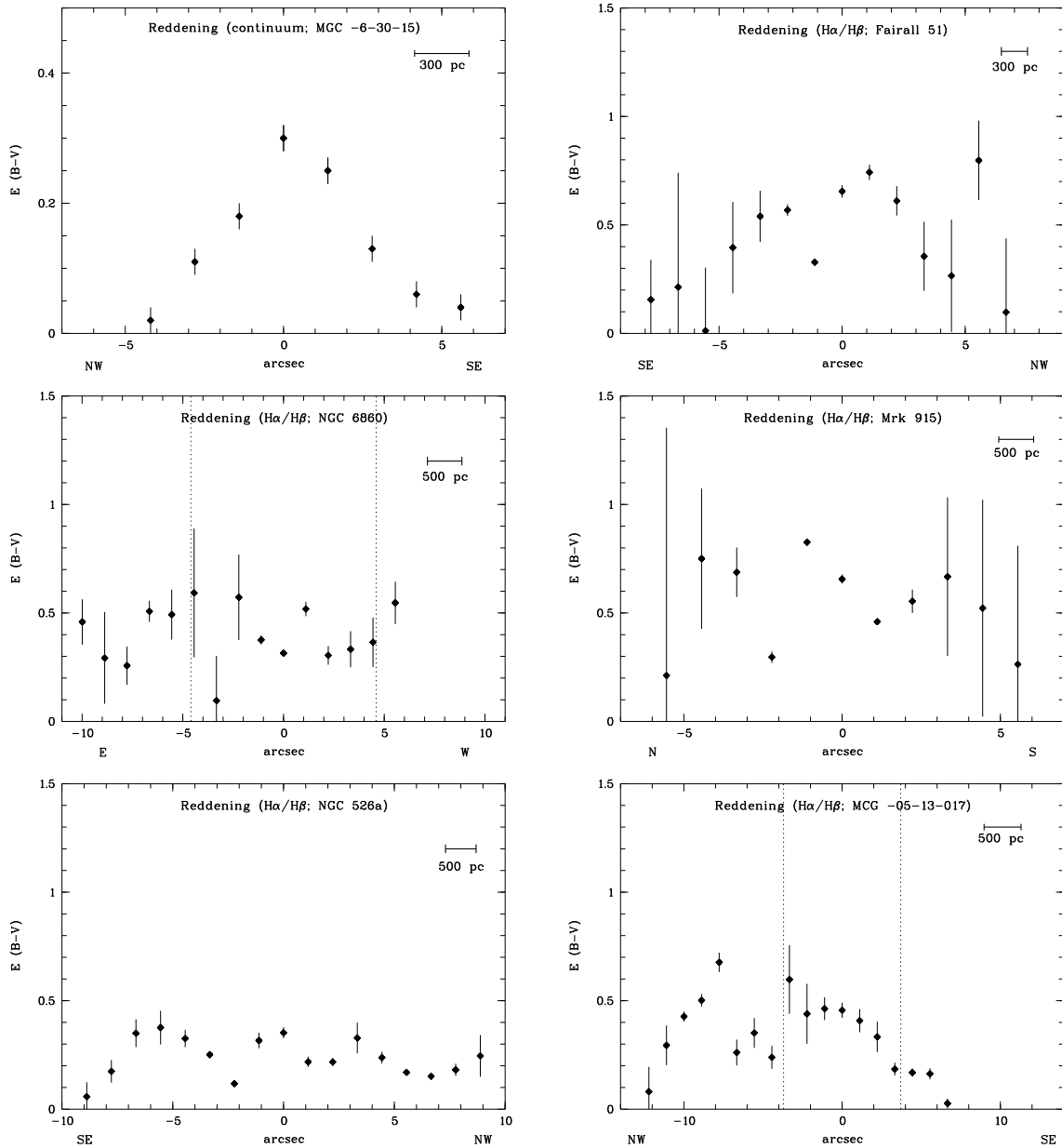


Figure 4.14: Reddening distributions of the Seyfert-1 galaxies MCG -6-30-15, Fairall 51, NGC 6860, Mrk 915, NGC 526a, and MCG -05-13-017. The reddening was derived from the recombination value of the narrow $H\alpha/H\beta$ emission-line ratio except for MCG -6-30-15 where we could not disentangle the broad and narrow Balmer lines (in the central $\sim 3''$). Instead, we show for this object the reddening distribution of the continuum with respect to the stellar template. On the contrary, the continuum slope reddening is not available for the other type 1s as no stellar template was fit. The edge of the NLR as determined from the diagnostic diagrams is indicated by dotted lines (NGC 6860 and MCG -05-13-017).

4.4.3 Diagnostic Diagrams

Diagnostic line–ratio diagrams of the type pioneered by Baldwin et al. (1981) are commonly used to distinguish between emission–line object classes (e.g. Seyfert galaxies, LINERs, Starbursts, transition objects), referring to a “total” spectrum or the central spectrum of *one* object. Here, we make use of the spatially–resolved spectra to discriminate between different regions in the *same* object, for example the NLR and circumnuclear or extended H II regions. We developed this method independently from literature and, moreover, use it to probe the “real” NLR size, i.e. the central region which is photoionized by the AGN, discriminating the contribution from circumnuclear starbursts.

The high S/N ratio of our spectra enables us to measure line ratios for all three diagrams out to several arcseconds from the nucleus.

In four Seyfert galaxies of our sample (the two Sy2s NGC 1386 and NGC 5643 as well as the two Sy1s NGC 6860 and MCG –05–13–017), we see a clear transition between line ratios falling in the AGN regime and those typical for H II regions. We therefore present all three diagnostic diagrams of these four objects in Figures 4.15 and 4.16.

The symbols are chosen such that “O” refers to the central row, the small letters mark regions corresponding to “–” arcseconds from the nucleus, the capital ones mark regions corresponding to “+” arcseconds from the nucleus (see Table 4.10 for orientation and distance from the nucleus). In the second diagnostic diagram, the data points of the outer regions are upper limits, due to the faintness of the [O I] $\lambda 6300$ Å line involved.

For NGC 1386, NGC 6860, and MCG –05–13–017, the transition is rather sharp, while for NGC 5643, the line ratios are gradually changing from AGN–type to H II–like ratios with line ratios of two outer spectral rows falling in the corner between LINER, AGN and H II regions.

We present representative spectra of the AGN region and that of circumnuclear [H II] regions in Figure 4.17.

For the remaining eight galaxies, no such transition is observed but all emission–line ratios are typical for gas ionized by an AGN power–law continuum. As the distributions in the three diagnostic diagrams are comparable, we present only the third diagnostic diagram for these objects in Figure 4.18. (We do not show the diagnostic diagram for MCG –6–30–15 as we could not disentangle the broad and narrow Balmer emission lines in the central $\sim 3''$.)

For some objects, the line ratios show very little scatter (e.g. IC 5063, NGC 7212) within the AGN region while others show a large range of ratios, especially those objects which show a transition towards H II regions.

We use the diagnostic diagrams to determine the NLR size. The results are summarized in Table 4.10. For those objects which show a transition of emission–line ratios from the central AGN region to H II regions, this method gives a measure of the NLR size without [O III] contamination from circumnuclear starbursts. For the other objects, the estimated NLR size is a lower limit.

In Figures 4.19, 4.20, 4.21, and 4.22, we show the strongest reddening–corrected line ratios as a function of radius. (Note that these line ratios were used as values on the x– and y–axis of the diagnostic diagrams.)

The [N II]/H α and [S II]/H α line ratios show a comparable distribution, running roughly parallel to each other (Figs. 4.19 and 4.20).

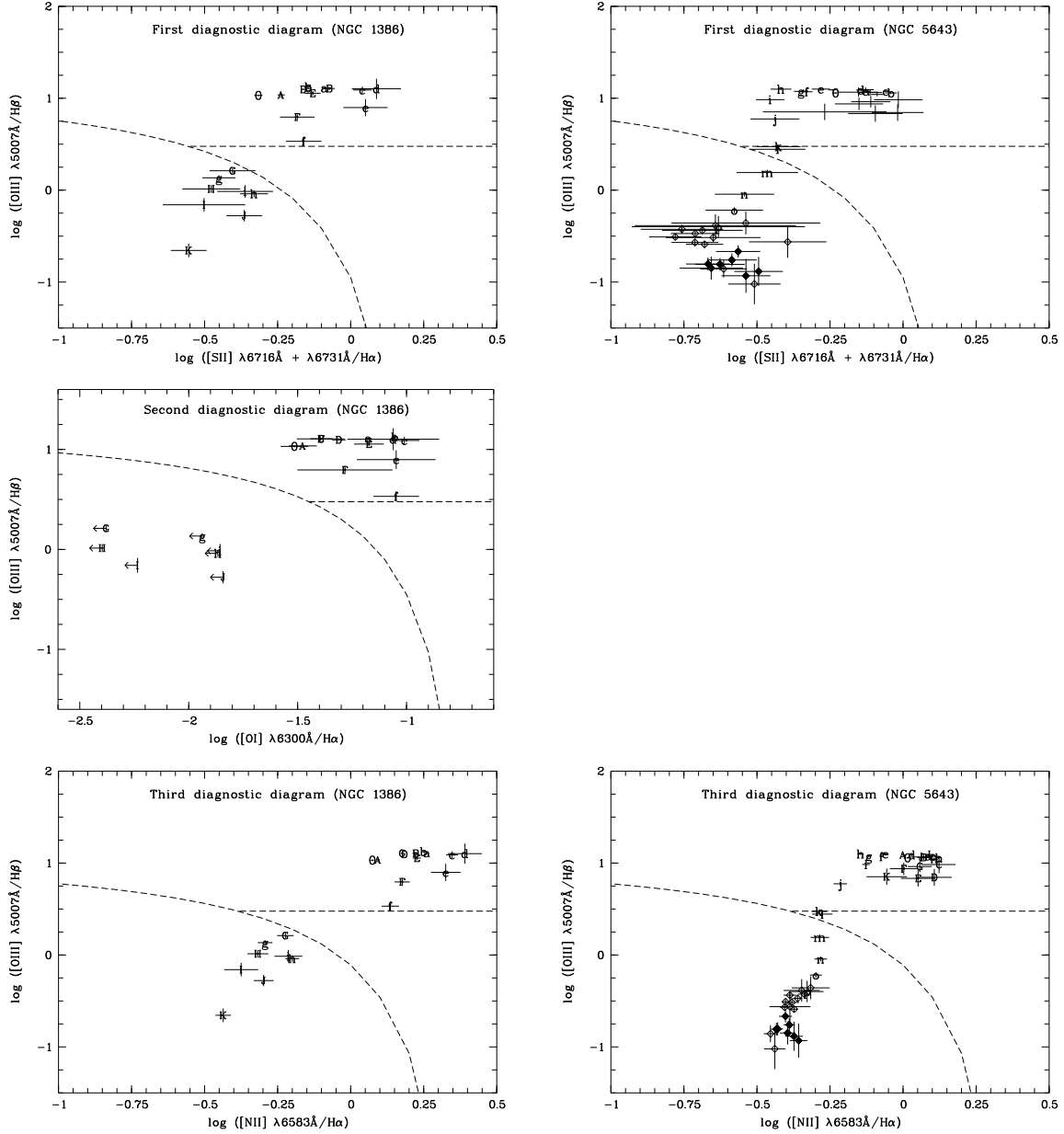


Figure 4.15: Diagnostic diagrams for spatially-resolved emission-line ratios in the Seyfert-2 galaxies NGC 1386 and NGC 5643. The dividing lines were taken from the analytic AGN diagnostics of Kewley et al. (2001). Both objects show a transition between line ratios falling in the AGN regime and those typical for H II regions in all three diagnostic diagrams. Note that in the second diagnostic diagrams, due to the faintness of the [O I] emission line, the [O I]/H α ratios of the outer part of the spectra are only upper limits. For NGC 5643, the spectral range does not cover the [O I] emission line and we therefore cannot show the second diagnostic diagram. The open and filled diamonds in the diagnostic diagrams of NGC 5643 show line ratios of H II regions further out in the galaxy.

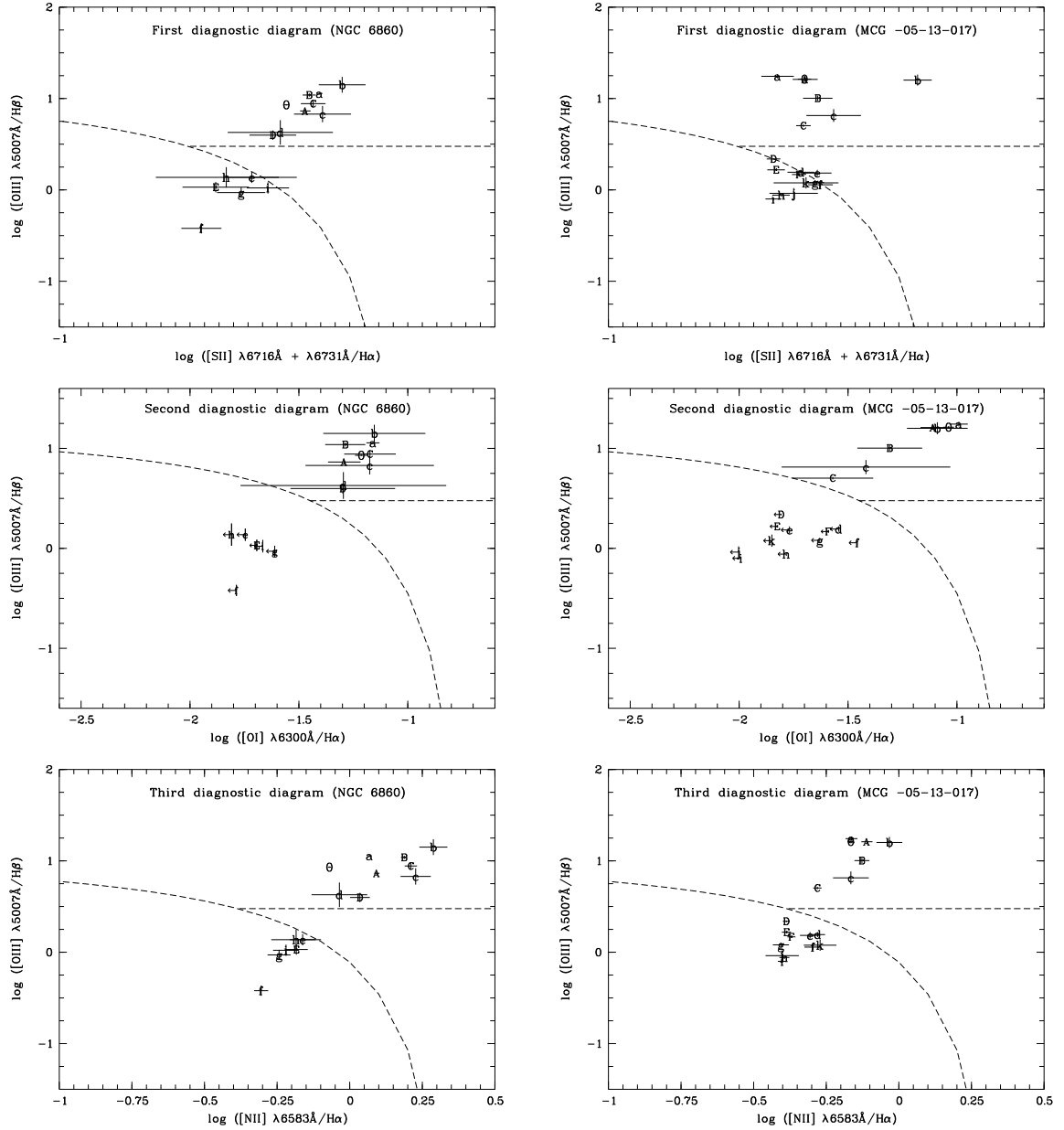


Figure 4.16: The same as in Figure 4.15 for the Seyfert-1 galaxies NGC 6860 and MCG -05-13-017. Both objects show a transition between line ratios falling in the AGN regime and those typical for H II regions in all three diagnostic diagrams.

This trend is expected as the [N II] and [S II] lines have comparable ionization potentials [lower ionization potential 14.5 eV versus 10.4 eV; Appendix C, Table C.2] and critical densities [$8.7 \cdot 10^4 \text{ cm}^{-3}$ versus $3.9 \cdot 10^3 \text{ cm}^{-3}$; Appendix C, Table C.2].

Thus, they are expected to arise in the same regions. In most objects, both line ratios do not show a clear trend in variation with radius. However, in the four objects for which we observe a transition between AGN-like line ratios and that typical for H II regions, the line ratios are in general higher in the NLR due to the increase of H α in the surrounding H II regions. For ESO 362-G008, we consider the increase of both [N II] and [S II] relative to H α with distance from the center as artificially induced from the mismatch of the stellar template in the inner part where we have underestimated the H α emission due to underlying absorption lines.

In Figures 4.21 and 4.22, we compare the oxygen line-ratios relative to the Balmer emission lines. The [O III]/H β ratio was divided by a factor of 30, for comparison. [O I] and [O III] are in general expected to show the opposite behavior: if one value is high, the other is low, as both lines come from the same atom. In regions with high ionization, oxygen is expected to be in the form O⁺⁺ [upper ionization potential 54.9 eV versus upper ionization potential of O of 13.6 eV; Appendix C, Table C.2]. In principle, our results show this trend. Within the NLR, [O III]/(30 · H β) is very high and it drops to a value comparable to [O I]/H α in the H II regions.

4.4.4 Photoionization Modeling and NLR size

The determination of the NLR size depends on the definition of the NLR itself. We here assume that the NLR consists of gas photoionized by the central AGN. Thus, we are able to determine the NLR size from the observed transition of line ratios in the diagnostic diagrams from the AGN regime to that typical for H II regions.

We have checked if any mechanism exists which drives line ratios in the diagnostic diagrams from the AGN regime towards and into the regime usually covered by H II regions, despite photoionization by an intrinsic AGN continuum source. This question is of interest not only for the determination of the NLR radius, but also for galaxy classifications based on diagnostic diagrams in general.

Under the assumption of a single continuum source (the central AGN) being responsible for the ionization, the following parameters could potentially shift line ratios from AGN- towards H II-like ones in individual diagnostic diagrams: (i) extinction; (ii) ionization parameter in combination with (iii) metallicity gradients; or (iv) electron density. We discuss each of them in turn.

(i) Extinction can be excluded to have a large effect on the observed line ratios in the diagnostic diagrams. The line ratios in all three diagnostic diagrams were chosen to minimize reddening effects by using neighbouring lines. In addition, we measured the reddening distribution directly and use these results to correct for the reddening. Using the different reddening distribution determined by the continuum slope does not change the results within the errors.

Models (ii)–(iv) presented below are based on the photoionization code CLOUDY [e.g. Ferland et al. (1998)] and were carried out in close cooperation with Dr. Stefanie Komossa. They assume a pointlike AGN continuum source which illuminates clouds of constant density. The spectral energy distribution is a typical mean Seyfert continuum composed of piecewise power laws (Komossa & Schulz, 1997).

Table 4.10: Results from diagnostic diagrams

Galaxy	“a/A” Distance (″)	“a/A” Orientation	$R_{[\text{O III}]}$ Literature (″)	$R_{[\text{O III}]}$ Our Data (″)	R_{NLR} Our Data (″, pc)
NGC 1386	1	S/N	3 ^a	12	6 of 10 (310 of 520)
NGC 3281	1.4	SW/NE	3 ^a	9	>5 (1180)
NGC 5643	1	E/W	6 ^b	16	11 of 16 (1045 of 1520)
IC 5063	1	NW/SE	3 ^a	20	>13 (2860)
NGC 7212	1	SE/NW	3 ^a	12	>10 (5040)
ESO 362–G008	1	SE/NW	10 ^c	4	>3 (960)
MCG –6–30–15	1.4	NW/SE	2 ^a	12	4? (700) ^d
Fairall 51	1	SE/NW	2 ^a	9	>8 (2260)
NGC 6860	1	E/W	3 ^a	10	5 of 10 (1465 of 2930)
Mrk 915	1	N/S	2 ^a	12	>6 (2720)
NGC 526a	1	SE/NW	11 ^b	20	>9 (3260)
MCG –05–13–017	1	NW/SE	1 ^a	17	3 of 11 (730 of 2670)

Note. – The second column gives the distance from the center of the first row (marked with the letters “a” and “A” in the diagnostic diagrams) in ″. In the third column, the orientation of the small and capital letters is listed. The maximum [O III] radius (S/N > 3) at the same p.a. taken from literature is given in the fourth column (in ″). We also give the [O III] radius (S/N > 3) in ″ observed from our spectra (column 5). In the last column, the extension of line ratios used in diagnostic diagrams and the radius of NLR in given in ″ and, in brackets, pc, respectively. The four objects with a clear transition between NLR and H II region are marked in bold.

^a Taken from HST image of Schmitt et al. (2003a)

^b Taken from HST image of Simpson et al. (1997)

^c Taken from groundbased image of Mulchaey et al. (1996a)

^d In the central 3″ of MCG –6–30–15, we cannot disentangle the broad and narrow Balmer components and therefore do not determine the line ratios. In the outer region to a distance of ± 4 ″, they fall in the AGN regime.

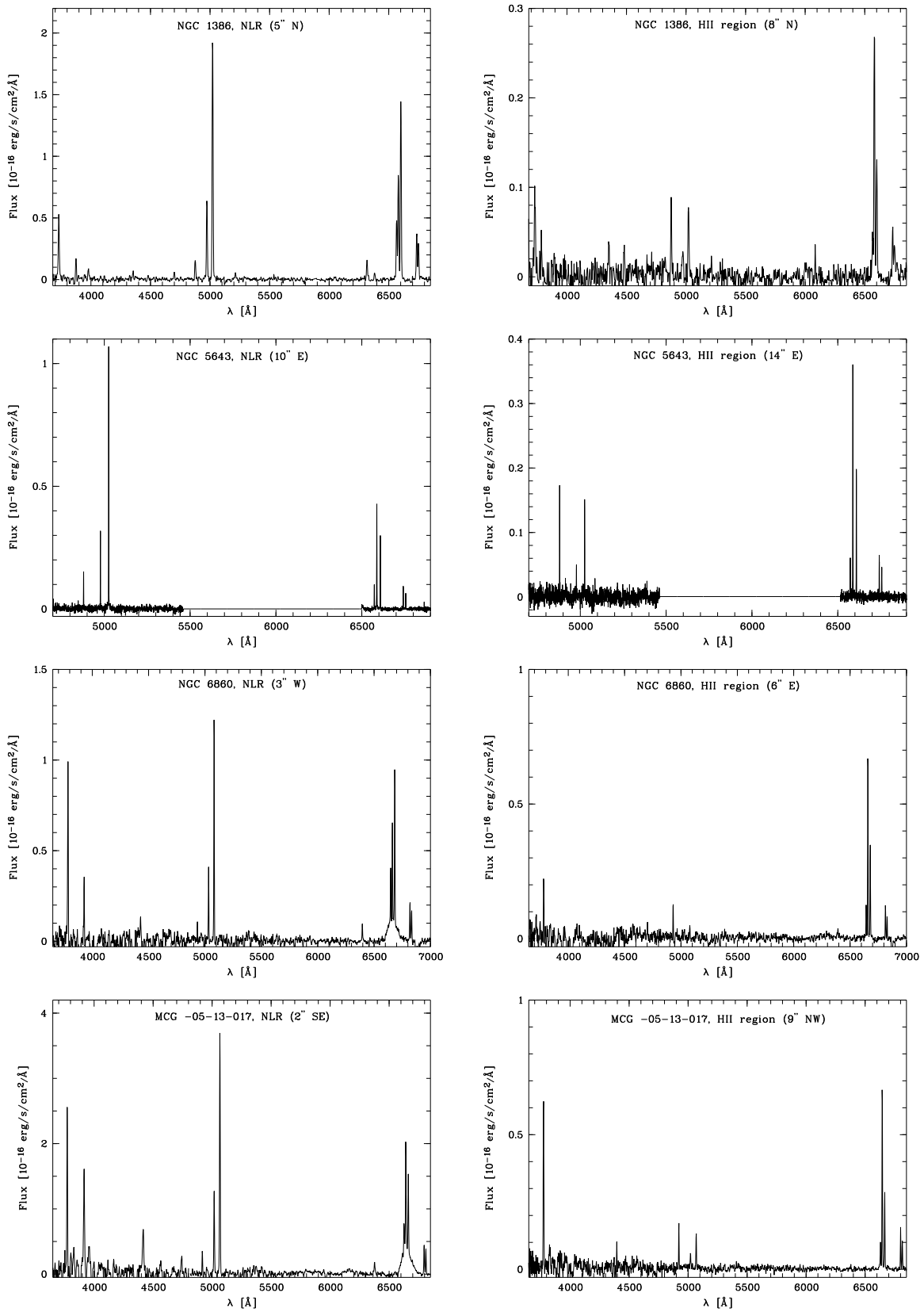


Figure 4.17: Comparison of representative spectra with emission–line ratios falling in the AGN regime (i.e. $[\text{O III}]/\text{H}\beta > 3$, $[\text{N II}]/\text{H}\alpha > 1$) in the diagnostic diagrams (*left panels*) and those typical for H II regions (i.e. $[\text{O III}]/\text{H}\beta < 3$, $[\text{N II}]/\text{H}\alpha < 1$) (*right panels*) for the four galaxies which show such a transition in their spectra. *From top to bottom*: NGC 1386 (Sy2), NGC 5643 (Sy2), NGC 6860 (Sy1), and MCG -05-13-017 (Sy1.2).

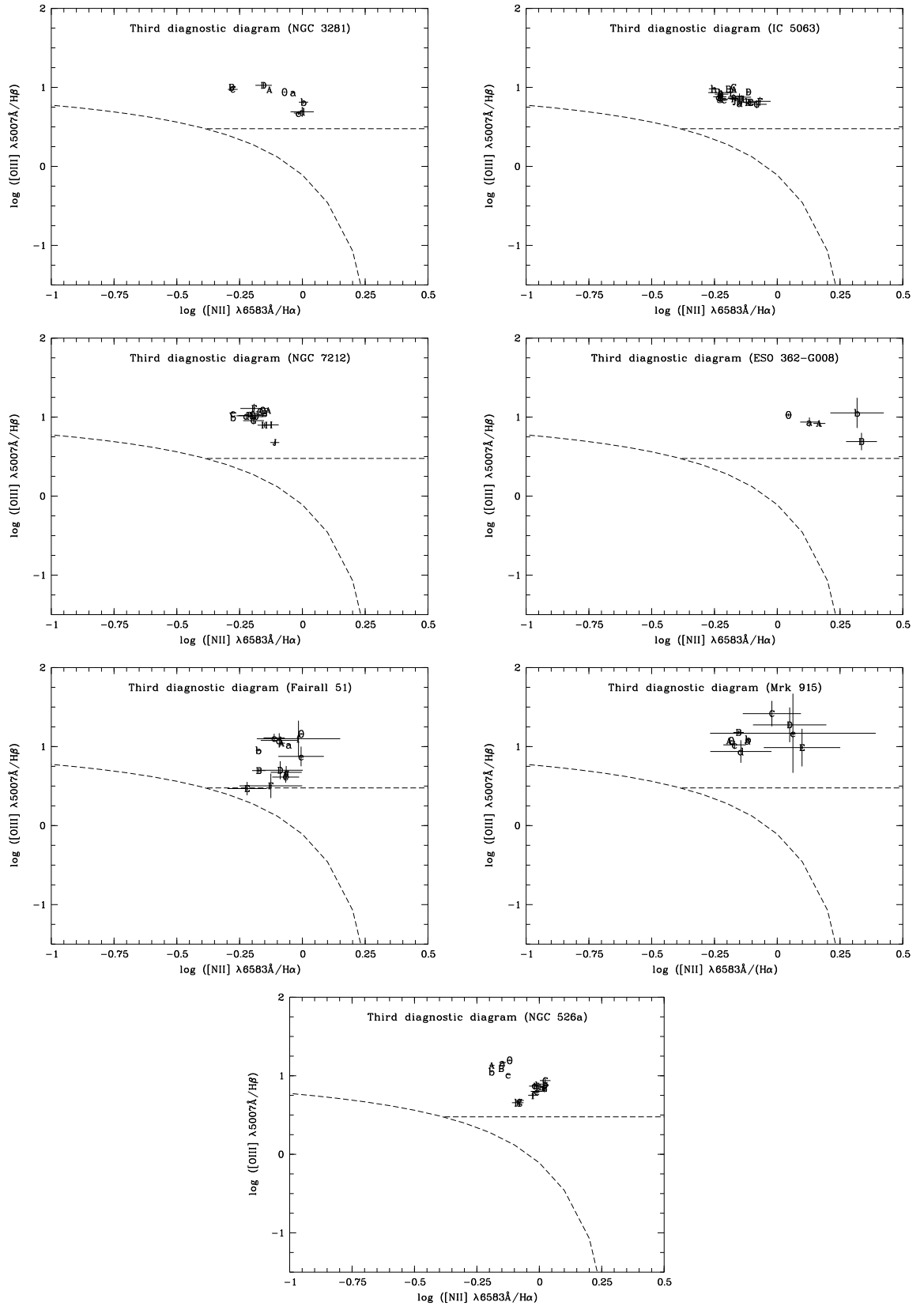


Figure 4.18: The same as in Figure 4.15 for the third diagnostic diagram only for the Seyfert–2 galaxies NGC 3281, IC 5063, NGC 7212, and ESO 362–G008 as well as the Seyfert–1 galaxies Fairall 51, Mrk 915, and NGC 526a. All line ratios fall in the AGN regime.

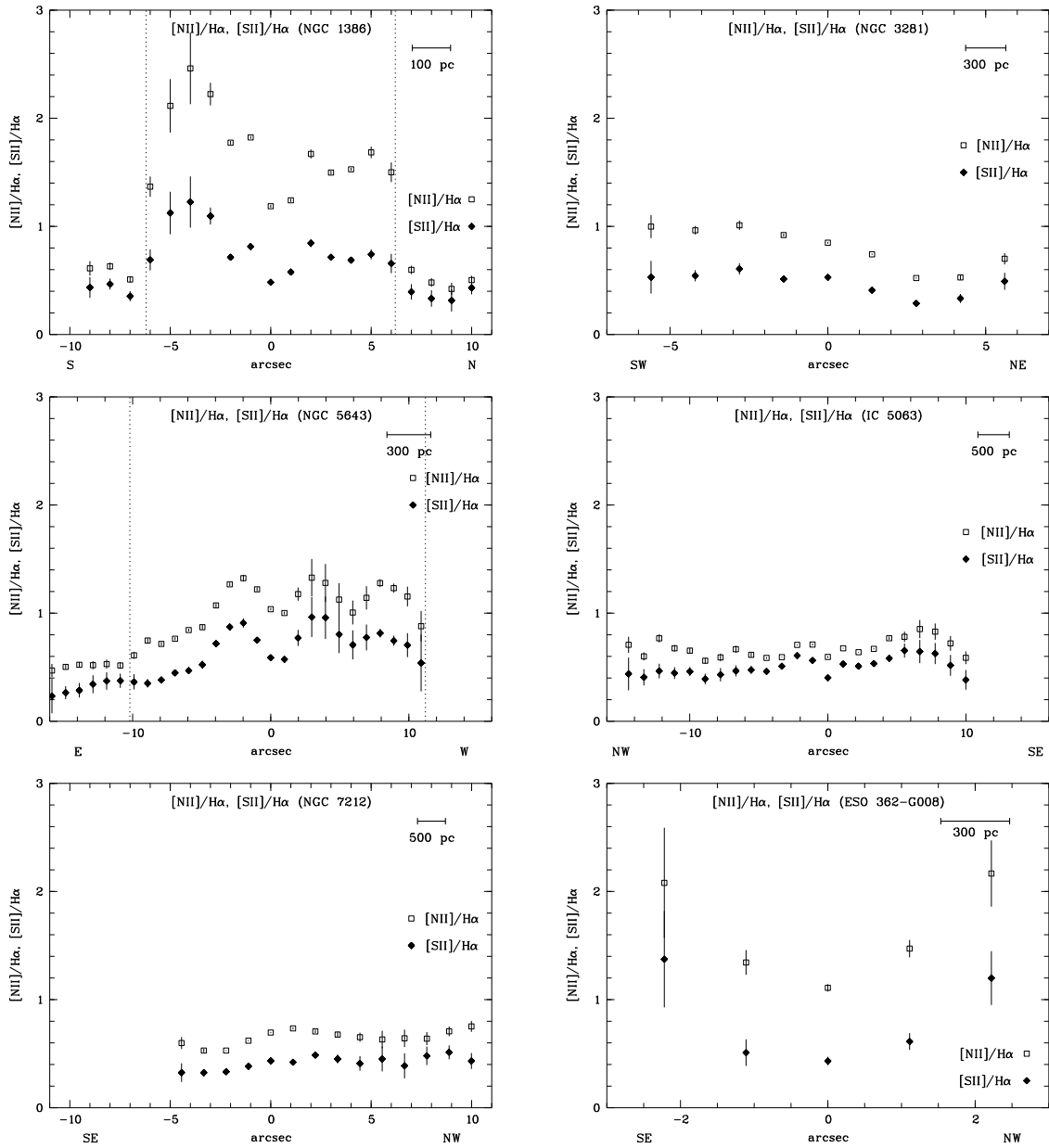


Figure 4.19: Reddening corrected $[\text{NII}]/\text{H}\alpha$ (open squares) and $[\text{SII}]/\text{H}\alpha$ (filled diamonds) emission-line ratios for the Seyfert-2 galaxies NGC 1386, NGC 3281, NGC 5643, IC 5063, NGC 7212, and ESO 362-G008. The edge of the NLR as determined from the diagnostic diagrams is indicated by dotted lines (NGC 1386 and NGC 5643).

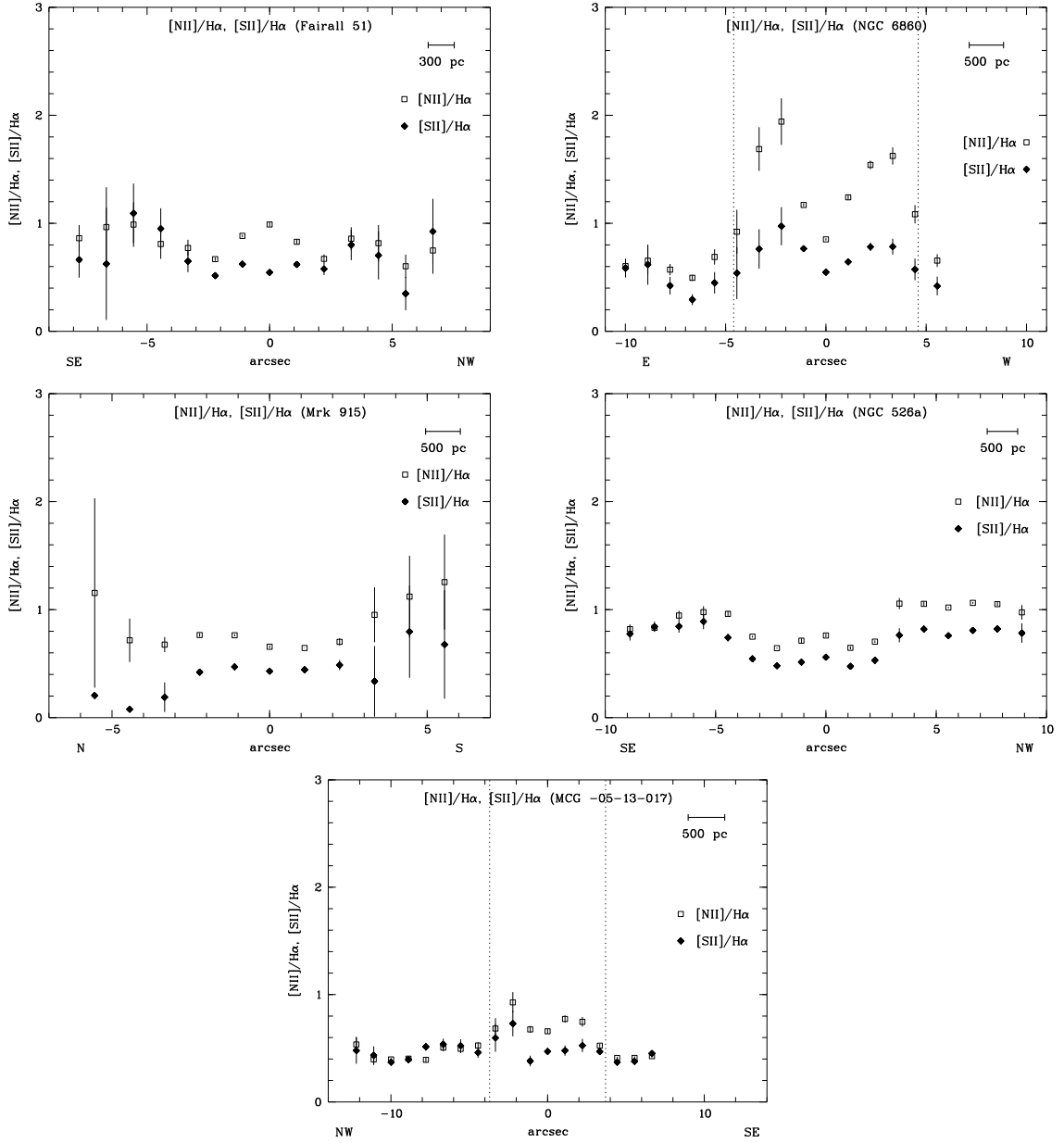


Figure 4.20: Reddening corrected $[\text{NII}]/\text{H}\alpha$ (open squares) and $[\text{SII}]/\text{H}\alpha$ (filled diamonds) emission-line ratios for the Seyfert-1 galaxies Fairall 51, NGC 6860, Mrk 915, NGC 526a, and MCG -05-13-017. The edge of the NLR as determined from the diagnostic diagrams is indicated by dotted lines (NGC 6860 and MCG -05-13-017).

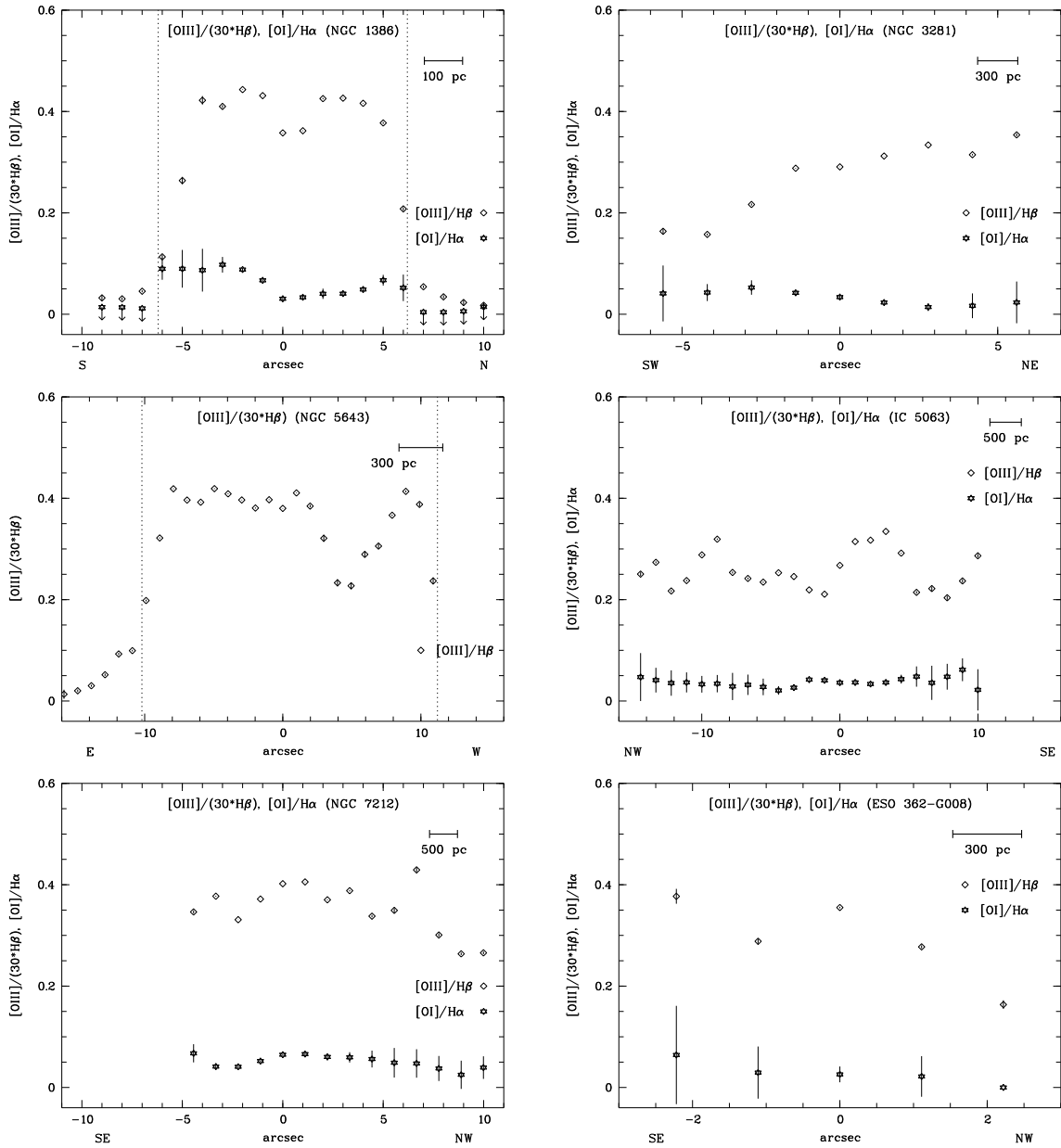


Figure 4.21: Reddening corrected $[OIII]/H\beta$ (open diamonds) and $[OI]/H\alpha$ (stars) emission-line ratios for the Seyfert-2 galaxies NGC 1386, NGC 3281, NGC 5643, IC 5063, NGC 7212, and ESO 362-G008. The edge of the NLR as determined from the diagnostic diagrams is indicated by dotted lines (NGC 1386 and NGC 5643).

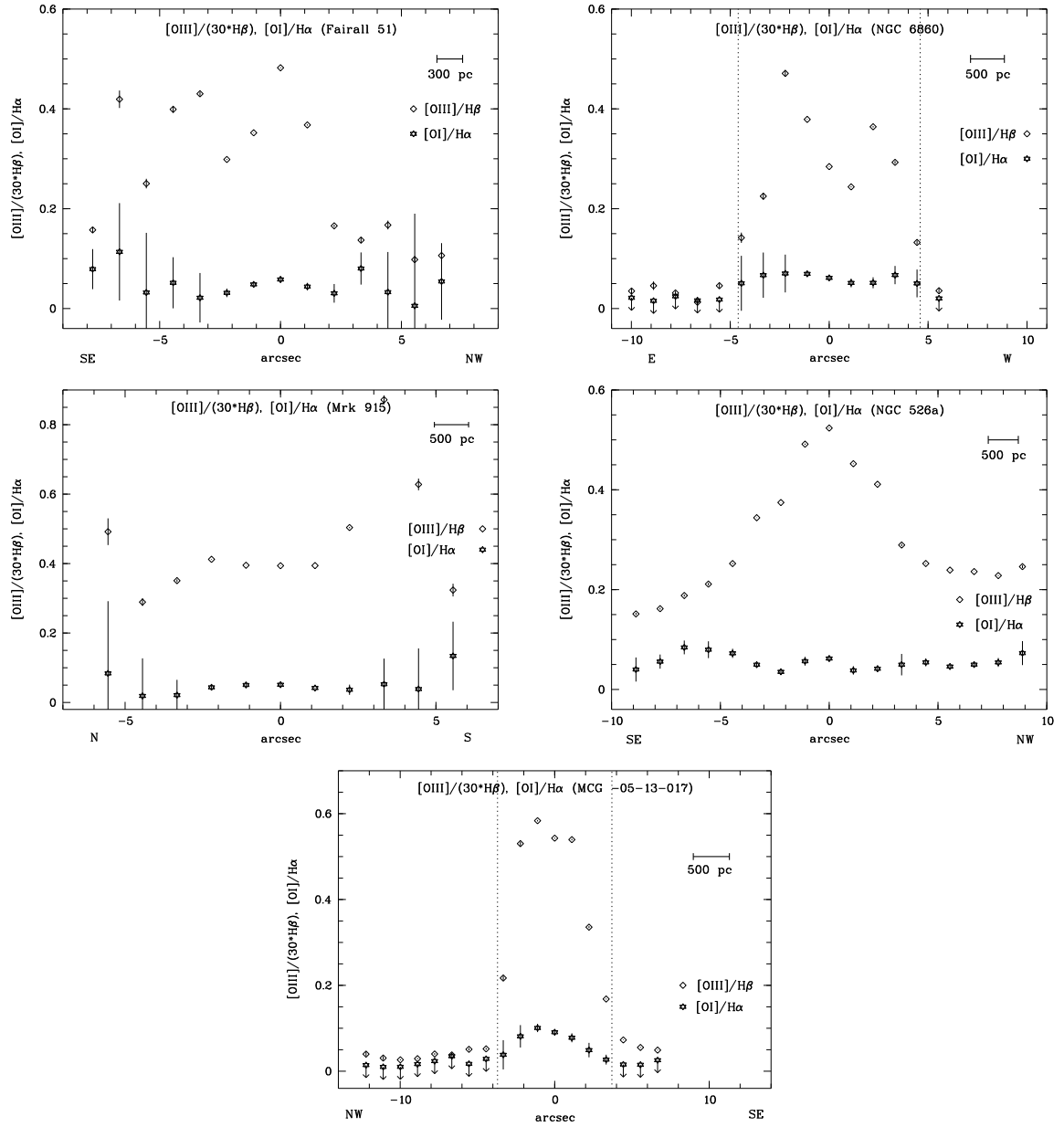


Figure 4.22: Reddening corrected $[O III]/H\beta$ (open diamonds) and $[O I]/H\alpha$ (stars) emission-line ratios for the Seyfert-1 galaxies Fairall 51, NGC 6860, Mrk 915, NGC 526a, and MCG-05-13-017. The edge of the NLR as determined from the diagnostic diagrams is indicated by dotted lines (NGC 6860 and MCG-05-13-017).

In particular, it has an energy index $\alpha_{uv-x} = -1.4$ in the EUV and a photon index $\Gamma_x = -1.9$ in X-rays. The clouds are assumed to be ionization bounded and of solar metallicity, unless stated otherwise.

In Figure 4.23, we present the effects of varying ionization parameter (solid line 1), varying metal abundances (dotted lines 2 & 3), varying nitrogen (N) and sulphur (S) abundances (dash-dotted lines 4 & 5), and high density (dashed line 6) on the emission-line ratios in the diagnostic diagrams.

(ii) Variations in ionization parameter alone have been studied by many authors and generally lead into the LINER-region of diagnostic diagrams for small ionization parameters under the assumption of solar abundances [e.g. Stasinska (1984); Osterbrock (1989)]. This trend is shown in Figure 4.23 (solid line 1) which includes the range of ionization parameters we measure for NGC 1386, varying from $\log U = -4.0 \dots -1.5$ in steps of 0.5 (marked by circles) from bottom to top. Sequences were calculated three times, using densities $n = 800, 400,$ and 200 cm^{-3} and $r = 50, 100,$ and 250 pc , respectively (printed as circles from right to left; only the data points for $n = 800 \text{ cm}^{-3}$ and $r = 50 \text{ pc}$ are connected by a line). We come back to (ii) in combination with (iii_b) below.

(iii) The strongest hint arguing against metallicity variations to change the line ratios in the observed direction is the similarity of all three diagnostic diagrams. In all three diagrams, each row falls in the same regime, either AGN or H II region. In fact, while extreme parameters may shift line ratios towards H II-like in individual diagrams, no mechanism does so for all three, as we will show in the following.

(iii_a) Metal abundances were varied between $Z = (0.05-3.0) \times \text{solar}$. Systematically decreasing abundances first lead to an *increase* in line ratios which can be partly traced back to oxygen being a strong coolant, and thus an increase of heating in case of oxygen depletion (Fig. 4.23).

The dotted lines 2 & 3 show models of varying metal abundances (3, 2.5, 1.7, 1.3, 1.0, 0.9, 0.5, 0.3, 0.1, $0.05 \times \text{solar}$; from right to left) for constant ionization parameter. The lower dotted line 2 corresponds to $\log U = -2.8$, the upper dotted line 3 to $\log U = -3.7$.

(iii_b) If, instead, only N and S abundances are varied, line ratios shift horizontally in the [N II] and [S II] diagrams towards the H II regime (Fig. 4.23). The dash-dotted lines 4 & 5 show models of varying N and S abundances (3, 2.5, 1.7, 1.3, 1.0, 0.9, 0.5, 0.3, 0.1, $0.05 \times \text{solar}$; from right to left) for constant ionization parameter. The upper dash-dotted line 4 corresponds to $\log U = -2.8$, the lower dash-dotted line 5 to $\log U = -3.7$.

Thus, a combination of outwards decreasing ionization parameter and decreasing metal abundances would place line ratios in the H II-regime in the observed way, despite AGN-intrinsic excitation. However, the same trend does not hold for the [O I] diagram. Just based on oxygen lines, this diagram is rather insensitive to variations in N and S abundances and line ratios remain well within the AGN regime for the whole parameter range. We conclude that combined ionization parameter and metallicity effects cannot explain the observations.

(iv) Finally, the presence of a high density component will again shift [N II] and [S II] towards the H II regime. To demonstrate an extreme, we plot in Figure 4.23 the case for $\log n_{\text{H}} = 6$ (dashed line 6). The ionization parameter varies from bottom to top in steps of 0.5 from $\log U = -4.0 \dots -1.5$. Again, while [N II] and [S II] decrease, [O I] is strongly boosted, moving line ratios away from H II-like excitation. This effect can be traced back to the different critical densities. ([O I] has a critical density of $1.8 \cdot 10^6 \text{ cm}^{-3}$ while the critical density for [S II] is with $1500-3900 \text{ cm}^{-3}$ significantly lower; Appendix C.)

We conclude that the observed distinction between H II–like and AGN–like line ratios of NGC 1386, NGC 5643, NGC 6860, and MCG –05–13–017 represents a true difference in ionization source, and thus our method to measure the NLR radius is valid. The second diagnostic diagram including the [O I] emission–line, new in our study compared to literature data, was essential to reach this conclusion, since our photoionization calculations show that there are means to reach the H II–regime with an AGN as ionizing source in the [N II] and [S II] diagrams.

However, we have to point out one remaining caveat of this method: Using diagnostic diagrams and the transition of line ratios between the central AGN and surround H II–region regime to determine the NLR size depends on the distribution and strength of young stars in the vicinity of the AGN. If the stellar ionization field is strong close to the AGN, at least along our line–of–sight, it soon starts to dominates over the AGN photoionization, thus limiting the measured NLR size. On the other hand, if only few or even no young stars are present in the central region, the NLR size cannot be determined from our method and the measured size once again depends on the sensitivity. This is apparently the case for eight of our 12 objects in which we do not observe line ratios in the H II region regime.

Thus, although using diagnostic diagrams gives a good method to determine the radius at which the stellar field starts to dominate the AGN in terms of ionization in individual galaxies which show such a transition, it may not be a good NLR size definition for the size–luminosity relation on a statistically large basis.

4.4.5 Surface–Brightness Distributions

The spatially varying luminosities in the [O III] and H α emission lines as well as the continuum (at 5450–5700 Å) were calculated and divided by the corresponding area in square parsecs at the galaxy to allow a comparison among all galaxies in our sample (Figs. 4.24 and 4.25). The surface–brightness distributions are similar to each other, centrally peaked and decreasing with distance of the nucleus. For the four objects which show a transition between line ratios typical for AGNs and that for H II regions (NGC 1386, NGC 5643, NGC 6860, MCG –05–13–017), the [O III] surface brightness is exceeding that of H α in the NLR. This behavior reverses in the outer parts as expected from the observed transition in the diagnostic diagrams.

For comparison, the [O III] surface–brightness distributions from the HST images of Schmitt et al. (2003a) are shown for those objects included in the HST snapshot survey. They were derived by averaging three vectorplots along the major axis of the NLR emission along p.a. = $x \pm 1^\circ$ (see also Chapter 2, Section 2.3.5). In all objects, they clearly show the higher spatial resolution of the HST image ($0''.0455 - 0''.1 \text{ pix}^{-1}$) compared to the 1–2'' spatial sampling of our spectral data. However, they also reveal the low sensitivity of the HST images compared to our spectroscopy: The [O III] emission at a S/N of 3 ends significantly earlier than what can be seen in our spectral data. In some cases, the HST [O III] surface–brightness distributions reveal several subpeaks of possibly individual NLR clouds, as can be already seen in the [O III] images (Figs. 4.1, 4.2, and 4.3). These substructures are smoothed out in our ~ 10 – 20 times lower spatial resolution spectra but are nevertheless still visible as a secondary or tertiary peak, mostly in emission lines.

We fitted a power–law function $L = L_0 r^\delta$ to the surface–brightness distributions of [O III], H α , and the continuum. The fitting parameters are shown in Table 4.11.

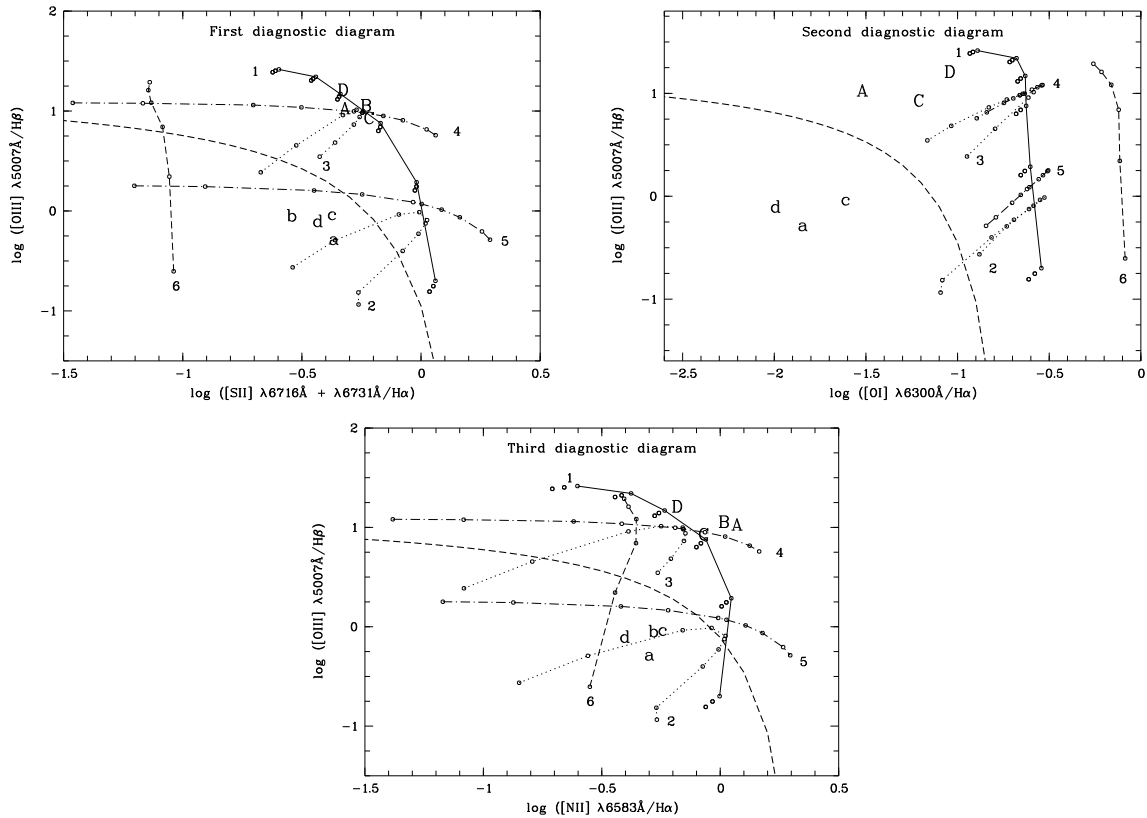


Figure 4.23: CLOUDY modeling results demonstrating the effects of varying ionization parameter (solid line 1), varying metal abundances (dotted lines 2 & 3), varying N and S abundances (dash-dotted lines 4 & 5), and high density (dashed line 6) (see text for details). The bold dashed line indicates the separation between AGN regime and H II regions. Representative line ratios of the nuclei as well as outer spectra are shown for the four Seyfert galaxies which show a transition: NGC 1386 (A,a), NGC 5643 (B,b; not included in the second diagnostic diagram), NGC 6860 (C,c), and MCG -05-13-017 (D,d). Here, the same letters correspond to one galaxy, with the capital ones marking line ratios falling in the AGN regime while small letters indicate regions with line ratios typical for H II regions. (Note that they do not correspond to the regions given in Table 4.10.)

Only data points within the NLR were included and taken as average from both sides of the nucleus (the data points given in Table 4.11 correspond to half the number of averaged values). The [O III] surface brightness falls faster with the radius than the H α surface brightness and also faster than the continuum ($\delta_{[\text{O III}],\text{ave}} \sim -2.62 \pm 0.22$; $\delta_{\text{H}\alpha,\text{ave}} \sim -2.37 \pm 0.25$; $\delta_{\text{cont},\text{ave}} \sim -1.43 \pm 0.12$).

This general trend is comparable to what has been found by Fraquelli et al. (2003) in their long-slit spectroscopic study of the NLR of 18 Seyfert-2 galaxies. However, they find on average a slightly steeper slope for especially [O III] ($\delta_{[\text{O III}],\text{ave}} \sim -3.6$; $\delta_{\text{H}\alpha,\text{ave}} \sim -2.6$; $\delta_{\text{cont},\text{ave}} \sim -1.4$; calculated from their Table 2). This discrepancy is most probably due to the fact that they include all visible emission in their fit, not concentrating on the NLR alone as they do not have a quantitative measure of the NLR size. Therefore, they possibly include [O III] emission from surrounding H II regions where the surface brightness drops significantly. This explanation is supported when comparing the results for objects common to both samples (NGC 1386 and NGC 5643): Fraquelli et al. (2003) report a steeper slope in the [O III] surface-brightness distribution but include emission out to distances from the nucleus where we can show from diagnostic diagrams that this emission can be attributed to surrounding H II regions. (A detailed comparison is presented when we discuss both objects individually in Section 4.4.12 and 4.4.13.)

For all three surface-brightness distributions ([O III], H α , continuum), Seyfert-1 galaxies show a steeper slope than Seyfert 2s ($\delta_{[\text{O III}],\text{ave},6\text{Sy}1} \sim -2.95 \pm 0.3$ versus $\delta_{[\text{O III}],\text{ave},5\text{Sy}2} \sim -2.24 \pm 0.2$; $\delta_{\text{H}\alpha,\text{ave},5\text{Sy}1} \sim -2.58 \pm 0.5$ versus $\delta_{\text{H}\alpha,\text{ave},5\text{Sy}2} \sim -2.16 \pm 0.2$; $\delta_{\text{cont},\text{ave},6\text{Sy}1} \sim -1.63 \pm 0.2$ versus $\delta_{\text{cont},\text{ave},5\text{Sy}2} \sim -1.19 \pm 0.1$).

4.4.6 Electron-Density Distributions

Applying the classical methods outlined in Osterbrock (1989), we derive the electron density as a function of distance to the nucleus using the ratio of the [S II] $\lambda\lambda 6716, 6731$ Å pair of emission lines (Appendix C, Section C.3). We used the observed central temperature to correct for the dependency of electron density on temperature¹¹. Due to the faintness of the involved [O III] $\lambda 4363$ Å emission line, we were not able to measure the temperature in the outer parts. For those objects in which no temperature was determined, we assumed $T = 10000$ K.

In all objects, the electron density is highest at the nucleus and decreases outwards down to the low-density limit (assumed to be 50 cm^{-3} ; Figs. 4.26 and 4.27). In some cases, it reveals a secondary or tertiary peak on one or both sides of the optical center. A characteristic structure with a central peak and two smaller peaks on both sides of the nucleus can be identified in seven objects (NGC 1386, NGC 5643, IC 5063, Fairall 51, NGC 6860, NGC 526a, MCG -05-13-017). The outer peaks are often close to the boundary of the NLR. These density enhancements may indicate shocks occurring at the edge of the NLR.

In Table 4.12, we give the results of fitting a power-law function $n_e = n_{e,0} r^\delta$ to the observed electron densities. Note that we did include only data points within the NLR and averaged the electron densities from both sides of the nucleus (the data points given in Table 4.12 correspond to half the number of averaged values). δ ranges between -0.8 and -2.3 . On average, the density decreases with $r^{-1.3 \pm 0.14}$.

¹¹ $n_e(T) = n_e(\text{obs}) \cdot \sqrt{(T/10000)}$

Table 4.11: Fitting parameters of surface-brightness distributions

Galaxy	Data Points	$\delta_{[\text{OIII}]}$	$\log L_{[\text{OIII}],0}$	$\delta_{\text{H}\alpha}$	$\log L_{\text{H}\alpha,0}$	δ_{cont}	$\log L_{\text{cont},0}$
NGC 1386	6	-2.56 ± 0.82	37.89	-2.27 ± 0.60	37.19	-1.26 ± 0.48	35.82
NGC 3281	4	-2.35 ± 0.60	37.35	-2.34 ± 0.64	36.86	-1.02 ± 0.18	34.96
NGC 5643	10	-1.42 ± 0.19	36.00	-1.34 ± 0.16	35.38	-1.54 ± 0.11	33.97
IC 5063	9	-2.73 ± 0.33	37.48	-2.75 ± 0.31	37.07	-1.37 ± 0.18	34.73
NGC 7212	4	-2.13 ± 0.57	36.96	-2.09 ± 0.56	36.38	-0.77 ± 0.26	34.03
ESO 362-G008	—	—	—	—	—	—	—
MCG -6-30-15	3	-2.52 ± 0.41	35.97	—	—	-0.94 ± 0.10	34.26
Fairall 51	6	-3.55 ± 0.25	36.54	-3.16 ± 0.48	35.93	-2.15 ± 0.30	34.82
NGC 6860	4	-3.06 ± 0.12	36.26	-2.59 ± 0.45	35.64	-1.62 ± 0.43	35.51
Mrk 915	5	-3.92 ± 0.32	37.00	-3.88 ± 0.33	36.34	-1.72 ± 0.45	34.61
NGC 526a	8	-1.72 ± 0.19	36.14	-1.28 ± 0.19	35.41	-1.71 ± 0.06	34.04
MCG -05-13-017	3	-2.90 ± 0.07	36.49	-1.98 ± 0.48	35.64	-1.66 ± 0.02	34.26

Note. – A linear least-squares fit was applied with $\log L = \delta \cdot \log r + \log L_0$. The number of data points included in the fit is given in column 2. For those objects which show a transition between line ratios typical for AGNs and H II-region like ones in the diagnostic diagrams, determining the size of the NLR, only data points within the NLR were included (NGC 1386, NGC 5643, NGC 6860, and MCG -05-13-017). For ESO 362-G008, too few data points were available for a fit. For MCG -6-30-15, no narrow H α line was fitted.

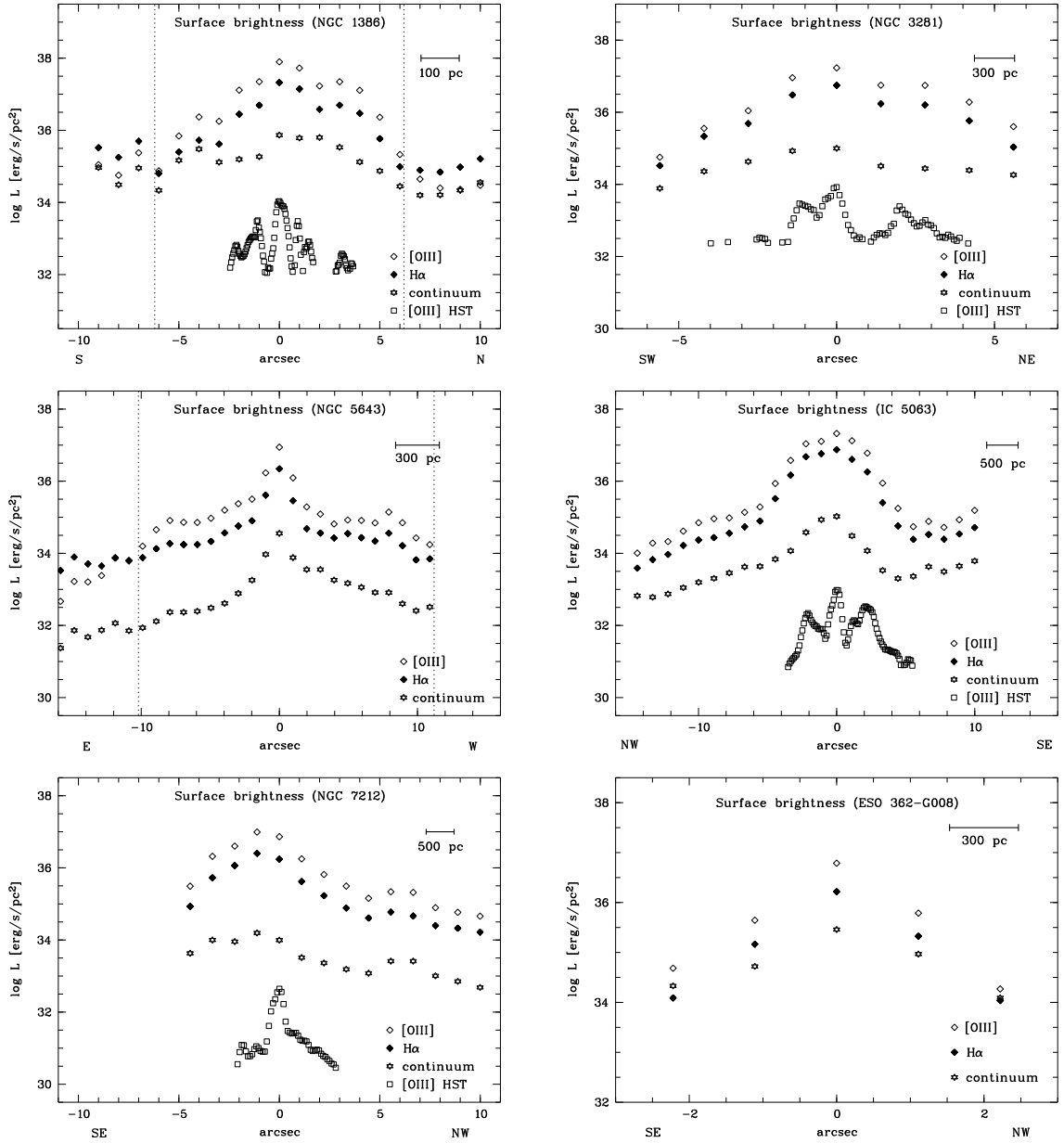


Figure 4.24: Surface-brightness distributions of the Seyfert-2 galaxies NGC 1386, NGC 3281, NGC 5643, IC 5063, NGC 7212, and ESO 362-G008 in [O III] (open diamonds), H α (filled diamonds), and continuum (at 5450–5700 Å, stars). The [O III] surface-brightness distributions from the HST images shown as open squares were shifted for comparison (by $\log L_{[\text{O III}]} = -3, -2, -3.5, -4.5$ for NGC 1386, NGC 3281, IC 5063, and NGC 7212, respectively; HST pixel scale $\sim 0''.05 \text{ pix}^{-1}$ for NGC 1386, $\sim 0''.1 \text{ pix}^{-1}$ for the other objects). Only data points with $S/N > 3$ were included. Error bars are smaller than the symbol size. The HST image has a 10 to 20 times higher spatial resolution but a significantly lower sensitivity, not allowing to measure the outer parts of the NLR. The edge of the NLR as determined from the diagnostic diagrams is indicated by dotted lines (NGC 1386 and NGC 5643).

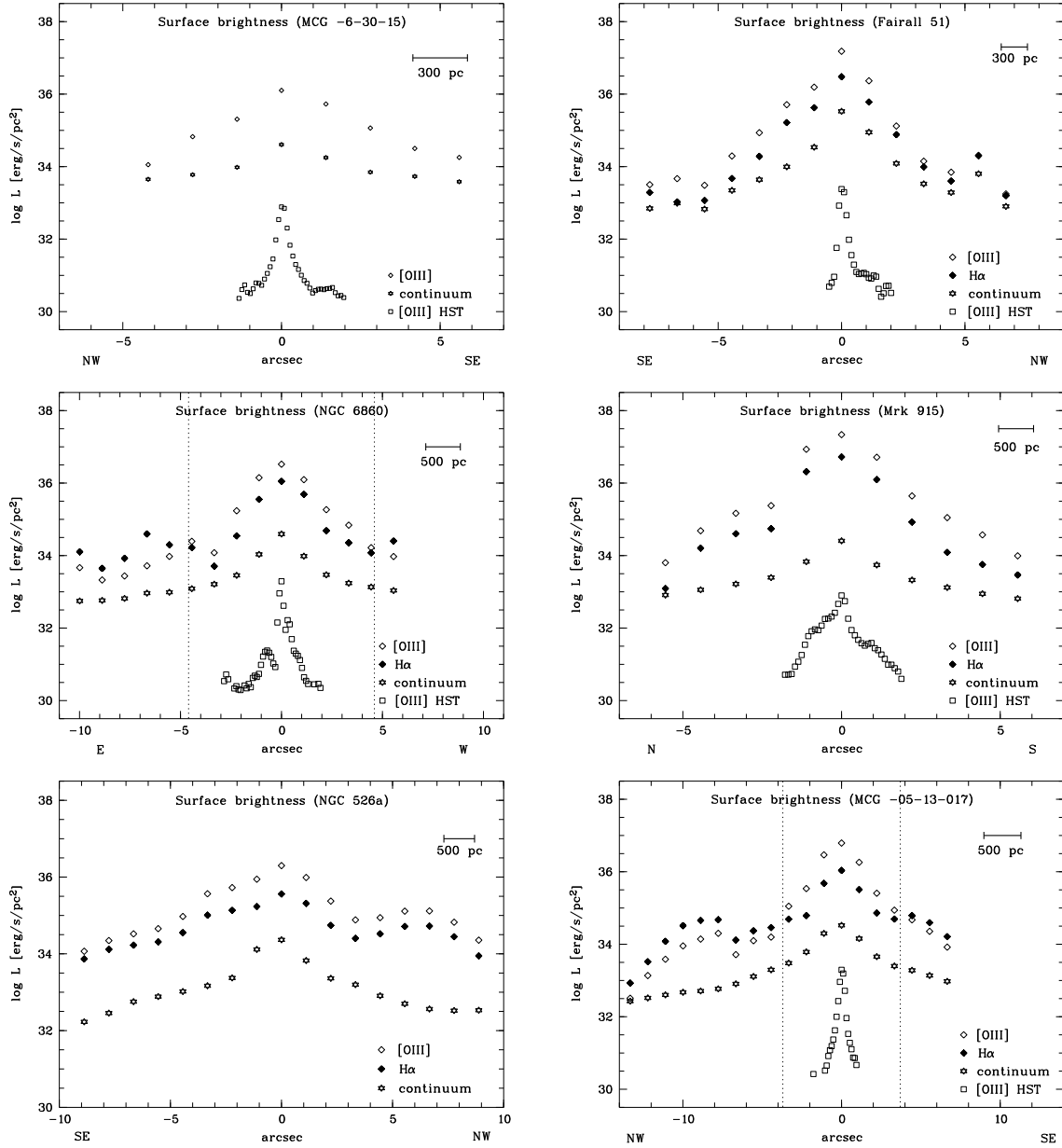


Figure 4.25: The same as in Figure 4.24 for the Seyfert-1 galaxies MCG -6-30-15, Fairall 51, NGC 6860, Mrk 915, NGC 526a, and MCG -05-13-017. The [O III] surface-brightness distribution from the HST image was shifted by $\log L_{[\text{OIII}]} = -4, -4, -3.8, -4, -4$ for MCG -6-30-15, Fairall 51, NGC 6860, Mrk 915, and MCG -05-13-017, respectively (HST pixel scale $\sim 0''.1 \text{ pix}^{-1}$). The edge of the NLR as determined from the diagnostic diagrams is indicated by dotted lines (NGC 6860 and MCG -05-13-017).

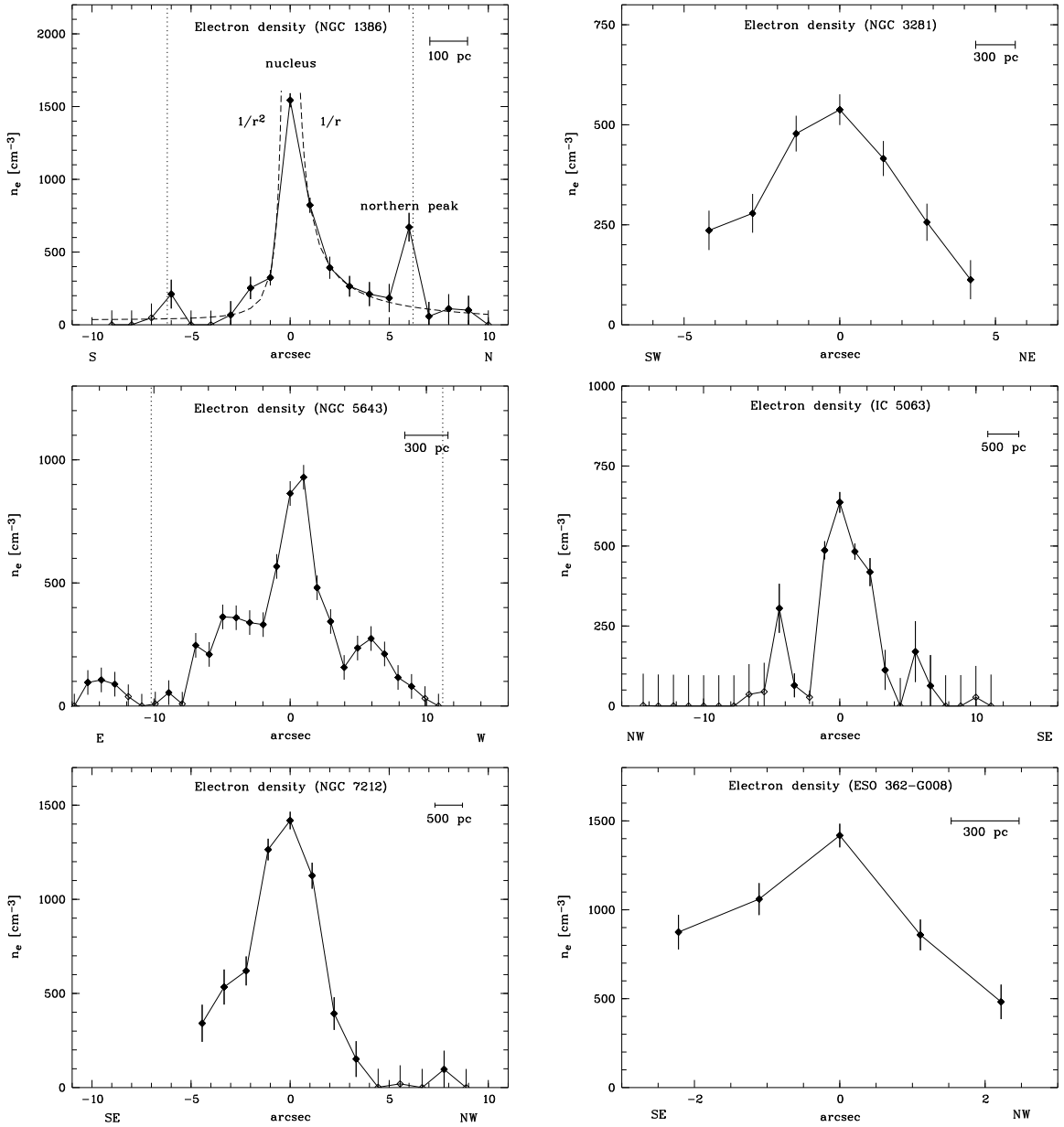


Figure 4.26: Electron density obtained from the $[\text{S II}] \lambda 6716 \text{ \AA} / \lambda 6731 \text{ \AA}$ ratio as a function of the distance from the nucleus for the Seyfert-2 galaxies NGC 1386, NGC 3281, NGC 5643, IC 5063, NGC 7212, and ESO 362-G008. Open symbols indicate locations where n_e is in the low-density limit (assumed $\leq 50 \text{ cm}^{-3}$). For NGC 1386, the fits $n_e(r) = n_{e,0} \cdot r^{-1}$ and $n_e(r) = n_{e,0} \cdot r^{-2}$ are shown as dashed line (neglecting the northern peak; see text for details). The edge of the NLR as determined from the diagnostic diagrams is indicated by dotted lines (NGC 1386 and NGC 5643).

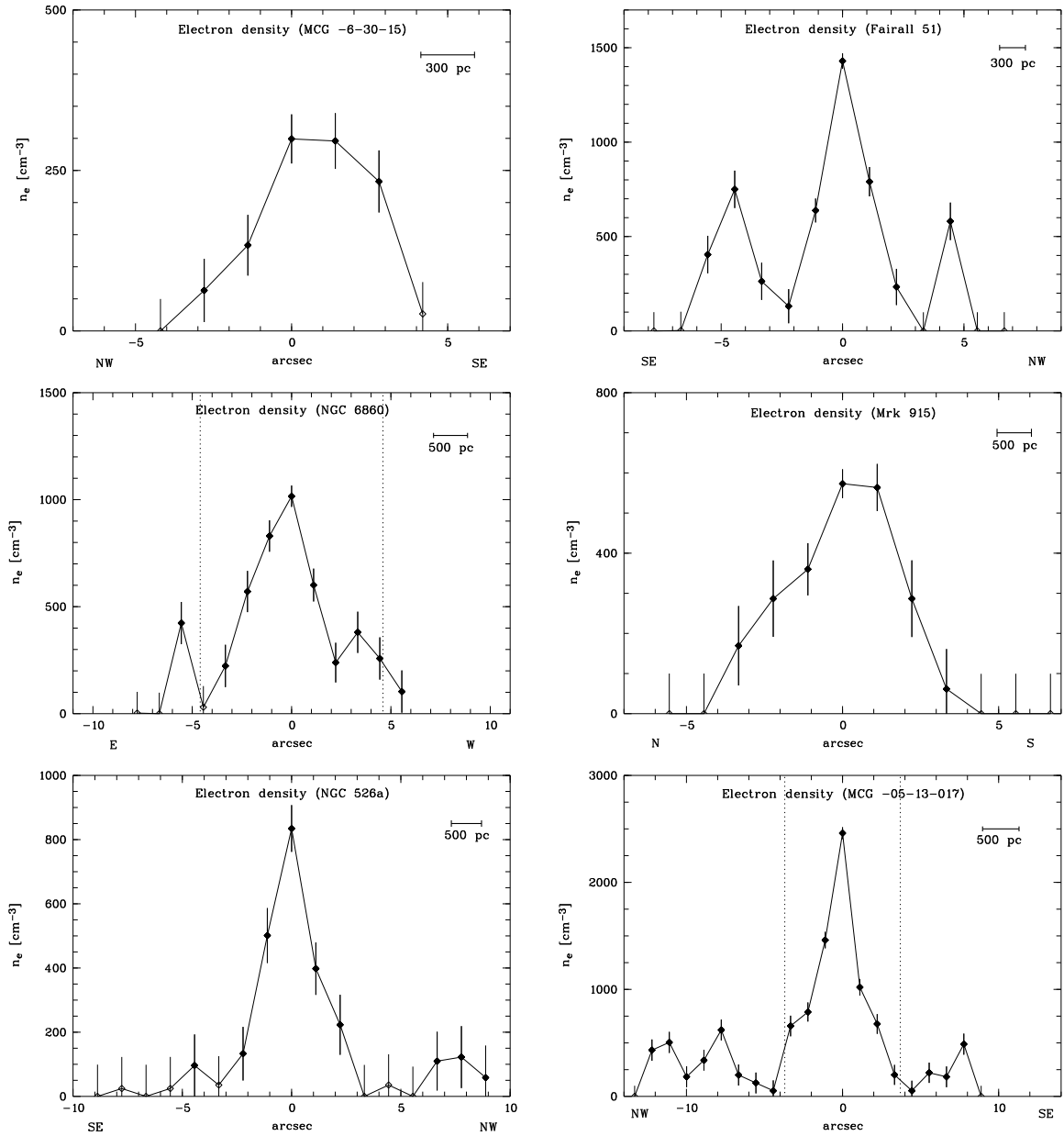


Figure 4.27: The same as in Figure 4.26 for the Seyfert-1 galaxies MCG -6-30-15, Fairall 51, NGC 6860, Mrk 915, NGC 526a, and MCG -05-13-017. The edge of the NLR as determined from the diagnostic diagrams is indicated by dotted lines (NGC 6860 and MCG -05-13-017).

Compared to the results of Fraquelli et al. (2003) who give power-law fits to electron densities of 14 Seyfert-2 galaxies, both their range and average value is slightly lower ($\delta \sim -0.4$ to -1.6 , $\delta_{\text{ave}} \sim -0.94$). When including our Seyfert-2 galaxies only, the results are comparable within the errors: $\delta_{5\text{Sy}2} \sim -1.14 \pm 0.1$. Seyfert-1 galaxies tend to show a steeper slope ($\delta_{6\text{Sy}1} \sim -1.46 \pm 0.2$). However, the individual scatter is rather large. For NGC 1386, we exemplarily show a fit with $\delta = -1$ and -2 in Figure 4.26 (*upper left panel*).

Following the approach of Fraquelli et al. (2003), we can use the average values of δ for the H α surface-brightness distribution and the electron density distribution to estimate the volume occupied by the ionized gas as a function of radius: $V_{\text{gas}} \propto \frac{L_{\text{H}\alpha}}{n_e^2} \sim r^{-0.9}$. For their sample of 18 Seyfert-2 galaxies, Fraquelli et al. (2003) find a slope of -0.6 . They quote that within the uncertainties, it is also consistent with $V_{\text{gas}} \sim \text{constant}$ along the NLR.

The temperature can be a function of distance from the central AGN. Unfortunately, we are not able to determine the temperature dependency on distance from the nucleus. In those objects where we are able to trace the electron temperature in the inner few arcseconds, it remains roughly constant. One may expect that the temperature is decreasing if the AGN is the only heating source. In that case, correcting with the central temperature overestimates the electron density in the outer parts. The observed decreasing slope can therefore not be artificially introduced by a wrong temperature correction. On the other hand, some authors report an increasing temperature with distance from the nucleus [e.g. Bergeron et al. (1983)] and explain it with a decrease in electron density faster than $n \propto r^{-2}$. However, the average decrease of electron density we observe is with $\delta \sim -1.3$ slower than that.

Note that the critical density for [S II] $\lambda\lambda 6716, 6731 \text{ \AA}$ is $\sim 1500 \text{ cm}^{-3}$ and 3900 cm^{-3} , respectively (Appendix C, Table C.2). Thus, these lines can only be used to measure the density in an environment with densities below $\sim 1500 \text{ cm}^{-3}$. Especially the central value may be significantly higher than what can be measured from these ratios.

4.4.7 Ionization-Parameter Distributions

The line ratio $[\text{O II}] \lambda 3727 \text{ \AA} / [\text{O III}] \lambda 5007 \text{ \AA}$ can be used to estimate the value of the ionization parameter U [e.g. Penston et al. (1990)]. A description of this method is summarized in Appendix C (Section C.4).

In most objects, the ionization parameter peaks at the optical nucleus and decreases with distance. The two exceptions are the Seyfert-2 galaxies NGC 3281 and IC 5063 where the ionization parameter reaches its maximum value several arcseconds to one side of the center. However, the optical nucleus needs not necessarily coincide with the position of the ionizing source, the AGN, which may also be hidden by dust. We will discuss this issue when discussing the objects individually. In NGC 1386 and NGC 6860, a secondary distinct peak is visible.

We fitted a power-law function $U_{\log(n_e)=2} = U_0 \cdot r^\delta$ to the observed ionization parameter (Table 4.13). We include only data points within the NLR and averaged the ionization parameters of both sides of the nucleus. δ ranges between -0.4 and -1 . On average, the ionization parameter decreases with $r^{-0.72 \pm 0.08}$. Seyfert-1 galaxies tend to show a steeper slope than Seyfert-2 galaxies ($\delta_{5\text{Sy}1} \sim -0.81 \pm 0.07$ versus $\delta_{2\text{Sy}2} \sim -0.51 \pm 0.08$).

Table 4.12: Fitting parameters of electron-density distribution

Galaxy	Data Points	δ	$n_{e,0}$
NGC 1386	5	-1.23 ± 0.09	615
NGC 3281	3	-0.84 ± 0.08	600
NGC 5643	10	-1.22 ± 0.30	1150
IC 5063	6	-1.08 ± 0.25	515
NGC 7212	4	-1.33 ± 0.15	1450
ESO 362-G008	–	–	–
MCG -6-30-15	3	-2.32 ± 1.42	660
Fairall 51	6	-2.10 ± 1.50	1585
NGC 6860	4	-1.06 ± 0.22	870
Mrk 915	3	-1.20 ± 0.40	575
NGC 526a	8	-1.15 ± 0.50	300
MCG -05-13-017	3	-0.94 ± 0.14	1410

Note. – A linear least-squares fit was applied with $\log n_e = \delta \cdot \log r + \log n_{e,0}$. The number of data points included in the fit is given in column 2. For those objects which show a transition between line ratios typical for AGNs and H II-region like ones in the diagnostic diagrams, determining the size of the NLR, only data points within the NLR were included (NGC 1386, NGC 5643, NGC 6860, and MCG -05-13-017). For ESO 362-G008, too few data points were available for a fit.

However, first the individual scatter is rather large and second, only two Seyfert-2 galaxies were included in this comparison. Note that we did not measure the slope of the ionization parameter in the Seyfert-2 galaxies NGC 3281 and IC 5063 as the ionization parameter is not peaked in the center. For NGC 1386, we exemplarily show a fit with $\delta = -1$ in Figure 4.28 (*upper left panel*).

The ionization parameter is the only physical parameter in our study which is strongly sensitive to reddening, derived using the line ratio $[\text{O II}]/[\text{O III}]$. We briefly discuss the influence of the different reddening measures on the ionization parameter for the representative spectra of NGC 1386 in Section 4.4.12 (see also Fig. 4.28).

In principle, the dependency on radius of both the electron density and the ionization parameter is in agreement with the NLR being ionized by photons and not by e.g. shocks: Inserting the fit $n_e \propto r^{-1}$ to the definition of $U = Q/(4\pi c n_e r^2)$ (with Q = rate of H-ionizing photons and r = distance between photoionizing source and emission-line clouds) yields $U \propto r^{-1}$. This is roughly in agreement with the fit of the ionization parameter, taking into account the errors and the individual scatter. In the case of MCG -05-13-017, for example, the measured δ (n_e) is -0.94 and δ ($U_{\log(n_e)=2}$) = 1.01 . It indicates that the excitation of the bulk of the NLR is due to photoionization and that ionization by e.g. shocks is negligible.

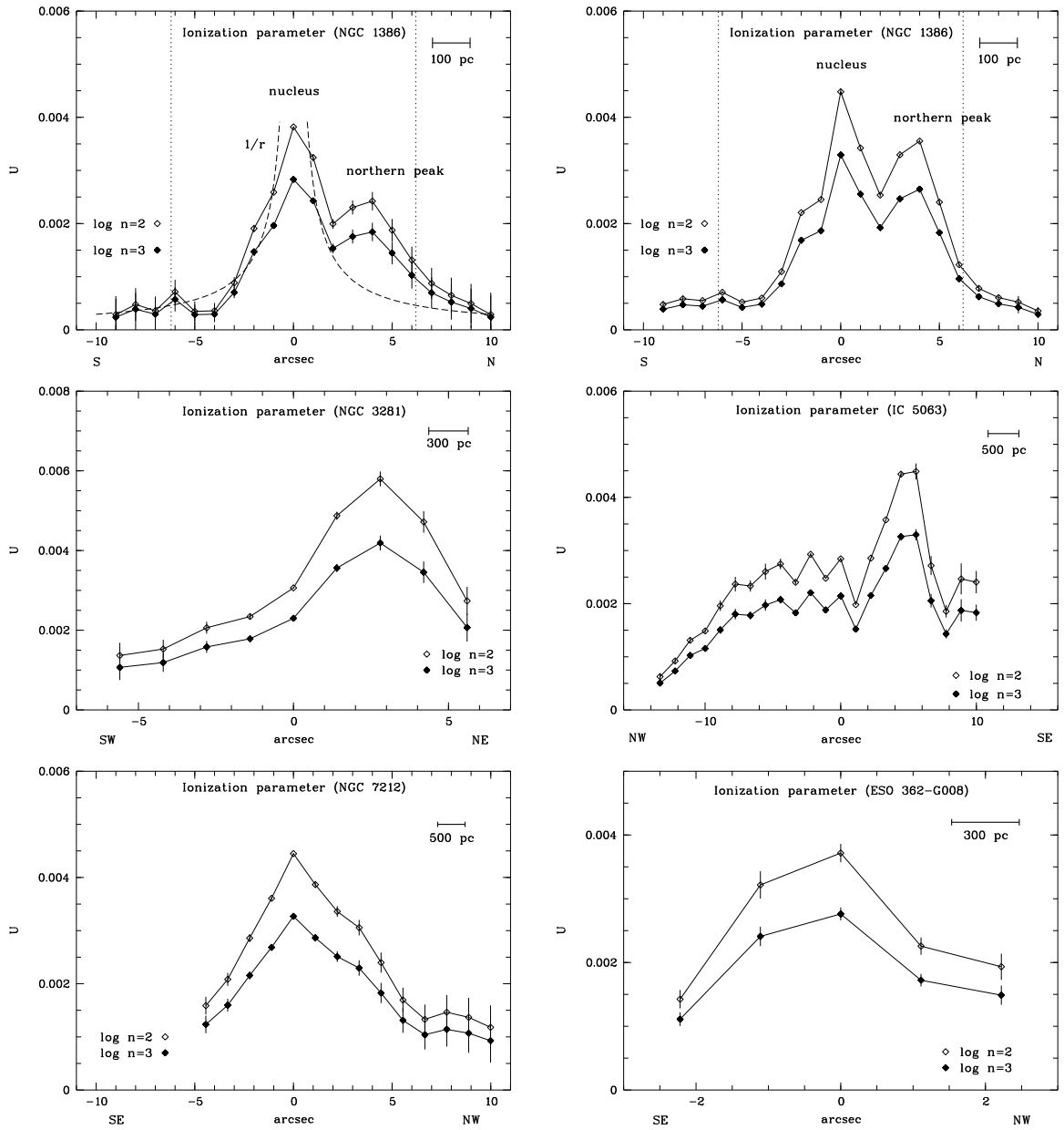


Figure 4.28: Ionization parameter derived from $[\text{O II}]/[\text{O III}]$ ratio as a function of the distance from the nucleus for the Seyfert-2 galaxies NGC 1386, NGC 3281, IC 5063, NGC 7212, and ESO 362-G008 (open symbols: $n_H = 100 \text{ cm}^{-3}$, filled ones: $n_H = 1000 \text{ cm}^{-3}$). The edge of the NLR as determined from the diagnostic diagrams is indicated by dotted lines. For NGC 1386, a fit $U(r) = U_0 \cdot r^{-1}$ is shown as dashed line (neglecting the northern peak; see text for details). Note that for NGC 5643, the $[\text{O II}]$ line was not included in the observed spectral range and we do not present the ionization parameter. The edge of the NLR as determined from the diagnostic diagrams is indicated by dotted lines (NGC 1386). For NGC 1386, we show in the *upper right panel* the ionization parameter using the reddening determined from the continuum slope instead of the Balmer decrement as in the *upper left panel*, for comparison. Clearly, the differences are small and do not change the general trend.

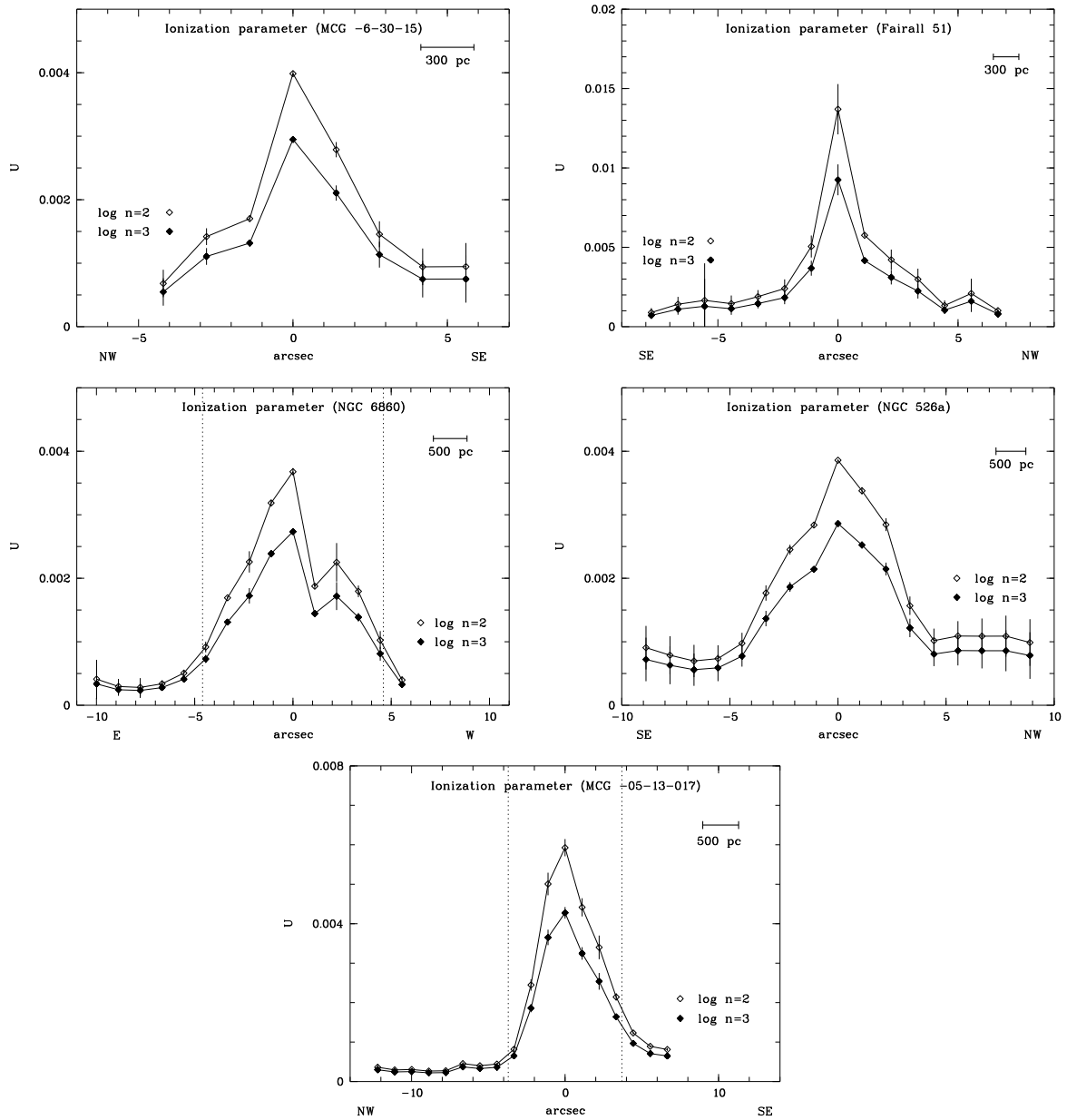


Figure 4.29: The same as in Figure 4.28 for the Seyfert-1 galaxies MCG -6-30-15, Fairall 51, NGC 6860, NGC 526a, and MCG -05-13-017. The edge of the NLR as determined from the diagnostic diagrams is indicated by dotted lines (NGC 6860 and MCG -05-13-017).

Table 4.13: Fitting parameters of ionization-parameter distribution

Galaxy	Data Points	δ	U_0
NGC 1386	6	-0.58 ± 0.03	0.003
NGC 3281 ^a	–	–	–
NGC 5643 ^b	–	–	–
IC 5063 ^a	–	–	–
NGC 7212	4	-0.43 ± 0.08	0.0041
ESO 362–G008	–	–	–
MCG –6–30–15 ^c	3	-0.90 ± 0.20	0.0032
Fairall 51	6	-0.81 ± 0.12	0.006
NGC 6860	4	-0.62 ± 0.25	0.0031
Mrk 915 ^b	–	–	–
NGC 526a	8	-0.69 ± 0.10	0.0035
MCG –05–13–017	3	-1.01 ± 0.26	0.0056

Note. – A linear least-squares fit was applied with $\log U_{\log(n_e)=2} = \delta \cdot \log r + \log U_0$. The number of data points included in the fit is given in column 2. For those objects which show a transition between line ratios typical for AGNs and H II-region like ones in the diagnostic diagrams, determining the size of the NLR, only data points within the NLR were included (NGC 1386, NGC 5643, NGC 6860, and MCG –05–13–017). For ESO 362–G008, too few data points were available for a fit.

^a As the ionization parameter does not peak in the center, no fit was applied.

^b The [O II] line was not covered by the observations.

^c Correction with reddening determined from continuum slope

4.4.8 Consequences for the NLR Size–Luminosity Relation

In Chapter 2, we studied the NLR size and its relation to [O III] luminosity from narrow-band imaging and compared it to the results of Bennert et al. (2002) and Schmitt et al. (2003b). We find that the NLR sizes of type-1 AGNs scale with roughly the square root of [O III] luminosity, while the relation for type-2 AGNs is close to $R \propto L_{[\text{OIII}]}^{0.33}$. A physical interpretation of these results was already discussed in Chapter 2 (Section 2.3.2).

If the NLRs were ambient circumnuclear gas fully photoionized by the nuclear continuum source, a Strömgen-type radius–luminosity relationship $R \propto L^{0.33} n^{-0.66}$ and thus a slope of 0.33 is indeed expected in the case of a constant density. However, the average decrease of electron density we observe ($n_e = n_{e,0} r^{-1.3 \pm 0.1}$) seems to be common to several Seyfert galaxies [e.g. Storchi-Bergmann et al. (1992a); Fraquelli et al. (2000, 2003)], contradicting the simple “Strömgen explanation”. For a dependency of density on radius $n_e \propto R^{-1}$, a relation of $R \propto L$ is instead expected, a relation which differs from the observed slopes of the NLR size–luminosity relation of 0.5 and 0.33. To gain a slope of 0.33, a constant density is needed; for a slope of 0.5, the density is expected to decrease less steep with radius than what we observe ($n_e \propto R^{-0.5}$). Thus, our observations argue against a Strömgen-type radius–luminosity relationship. Furthermore, a Strömgen behavior is expected for gas distributed in a sphere while the NLR gas is assumed to be in an ionization–cone structure within the unified scheme and it may also be distributed in a disk. In close cooperation with Bruno Jungwiert, we started numerical simulations to investigate these issues in detail.

A slope of 0.5 suggest a self-regulating mechanism that determines the size of the NLR to scale with the ionization parameter. It can be explained if on average, all AGNs have the same ionization parameter, density, and ionizing spectral energy distribution. Thus, the observed spatially decreasing ionization parameter and density in all our objects do not contradict the explanation of the NLR size–luminosity relation in terms of a constant (in all objects) ionization parameter and density. Indeed, all objects show a comparable value of U and n_e at the edge of the NLR ($U_{\log(n_e)=2} \sim 0.001 - 0.0005$, $n_e \sim 50 - 100 \text{ cm}^{-3}$). In Chapter 3, theoretical NLR size–luminosity relations for type-1 and type-2 AGNs closed to the observed ones were derived with the assumption that intrinsically, the size of the ionization cone increases with $L_{\text{UV}}^{0.5}$. Thus, both the theoretical and observational results speak in favor of an intrinsic slope of the NLR size–luminosity relation of 0.5 and rule out a simple Strömgen behavior of the NLR gas.

However, the NLR size–luminosity relation was so far derived from [O III] images, but the size determination using [O III] images alone bears various uncertainties due to e.g. the sensitivity dependency of the observation and contributions from circumnuclear starbursts as has been shown in this Chapter. Compared to the spatially-resolved spectral diagnostics measuring the “real” NLR size, the apparent NLR size determined by [O III] images can be either smaller in case of low sensitivity or larger in case of contributions of circumnuclear starbursts. Applying the methods described here to a larger sample of objects will help to scrutinize the NLR size–luminosity relation, although also this NLR size definition may not be robust enough as it depends on the distribution and strength of young stars in the vicinity of the AGN. Nevertheless, the uncertainty of the NLR size due to different determination methods is small enough to not affect the general slopes of the NLR size–luminosity relation which extends over four orders of magnitudes in luminosity and two orders of magnitudes in size.

4.4.9 Velocities

In most cases, we derived the NLR velocity curve from the average of the peak wavelengths of the $H\alpha$ and $[\text{N II}]$ emission lines; in some cases, we used only one line ($H\alpha$, $[\text{N II}]$ or $[\text{O III}]$). In addition, given the high S/N ratio of our spectra, we are able to trace the velocity field from the “peak wavelengths” of the stellar absorption line Ca II K for several objects (before subtraction of the stellar template) throughout the whole region as this line is not blended with emission lines. The uncertainty in velocity values estimated by comparing repeated measurements at the same point is 20 km s^{-1} .

Several objects show a rather “random” velocity field. In those objects with measured stellar velocities, the two curves show in general a similar behavior although the maximum amplitude is often smaller. In some cases, the gaseous velocity curves show a typical rotational pattern (e.g. NGC 1386, IC 5063, and MCG –05–13–017), indicating that the NLR may be distributed in a disk rather than a sphere. However, this interpretation is not unambiguous and the velocities may at least partly originate from a jet/NLR interaction and outflows or may be influenced by a barred potential. We will discuss these issues for each galaxy individually. If the rotational interpretation applies, we can determine the enclosed mass.

For NGC 1386 and MCG –05–13–017 where we observed the transition of line ratios between AGN-like and H II-region like in the diagnostic diagrams and for which we are able to determine the stellar velocity curve, the gaseous velocities do not change significantly in the NLR and the surrounding H II-region regime. This observation indicates that the NLR does not consist of an intrinsically different gas component but is ambient gas photoionized by the AGN.

4.4.10 Extended Broad Lines?

In Table 4.14, we compare the spatial extension of broad $H\alpha$ and $H\beta$ in the six Seyfert-1 galaxies in our sample. For the five Seyfert-1 galaxies observed at the NTT, both lines were taken from the red spectral wavelength range covered by the REMD chip, for comparison. Additionally, we checked that the $H\beta$ profile observed on the BLMD chip is comparable to the one taken with the REMD chip.

Intrinsically, the BLR sizes are expected to be $\ll 1''$, using the BLR size–luminosity relation from Kaspi et al. (2000) (their Eq. 6) and the observed luminosities in our galaxies with an average scale of $\sim 300 \text{ pc}''$. However, the observed spatial emission will be broadened according to seeing and instrumental effects.

For three objects (MCG –6–30–15, NGC 526a, and MCG –05–13–017), the broad $H\alpha$ and $H\beta$ components are limited to the central $2\text{--}3''$. This corresponds to approximately twice the seeing value during the individual observations (see Tables 4.2 and 4.5 for details). To probe any possible instrumental effect, we used the spectra of two fairly bright stars observed at the NTT on the same chip as two of our objects (ESO 362–G008 and MCG –05–13–017). We created a seeing profile as a function of wavelength and distance from the center and compared it to the observed extension in the broad $H\alpha$ line. The seeing profile of the stars shows that in the central $2''.2$ (at a wavelength of $H\beta$) and $2''.5$ (at $H\alpha$, respectively), 98% (3σ) of the central flux should be included. Thus, we cannot rule out that a combination of seeing and instrumental effect produce the observed extended broad lines out to $2\text{--}3''$.

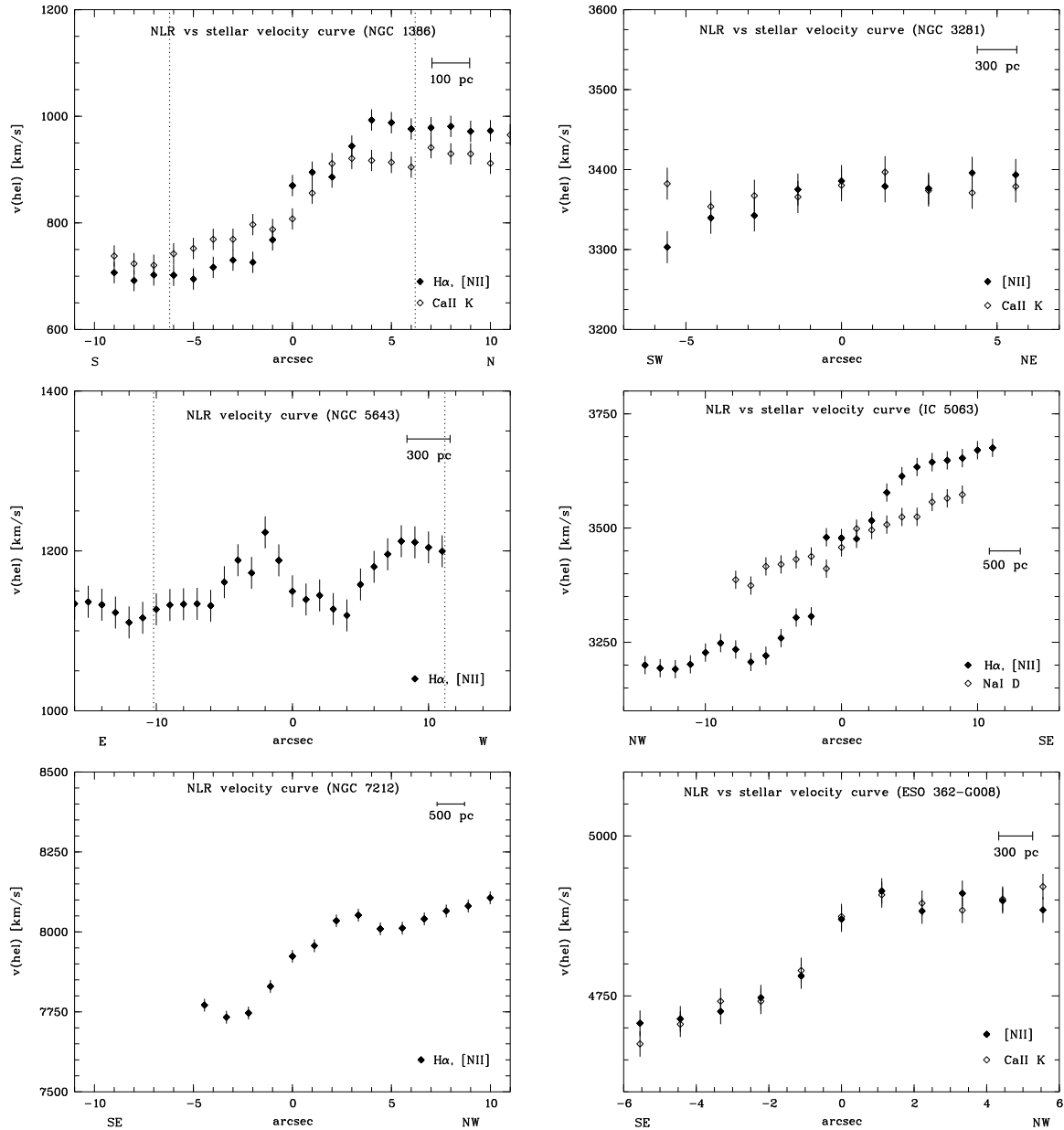


Figure 4.30: Velocity fields of the Seyfert-2 galaxies NGC 1386, NGC 3281, NGC 5643, IC 5063, NGC 7212, and ESO 362-G008. The velocities of the NLR were derived from the average value of the peak wavelengths of the $\text{H}\alpha$ and [N II] emission lines (filled symbols), with the exceptions of NGC 3281 and ESO 362-G008 where only [N II] was used. The stellar velocities were in most cases determined from the Ca II K absorption line “peak wavelength” as seen in the “raw” spectrum (open symbols) if visible at a good S/N with the exception of IC 5063 where Na D was used instead. The edge of the NLR as determined from the diagnostic diagrams is indicated by dotted lines (NGC 1386 and NGC 5643).

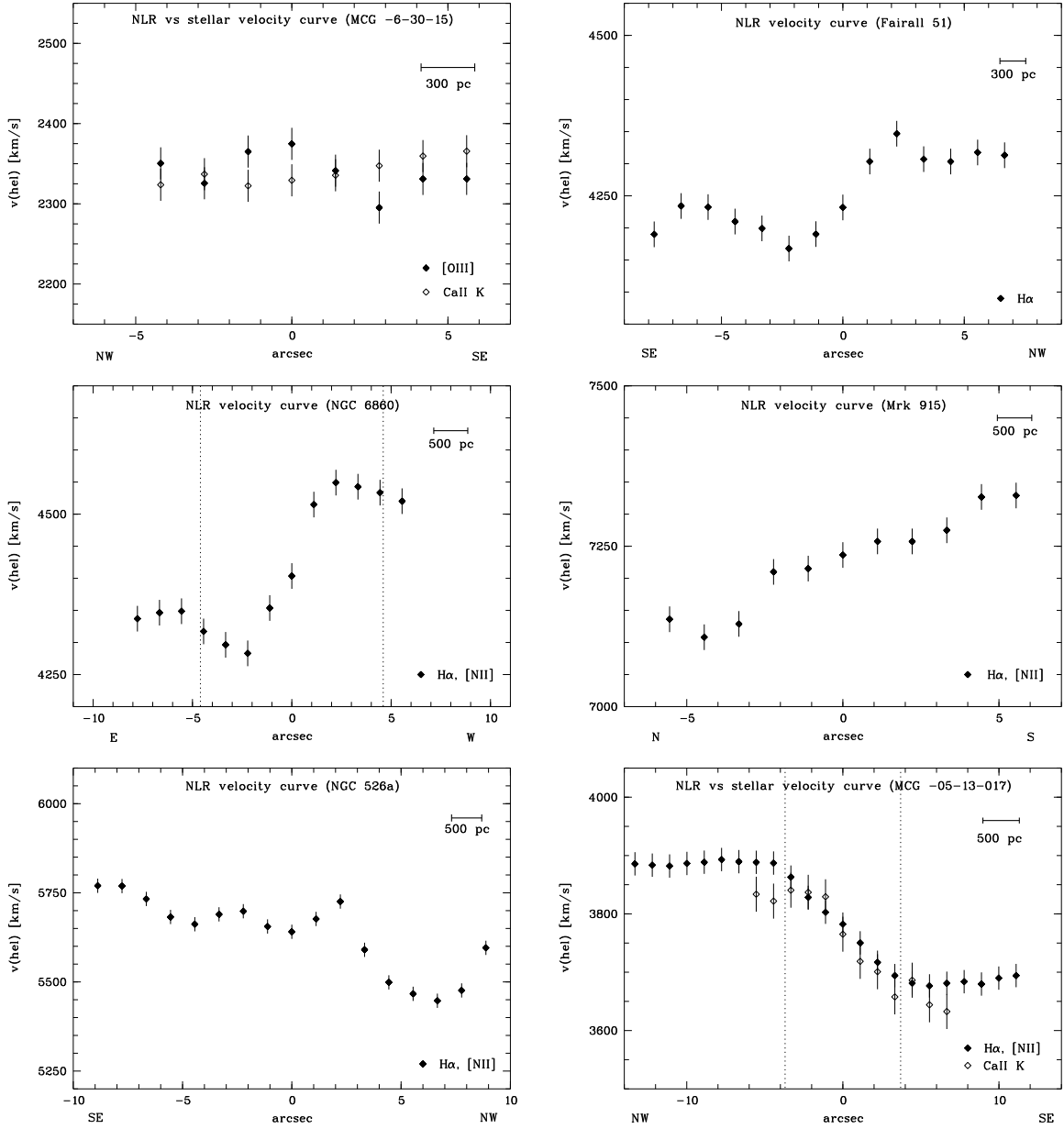


Figure 4.31: Velocity fields of the Seyfert-1 galaxies MCG -6-30-15, Fairall 51, NGC 6860, Mrk 915, NGC 526a, and MCG -05-13-017. The velocities of the NLR were derived from the average value of the peak wavelengths of the H α and [N II] emission lines (filled symbols), with the exceptions of MCG -6-30-15 and Fairall 51 where [O III] and H α were used, respectively. The stellar velocities were determined from the Ca II K absorption line “peak wavelength” as seen in the “raw” spectrum (open symbols) if visible at a good S/N. The edge of the NLR as determined from the diagnostic diagrams is indicated by dotted lines (NGC 6860 and MCG -05-13-017).

Table 4.14: Broad H β and H α emission in Seyfert-1 galaxies

Galaxy	Broad H β extension ["]	Broad H α extension ["]
MCG-6-30-15	2.8	2.8
Fairall 51	2.2	13
NGC 6860	2.2	9
Mrk 915	2.2	9
NGC 526a	none	2.2
MCG-05-13-017	2.2	3.3

Note. – The total extension of the broad H β and H α emission lines is given. Note that this is no sharp edge but rather a lower limit; there may still be underlying broad emission further out where we are limited by the S/N. The galaxies were observed with NTT/EMMI and a seeing $< 1''$ with the exception of MCG-6-30-15 which was observed with the lower spectral resolution of VLT/FORS1 and at a seeing of $1''.5$.

The same holds for the broad H β line in the remaining three objects (Fairall 51, NGC 6860, and Mrk 915). However, the broad H α emission line in these objects extends out significantly further ($d \sim 9\text{--}13''$; Figs. 4.32, 4.34, and 4.36). Note that we do not find a sharp edge beyond that no broad emission is seen, we are limited rather by the S/N in the outer parts.

A detailed study of the broad H α emission and its variation with distance from the center using Gaussian fitting yields the following results (see also Figs. 4.33, 4.35, and 4.37). In all three objects, the best fit was achieved by applying three Gaussians to the observed profile: a narrow one (FWHM: $5\text{--}11 \text{ \AA} \sim 230\text{--}500 \text{ km s}^{-1}$), one with an intermediate width (FWHM: $40\text{--}85 \text{ \AA} \sim 1830\text{--}3880 \text{ km s}^{-1}$), and a broad one (FWHM: $110\text{--}255 \text{ \AA} \sim 5025\text{--}11650 \text{ km s}^{-1}$). The width of the narrow Gaussian is in agreement to what is expected for the width of narrow lines ($10^{2-3} \text{ km s}^{-1}$), while both the widths of the intermediate and the broad line fall in the typical range of line widths observed from the BLR ($10^{3-4} \text{ km s}^{-1}$). The widths of the fitted Gaussians do not show a significant variation with radius in none of the objects. Moreover, the general profile shape does not change with distance from the center. In Figure 4.38 (*left panel*), we show the broad H α flux on logarithmic scales as a function of distance from the center. For all three objects, it is high in the center and decreases outwards. While it is still fairly high at $\pm 1''$ distance from the nucleus, it is much lower and remains on roughly a comparable flux level further out. The ratio of the broad H α flux to the narrow H α flux shows another trend which is similar for all three objects: While it is relatively high in the center, it decreases outwards to the next $1\text{--}2''$ and then increases again (Fig. 4.38; *right panel*).

These observations will be discussed in line with the origin of the extended broad emission. However, we want to stress that using a broad, an intermediate, and a narrow component to fit the observed H α and H β profiles in all rows where we see underlying broad emission (Section 4.3.5) yields an accurate fit to the observed profiles.

Thus, independent of the origin of the broad extended emission lines, the deduced narrow emission line flux should not be affected by the underlying broad emission.

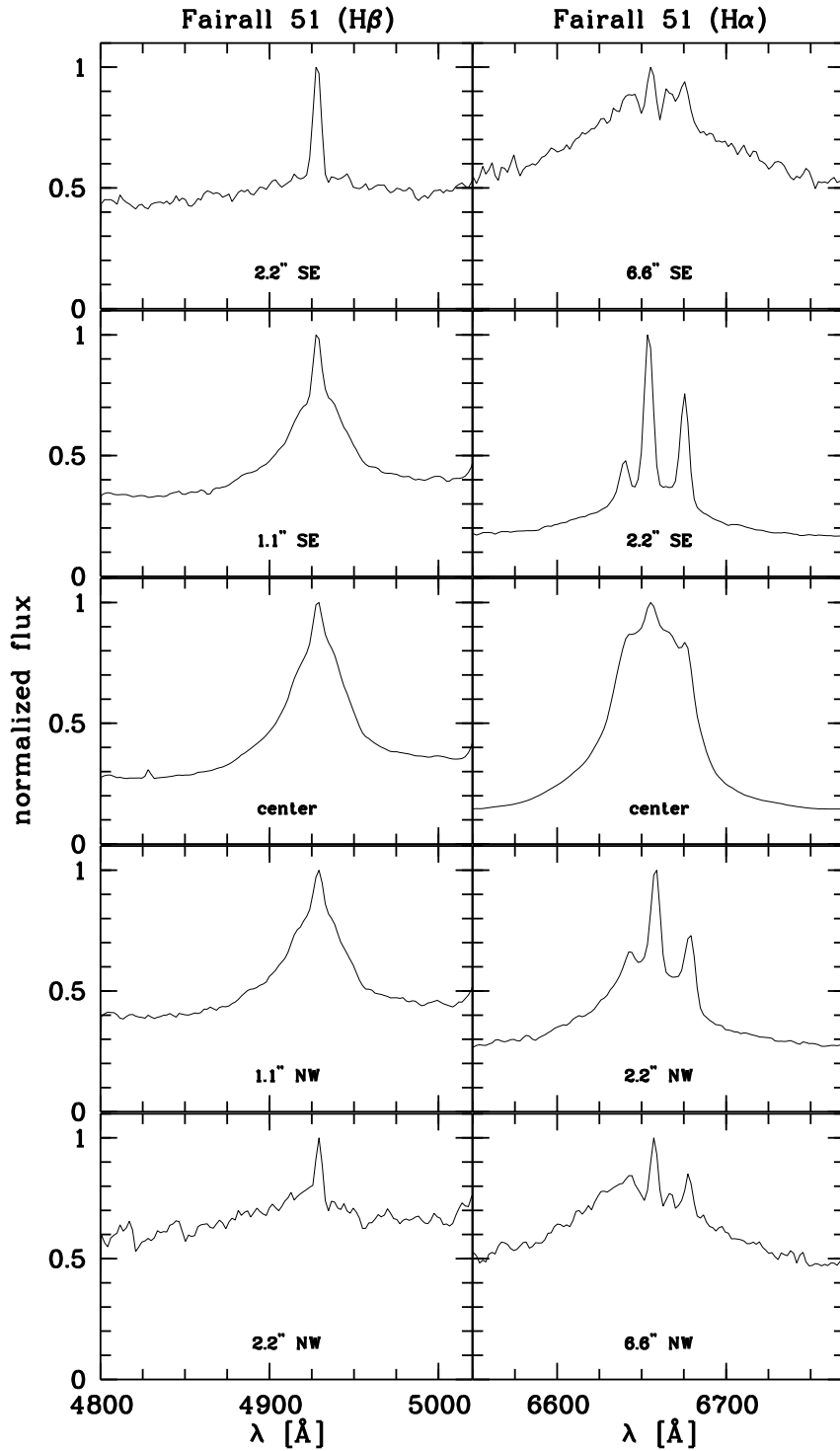


Figure 4.32: Broad $H\beta$ (left panel) and $H\alpha$ (right panel) emission in Fairall 51. While a broad $H\alpha$ component is visible out to $r \sim 7''$ from the nucleus, a broad $H\beta$ component extends out to $r \sim 1''$ from the nucleus. The peak fluxes of both emission lines were normalized to 1, for comparison. Note that no continuum slope was subtracted to show the “original” broad emission.

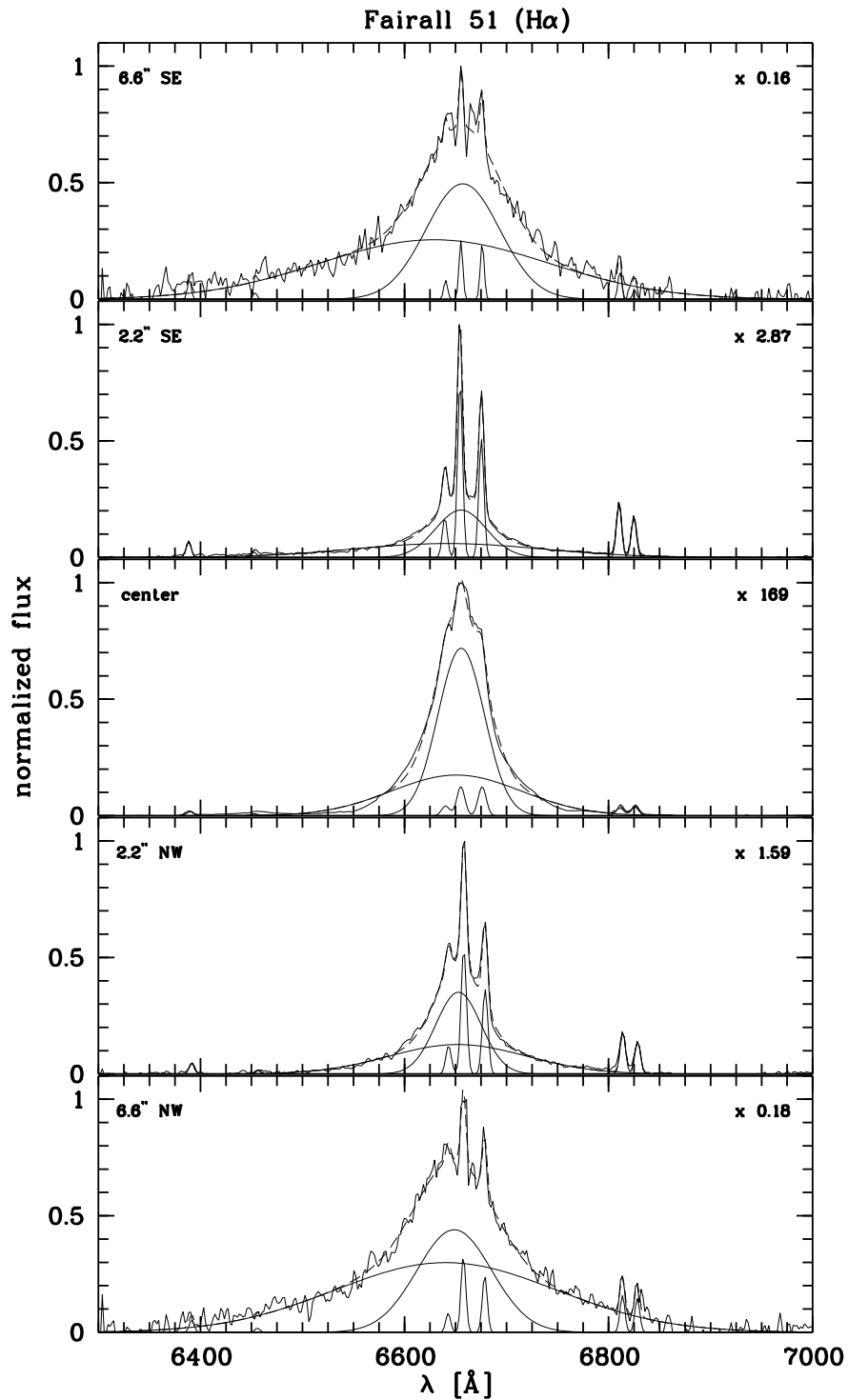


Figure 4.33: Broad H α emission in Fairall 51 with three Gaussian fits (a narrow one, one with an intermediate width and a broad one) shown as overlay. Single Gaussians are shown as solid line, the total fit is shown as dotted line. The H α narrow peak fluxes were normalized to 1, for comparison. The spectra have to be multiplied by the factor given in the upper right corner to gain the flux in $10^{-16} \text{ erg s}^{-1} \text{ cm}^{-2} \text{ \AA}^{-1}$. As the broad-to-narrow H α flux ratio increases towards the outer part (Fig. 4.38), the broad lines appear to be boosted in the normalized outer spectra. In contrary to Figure 4.32, a continuum slope was subtracted before fitting the H α profile. The [N II] and [S II] lines were fitted by one narrow Gaussian only.

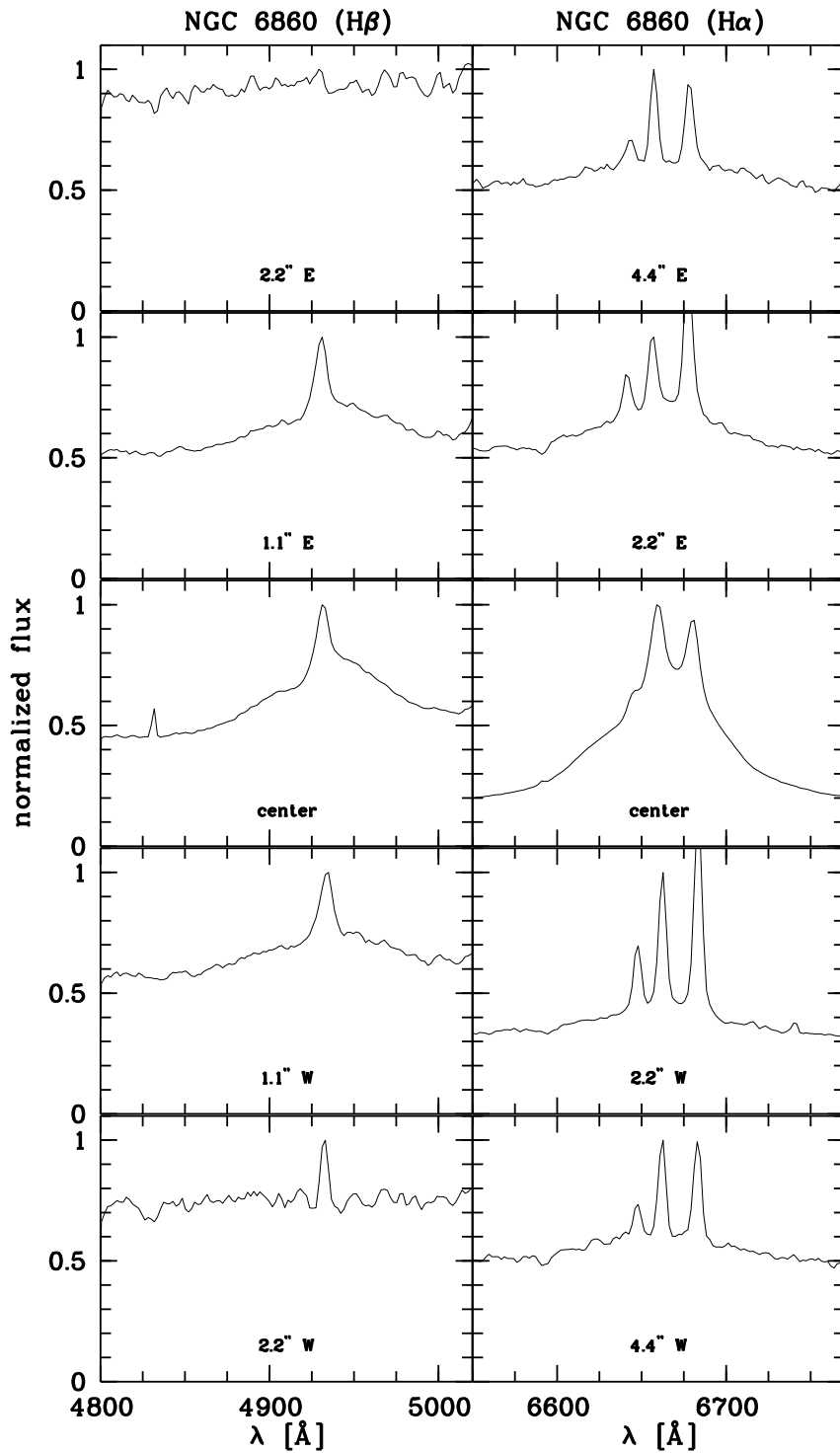


Figure 4.34: The same as in Figure 4.32 for NGC 6860. While a broad H α component is visible out to $r \sim 4''.5$ from the nucleus, a broad H β component extends out to $r \sim 1''$ from the nucleus.

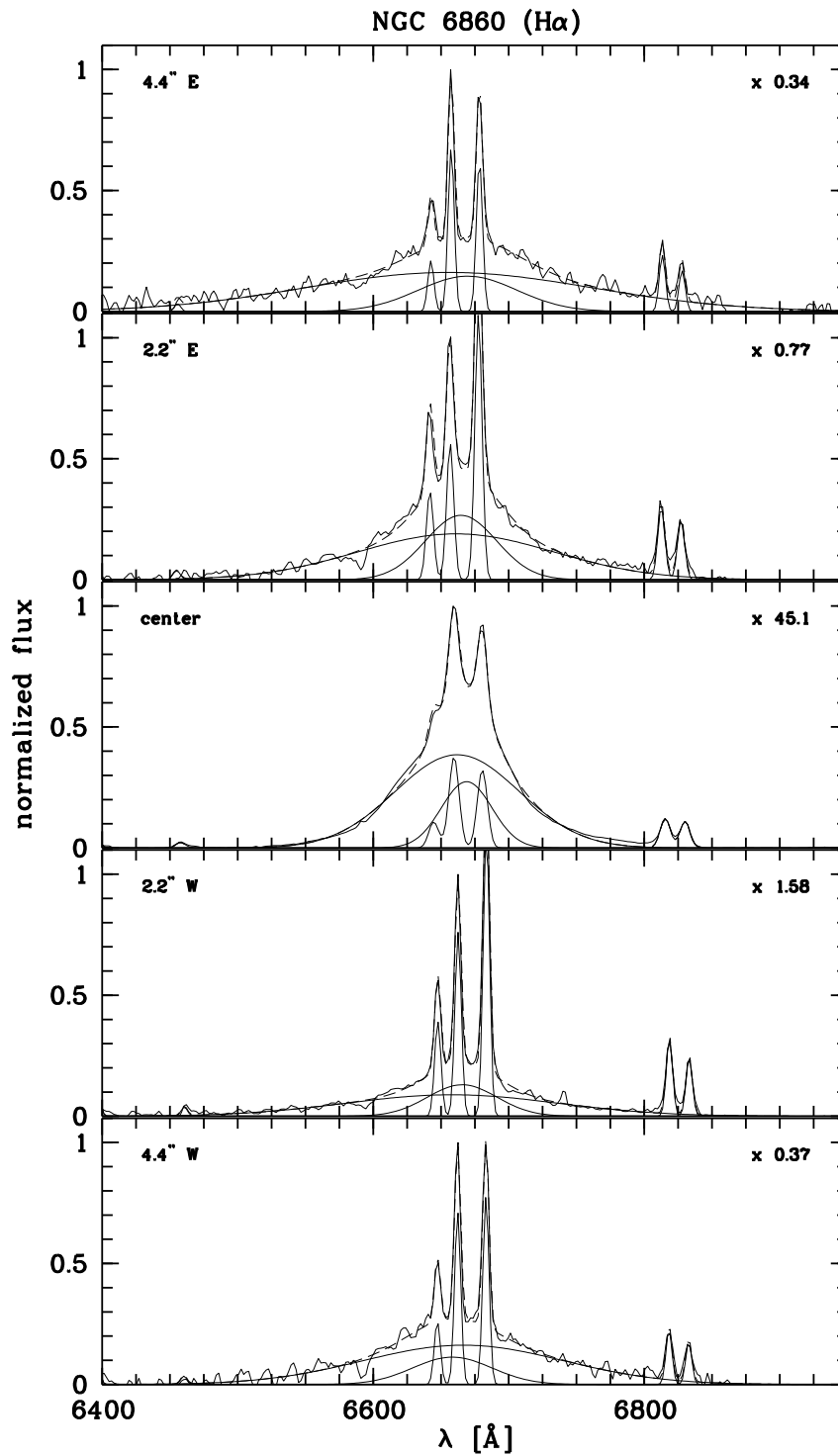


Figure 4.35: The same as in Figure 4.33 for NGC 6860. Note that in the wavelength range $\lambda 6860\text{--}6910$ Å, there are underlying telluric absorption bands.

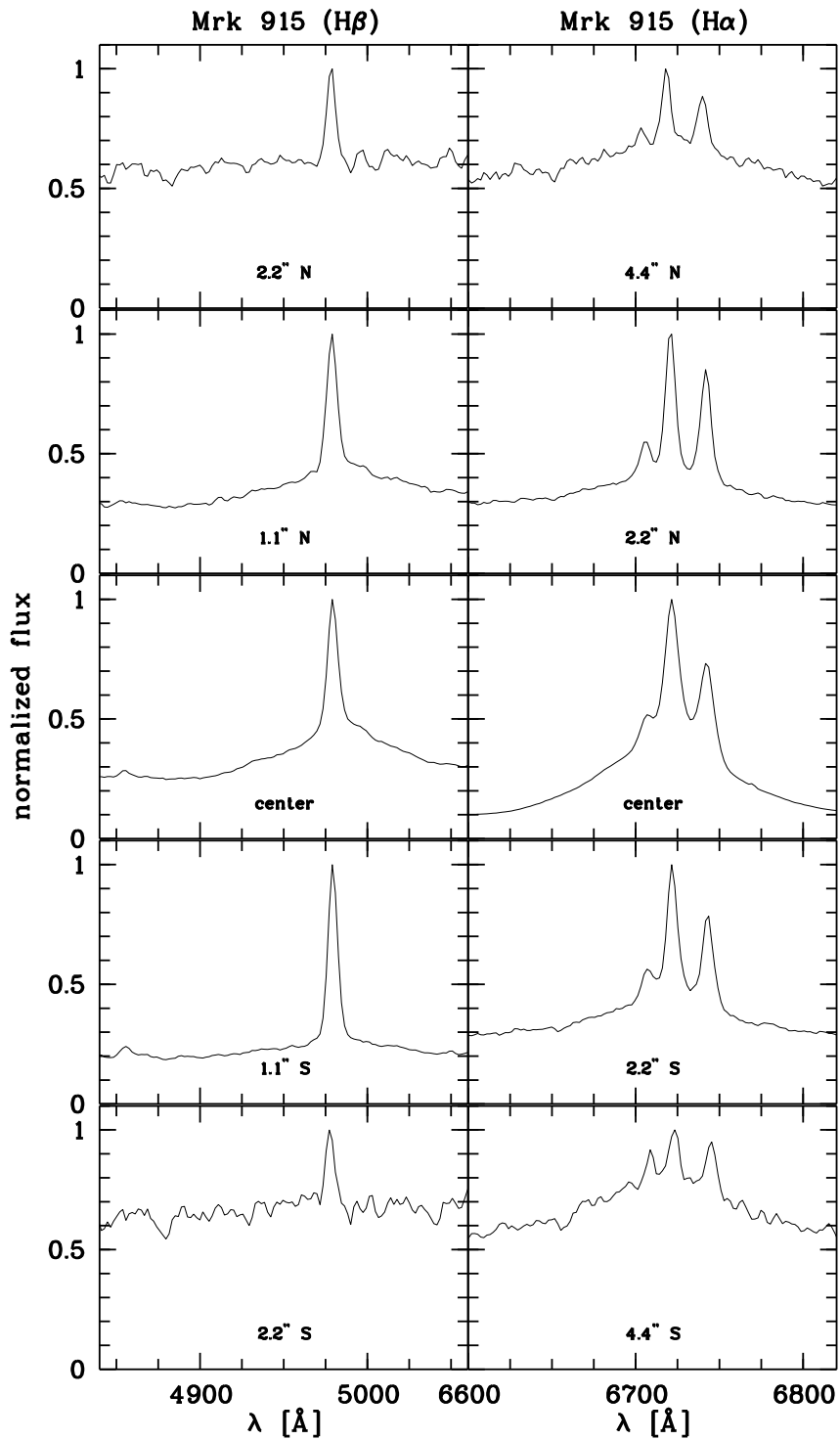


Figure 4.36: The same as in Figure 4.32 for Mrk 915. While a broad $H\alpha$ component is visible out to $r \sim 4''.5$ from the nucleus, a broad $H\beta$ component extends out to $r \sim 1''$ from the nucleus.

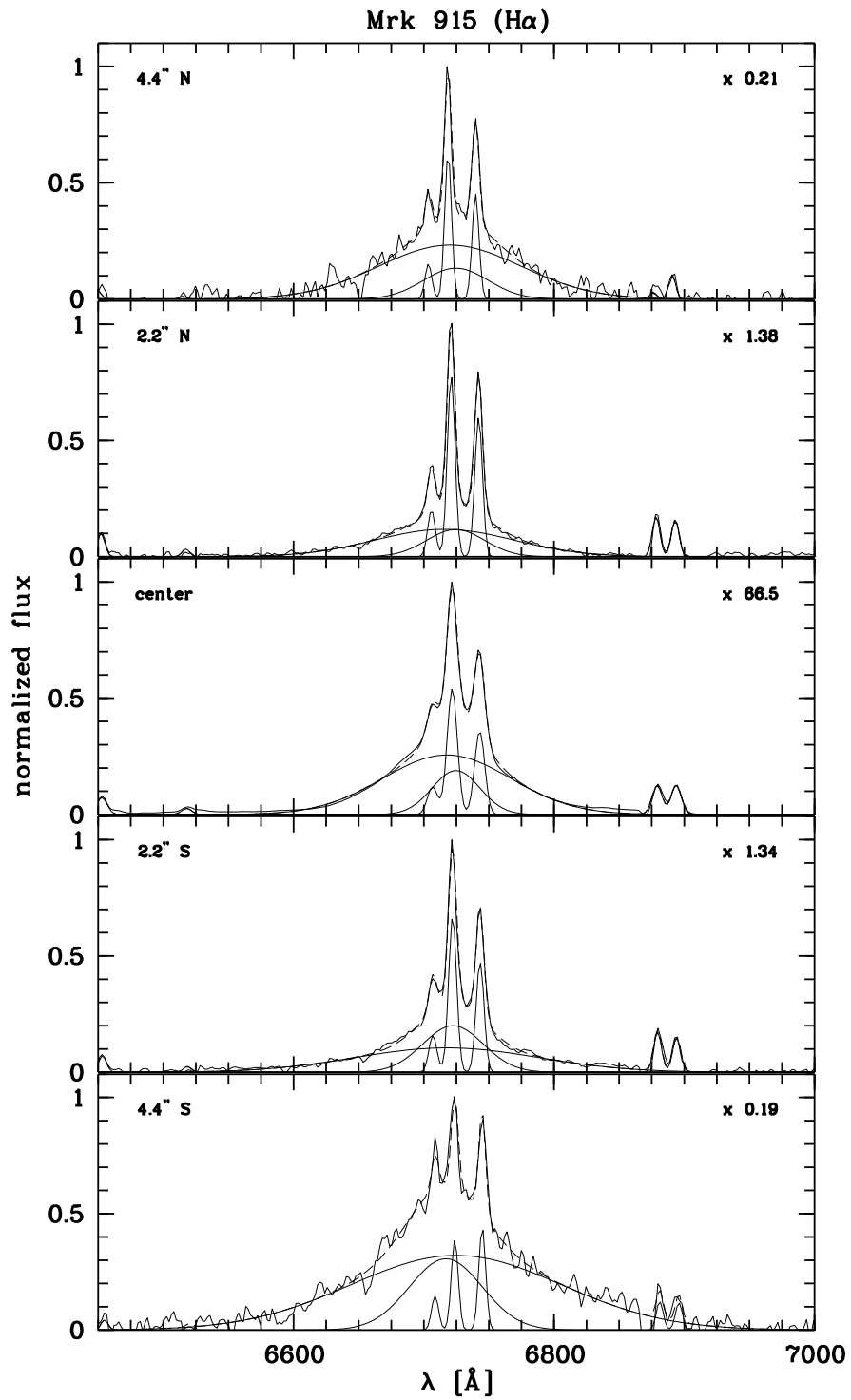


Figure 4.37: The same as in Figure 4.33 for Mrk 915.

What is the origin of the extended broad H α emission seen in Fairall 51, Mrk 951, and NGC 6860? Neither seeing nor instrumental effects can produce broad H α lines at these distances from the nucleus. We believe that the observed extended broad H α emission can directly be attributed to the objects.

The fact that we do not see the same extension in the broad H β component can originate from a combination of the low S/N which does not allow to detect an underlying broad H β line far from the nucleus (intrinsic Balmer decrement H α /H β \sim 3) and reddening, decreasing the broad H β flux relative to H α . Fitting any spurious underlying broad H β flux in those outer rows in which we still see a significant broad H α line, we estimate values of H α_{broad} /H β_{broad} $>$ 10 in all three objects. This is significantly higher than what is observed in the NLR and, moreover, also significantly higher compared to the reddening of the central BLR which is comparable to that of the NLR (H α_{broad} /H β_{broad} \sim 5).

There are three possible explanations: (i) a “real” extended broad-line region, (ii) shock induced high velocities e.g. from jet/NLR interactions and outflowing gas, (iii) scattering of the central BLR emission.

Explanation (i) is unlikely: If the broad lines indeed arise in an extended BLR, it is surprising why they arise at the same (projected) distance from the nucleus as the narrow lines do. It would imply two distinct regions at roughly the same distance from the nucleus, one with a high and one with a low velocity dispersion. In addition, the region with the high velocity dispersion creating the broad lines must have high densities to explain the fact that no broad forbidden lines are observed at the same time. [This argument is commonly used to explain the observational evidence that no broad forbidden lines are seen in the BLR; e.g. Osterbrock (1989)]. Also, the high observed reddening of the extended broad lines (H α_{broad} /H β_{broad} $>$ 10) implies a large amount of dust in this extended BLR which is not seen in the NLR at the same distance. Moreover, explanation (i) does not explain why such high velocity dispersions at these distances should occur. This could be explained by (ii), i.e. shocks from e.g. radio jets impinging on the emitting gas clouds and accelerating them to high velocities, and at the same time possibly creating high densities, resulting in collisional de-excitation of the forbidden lines. However, our observations argue against this explanation: The profile and width of the underlying broad H α line do not change with distance. Moreover, the profile is rather smooth, i.e. it does not show blue- or redshifted wings as expected for outflowing gas. In addition, an outflow scenario cannot explain why we do not see a comparable amount of broad extended H β emission. We favor explanation (iii), i.e. that the broad H α line originates from scattered light of the central BLR.

Before discussing the scattering of broad lines in detail, we want to point out that our observations of (a) no significant changes of profile and width with radius, (b) high broad H α flux in the center which is decreasing outwards ending in significant lower fluxes at a distance of 2'' from the nucleus and further out (Fig. 4.38, *left panel*), and (c) distribution of broad-to-narrow H α flux (Fig. 4.38, *right panel*) are all in agreement with the scattering scenario:

(a) If the broad extended emission arises from scattering, we do not expect changes in the profile.

(b) The high flux of broad H α emission in the center and at $\pm 1''$ distance from the nucleus can be explained by a direct view of the broad emission (plus spatial broadening by seeing and instrumental effects) and is similar to the extension of the broad H β flux.

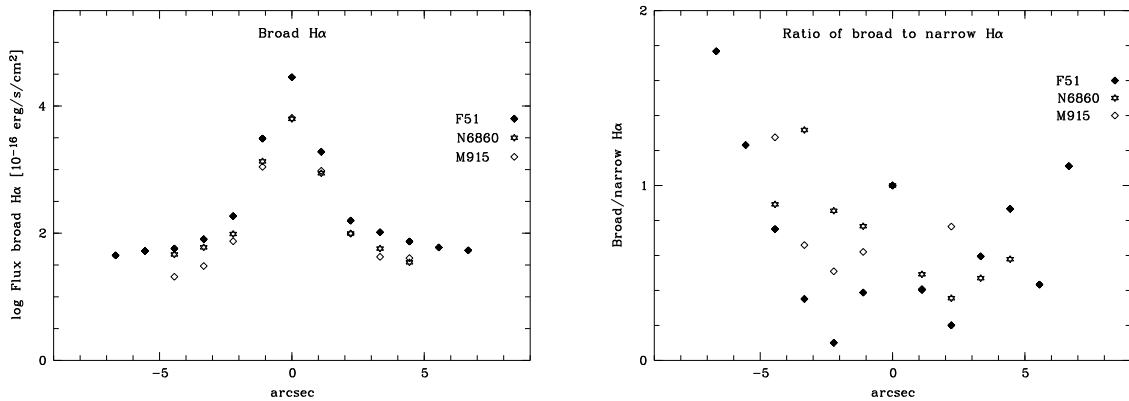


Figure 4.38: *Left panel:* Broad H α flux on logarithmic scales (in $10^{-16} \text{ ergs}^{-1} \text{ cm}^{-2}$) as a function of distance from the nucleus for all three Seyfert-1 galaxies with extended broad H α flux (filled diamonds = Fairall 51, stars = NGC 6860, open diamonds = Mrk 915). *Right panel:* Ratio of broad-to-narrow H α flux. In the center, the ratio was normalized to 1, for comparison (Fairall 51: divided by ~ 56 , NGC 6860: divided by ~ 16 , Mrk 915: divided by ~ 8). The same symbols as in the *left panel* were used.

The decrease further out can be explained by scattered broad emission.

(c) The ratio of broad H α flux to narrow H α flux peaks at the center, decreases outwards in the first 1–2'', and then increases again. In the center, we directly see the BLR, resulting in a high ratio of broad-to-narrow H α flux. In the surrounding 1–2'', the NLR emission is strong while the BLR contribution from the center, scattered by seeing and instrumental effects decreases, resulting in a decreased broad-to-narrow H α flux. Further out, the NLR emission gets fainter while the broad scattered flux remains at roughly the same level, resulting in an increase of the observed broad-to-narrow H α flux.

Scattering of broad lines

Seyfert-2 galaxies

Scattered broad lines are well known for several Seyfert-2 galaxies with BLRs hidden from direct view [e.g. Miller & Goodrich (1990), Tran et al. (1992)]. In fact, the observation of polarized broad lines was a key step in the development of the unified scheme for AGNs (Antonucci & Miller, 1985). The scattering medium is thought to be dust or free electrons, e.g. in the NLR. Dust scattering is more efficient than scattering by free electrons, but its scattering behavior is more complicated. For example, while electron scattering is wavelength independent, dust scattering seems to be in general stronger for blue than for red light [$S_\lambda \propto \lambda^{-1}$; Zubko & Laor (2000); Schmid et al. (2001)].

In the Seyfert-2 galaxy IC 5063, Wagner & Appenzeller (1989) report a broad off-nuclear emission-line region at 1''8 north-west. They interpret this emission as an extreme example of scattering with a very high intrinsic BLR emission from the nucleus.

Seyfert–1 galaxies

Several spectropolarimetric studies of Seyfert–1 galaxies have revealed polarized light in Seyfert 1s as well, although the geometry of the scattering region seems to differ from type 2s: In type 2s, the optical polarization p.a. is almost always perpendicular to the projected radio source axis [e.g. Antonucci (1983), Brindle et al. (1990)], as expected for scattering within the ionization cone (assuming that the radio source is aligned with the torus axis). This scattering is also called polar scattering. In contrast, in type 1s, the optical polarization p.a. is more often aligned with the radio axis [e.g. Antonucci (2001); Smith et al. (2002)]. A second source of polarized light in addition to polar scattering seems to be necessary. Smith et al. (2002) studied the optical polarization spectra of Seyfert 1s in detail and find in several cases polarization characteristics best explained by BLR emission arising in a rotating disc which is scattered by material in the equatorial plane of the disc. This equatorial scattering is thought to be the main source for the polarized light observed in most Seyfert–1 galaxies. However, there is growing evidence that polar scattering also occurs in Seyfert 1s (Smith et al., 2002) and can in some cases even dominate over equatorial scattering (Smith et al., 2004).

To prove our assumption of scattered broad emission in these Seyfert 1s, we searched for published spectropolarimetry measurements. For NGC 6860, no spectropolarimetric data are available and the observations of Mrk 951 are too noisy to confirm evidence of intrinsic polarization (Smith et al., 2002). But Fairall 51 is indeed one of the most highly polarized Seyfert 1s (Smith et al., 2002).

Fairall 51

Fairall 51 exhibits optical polarization characteristics which classify it as one of the rare cases in which polar scattering dominates over equatorial scattering. It is considered as prototype of this new type of Seyfert 1s with polarized emission, the so-called polar-scattered Seyfert–1 galaxies (Smith et al., 2004). Smith et al. (2004) propose the following scenario for these objects: The direct line-of-sight to the AGN passes through the upper layers of the torus which blocks the view towards the equatorial scattering region such that the polar scattering region dominates the polarized light. Thus, the scattering geometries of these objects are similar to Seyfert–2 galaxies and of special interest in terms of unification theory. In type–1 objects, such a scattering configuration with the scattering region located far from the BLR and the continuum source gives the unique possibility to see the BLR both in direct light and via the scattering region. Schmid et al. (2001) used VLT/FORS1 spectropolarimetry to study the broad-line profiles of Fairall 51 in polarized and total light. They find them to be indistinguishable concluding that the velocity field of the BLR is essentially spherically symmetric.

In their central extracted spectra, $H\beta$ shows a polarization fraction of 8.5%, while the broad $H\alpha$ flux has a lower linear polarization value of $p_{\text{obs}} \sim 5.8\%$. It is the same wavelength dependency as observed for the continuum, but about 1.6 times higher (Schmid et al., 2001). This observation may explain why we do not find extended broad $H\beta$ flux: If dust scattering is stronger for blue wavelengths, the extended broad $H\beta$ line may be scattered out of our line-of-sight in the outer regions whereas in the central part, we observe the BLR light directly. Moreover, $H\beta$ is more heavily absorbed by the scattering medium, i.e. the dust torus, than $H\alpha$. Thus, the observed ratio of broad $H\alpha/H\beta > 10$ may be explained by a mixture of scattering and absorption.

Schmid et al. (2001) do not discuss the extension of the broad emission in their paper but simply use the central $8''$ as central spectrum, indicating that they consider the broad emission to be more extended than just the few inner arcseconds. To probe this, we compared their VLT spectra taken from the archive with our NTT data focussing on the extent of the broad $H\alpha$ lines. Indeed, the FORS1 spectra do also reveal broad $H\alpha$ emission in at least the central $3''$ observed with a seeing of $0''.8$. Although this extent is significantly larger than the seeing value, it is smaller than the extension derived from our data. A possible explanation lies in the different position angles used (0° VLT compared to 140° in our NTT data). Comparing the different position angles with the HST [O III] image of Schmitt et al. (2003a) shows that the p.a. of 140° closely follows the extended [O III] emission while Schmid et al. (2001) may miss extended emission: The scattering is probably more efficient at a p.a. of 140° than at 0° , if the scattering originates from the dust torus which can be considered as roughly perpendicular to the axis of the ionization cone, in the framework of the unified scheme. This suggests that more (extended) broad-line flux may be observable along p.a. = 140° .

The special scattering geometry of Fairall 51 with polar scattering and a small scattering angle compared to equatorial scattering may give an explanation to why we see extended broad lines already in non-polarized light: The forward scattering by dust may be more efficient than scattering in perpendicular direction (as required e.g. for BLR scattering in Seyfert 2s). Our observations and comparison with polarization data of Fairall 51 suggest that we can expect a similar scattering geometry in NGC 6860 and Mrk 915. However, to finally prove this scenario, spectropolarimetry long-slit data along the same position angle are required for all three objects.

4.4.11 Differences between Type-1 and Type-2 Seyferts

Differences between the NLRs in Seyfert-1 and Seyfert-2 galaxies are known from both imaging and spectroscopy and have been discussed by various authors on the basis of the unified model [e.g. Mulchaey et al. (1996b); Schmitt (1998); Nagao et al. (2001); Schmitt et al. (2003b)].

Statistics have shown that high-ionization emission lines as well as those with high critical densities tend to be stronger in Seyfert-1 galaxies than in type 2s [e.g. Shuder & Osterbrock (1981); Schmitt (1998); Nagao et al. (2000)]. One explanation is that the highly-ionized gas clouds are located close to the nucleus and can be hidden by the dust torus (Murayama & Taniguchi, 1998a,b; Nagao et al., 2000). On the contrary, Schmitt (1998) proposed that the NLR sizes in Seyfert-1 galaxies are (intrinsically) smaller than those of type 2s (and not only due to projection effects): If the torus of Seyfert-1 galaxies is more likely to be aligned with the galaxy plane (but has random orientations in Sy2s) and the ionization cone in type-1 AGNs is thus perpendicular to the galaxy plane, there is a smaller number of ionization-bounded clouds in Seyfert-1 galaxies. Based on a sample of 355 Seyfert galaxies, Nagao et al. (2001) favor the first explanation.

General trends from nuclear spectra

Compared to the Seyfert-2 galaxies, the Seyfert 1s in our sample show on average higher iron emission line fluxes such as [Fe VII] and [Fe X] relative to $H\beta$, i.e. high-ionization lines (upper ionization potential 125 eV and 262.1 eV, respectively), as well as higher

[O III] $\lambda 4363 \text{ \AA}$ intensities, a line with a rather low ionization potential compared to these iron lines (upper ionization potential of 54.9 eV; Appendix C, Table C.2) but high critical densities ($3.3 \cdot 10^7 \text{ cm}^{-3}$; Section 4.4.1; Tables 4.8, 4.7), in agreement with the results of Nagao et al. (2001). Moreover, we find Seyfert–1 galaxies tending to have higher electron temperatures and ionization parameters in their nuclear spectra. While the central electron densities are comparable within the individual scattering, the nuclear reddening is on average higher in the six Seyfert–2 galaxies.

The difference in the flux ratio of [O III] $\lambda 4363 \text{ \AA}$ /[O III] $\lambda 5007 \text{ \AA}$ seen between Seyfert–1 and Seyfert–2 galaxies has been interpreted by Osterbrock (1978) as a difference in densities ($n_{\text{H}} \sim 10^{6-7} \text{ cm}^{-3}$ for Seyfert–1 galaxies and $n_{\text{H}} < 10^5 \text{ cm}^{-3}$ for Sy2s). However, we interpret it as a difference in temperature [$T_{e,\text{ave},4\text{Sy}1\text{s}} \sim 33600 \pm 7100 \text{ K}$ versus $T_{e,\text{ave},4\text{Sy}2\text{s}} \sim 14465 \pm 445 \text{ K}$] in agreement with the suggestions by Heckman (1979) and Cohen (1983) ($T_e > 20000 \text{ K}$ for Sy1s; $T_e \sim 10000 \text{ K}$ for Sy2s).

The higher average central ionization parameter is related to the observation of stronger fluxes of high–ionization lines in Seyfert–1 galaxies and can be explained likewise: If the high–ionization lines, along with the Balmer and [O III] $\lambda 5007 \text{ \AA}$ emission lines, originate in gas clouds close to the BLR, they may be partly hidden by the dust torus in Seyfert–2 galaxies. Our observations of higher reddening in Seyfert–2 galaxies argue in favor of this scenario proposed by Nagao et al. (2001). It is reasonable to assume that lines with high ionization potential arise closer to the photoionizing source, leading to a stratification of emission lines. This is comparable to what has been found for the BLR using reverberation–mapping: Different lines have different time lags with lines from high–ionized gas responding earlier, showing that the ionization structure is radially stratified (Peterson, 1993).

The reason that we observe comparable nuclear densities in both type–1 and type–2 Seyferts may lie in the correction of the central electron temperature: When comparing the measured electron densities directly, i.e. not correcting for the temperature, we get on average slightly lower densities for Seyfert–1 galaxies (which have the higher central temperatures): $n_{e,\text{ave},6\text{Sy}1\text{s}} \sim 825 \pm 170 \text{ cm}^{-3}$ versus $n_{e,\text{ave},6\text{Sy}2\text{s}} \sim 950 \pm 160 \text{ cm}^{-3}$. Taking into account the critical densities of the involved forbidden emission lines, we cannot rule out that the temperature we measure originates from a region closer to the center than the electron density (if the density increase towards the center): While the critical densities of the [O III] lines are high [$3.3 \cdot 10^7 \text{ cm}^{-3}$ for $\lambda 4363 \text{ \AA}$, $7 \cdot 10^5 \text{ cm}^{-3}$ for $\lambda 5007 \text{ \AA}$; Appendix C, Table C.2], they are significantly lower for the [S II] $\lambda \lambda 6716, 6731 \text{ \AA}$ lines ($1500\text{--}3900 \text{ cm}^{-3}$). It implies that while the [O III] lines are still emitted in a dense central region with e.g. $n_e \sim 10000 \text{ cm}^{-3}$, allowing us to measure the temperature close to the nucleus, both [S II] lines are collisionally de–excited. Thus, the flux we measure in these lines comes from regions with lower densities further out along our line–of–sight.

Differences in radial distributions

When comparing the results of Seyfert–1 and Seyfert–2 galaxies assuming that the unified model is valid [e.g. Antonucci (1993)], one has to take into account the different geometry, we observe either along the ionization–cone axis or perpendicular to it, and thus the differing line–of–sight integrations: The observed emission–line fluxes and ratios are line–of–sight integrations along possibly varying values. Line–of–sight integration always occurs in observational astronomy, but very often, it is not taken into account.

The integration may alter the observed spatial variations of line fluxes and ratios especially in type-1 and type-2 AGNs depending on the viewing angle. Also, the velocities represent line-of-sight integrations, in general broadening the line profiles. As the effect of the line-of-sight integration on measured velocities and line profiles has been discussed in detail by e.g. Schulz et al. (1995), we here focus on line-of-sight integrations of (i) line fluxes and (ii) line ratios and the observed variations expected for type-1 and type-2 AGNs.

Line fluxes

When discussing the line-of-sight integration of emission-line fluxes one needs to consider the two cases of optically thin and optically thick emission. For optically thick emission, we simply see the emission of the surface of the ionization cone.

However, the NLR gas can be considered as emitting optically thin.¹² In that case, we sum up the line flux emitted along our line-of-sight. (Of course, dust obscuration can still play a role in absorbing some of the emission.) For type-1 AGNs (assumed viewing angle near 0°), the central integrational path crosses the whole NLR from the border to the center. The further out we go, the shorter gets the integrational path (Fig 4.39, *left panel*). For type-2 AGNs (viewing angle near 90°), it is the opposite: Through the ionized gas at the apex of the cone the integrational path is rather short, but it increases with distance from the center (Fig 4.39, *right panel*). Relative to the extended emission, we expect to see higher emission-line fluxes in the center for type 1s than for type-2 objects. If the gas emits homogeneously, we expect to see the maximum of emission in the center for type-1 galaxies. For type-2 objects, we would expect to see two maxima in the surface-brightness distribution at the edge of the emission. However, the strength of the emission-line fluxes is most probably decreasing with distance from the center if either the gas density is decreasing and/or the photoionizing continuum comes from the central source only. Then, we expect to see two maxima in the surface-brightness distribution of type-2 objects close to the center. In practice, these two maxima may be merged into one central maximum due to the limited spatial resolution of the observations (see e.g. observed surface-brightness profiles presented in Appendix B).

To summarize, in type-2 AGNs, the line-of-sight effect with different lengths of line-of-sight integrations can balance a radial distribution effect of decreasing gas density. For type-1 objects, both effects act in the same way.

When comparing the radial distribution of (optically thin) line fluxes in type-1 and type-2 objects, one expects to find a steeper slope in type-1 objects: For type-1 AGNs, the flux is high in the center due to the long integrational path and decreases towards low values at the edge of the observed emission.

For type 2s, the central value is not as high as in type 1s, compared to the outer regions, as we integrate along a smaller emitting region. With respect to the central peak, the slope is thus shallower in type-2 objects.

Indeed, we observe surface-brightness distributions in the $H\alpha$ and $[O III]$ emission line which show a steeper slope in the Seyfert-1 galaxies in our sample. Although we observe the same trend for the continuum values, the interpretation is not as straightforward as we cannot distinguish the amount of AGN and stellar contribution to the observed continuum.

¹² The NLR flux ratios are typical of “case B” recombination, implying that only the Lyman series is optically thick and that all Balmer lines are emitting optically thin (Peterson, 2003).

Line ratios

In the previous Sections, we examined radial distributions of several values deduced from emission–line ratios: (i) reddening (4.4.2), (ii) line ratios in diagnostic diagrams (4.4.3), (iii) electron density (4.4.6), and (iv) ionization parameter (4.4.7). We here discuss the influence of different line–of–sight integrations for these parameters.

(i) In case of the reddening value derived from the emission–line ratio of $H\alpha/H\beta$, the intrinsic value is expected to be roughly constant with radius as both lines arise from recombination of the same ion and are intrinsically at a fixed ratio at a given temperature (2.87 at $T = 10000$ K for case B recombination; Osterbrock (1989), page 80). If there are large changes of temperature across the NLR, this ratio may also change intrinsically: for $T = 2500$ K it is 3.3 and for $T = 20000$ K it is 2.76. However, this change is small compared to changes due to dust (typically observed range $H\alpha/H\beta \sim 3\text{--}7$). Therefore, dust has the major influence of the measured $H\alpha/H\beta$ ratio. The dust can be distributed at any position along our line–of–sight. We do not observe a trend in the reddening distributions in our objects; rather, the distributions vary from object to object, reflecting different dust distributions. The fact that we do not observe a significant difference between type–1 and type–2 objects indicates that most of the NLR emission arises beyond any putative obscuring torus. It seems that the reddening is due to dust in the NLR or in the host galaxy and does not arise from systematic differences. However, as pointed out in the previous Section, Seyfert–2 galaxies tend to have larger nuclear reddening which may indeed be attributed to an obscuring medium in the central line–of–sight.

(ii) The line ratios in the diagnostic diagrams do not show significant different spatial distributions for Seyfert–1 and Seyfert–2 galaxies. In four out of 12 objects (2 Sy1s, 2 Sy2s), we observe a transition between AGN–typical line ratios and that typical for H II regions. Using CLOUDY photoionization modeling, we can show that the type of ionizing continuum is responsible for the radial variation of line ratios and not the radial variation of metallicity, ionization parameter, and/or electron density. The spatial distribution of line ratios in the diagnostic diagrams depends rather on the ionizing continuum than the line–of–sight integration.

(iii–iv) Electron density, ionization parameter, and temperature are derived from the intensity ratio of two forbidden lines.¹³ The emission is optically thin and all emitted flux along the line–of–sight is integrated to the total observed line flux.

Three different cases can be distinguished when considering the intrinsic flux ratios as a function of radius: (a) The intrinsic values are constant with radius [$y = f(r) = c$], i.e. the flux ratios do not change. In that case, it does not make any difference whether we observe along the line–of–sight of type–1 or type–2 AGNs. (b) For random fluctuations, the observed value is a mean over these fluctuations and it is impossible to predict the intrinsic values. (c) If a value varies intrinsically with radius [$y = f(r) \propto r^\delta$], the observed slope will differ from the intrinsic one depending on the line–of–sight. We discuss case (c) in the following.

In a first step, let’s consider the electron density as an example, assuming that the density is highest at the center and decreases with distance. Then, in the center, the

¹³ While the temperature is deduced from the $[O\text{III}]\frac{4959+5007}{4363}$ ratio, the emission lines in the numerator occur in a fixed ratio of 1:3, thus in principle only two lines are involved. Note that although we do not trace the spatial variation of the temperature, the following considerations should in principle also be valid for the temperature.

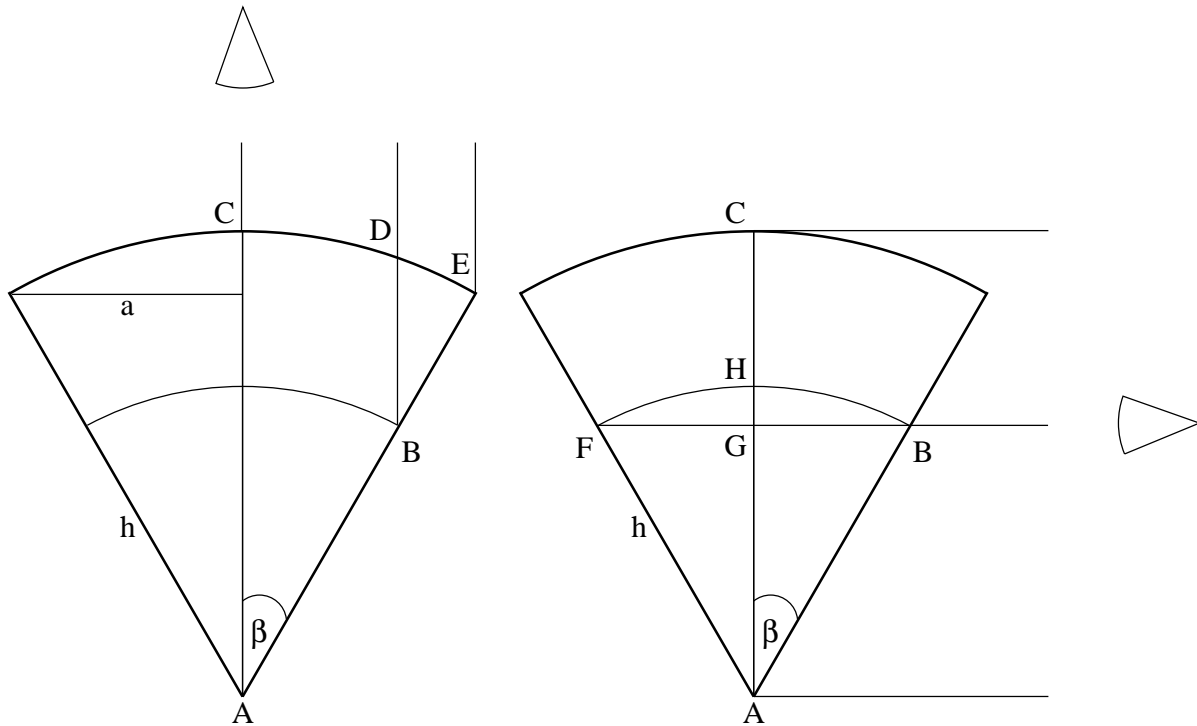


Figure 4.39: Line-of-sight integration for type-1 (*left panel*, $\iota = 0^\circ$) and type-2 AGNs (*right panel*, $\iota = 90^\circ$). The NLR gas is considered as distributed in a sphere with the emission forming a cone-like structure due to the photoionizing cone with half-opening angle $\beta = 30^\circ$.

flux in the [S II] $\lambda 6731 \text{ \AA}$ line is high compared to the flux in the [S II] $\lambda 6716 \text{ \AA}$ line (Appendix C, Fig. C.1). In the outer parts of the NLR where the density is low, the contrary is the case. The observed flux ratio now depends on the line-of-sight. For type-2 objects, the line-of-sight integration is close to the intrinsic radial variation and the observed slope is close to the intrinsic one (if β is small). For type-1 objects observed along the central line-of-sight, we integrate fluxes from both the central regions (where the [S II] $\lambda 6731 \text{ \AA}$ line is strong compared to the [S II] $\lambda 6716 \text{ \AA}$ line) and outer regions (where the [S II] $\lambda 6716 \text{ \AA}$ line is strong compared to the [S II] $\lambda 6731 \text{ \AA}$ line) and thus, the observed *averaged* line ratio indicates lower densities than the intrinsic central one. (As argued in the previous Section, our observations in principle agree with this prediction, i.e. we observe lower central electron densities for Seyfert-1 galaxies than for Seyfert-2 galaxies.) At the edge, we get close to the intrinsic value as the integrational path is short. Since the slope is measured relative to the observed central value which is in case of type-1 AGNs underestimating the intrinsic value, the slope seems to be less steep for type-1 than for type-2 AGNs.

Now, we discuss the effects of the line-of-sight integration in a more general way. We assume that the NLR gas is distributed in a sphere, photoionized in a cone-like structure (i.e. we neglect a possible NLR gas distribution in a disk as well as the influence of the host galaxy). With the viewing angle ι , we refer in the following to the angle between the observer and the ionization cone of NLR emission.

Consider the case of a type-2 object with a viewing angle towards the cone of $\iota = 90^\circ$ and a half opening angle of the ionization cone of $\beta = 30^\circ$ (Fig 4.39, *right panel*).

In the center, the line-of-sight through the cone with line emission is very small and we directly observe the intrinsic value. (We neglect the influence of the obscuring dust torus present in the center as it probably has dimensions which are negligible against the total NLR extension.) Further out, the line-of-sight length through the emitting cone increases and we observe an averaged value over a larger region. For a radially varying profile, our line-of-sight does not run exactly along the radial curve (B, H, F) but does not differ from it very much (B, G, F). At point B and F , the value added to the observed one corresponds to the intrinsic one, but for G , it has not reached the intrinsic radial one yet (H). Qualitatively speaking, the deviation results in an observed radial profile which is less steep than the intrinsic one, as the mean values smooths out the radial values. However, in general, for type-2 objects, the deviation between the observed and the intrinsic radial profile should be negligible, especially if β is small and the viewing angle is large.

For type-1 objects, it is different and comparable to what one would observe in the case of a sphere, but not as “severe” due to the cutoff at the edge of the ionization cone. Consider the same cone with $\beta = 30^\circ$ and a viewing angle of 0° (Fig 4.39, *left panel*). For the center, the measured value corresponds to the mean over the whole profile variation (A to C). Towards the outer part, there is less and less central contribution (B to D) and at the edge (E), one finally gets the intrinsic value. (Note that we do not take into account the counter half-cone below the torus plane which, if not obscured, “doubles” the observed line-of-sight integration.) The deviation between the intrinsic radial variation and the observed one can be much larger than for type-2 objects.

However, up until now, we did not take into account the different radius measurements. The distance from the center to the outer edge of the measurable NLR is always smaller for type-1 objects ($\iota = 0^\circ$) than for type-2 AGNs ($\iota = 90^\circ$): In type-1 objects ($\iota = 0^\circ$), the radius of the cone h projects to the measured NLR radius a (Fig. 4.39; *left panel*) while in type 2s ($\iota = 90^\circ$), the measured radius corresponds directly to the radius of the cone h (Fig. 4.39; *right panel*). The difference depends on the opening angle of the ionization cone: $R_{\text{NLR},2} = R_{\text{NLR},1}/\sin \beta$ (for $\iota = 90^\circ$ and $\iota = 0^\circ$, respectively). For the here assumed opening angle of 30° , the measured NLR radius is twice as large for Seyfert-2 galaxies than for Seyfert 1s. (Note that for general ι with $\iota < \beta$ for type-1 AGNs and $\iota > \beta$ for type-2 AGNs, the measured radii changes; see Chapter 3, for a calculation of the projected NLR radii.) If we now consider the slope between the central observed value and the one at the edge of the measurable NLR emission, this slope seems to be steeper for Seyfert-1 objects due to the smaller distance between the central value and the outer one. Moreover, for type-1 objects, we may not be tracing the emission-line fluxes to the same radial distance: At the outer parts, the line-of-sight integrates over a smaller volume of emitting gas (while the opposite is the case for type 2s) resulting in observable emission-line fluxes which reach the sensitivity limits earlier.

To conclude, if we assume that, intrinsically, we are dealing with the same objects which have the same radial dependency of physical parameters, we expect to observe a different radial profile between type-1 and type-2 objects just because of the differing line-of-sight integration and NLR size measurements. We expect that Seyfert-1 galaxies show a steeper slope in radial distributions of emission-line ratios than Seyfert 2s. Indeed, our observations confirm this trend: Both electron density and ionization parameter tend to show a steeper decrease with radius in Seyfert-1 than in Seyfert-2 galaxies.

However, these results and interpretations have to be taken with some caution. For one, we have a very limited number of sources. Second, in practice, not only the integration along the line-of-sight plays a role, but also the finite spatial resolution due to seeing and slit width. Depending on the distance of the object, we are averaging over a region from 50 to 500 pc depending on the object. Third, the viewing angle can range between 0° and 90° (as already hinted by the intermediate Seyfert types 1.2, 1.5, and 1.9). Fourth, our simple scheme which assumes the validity of the unified model does not consider a disk NLR distribution which may exist at least in some Seyferts in the case where the torus axis lies in the plane of the galaxy. A line-of-sight integration through NLR gas distributed in a disk depends on the intersection between the ionization cone and the NLR gas and may alter the integration. Also, large scale dust in the galaxy such as dust lanes may absorb some of the NLR emission and alter the observed radial distributions. Finally, the forbidden-line emission depends on the corresponding critical densities: As already pointed out for the electron density, we may not be tracing the intrinsic central values if the density is higher in the center and suppress the line emission by collisional de-excitation. As a consequence, we integrate only along the outer parts of the emitting region and the difference between type-1 and type-2 AGNs gets smaller.

4.4.12 Detailed Case Study of the Seyfert-2 Galaxy NGC 1386

We here discuss exemplarily the results of the nearby Seyfert-2 galaxy NGC 1386 in detail before referring to the other 11 galaxies in Section 4.4.13. We chose NGC 1386 as these results can be characterized as prototypical for our sample and moreover, it is one of the nearest known Seyfert-2 galaxy ($v_{\text{hel}} = 868 \pm 5 \text{ km s}^{-1}$, NED), allowing for a detailed study of the extended NLR down to small spatial scales ($1'' \sim 52 \text{ pc}$). These results have been summarized in Bennert et al. (2005).

Literature data

The nearby Seyfert-2 galaxy NGC 1386 has been investigated by various authors.

Weaver et al. (1991) study the extended NLR by means of groundbased imaging as well as long-slit spectroscopy with multiple slit positions. They show a 2D coverage of the inner kpc of this galaxy and discuss the overall morphology, velocity field, electron-density distribution, and ionization structure. They use the galaxy itself as stellar template to correct for underlying absorption lines. Using one diagnostic line-ratio diagrams ($[\text{O III}]/\text{H}\beta$ versus $[\text{N II}] \lambda 6583 \text{ \AA}/\text{H}\alpha$), they determine the NLR to extend $\sim 6''$ to the north and south of the nucleus while emission lines further out can be attributed to H II regions. They find an electron density which is decreasing with radius. The velocity field is interpreted in terms of a combination of a normally rotating component and a component undergoing high-velocity infall or outflow.

Mauder et al. (1992) resolve the NLR down to a linear scale of $0''.3$ ($\simeq 15 \text{ pc}$) using speckle interferometry and detect individual NLR clouds on these scales. They argue that the ionizing radiation must be absorbed on scales $< 15 \text{ pc}$ in a clumpy structure of the NLR.

H_2O megamaser emission of NGC 1386 has been detected by Braatz et al. (1997).

Ferruit et al. (2000) present HST images showing the [O III] and $H\alpha + [N II]$ emission. The images show the presence of very strong dust features, especially on the north–west side of the galaxy and in the nuclear regions. They find gradients in the $[O III]/(H\alpha + [N II])$ ratio which at least partly cannot be due to dust lanes but may correspond to a real transverse change in the excitation conditions of the ionized gas. A faint inclined ring of H II–region emission extends up to $\sim 12''$ from the nucleus with a p.a. of 25° , along the p.a. of the photometric major axis (RC3). The [O III] image is included in the study of Schmitt et al. (2003a) and presented here in Figure 4.1 (*upper panel*) with the slit position of our observation overlaid (p.a. = 5°). It traces the direction of the maximum extent in [O III] which is displaced by 20° from the host galaxy major axis and by $\sim 15^\circ$ from the extended radio emission [at 3.6 cm; p.a. = 170° ; Nagar et al. (1999)].

Spectropolarimetry does not reveal any broad polarized lines (Moran et al., 2000) as expected from a hidden broad–line region seen in reflected light. Tran (2003) classify NGC 1386 as “real Seyfert–2 galaxy” that may not contain a genuine Seyfert–1 nucleus.

Rossa et al. (2000) and Schulz & Henkel (2003) study the kinematics of the inner emission–line region in detail. Both find evidence for a regular velocity field showing clear sign of rotation. The line profiles show pronounced substructure suggestive of non–circular motions like locally expanding gas systems. Schulz & Henkel (2003) suggest a near–edge–on warped rotating spiral disk as traced by $H\alpha$ with a central velocity gradient corresponding to a Keplerian mass estimate of $\sim 5 \cdot 10^9 M_\odot$ inside 0.8 kpc.

NGC 1386 is also included in the sample of 18 Seyfert–2 galaxies studied with long–slit spectroscopy by Fraquelli et al. (2003). They present reddening and surface–brightness distributions as well as a decreasing electron density observed along a p.a. of 169° . However, their data have a significant lower S/N than our data and, moreover, they did not take into account the underlying absorption owing to the contribution of the stellar population which we show to be important.

Due to the relatively high inclination of NGC 1386 ($i \simeq 77^\circ$; RC3), the morphological galaxy type has been a matter of debate: While several authors favor S0, an Sa classification is assumed by Weaver et al. (1991). Malkan et al. (1998) give a morphological type of Sb/c based on HST imaging, noting that they may have missed bars on larger spatial scales. In RC3 (De Vaucouleurs et al., 1991), NGC 1386 is indeed classified as barred SB0 galaxy. NED also gives SB(s)0+.

Comparison with our results

A stellar template was derived at a distance of $18''$ north of the nucleus, averaged over $3''$ in spatial direction and over three pixels in spectral direction to increase the S/N. Reddening correction was applied to fit the continuum slope of the template to that in the central emission–line region.

Nuclear spectra

NGC 1386 has the highest electron temperature of our Seyfert–2 sample ($T_e \sim 15650 \pm 1500$ K) as well as the highest electron density ($n_e \sim 1545 \pm 50$ cm $^{-3}$; Table 4.9).

Also, the coronal lines have the highest flux ratio relative to $H\beta$ compared to the other type 2s (Table 4.7). The [Fe VII] $\lambda 5721, 6087$ Å emission lines are comparable to that of [O I]. We find evidence for [Fe X] $\lambda 6375$ Å contribution in the central $2''$ ($[Fe X]/H\beta \sim 0.047$ in the center, $[Fe X]/H\beta \sim 0.049$ at $1''$ to the north). The intensity of [Ne III] $\lambda 3967$ Å is even highest for the whole sample.

These high ratios may at least partially be due to the high spatial resolution (52 pc'' compared to a typical range of 100–500 pc'' of the other Seyfert-2 galaxies in our sample) which allows us to measure the iron contribution of a smaller central region where it is high compare to H β . Indeed, the ratios decreases when calculating the iron-to-H β ratios of a larger region: In the central 250 pc, the ratios are on average 65% of those in the central 52 pc. However, they are still high compared to the other Seyfert-2 galaxies in our sample.

Reddening distribution

As already noted by Weaver et al. (1991), the continuum gets steadily redder towards the nucleus (Fig. 4.12, *top left panel*). The reddest continuum slope is found 1'' north of the nucleus. We observe a significant drop 3–4'' north of the nucleus not reported by Weaver et al. (1991). It can be directly attributed to a “blue” continuum seen 3'' north of the nucleus in the [F547M/F791W] color map by Ferruit et al. (2000). The blue continuum is associated with the northern tip of the central emission-line structure in the [O III] image (Fig. 4.1, *upper left panel*).

The reddening value obtained from the emission-line ratio H α /H β does not show a comparable regular distribution (Fig. 4.12, *top right panel*). The reddening of the continuum slope covers a range of ~ 0.3 mag in $E_{(B-V)}$, while a three times larger range is covered in the reddening distribution derived from the recombination value ($\Delta E_{(B-V)} \sim 1$ mag).

As pointed out above when discussing the general trend of the reddening distributions (Section 4.4.2), a direct comparison of the absolute values of $E_{(B-V)}$ is not possible as the reddening determined from the continuum slope is a value relative to the reddening of the outer region in the galaxy, i.e. the template. The smaller dispersion of $\Delta E_{(B-V)}$ found from the continuum slope hints extinction by foreground dust in e.g. the host galaxy which affects both the template and the central spectra and thus do not reflect in the relative reddening value. The different reddening distributions with higher values derived from the narrow emission line ratio indicate that the stellar population and the NLR are suffering different dust extinctions with the most probable explanation being dust intrinsic to the NLR clouds which varies locally.

Spatially-resolved spectral diagnostics

While [O III] emission (S/N > 3) is seen out to a distance of $r \sim 12''$, only the inner $r \sim 10''$ can be used to study line ratios (Table 4.10). In Figure 4.15 (*left panels*), we present three diagnostic diagrams of NGC 1386. The line ratios of the central regions up to 6'' lie in the AGN regime (0, A/a – F/f). The outer line ratios extending to 10'' (G/g – J/i) all lie in the lower left corner usually covered by H II regions. This is a rather sharp transition which can be interpreted as the edge of the AGN photoionized region, i.e. the NLR, occurring at a radius of 6'' (~ 310 pc), while emission extending to 10'' originates from circumnuclear H II regions. These H II regions can be attributed to the H II regions seen by Tsvetanov & Petrosian (1995) in their groundbased H α + [N II] image (classified as H α emission peaks), occurring at distances of $r \sim 6$ –11'' along a p.a. of 5°.

Our results agree with that of Weaver et al. (1991) who report an NLR extension of $\sim 6''$ based on the third diagnostic diagram. In the first and second diagnostic diagram, their data only include the nuclear region due to the faintness of the involved [O I] and [S II] lines in the outer regions.

In their third diagnostic diagram, Weaver et al. (1991) find some evidence for high $[\text{N II}]/\text{H}\alpha$ plus low $[\text{O III}]/\text{H}\beta$ ratios typical for LINERs surrounding the highest ionization gas near the nucleus. Our data do not show LINER-type ratios. The discrepancy between the two results may arise from different stellar templates used (see following Section).

Compared to pure imaging, using diagnostic diagrams to determine the NLR size has the advantage to be less sensitive to flux depth and to exclude contributions of circumnuclear starbursts. Comparing the NLR size (radius $6'' = 310$ pc) determined from our diagnostic diagrams with literature values, we find that it is twice as large as the one found by Schmitt et al. (2003a) ($3''$, Fig. 4.1, *upper panel*), possibly due to the low sensitivity of the HST snapshot survey (short integration time of 800 s using the 2.4 m HST mirror compared to 1800 s with the 8 m VLT mirror and a 20 times larger pixel size¹⁴). Fraquelli et al. (2003) detect line emission which they classify as extended NLR out to a distance of $\sim 10''$ from the nucleus. However, our analysis shows that the extended emission between $6''$ and $10''$ (~ 310 – 520 pc) originates from circumnuclear H II regions and cannot be attributed to the NLR. Note that the total $[\text{O III}]$ emission with a $\text{S/N} > 3$ in our spectra covers a region extending out to $r \sim 12''$, but only the central $r \sim 6''$ can be attributed to the NLR.

As already pointed out by Weaver et al. (1991), the sharp transition can be interpreted as a real physical transition between the AGN powered NLR and the surrounding H II regions in the disk. H II regions may be present over the entire emission-line region but inside a distance of $6''$, the AGN ionization dominates. Therefore, it is reasonable to define the radius determined from the transition seen in the diagnostic diagrams as the size of the NLR. This conclusion is further supported by photoionization models presented in Section 4.4.4.

Influence of stellar template

To probe the general influence of the stellar template used, we carried out two approaches of (i) removing the weak emission lines of $[\text{O II}]$, $[\text{O III}]$, and $[\text{N II}]$ still visible in the template and (ii) not using any template at all.

If we remove the weak emission lines in the stellar template (approach i), the resulting line ratios are the same within the errors for most rows, i.e. the weak emission is negligible against the strong NLR emission. The exceptions are two outer rows (H, I) which are shifted towards higher $[\text{N II}]/\text{H}\alpha$ values and now lie at the edge between H II region and LINER region. This is a possible explanation for the discrepancy between our results and that of Weaver et al. (1991) who find LINER-type line ratios in the outer region. They modified their stellar template derived from the galaxy by removing the remaining weak $[\text{N II}]$ and $\text{H}\alpha$ emission and replacing $\text{H}\alpha$ by an artificial absorption line. This is a more physical approach than method (i), i.e. not only removing the remaining weak emission, but at the same time deepening the $\text{H}\beta$ and $\text{H}\alpha$ absorption trough. The true absorption will probably be underestimated due to weak emission in these lines.

However, such a correction is difficult to estimate and the $\text{H}\alpha$ absorption used by Weaver et al. (1991) probably still underestimates the true absorption.

We decided to not remove the weak emission: On the one hand, increasing the observed $[\text{O III}]$ and $[\text{N II}]$ emission by clipping the weak emission in the template and at the same time increasing the observed $\text{H}\alpha$ and $\text{H}\beta$ emission by deepening the absorption

¹⁴ Note, however, that the HST observations were an imaging campaign while we carried out spectroscopy, thus these values are not directly comparable.

lines in the template will result in approximately the same line ratios and thus will not have a great influence on the diagnostic diagrams. On the other hand, the weak emission lines are attributable to ionized regions around young stars in the galaxy lying along our line-of-sight and do not originate from the NLR emission. Thus, they truly contaminate the NLR emission and need to be subtracted.

Applying no correction for underlying absorption at all (approach ii) yields extremely large $[\text{O III}]/\text{H}\beta$ values (≥ 25) near the nucleus as has already been pointed out by Weaver et al. (1991). In the outer parts, the absorption trough is clearly visible with a small $\text{H}\beta$ emission peak in the center. In addition, the spectra show galaxy absorption features which accompany the absorption in $\text{H}\beta$. These findings show the need for correcting the stellar absorption lines using a suited stellar template.

Surface-brightness distribution

In Figure 4.24 (*upper left panel*), we present the surface-brightness distribution of the $[\text{O III}]$ and $\text{H}\alpha$ emission line as well as of the continuum (at 5450–5700 Å). The surface-brightness distributions are similar to each other, centrally peaked and all decreasing with distance to the nucleus. They reveal a secondary peak $\sim 3''$ north of the nucleus and a slightly lower tertiary peak $\sim 4''$ south of the nucleus. While the $[\text{O III}]$ surface brightness is exceeding that of $\text{H}\alpha$ in the central parts, this behavior changes at the edge of the NLR as determined from our 2D diagnostic diagrams (indicated by the dotted lines).

For comparison, the $[\text{O III}]$ surface-brightness distribution from the HST image of Schmitt et al. (2003a) is also shown (shifted by $\log L_{[\text{O III}]} = -3$). It was derived by averaging three vectorplots along the major axis of the NLR emission along p.a. = $5^\circ \pm 1^\circ$. It clearly shows the higher spatial resolution of the HST image ($0''.0455 \text{ pix}^{-1}$) compared to the $1''$ spatial sampling of our spectral data. It once again reveals the low sensitivity of the HST image compared to our spectroscopy as it detects $[\text{O III}]$ emission at a S/N of 3 only out to 3–4'' from the nucleus. The HST $[\text{O III}]$ surface-brightness distribution reveals several subpeaks of possibly individual NLR clouds, as can be already seen in the $[\text{O III}]$ image (Fig. 4.1, *upper left panel*). These substructures are smoothed out in the ~ 20 times lower spatial resolution of our spectra.

Electron-density distribution

The electron density is highest at the nucleus with $n_e \simeq 1540 \text{ cm}^{-3}$ and decreases outwards down to the low-density limit (assumed to be 50 cm^{-3} ; Fig. 4.26, *top left panel*). A secondary peak can be seen at a distance of $6''$ to the north of the nucleus ($n_e \simeq 670 \text{ cm}^{-3}$).

Comparing the position of the observed northern n_e peak with the 2D electron density distribution of Weaver et al. (1991), the closest data point is at $\sim 6''.5$ north-east from the center at roughly a p.a. of 3° with $n_e \leq 100 \text{ cm}^{-3}$ (their Fig. 10d). The spatial distance between this data point and our n_e peak at $6''$ north of the center is $\sim 0''.5$ ($\sim 25 \text{ pc}$). Thus, the n_e peak observed in our spectra may be attributed to an individual NLR cloud or local density inhomogeneities which our line-of-sight happens to pass.

Mauder et al. (1992) also detect individual NLR clouds using speckle interferometry and conclude that the ionizing radiation must be absorbed on scales $< 15 \text{ pc}$ in a clumpy structure of the NLR.

Interestingly, the peak occurs at the edge of the NLR. Another, but significantly smaller peak at the southern edge is also visible ($n_e \simeq 210 \text{ cm}^{-3}$).

We applied a power-law fit to estimate the radial dependency: The best fit with $n_e = n_{e,0} \cdot r^{-\delta}$ was derived with δ between 1 and 2 for the electron density (Fig. 4.26; $\delta \sim 1.23$, Table 4.12), neglecting the data point $6''$ north of the nucleus which may have another origin.

Ionization-parameter distribution

While Weaver et al. (1991) propose a decreasing ionization parameter to explain the observed line ratios in NGC 1386, we can determine the ionization parameter directly and indeed find that it is decreasing with distance from the nucleus (Fig. 4.28, *top left panel*). It varies between $U_{\log(n_e)=3} = (2.83 \pm 0.01) \cdot 10^{-3}$ and $2.4 \cdot 10^{-4}$ within the NLR with the highest value in the center. It reveals a secondary peak at $4''$ to the north of the center which is at the north edge of a “blob” of emission clearly visible in the [O III] image from Schmitt et al. (2003a) (Fig. 4.1, *upper left panel*). Compared to the electron density, the secondary peak is $2''$ closer to the nucleus and significantly broader.

We estimated the general dependency of the decrease of U on r . The best fit of a power-law function with $U(r) = U_0 \cdot r^{-\delta}$ is derived with $\delta \sim 1$ (Fig. 4.28, *upper left panel*), again neglecting the “northern peak”. When including all data points out to $6''$, the slope flattens ($\delta \sim 0.6$; Table 4.13).

The ionization parameter was determined with a reddening correction of the observed [O II]/[O III] ratio using the recombination value $H\alpha/H\beta$. However, there is a clear difference between the reddening of the continuum slope and that determined from the Balmer decrement: While the reddening distribution determined by the ratio $H\alpha/H\beta$ shows a rather random distribution, the continuum slope reddening steadily increases towards the nucleus with the exception of the blue continuum at $3-4''$ to the north of the nucleus (Fig. 4.12, *upper left panel*). Can these differences explain the observed slope of the ionization parameter, i.e. the general decrease with radius and the secondary peak at that position at which we see a blue continuum? Is it possible that we did not correct for the reddening intrinsic to the NLR gas by using the reddening value determined by recombination lines but would the continuum slope be a better tracer for the reddening distribution? To probe the difference, we used the reddening determined from the continuum slope to correct the observed [O II]/[O III] emission-line ratio. The resulting ionization-parameter distribution changes only slightly showing an even steeper increase towards the center and a more pronounced secondary peak (Fig. 4.28, *upper right panel*).

Thus, the observed slope in Fig. 4.28 (*upper left panel*) is not an artefact due to a “wrong” reddening correction from the recombination value: Using the reddening determined from the continuum slope, the ionization-parameter distribution does not flatten but, in contrary, steepens. The general conclusion of a decreasing ionization parameter with radius which shows a secondary peak $3-4''$ north of the nucleus remains unchanged. However, we consider the recombination value $H\alpha/H\beta$ as a better indicator of the reddening distribution within the NLR as it uses emission lines originating in the NLR itself. We suggest that the differences in the reddening measurements originate from locally varying dust within the NLR.

Northern Peak in NGC 1386: Evidence for Shocks

Our observations show that both the electron density and the ionization parameter are decreasing with radius. They show a secondary peak $\sim 6''$ and $4''$ north of the center, respectively. The peak at $4''$ is close to the northern tip of the [O III] emission (Fig. 4.1, *upper left panel*).

In the same region, a blue continuum is observed, indicating low extinction [Fig. 4.12, *upper left panel*, see also Ferruit et al. (2000)].

Can both the increased density and the ionization parameter originate from a shock of a radio jet? Extended radio emission is found to be displaced by $\sim 15^\circ$ to the observed slit p.a. tracing the major [O III] extension [p.a._{radio} 170° versus p.a._[OIII] 5° ; Nagar et al. (1999)]. A scenario in which the outflowing material causing the radio emission compresses the line-emitting gas by shocks, increasing the ambient density, seems to be rather common for Seyfert galaxies [e.g. Capetti et al. (1996); Falcke et al. (1998)]. While the shock front results in a locally increased density, the continuum of the shock can possibly ionize a larger area of the surrounding medium and produce a change in the observed line ratios, resulting in an U bump which is broader than the sharp peak of n_e . Fast autoionizing shocks can produce such a local continuum ionizing the surrounding medium (Dopita & Sutherland, 1996).

To check the shock scenario, we searched for high-ionization emission lines (e.g. [Fe X] $\lambda 6375 \text{ \AA}$). In the nuclear spectra, we find strong [Fe VII] $\lambda 5721 \text{ \AA}$ and [Fe VII] $\lambda 6087 \text{ \AA}$ emission, comparable to that of [O I]. We find evidence for [Fe X] contribution in the central $2''$ ([Fe X]/H β ~ 0.047 in the center, [Fe X]/H β ~ 0.049 at $1''$ to the north) and at $6''$ ([Fe X]/H β ~ 0.049), i.e. at the same region where we observe an increased electron density.

The observed minimum in the reddening of the continuum slope roughly $3\text{--}4''$ north of the nucleus (Fig. 4.12, *upper left panel*) could be mimicked by an additional local continuum contribution. The extinction in the NLR measured from the H α /H β value reaches a minimum at $6\text{--}7''$ north of the nucleus (Fig. 4.12, *upper right panel*). This can be explained by the destruction of dust by local shocks.

To conclude, we find several signs of shocks in NGC 1386. A radio jet interacting with the NLR gas is a plausible explanation for the northern peak observed in the electron-density and the ionization parameter distribution.

NLR versus stellar velocity curve

Both, the gaseous and the stellar velocity curves, have a similar shape (Fig. 4.30, *upper left panel*). The velocities derived from the emission of [O II], H β , and [O III] also show a curve similar to that of H α , [N II]. The stellar velocity curve covers an overall smaller range of $\sim (720\text{--}940) \pm 20 \text{ km s}^{-1}$, while the emission lines show velocities ranging from $\sim (690\text{--}990) \pm 20 \text{ km s}^{-1}$. We define the kinematical center by taking the symmetry center of the outer portions of the velocity curve. The kinematical centers of the stellar and gaseous velocity curve are slightly displaced to each other and the photometrical center (“0” on the spatial scale): While the kinematical center of the NLR velocity curve is $\sim 0''.5$ south of the optical nucleus, the stellar velocity curve has its kinematical center $\sim 1''$ north of the nucleus. The offset of the stellar kinematical center from the photometrical center is in agreement with the analysis of the H α peak velocity field by Weaver et al. (1991) and Schulz & Henkel (2003) who report an offset of the kinematical center of $\sim 1''$ north-east of the optical nucleus. The kinematical center is suggestive of a hidden nucleus residing $1''$ north of the optical nucleus (Rossa et al., 2000).

However, the kinematical center obtained from the NLR velocity curve obtained at a p.a. of 5° [compared to 23° of Schulz & Henkel (2003)] is not displaced in the same direction but $\sim 0''.5$ south of the optical nucleus. It may be indicative of a disturbed velocity field from outflows or shocks at our observed slit orientation.

While the kinematics of the emission-line region in NGC 1386 has been investigated by several authors, an interpretation of the observed velocity field is not unambiguous. Though the natural explanation is that of a slightly projected rotation curve from an inclined emission-line disk in the center, an interpretation by a clean bipolar flow accidentally aligned with the kinematical major axis of the rotating disk is also possible (Schulz & Henkel, 2003). However, as the velocity curves of both NLR gas and stars are similar, a bipolar outflow of the NLR is rather unlikely as it had to be decoupled from the stellar gravitational field and its accordingly stratified interstellar medium.

Instead, the NLR seems to follow the stellar rotation indicating that the NLR gas is distributed in the galaxy's disk rather than a sphere. Galactic rotation of narrow-line gas seems not to be uncommon [e.g. Schulz & Henkel (2003); Bennert et al. (2004a)]. Mulchaey et al. (1996b) propose that the NLR gas is distributed in a disk to explain differences of the observed NLR structure with that expected from the unified model in the case of a spherical distribution of the NLR gas.

The gaseous velocity curve does not show a different behavior in the NLR ($r < 6''$) and H II-region regime ($r > 6''$). This indicates that the NLR does not consist of a gas component with its own kinematic, but is ambient gas in the galaxy disk, photoionized by the AGN.

Our results reveal some differences between the stellar and the NLR velocities in NGC 1386. The NLR velocities are in general higher than those of the stellar absorption lines. The difference is pronounced in both the outer southern and northern part of the NLR. These differences can be due to many effects, e.g. rotating gas disk/ring within a kinematically hotter stellar component, gas moving along elliptical streamlines in a barred potential, or outflow/jet interaction.

4.4.13 Comments on Individual Objects

We searched the available literature for the other 11 Seyfert galaxies in our sample and here summarize the most important results and compare them with our study.

NGC 3281

Literature data

The morphological classification of NGC 3281 given by NED is SAB(rs+)a. Márquez et al. (1999) clearly see a weak bar in their near-infrared images. The inclination of the galactic disk is relatively high ($i \sim 66^\circ$).

Durret & Bergeron (1988) discover an extended ionized envelope of $d \sim 21''$ in NGC 3281. They find a large reddening value of $E_{(B-V)} = 0.78$ mag in the nuclear region. The derived electron temperature equals to 28000 K in the high excitation zone.

NGC 3281 has been classified as a proto-typical Seyfert-2 galaxy by Storchi-Bergmann et al. (1992b) as it clearly shows features expected from the unified model: an ionization cone, heavy obscuration towards the (hidden) nucleus, a wind outflow along the cone, and emission-line ratios consistent with photoionization by a power-law continuum. They carried out the most extensive study of NGC 3281 including direct images in continuum, [O III], and $H\alpha + [N II]$ as well as long-slit spectroscopy at 13 slit positions covering a region of $9''$ radius with a p.a. of 137° .

The [O III] emission resembles the projection of a cone extending to high latitudes relative to the plane of the galaxy by $\sim 9''$ from the apex to the north-east edge. South-west of the cone, another blob of emission is visible, possibly from the counter cone largely obscured by dust in the galactic disk. The excitation map shows that either the reddening decreases from south to north or the excitation increases. The reddening distribution indicates that the nucleus is hidden by a dust lane. This is strengthened by nuclear spectra which show no dilution by a featureless continuum. The stellar population is old and typical of early-type galaxies. An S2 template from synthetic spectra by Bica (1988) was used to subtract the absorption lines and reddened to match several spectra which were heavily reddened. The stellar population seems not to vary much in the inner $22'' \times 10''$ region as suggested from the uniform equivalent width of absorption lines with the exception of Na I D. Storchi-Bergmann et al. (1992b) interpret this observation by additional contribution to Na I D from interstellar absorption: Loci of higher Na I D equivalent widths correspond to regions with high $E_{(B-V)}$. The electron densities are found to be highest around the apex of the cone and decreasing with distance. The gaseous velocity field reveals a rotational pattern. Under the assumption that the visible spiral arms are trailing, they conclude that the south-west is the near and the north-east is the far side of the disk. A dust lane south-west of the nucleus confirms that scenario. Residual velocities indicate an outflow from the nucleus at 150 km s^{-1} within the cone. This interpretation is supported by double-peaked [O III] profiles within the cone. The emission-line ratios are well described by photoionization models with varying ionization parameter. It seems that the ionization parameter increases away from the apex along the axis of the cone, possibly due to a decrease of the density faster than r^{-2} .

The HST [O III] image resembles the groundbased one (Schmitt et al., 2003a). It reveals a conically shaped NLR with opening angle of $\sim 80^\circ$ towards the north-east. The emission extends by $6''.1$ towards the north-south direction and $3''.9$ along the cone axis. Compared to the groundbased image, this extension is less than half the one measured by Storchi-Bergmann et al. (1992b). This discrepancy is explained by Schmitt et al. (2003a) by the limited field-of-view of the linear-ramp filter ($\sim 13''$), but can also be due to less sensitivity of the 800 s exposure taken with the 2.4 m HST mirror compared to the 900 s exposure using the 4 m CTIO telescope. The counter ionization cone is mostly hidden by the host galaxy disk and only seen as a small blob of emission $4''.5$ south of the nucleus. The [O III] emission is nearly perpendicular to the photometric major axis of the host galaxy (p.a. = 140° , RC3).

Vignali & Comastri (2002) study the broad-band X-ray spectrum of NGC 3281, revealing its Compton-thick nature. The nuclear continuum is heavily absorbed (column density $\sim 2 \cdot 10^{24} \text{ cm}^{-2}$).

Comparison with our results

We used a p.a. of the long slit of 31° to trace the extended [O III] emission (Fig. 4.1, *upper right panel*).

The [O III] line emission at a S/N > 3 can be traced out to a distance of $r \sim 9''$ from the nucleus, i.e. three times as far as the maximum radius seen in the HST [O III] image of Schmitt et al. (2003a). It is comparable to what has been found by Durret & Bergeron (1988) and Storchi-Bergmann et al. (1992b).

Line ratios with a S/N > 3 have been measured in the central $r \sim 5''$, showing values typical for AGN ionization in all three diagnostic diagrams.

(As example, the third diagram is shown in Fig. 4.18, *top left panel*). Thus, the NLR extends out to at least $r \sim 5''$ from the optical nucleus.

A stellar template obtained at a distance of $11''$ south–west from the nucleus was used to subtract the stellar absorption lines (averaged over a spatial region of $1''.5$ and in spectral direction by three pixels to increase the S/N).

The nuclear line intensity ratios relative to $H\beta$ are comparable to those of the other Seyfert–2 galaxies in our sample (Table 4.7). However, NGC 3281 has the lowest nuclear electron density of the type–2 sample ($n_e \sim 540 \pm 40 \text{ cm}^{-3}$; Table 4.9). In addition, the ionization parameter determined in the nuclear spectrum is rather low ($U_{\log(n_e)=3} \sim (2.3 \pm 0.02) \cdot 10^{-3}$). The central temperature is also the lowest observed one with $T_e \sim 13715 \pm 440 \text{ K}$. This is significantly lower to what has been reported by Durret & Bergeron (1988) ($T_e \sim 28000 \text{ K}$).

The reddening determined from the $H\alpha/H\beta$ line ratio is highest at $1''.5$ south–west of the optical nucleus ($E_{B-V} \sim 0.64 \text{ mag}$) and decreases outwards to a minimum in the south–east (Fig. 4.12, *middle right panel*). From $3''$ north–east on, it increases again slightly. The reddening determined from the continuum slope shows a similar distribution (Fig. 4.12, *middle left panel*). It also peaks at $1''.5$ south–west with a relative value of $E_{B-V} \sim 0.3 \text{ mag}$. Outwards, it decreases in both directions. The similarity indicates that both the continuum and the emission lines are suffering extinction from foreground dust, e.g. the dust lane seen south–west of the nucleus (Storchi–Bergmann et al., 1992b).

The surface–brightness distributions fall smoothly with distance from the center and show a secondary peak at $3''$ north–east of the nucleus in the emission lines (Fig. 4.24, *top right panel*). In the outer parts south–west of the photometric center, the $H\alpha$ surface brightness approaches the value of $[O III]$, indicating that the NLR may end somewhere close by. Unfortunately, we are limited by the S/N to observe a transition towards H II regions. The HST $[O III]$ surface–brightness distribution reveals substructure and shows the secondary peak $3''$ north–east of the nucleus more clearly. However, it does not extend to the same distance but is limited to the central $\sim 6''$.

In Figure 4.26 (*upper right panel*), the electron–density distribution in NGC 3281 is shown. It peaks at the center and decreases slowly outwards down to $n_e \sim 110\text{--}240 \text{ cm}^{-3}$, in agreement with the results of Storchi–Bergmann et al. (1992b).

The ionization parameter presented in Figure 4.28 (*middle left panel*) reaches the maximum value at $3''$ north–east of the center, coinciding with the secondary peak in the emission–line surface–brightness distribution. While it has a value of $U_{\log(n_e)=3} \sim 2.3 \cdot 10^{-3}$ at the center, it increases to $U_{\log(n_e)=3} \sim 4.2 \cdot 10^{-3}$ in the north–east. The increase towards the north–east is in agreement with the results of Storchi–Bergmann et al. (1992b), but they also find an increase towards the south–west which we cannot confirm. It seems that this increase starts at a distance $>5''$ south–west from the nucleus where we do not trace the ionization parameter any more due to limited signal. As the electron density does not drop off faster than r^{-2} [neither in our observations nor in those of Storchi–Bergmann et al. (1992b)], this straightforward explanation of the observed increasing ionization parameter with distance can be ruled out. Storchi–Bergmann et al. (1992b) suggest that the gas near the apex of the cone where the reddening is large sees a partially obscured nuclear ionizing source, resulting in a low ionization parameter. Comparing CLOUDY photoionization modeling with the observed emission–line ratios, they rule out shocks as primary ionization mechanism. Moreover, no extended radio emission is observed which could hint the existence of radio jets (Schmitt et al., 2001).

Our observations do not help to further elucidate the origin of the increased ionization parameter towards the north-east.

We do not see double-peaked [O III] emission within the cone (i.e. from the center towards the north-east), probably due to the low spectral resolution. Indeed, the profiles are very broad in the center and out to $\sim 3''$ north-west.

The velocity curve along p.a. of 31° does not show a regular pattern, neither for the emission lines nor for the stellar velocities (Fig. 4.30, *upper right panel*). It is not surprising that we do not see any rotational pattern as the obtained p.a. is roughly perpendicular to the photometrical major axis along which Storchi-Bergmann et al. (1992b) find a clear trend for velocities to be blueshifted to the south-east and redshifted to the north-east. However, we observe an increase of gaseous velocities from south-west to north-east with a maximum amplitude of $\delta v \sim 100 \text{ km s}^{-1}$. This may correspond to the deviations of the rotation curve observed by Storchi-Bergmann et al. (1992b) with a maximum velocity of 150 km s^{-1} which they interpret as outflow along the cone.

NGC 5643

Literature data

The Seyfert-2 galaxy NGC 5643 is a barred spiral galaxy, classified as SAB(rs)c (NED). The bar is orientated east-west (p.a. = 90°). According to Ryder & Dopita (1993), the disk has a low inclination of $i = 33^\circ$, RC3 gives $i = 31^\circ$.

Morris et al. (1985) studied the velocity field and radio structure of NGC 5643. The velocity pattern indicates rotation with distortions near the bar, similar to gas flow in a barred potential. The extended NLR east of the nucleus follows the galactic rotation. At $3''$ west of the continuum peak, the emission lines are blueshifted, have blue wings, and the greatest line width. At the same time, the reddening value is high. The VLA data show a core, coinciding with the optical peak and the kinematic center as well as two lobes in the direction of the bar. Morris et al. (1985) measure a photometric major axis p.a. of 128° and a kinematic major axis p.a. of 136° .

NGC 5643 was studied in detail by Schmitt et al. (1994) by means of groundbased narrow-band imaging in [O III] and $\text{H}\alpha + [\text{N II}]$ and long-slit spectroscopy. High excitation gas in a bi-conical morphology is elongated along the bar (p.a. = 90°) out to $\sim 16''$ on each side of the nucleus and out to $\sim 7''$ perpendicular. Further out, the $\text{H}\alpha$ image reveals several H II regions on both edges of the bar. Schmitt et al. (1994) speculate that the active nucleus is hidden $\sim 3''$ west of the continuum peak where both the highest reddening value and the highest gas density are observed. This region coincides with the blueshifted line emission found by Morris et al. (1985). NGC 5643 is another Seyfert-2 galaxy fitting the unified model with the torus obscuring the nucleus and collimating the ionizing radiation leading to the bi-conical morphology. In the central region, the stellar population is old corresponding to an S3 to S4 template, while in the H II regions, the stellar population is younger (S6-S7). Schmitt et al. (1994) did not use a stellar template to correct for the underlying absorption lines. Instead, only the $\text{H}\alpha$ and $\text{H}\beta$ lines were corrected using the corresponding equivalent widths. Dilution from a blue continuum probably due to scattered light is found in the inner $10''$. The ratio [O III]/[O II] was used as tracer of the ionization parameter. It is high throughout the extended NLR, decreasing more or less abruptly at its edges.

Schmitt et al. (1994) found increasing oxygen (O) and nitrogen (N) abundances towards the center where the O/H ratio reaches solar and N/H twice the solar value.

Tsvetanov & Petrosian (1995) list 214 H II regions in NGC 5643, most of them distributed in a ring-like structure at 20–60'' from the nucleus, suggesting that current star formation is occurring in the nearly circular spiral arms. At a p.a. of 90° along the bar, the nearest H II regions are seen $\sim 10''$ east of the nucleus.

HST images in [O III] and H α + [N II] were taken by Simpson et al. (1997) to study the NLR with a high-resolution of 0''.1 (Fig. 4.1, *lower right panel*). As already indicated by groundbased images, the one-sided conical distribution of the high-excitation gas is clearly seen. The peak of the red continuum emission coincides with the apex of the cone. The radio structure seen by Morris et al. (1985) is closely aligned with the overall shape of emission. A more detailed VLA A-array radio map (8.4 GHz) with radio structure closely matching the distribution of the NLR gas is presented by Leipski et al. (2005). It shows a diffuse radio jet extended by $\sim 15''$ to both sides of the center (while in optical wavelength, the counter cone to the west is absorbed by dust).

Under the assumption that the spiral arms of NGC 5643 are trailing, the velocity field of Morris et al. (1985) shows that the south-west part of the galaxy is on the near side. A dust lane to the south-west of the nucleus supports this assumption. Simpson et al. (1997) suggest that the absence of a visible counter cone is the consequence of its obscuration by the galaxy disk. An extended blue continuum region is seen out to 0''.9 east of the nucleus. It is not clear whether this emission is scattered nuclear continuum or due to e.g. a stellar ionizing continuum.

Quillen et al. (1999b) studied the molecular hydrogen distribution in NGC 5643 and find strong H₂ emission near the nucleus and in the extended NLR. The emission arises close to dust lanes seen in the optical/near-infrared color map. This is interpreted as multiphase medium near the ionization cone with the morphology of line emission depending on the density of the surrounding medium.

Evans et al. (1999) studied HST UV/optical spectrophotometry to find clues to the excitation mechanism of the NLR in NGC 5643. They did not find an unambiguous shock plus precursor signature suggesting that the mechanical energy input does not play a dominant ionizing role.

No BLR is seen in polarized light (Moran et al., 2000). Also, no broad Brackett α line is found in infrared spectroscopy by Lutz et al. (2002), but coronal line emission of [S IX] $\lambda 3.94 \mu\text{m}$ at a low ratio to Brackett α . A possible starburst contribution to [S IX] cannot be excluded.

NGC 5643 present spectroscopic signatures of a dominant “post-starburst” population with 73% of the total light at 4861 Å due to old stars, 20% due to 100 Myr stars and a small contribution of a featureless continuum plus stars younger than 10 Myr (7%) (Cid Fernandes et al., 2001). In agreement with Schmitt et al. (1994), Cid Fernandes et al. (1998) classify the stellar population as moderately old in the central region with evidence of absorption lines diluted by a blue continuum, possibly from scattered nuclear light.

Apart from NGC 1386, NGC 5643 is the second object from our list which was included in the sample of 18 Seyfert galaxy studied by Fraquelli et al. (2003). They present density and reddening as a function of distance from the nucleus as well as surface-brightness distributions. However, their data have a significant lower signal-to-noise ratio (S/N) than our data and, moreover, they did not take into account the underly-

ing absorption owing to the contribution of the stellar population which we show to be important.

Greenhill et al. (2003) detected an H₂O megamaser in NGC 5643. As the maser emission at the observed strength has not been detected in previous studies of NGC 5643, they conclude that the maser emission varies significantly with time.

Comparison with our results

The high-resolution NTT spectra of NGC 5643 (p.a. = 90°) provided by Christian Leipski do only cover the H β + [O III] and the H α + [N II]+ [S II] wavelength range. We therefore do not derive either the temperature or the ionization parameter.

The high sensitivity VLT spectra (p.a. = 66°) were used to derive a stellar template at a distance of 26'' south-west of the center, averaged over 2'' and median-filtered in spectral direction over three pixel to increase the S/N (Table 4.6; Fig. 4.5, *middle left panel*). As the match between the stellar template and the continuum in each spectral row was quite close within the errors, no reddening correction was applied.

We detect [O III] emission at a S/N > 3 out to a distance of $\pm 16''$ from the nucleus (Table 4.10), i.e. comparable to the results of Schmitt et al. (1994). However, only the central $\pm 11''$ originate from the NLR as can be seen in the first and third diagnostic diagram (Fig. 4.15, *top and bottom right panels*). Further out, the emission originates from circumnuclear H II regions, in agreement with the results of Tsvetanov & Petrosian (1995) who find the nearest H II regions at 10'' east of the nucleus. The transition between line ratios typical for AGN ionization and H II-region like ionization occurs at a distance of 11'' from the center and determines the size of the NLR to 11'' ($\simeq 1050$ pc). This size coincides with the region in which Schmitt et al. (1994) report dilution from a blue continuum. While Fraquelli et al. (2003) detect line emission which they classify as extended NLR out to a distance of ~ 15 -20'', our analysis shows that the extended emission beyond 11'' originate from circumnuclear H II regions and can therefore not be attributed to the NLR.

Unfortunately, the [O I] is not covered by the observed wavelength range and we therefore cannot calculate line ratios for the second diagnostic diagram. In principle, we cannot exclude that a combination of outwards decreasing ionization parameter (as is indeed observed) and decreasing metal abundances result in line ratios in the H II regime despite AGN-intrinsic excitation (Section 4.4.4). However, a transition of line ratios is observed in NGC 1386, NGC 6860, and MCG -05-13-017 in all three diagnostic diagrams, thus ruling out the possibility of such an effect. We believe that the observed transition in NGC 5643 is also due to a change in the dominating ionization source from AGN to circumnuclear H II regions.

In addition to the central [O III] emission, line-emission is found at distances of $47 \pm 3''$ west from the center as well as $36 \pm 5''$ east and again $73 \pm 2''$ east from the photometrical center. This emission can be attributed to H II regions which can be identified in the H α images by Tsvetanov & Petrosian (1995) and Schmitt et al. (1994). This is strengthened by the line ratios which all fall in the H II-region regime in the diagnostic diagrams (open and filled diamonds in Fig. 4.15, *top and bottom right panels*). When comparing the line ratios of these H II regions with those of the circumnuclear H II regions, it is notable, that the ones from the center (out to 16'' east) slowly approaches the outer ones in terms of the [O III]/H β ratio. It shows that the transition between NLR and circumnuclear H II regions is not abrupt but that the dominating ionization

field slowly changes from the central AGN to that of the circumnuclear stellar one. At $16''$ east (marked with the small letter “p” in Fig. 4.15, *top and bottom right panels*), the line ratios are finally identically with those observed in the H II regions in the spiral arms. This observation strengthens our interpretation of the observed transition as true border between NLR and surrounding H II regions.

The reddening is highest in the center ($E_{B-V} \sim 0.73 \pm 0.02$ mag) and falls quickly towards the east and also $2''$ to the west where it then again rises to $E_{B-V} \sim 0.6$ mag at $3''$ and stays high throughout the western NLR (Fig. 4.12, *bottom right panel*). The high reddening in the west may originate from obscuration of dust lanes seen in broadband NICMOS/WFPC color maps (Simpson et al., 1997; Quillen et al., 1999a). The obscuration from dust seems to be responsible for the one-sided ionization cone structure seen in the HST images of Simpson et al. (1997).

Schmitt et al. (1994) observe the highest reddening at $3''$ west of the continuum peak and speculate that the AGN is hidden there while we observe the highest reddening value in the center. However, one has to take into account their spatial resolution of $2''$ compared to our spatial resolution of $\sim 1''$. Moreover, the coincidence of the highest reddening with the most luminous row (continuum, H α and [O III]) we find is in agreement with the schematic model proposed by Simpson et al. (1997) (their Fig. 6).

The surface-brightness distributions are centrally peaked, rapidly decreasing with distance from the center (Fig. 4.24, *middle left panel*). While the [O III] surface brightness is higher than the H α one throughout the NLR, H α is higher in the circumnuclear H II region in the east. A secondary peak can be seen in both the [O III] and H α surface-brightness distribution at $\sim 9''$ west of the center. As NGC 5643 is not included in the HST sample of Schmitt et al. (2003a), we cannot compare our results to the HST [O III] surface-brightness distribution.

The electron density is slightly higher $1''$ west of the photometrical center than in the center itself ($n_e \sim 930 \pm 40 \text{ cm}^{-3}$ versus $n_e \sim 860 \pm 30 \text{ cm}^{-3}$ using a temperature of $T_e = 10000 \text{ K}$ for correction). Schmitt et al. (1994) also report the highest density at $1''.8$ west of the nucleus (their first data point west of the photometrical center). The AGN may indeed reside slightly offset to the west of the [O III] and H α peak as suggested by Simpson et al. (1997). In general, the electron density decreases with distance from the center and reaches the low density limit at the edge of the NLR (Fig. 4.26, *middle left panel*). Two subpeaks can be seen at $5\text{--}6''$ on both sides of the nucleus with a density of $n_e \sim 360 \text{ cm}^{-3}$ (east) and $n_e \sim 270 \text{ cm}^{-3}$ (west).

We estimate a systematic heliocentric velocity of NGC 5643 from the average of the peak wavelength of the H α and [N II] emission lines in the photometrical center of $\sim 1150 \pm 20 \text{ km s}^{-1}$, close to the one measured from H I observations [1200 km s^{-1} ; Reif et al. (1982)]. The largest velocity scatter in the NLR along p.a. = 90° is observed from $2''$ east to $4''$ west with $\delta v \sim 100 \text{ km s}^{-1}$ (Fig. 4.30, *middle left panel*). The velocity field does not show clear signs of rotation. This is not surprising if the photometrical major axis runs along 137° rather than 90° (Morris et al., 1985).

Moreover, the observed non-circular motion along the bar direction (p.a. = 90°) with changes of redshifts to blueshifts within the NLR is already noted by Morris et al. (1985). They interpret the motions as driven by the bar potential.

Due to the fairly high spectral resolution of the NTT data taken by Christian Leipski ($\sim 1.5 \text{ \AA} \simeq 90 \text{ km s}^{-1}$), we are able to study the emission-line profiles in detail. Interestingly, the velocity field is reflected in the profiles of H β , [O III], and H α .

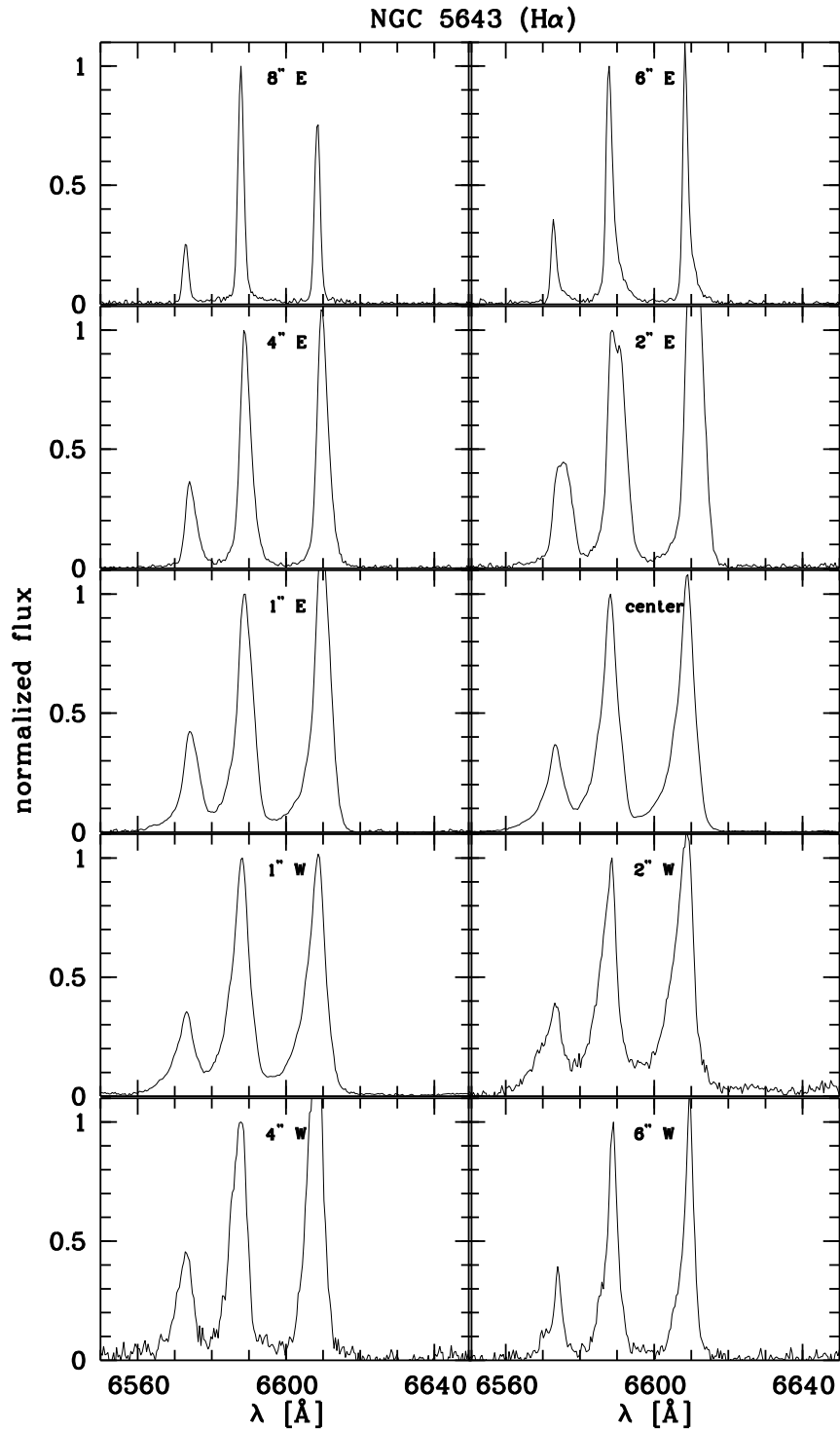


Figure 4.40: $H\alpha$ profile variations in NGC 5643. The peak flux of $H\alpha$ is normalized to 1.

At the location of the redshifted velocities to the east of the nucleus, we see red wings in the profiles out to $\sim 8''$. The strongest red contribution leading even to a secondary peak is observed at $2''$ east of the nucleus, i.e. coinciding with the region where the highest velocity occurs. From $1''$ east of the nucleus out to $\sim 7''$ west of the nucleus, a blue wing is observed which reaches its maximum contribution to the total flux at $\sim 3 - 4''$ west of the nucleus, i.e. coinciding with the maximum blueshifted velocity. Along with the profile asymmetries, the observed profiles get also broader. Whittle (1982) already reported that the line profiles are identical within observational uncertainties across the nuclear region and reveal profile asymmetries such as blue wings. Examples of the observed profile changes are presented in Figures 4.7 and 4.40. The pronounced profile substructure is confined to the NLR, i.e. the central $22''$ as determined from the diagnostic diagrams.

The observed profile substructure may also reflect the influence of the bar potential. However, we cannot rule out that both the observed profile substructure and the red- and blueshifted velocities originate from outflowing gas due to jet/NLR interactions: Two radio lobes extend in the direction of the bar (Morris et al., 1985).

IC 5063

Literature data

IC 5063 is a Seyfert-2 galaxy with a hidden BLR seen in polarized light (Inglis et al., 1993). Its radio luminosity is two orders of magnitude greater (Colina et al., 1991) than that typical of nearby Seyferts (Ulvestad & Wilson, 1984). Thus, IC 5063 is also classified as narrow-line radio galaxy (NLRG). Its morphological classification is SA(s)0+: (NED). Laine et al. (2002) do not find evidence for a bar. The galaxy inclination is 51° (RC3).

Bergeron et al. (1983) studied the extended ionized gas with long-slit spectroscopy. Ionized gas is reported out to a distance of 19 kpc to the north-west of the nucleus ($\sim 60''$ using their adopted distance to the galaxy and Hubble constant) and 9 kpc ($\sim 36''$) to the south-east. The gas velocity field shows a clear rotational pattern. The stellar velocity curve has a similar slope but a much smaller gradient and some irregularities, possibly due to a different rotation axes of the gas and the stars. Bergeron et al. (1983) find both an increasing temperature and ionization parameter with increasing distance from the nucleus. Under the assumption of one central ionizing source, this implies that the gas density decreases faster than $n \propto r^{-2}$.

Wagner & Appenzeller (1989) report the detection of an off-nuclear broad emission-line region at $1''.8$ north-west of the nucleus. They interpret this emission as an extreme example of scattered nuclear emission with a very high intrinsic line emission from the nucleus. An apparently counter-rotating gaseous mass is observed in the vicinity of the center of the galaxy. The enhanced nuclear activity, the irregular gas motions, and strong obscuration and scattering effects are interpreted as IC 5063 being a recent merger remnant.

Colina et al. (1991) used high spatial resolution optical and infrared imaging as well as optical spectroscopy to study the physical and kinematic conditions of the ionized gas. They find a highly anisotropic ionizing radiation field with a conical morphology and an opening angle of 50° along a p.a. of 120° . The cone axis coincides with the photometric major axis of the galaxy (p.a. = 116° ; RC3). The ionized gas extends over $d \simeq 69''$. Inside the cone, the excitation conditions are roughly uniform but drop very rapidly outside. The results of Colina et al. (1991) are similar to that of Bergeron et al.

(1983), confirming a positive excitation gradient outwards from the nucleus. However, the observed radial dependency of the electron density along $\text{p.a.} = 109^\circ$ suggest $n \propto r^\delta$ with $\delta = -0.6$. This is not consistent with the requirement of $\delta < 2$, needed to explain the increasing ionization parameter. They suggest that a combined effect of decreasing density and abundance may explain the increasing excitation outwards from the nucleus. Like Wagner & Appenzeller (1989), Colina et al. (1991) report a counter-rotating feature in the velocity field at $1''.5$ south-east of the nucleus ($\text{p.a.} = 289^\circ$). Several dust lanes are concentrated in the northern side of IC 5063, running approximately parallel to the major optical axis. High-excitation [Fe VII] and [Ca V] emission lines are detected in the central arcseconds.

The 3.6 cm radio map reveals a linear triple radio structure extending over $4''$, associated with the NLR (Morganti et al., 1998). At 21 cm, broad blueshifted HI absorption is visible, indicating a fast net outflow. In the central region, there is clear evidence for a strong interaction between the radio jet and the ISM. The shock scenario is supported by HST/NICMOS observations by Kulkarni et al. (1998) who find three emission-line regions in [Fe II], Pa α , and H₂ along the major axis aligned with knots seen in radio emission. The NICMOS data show a very red point source in the nucleus of IC 5063, interpreted as dust-obscured active nucleus.

A groundbased [O III] image was presented by Morganti et al. (1998), confirming the result of Colina et al. (1991) that the high-ionization line-emitting gas has an “X-shaped” morphology with a basic symmetry axis of $\text{p.a.} \sim 120^\circ$. The ionized gas can be traced out to a distance larger than $r \sim 30''$. Although the HST [O III] image from Schmitt et al. (2003a) reveals the same shape, the [O III] extension is the fifth part of the groundbased one ($r \sim 6''$). Schmitt et al. (2003a) explain the small size by the limited field-of-view of the linear-ramp filter ($\sim 13''$) which is, however, twice as large as the observed extension. Thus, it may rather be due to the low sensitivity of the HST snapshot survey (600 s with the 2.4 m HST) compared to the groundbased image (1200 s with the 3.6 m ESO telescope).

Comparison with our results

In our long-slit observations ($\text{p.a.} = 115^\circ$ tracing the [O III] major extension, Fig. 4.3, *upper right panel*), we detect [O III] emission at a $\text{S/N} > 3$ out to a distance of $r \sim 20''$ from the nucleus in both the south-east and north-west direction (Table 4.10). This is smaller than what has been reported by Bergeron et al. (1983), but they also find a decrease of line intensities by a factor of 10–30 at a distance $> 6''$ from the nucleus and therefore average over a large spatial range to gain a constant S/N. The groundbased [O III] image of Morganti et al. (1998) also reveals a larger extension, but the HST [O III] extension is three times smaller. This discrepancy once again shows the need for alternative measures of the NLR size rather than using the [O III] extension alone.

We use a stellar template to subtract the underlying absorption lines, determined from averaging over a region of $7''$ at a distance of $23''$ north-west of the center. Apart from the reddening correction, we also applied a velocity correction, as the velocity gradient across the NLR was large compared to our spectral resolution. We rebinned the stellar template to the stellar velocity of each individual row.

Line ratios at a $\text{S/N} > 3$ can be measured out to a distance of $r \sim 13''$ from the photometrical center and all fall in the upper right corner in the three diagnostic diagrams (Fig. 4.18, *top right panel*). Moreover, they show a remarkably small scatter compared to

the AGN–typical line ratios of other galaxies, e.g. NGC 1386 or NGC 5643. We classify the corresponding gas as NLR, but we cannot exclude that the NLR extends even further out where we are not able to measure line ratios to a high accuracy.

In the center, IC 5063 has the highest $[\text{O II}]/\text{H}\beta$ flux ratio ($F_{\text{dered}} \sim 2.96$) and at the same time the lowest $[\text{O III}]/\text{H}\beta$ ratio ($F_{\text{dered}} \sim 8.03$) of our type–2 sample (Table 4.7). This translates to the lowest ionization parameter in the optical nucleus ($U_{\log(n_e)=3} \sim 2.15 \pm 0.01 \cdot 10^{-3}$) (Table 4.9). All values are indicative of a less strong ionization field in the center of IC 5063 compared to the other AGNs in our sample. The central electron temperature is with $T \sim 13865 \pm 1800 \text{ K}$ comparable to that of other type 2s in our sample as well as to the central value measured by Colina et al. (1991) within the errors ($T \sim 15000 \text{ K}$). High excitation lines such as $[\text{Fe VII}]$ and $[\text{Fe X}]$ are observed in the central spectra.

IC 5063 is the only object in our sample where we can follow the $[\text{O III}] \lambda 4363$ emission line at a $\text{S/N} > 3$ over several arcseconds from the nucleus (from $\sim 8''$ north–west to $\sim 5''$ south–east). The resulting temperature ranges between $T_e \sim 15310 \text{ K}$ to $T_e \sim 12245 \text{ K}$, without a clear tendency with radius. The average value of the outer regions is with $T_e \sim 13789 \pm 290 \text{ K}$ close to the central temperature of $T_e \sim 13865 \pm 1800 \text{ K}$. We cannot confirm the results of Bergeron et al. (1983) who reported an increasing temperature with distance from the nucleus.

The central reddening determined from the Balmer decrement is the highest one of our 12 objects ($E_{B-V} \sim 0.89 \pm 0.01 \text{ mag}$). It probably coincides with the red point source seen in NICMOS images of the nucleus of IC 5063. The reddening remains high $1''$ northwest and decreases outwards (Fig. 4.13, *top right panel*). In the south–east, it reaches a minimum at $\sim 4''$ and then increases again to a value comparable to the central one at a distance of $10''$. This increase in the south–east is not observed in the reddening determined from the continuum slope relative to the stellar template (Fig. 4.13, *top left panel*), indicating that it is most likely due to dust intrinsic to the NLR. Overall, both reddening measures show a comparable reddening distribution, with the continuum slope reddening covering a smaller range of $\Delta E_{B-V} \sim 0.2 \text{ mag}$, while the Balmer decrement yields a reddening distribution with an amplitude of $\Delta E_{B-V} \sim 1 \text{ mag}$. We use the reddening determined from the $\text{H}\alpha/\text{H}\beta$ ratio to correct the observed line ratios.

The surface–brightness distributions of $[\text{O III}]$, $\text{H}\alpha$, and the continuum have a similar slope and run parallel throughout the observed region, indicating no changes in ionizing continuum in agreement with the line ratios in the diagnostic diagrams. They are highest in the center and decrease outwards. From $7''$ south–east on, they increase again. The HST $[\text{O III}]$ surface–brightness distribution reveals two subpeaks symmetrically placed at $\sim 2''$ from the nucleus which are nearly as bright as the central peak. In the low resolution of our spectra, the three central peaks are smoothed out to one broad peak in the center. The HST image traces the $[\text{O III}]$ emission out to only $\pm 5''$ from the center.

The electron–density distribution peaks at the center ($n_e \sim 635 \pm 30 \text{ cm}^{-3}$) and decreases outwards to the low density limit with two subpeaks at $\sim 5''$ on both sides of the optical nucleus ($n_e \sim 300 \text{ cm}^{-3}$ to the north–west, $n_e \sim 170 \text{ cm}^{-3}$ to the south–east; Fig. 4.26, *middle right panel*). This general behavior is similar to the results of Bergeron et al. (1983) and Colina et al. (1991) with a central electron density comparable to that of Bergeron et al. (1983) ($n_e \sim 600 \text{ cm}^{-3}$) and slightly higher compared to Colina et al. (1991) ($n_e \sim 540 \text{ cm}^{-3}$ without temperature correction versus their value of $n_e \sim 450 \text{ cm}^{-3}$ along a comparable p.a. of $\sim 110^\circ$; their Fig. 9a).

IC 5063 is besides NGC 3281 the second object in our sample where the ionization parameter does not peak at the optical nucleus. The highest ionization is observed instead at $5''.5$ south-east of the nucleus ($U_{\log(n_e)=3} \sim 3.3 \cdot 10^{-3}$; Fig. 4.28, *middle right panel*). This increase towards the south-east is in agreement with the increasing ionization parameter reported by Bergeron et al. (1983) and Colina et al. (1991), but towards the north-west, we observe a decreasing ionization parameter. Interestingly, the position at which the ionization parameter peaks is the same at which the surface-brightness distributions start to increase again outwards. Moreover, it coincides with the south-eastern region of enhanced electron density.

Colina et al. (1991) consider combined effects of abundance and density gradients as the most likely interpretation of these observations. However, the line ratios in all three diagnostic diagrams show a very small scatter, arguing against a steep abundance gradient. Moreover, the slope of decreasing electron density < 2 needed to explain the increase in excitation conditions is not observed, neither in their data nor in our data ($n_e \propto r^{-1.1}$; Table 4.12).

We instead favor a shock scenario from the interaction of the radio jet and the NLR gas. This is strengthened by the close match between the radio map and the NLR as well as the blueshifted H I absorption and the broad profile of the H I absorption observed by Morganti et al. (1998). The shocks may result in a locally increased density and ionize the surrounding medium, resulting in the increased ionization parameter and surface brightness.

The shock scenario is supported by the emission-line profiles which show substructures in the central $9''$ with a blue asymmetry on the north-west side and a red asymmetry on the south-east side of the center (Fig. 4.7, *right panels*). The profiles get significantly broader especially $1-2''$ on both sides of the nucleus. Unfortunately, our observations are limited by spectral resolution to allow for a detailed discussion of profile variations.

To probe the shock scenario, we looked for the presence of [Fe X] emission: It is negligible throughout most of the region, with the exception of the central $2''$ (center: $F_{\text{dered}} \sim 0.02$, $1''$ north-west: $F_{\text{dered}} \sim 0.003$, $1''$ south-east: $F_{\text{dered}} \sim 0.001$, respectively) and at $3''$ south-east ($F_{\text{dered}} \sim 0.001$), i.e. close to the region where we observe an increased density. However, we are limited by both the signal and the low resolution which makes it difficult to disentangle the weak [Fe X] from [O I] $\lambda 6363 \text{ \AA}$.

As already indicated by Bergeron et al. (1983) and Colina et al. (1991), the velocity field of IC 5063 (Fig. 4.30, *middle right panel*) can be interpreted as rotational pattern with the steepest gradient in the central $\pm 8''$. We find a maximum amplitude of $\Delta v \sim 485 \text{ km s}^{-1}$ and a central velocity of $v_{\text{hel}} \sim 3410 \text{ km s}^{-1}$ when extrapolating the rotation curve. Both the optical nucleus and $1''$ north-west display a redshifted velocity of $v_{\text{hel}} \sim 80 \text{ km s}^{-1}$ with respect to what would be expected as rotational value. This may be due to gas outflowing away from our line-of-sight or indicate a net inflow in the central arcsecond. As we observed close to the photometrical major axis of the galaxy, the general velocity pattern indicates emitting gas lying in a disc in the plane of the galaxy. Under this assumption, we can estimate the central mass in a radius of $r \sim 11''$ (2.4 kpc) using an inclination $i \sim 51^\circ$ and $v_{\text{obs}} \sim 243 \text{ km s}^{-1}$. It yields a lower mass limit within 2.4 kpc of $M \sim 3.3 \pm 0.5 \cdot 10^{10} M_\odot$ (see Appendix C, Eq. C.14 for details).

The stellar velocity curve was derived from the peak wavelength of the Na I D absorption line as the Ca II K line is too weak. Although the velocities show an overall similar behavior, i.e. blueshifted velocities to the north-west and redshifted ones towards

the south–east, the amplitude is much smaller ($\Delta v \sim 200 \text{ km s}^{-1}$). It is possible that at least part of the observed gaseous velocities are not due to rotational motion but reflects outflowing gas components. However, the Na I D absorption needs not necessarily arise from stellar spectra but can also be due to interstellar absorption and thus may not trace the stellar velocity curve.

NGC 7212

Literature data

NGC 7212 is a Seyfert–2 galaxy in a system of three interacting galaxies (Wasilewski, 1981). The morphological type of the host galaxy is classified as Sab by Keel (1996) (also given in NED), with a photometric major axis of p.a. = 42° . The galaxy is inclined by $i \sim 66^\circ$ from face–on–view. The maximum velocity range covered by the rotation curve is $\pm 300 \text{ km s}^{-1}$ (Keel, 1996).

Line emission from ionized gas extending over $\sim 17''.5$ along both p.a. of 37° and 127° has been reported by Durret & Warin (1990) as observed by means of optical long–slit spectroscopy in the $H\beta + [\text{O III}]$ wavelength range. They find a high excitation value $R = I([\text{O III}] \lambda 5007 \text{ \AA} + 4959 \text{ \AA}) / I(H\beta) = 19$ in the nucleus, while the nebulosity is of variable excitation with R ranging from 5–28. They quote that the large values are uncertain as $H\beta$ is close to the detection limit. Durret & Warin (1990) report a maximum velocity range of $\Delta v \sim 235 \text{ km s}^{-1}$ along p.a. = 37° and $\Delta v \sim 60 \text{ km s}^{-1}$ along p.a. = 127° .

Tran et al. (1992) find a broad $H\alpha$ component in the polarized light of NGC 7212. However, Tran (1995) argues that a significant amount of polarization is probably not intrinsic to the nucleus of NGC 7212 but due to transmission through aligned dust grains in the host galaxy. This is supported by several observational evidences, showing that dust obscuration plays a significant role in the source. Moreover, the narrow permitted and forbidden lines also possess a substantial amount of polarization. That is possibly the reason why, later on, Tran (2003) lists NGC 7212 as non–hidden BLR Seyfert–2 galaxy.

Tran (1995) finds a jet–like high–ionization feature extending up to $10''$ from the nucleus at a p.a. of $\sim 170^\circ$ in groundbased $[\text{O III}]$ and $H\alpha$ image, possibly due to collimated radiation of the nucleus. This direction coincides with a double radio source on a much smaller spatial scale discovered by Falcke et al. (1998) who compare HST and VLA observations of NGC 7212. The continuum image of Falcke et al. (1998) shows multiple dust lanes. Their $[\text{O III}]$ image is also included in the sample of Schmitt et al. (2003a) and presented here in Figure 4.3 (*lower left panel*) with the p.a. of the long slit overlaid. It exhibits extended emission out to $\sim 3''$ from the nucleus along p.a. = 170° . The emission is diffuse and composed of several individual knots to the north and south of the nucleus.

The stellar lines are similar to those of an old population (González Delgado et al., 2001), with a dominant 10 Gyr metal rich stellar population (Raimann et al., 2003) and no clear signs of starburst activity (Cid Fernandes et al., 2001). González Delgado et al. (2001) report the presence of scattered light produced by the hidden nucleus. Compared to the circumnuclear region, they find no dilution of a featureless continuum in the central region and interpret that by the presence of a spatially extended featureless continuum.

Comparison with our results

Along a p.a. of 170° , we observe [O III] emission extending out to $12''$ from the nucleus (Table 4.10), i.e. four times larger than the extension seen in the HST image in the same direction. It is somewhat smaller than the maximum extent observed by Durret & Warin (1990) (p.a. of 127° and 37°). The excitation value we observe in the central row is with $R_{\text{obs}} \sim 17$ comparable high to what has been observed by Durret & Warin (1990). It is the highest value in our type-2 sample. (Note that the [O III]/H β ratio given in Table 4.8 does not include the [O III] $\lambda 4959 \text{ \AA}$ line which is one third of the flux of the [O III] $\lambda 5007 \text{ \AA}$ line. Thus, one third of F_{obs} given in Table 4.8 has to be added to gain R .) The reddening-corrected value in the center is $R_{\text{dered}} \sim 16$ and varies between 6 and 17 in the central $24''$ region, i.e. it stays high in the whole region which we classify as NLR. Emission-line ratios at a S/N > 3 were obtained out to $\sim 5''$ south-east of the nucleus and $\sim 10''$ north-west. The electron temperature observed in the nuclear spectrum is $T_e \sim 14635 \pm 1500 \text{ K}$ (Table 4.9).

The reddening in the center is rather low ($E_{B-V} = 0.33 \pm 0.01 \text{ mag}$) and decreases to a value of $\sim 0.07 \text{ mag}$ at $1''$ north-west of the nucleus (Fig. 4.13, *middle right panel*). On both sides of this region, it increases and reaches its maximum value at $4''$ south-east and $7''$ north-west of the photometrical center ($\Delta E_{B-V} \sim 1 \text{ mag}$). These maxima may be attributed to dust lines seen in the continuum image by Falcke et al. (1998).

The surface brightness is highest at $1''$ south-east of the center (Fig. 4.24, *bottom left panel*). Although the highest [O III] and H α flux as well as the highest continuum is observed at $0''$ (this is how we defined the photometrical center), the reddening-corrected luminosities peak at $1''$ south-east due to the higher reddening observed in this part. The surface-brightness distributions decrease outwards and show a secondary maximum at $\sim 6''$ north-west of the nucleus. In the same region, the highest R_{dered} value of 17 is observed. The [O III] surface brightness determined from the HST image decreases rapidly with distance from the center, is confined to the central $3''$ and do not show any significant substructure.

The electron density peaks at the optical nucleus ($n_e \sim 1420 \pm 50 \text{ cm}^{-3}$) and decreases out to the low density limit at $\sim 4''$ north-west (Fig. 4.26, *bottom left panel*). Note that the [S II] $\lambda 6716 \text{ \AA}$ is slightly affected by telluric absorption bands and thus, the deduced absolute electron density has to be taken with some caution, but it does not change the observed slope.

The ionization parameter reaches its maximum value in the photometrical center [$U_{\log(n_e)=3} \sim (3.27 \pm 0.02) \cdot 10^{-3}$] and steadily decreases towards the outer parts ($U_{\log(n_e)=3} \sim 0.1 \cdot 10^{-3}$; Fig. 4.28, *lower left panel*). Both electron density and ionization parameter show a slight increase at $\sim 8''$ north-west of the nucleus.

The velocity field in NGC 7212 along p.a. = 170° shows increasing velocities from south-east to north-west and may indicate gaseous rotation. The maximum velocity range covered from $\sim 4''$ south-east to $\sim 10''$ north-west of the nucleus is $\Delta v \sim 370 \text{ km s}^{-1}$, i.e. slightly higher than the value reported by Keel (1996) ($\Delta v \sim 300 \text{ km s}^{-1}$) in the direction of the photometric major axis (42°). The central velocity we obtain is $v_{\text{hel}} \sim 7925 \pm 20 \text{ km s}^{-1}$. An increased velocity is observed at $\sim 4''$ north-west of the nucleus.

As the radio maps of NGC 7212 show a double radio source extending in the direction of our long-slit observations, it is probable that the radio jet interacts with the NLR, resulting in the observed enhanced surface brightness, electron density, ionization parameter, and the high excitation at ~ 6 – $8''$ north-west of the nucleus.

ESO 362–G008

Literature data

The galaxy hosting this Seyfert–2 nucleus is highly inclined ($i \simeq 70^\circ$) with the major axis along p.a. = 167° (RC3).

Groundbased images were studied by Mulchaey et al. (1996a), revealing a very red continuum nucleus. The [O III] emission is strongest in the nucleus and extends out to $\sim 25''$ along the galaxy disk ($\sim 158^\circ$, see Fig. 4.3, *lower right panel*) and $\sim 10''$ along the galactic minor axis. The regions of high excitation gas are distributed in a cross-like morphology, with the highest ratio corresponding to an off-nuclear cloud to the north-east.

Colbert et al. (1996) interpret the presence of gas far out of the disk as sign of a large-scale outflow occurring in ESO 362–G008.

At 20 cm, the source is unresolved, but the 3.6 cm map shows a faint extension $\sim 2''$ to the north. A secondary peak $\sim 1''$ to the north shows extended emission to the west. Nagar et al. (1999) conclude that the radio extension at 3.6 cm has a p.a. of 165° , similar to the direction of the [O III] extension seen by Mulchaey et al. (1996a).

The stellar population studies of Cid Fernandes et al. (1998) indicate an S5–S6 template at the nucleus and an S4–S5 template at $4''$ and further out. The bluer templates in the nuclear region are due to the presence of young stars, visible in the spectra as strong Balmer absorption lines. The contribution of a featureless continuum is low [$\sim 5\%$; Cid Fernandes et al. (2001)], implying that the nuclear source is hidden from direct view.

Storchi–Bergmann et al. (2000) describe ESO 362–G008 as relatively evolved nuclear starburst due to its high order Balmer absorption lines. The continuum is very red due to a dust lane crossing the nuclear region as seen by Malkan et al. (1998) in broadband HST images.

Fraquelli et al. (2000) studied the extended NLR of the Seyfert–2 galaxy ESO 362–G008 in detail to compare it to that of the Seyfert–1 galaxy MCG –05–13–017. They use a stellar population template obtained from averaging the extranuclear spectra. In the nucleus, a dilution of an intermediate-age burst of star formation is found. Fraquelli et al. (2000) find no evidence of a featureless continuum contributing more than 5% in the near-UV, in agreement with the results of Cid Fernandes et al. (2001). Emission-line fluxes are measured along p.a. = 60° out to $14''$ from the nucleus. The $H\beta$ emission line is too weak to be measured, often not filling the absorption feature, indicating that the stellar template does not match the younger stellar population of the nuclear region. All ratios show a symmetric behavior on both sides of the nucleus. The increasing [O II]/[O III] ratio indicates a decreasing ionization parameter. Along p.a. of 165° , i.e. that of the photometric major axis, the gas and stars present a rotation curve consistent with circular motion in the plane of the galaxy, with the south-east side approaching. Fraquelli et al. (2000) conclude that the nuclear collimation axis is almost perpendicular to the disk. The high-excitation cloud seen north-east of the nucleus in the excitation map of Mulchaey et al. (1996a) is interpreted as a high-latitude cloud ionized by the AGN continuum and blown away from the galaxy disk, in agreement with the assumption of a large outflow from Colbert et al. (1996).

Comparison with our results

ESO 362-G008 is the only object in our sample in which strong underlying stellar absorption lines remain even after subtraction of a template determined in the outer parts of the galaxy (6'' south-east of the nucleus, averaged over 1'' and median-filtered in spectral direction over three pixel to increase the S/N; Table 4.6; Fig 4.5, *lower left panel*). This hints the existence of a nuclear starburst as is confirmed by the stellar population synthesis of Cid Fernandes et al. (1998) and the results of Storchi-Bergmann et al. (2000). As a consequence, our results have to be taken with some caution as the H β and H α emission are most probably underestimated. We indeed often see the underlying absorption trough in both lines. Also Fraquelli et al. (2000) who use a stellar population template averaged from extranuclear spectra report dilution of an intermediate-age burst of star formation, resulting in a mismatch of the stellar template and the younger stellar population of the nuclear region where the H β line is often not filling the absorption feature.

ESO 362-G008 is also the object in our sample with the smallest detectable [O III] extent ($r \sim 4''$). Moreover, due to the low S/N, the line ratio study is limited to the central $r \sim 3''$. Interestingly, the groundbased image reveals a more than twice as large [O III] extension (along roughly the same p.a.). Fraquelli et al. (2000) study emission lines out to $r \sim 14''$ from the nucleus but along p.a. = 60° and are also confined to the inner $d \sim 10''$ at a p.a. of 160°.

We decided not to apply more sophisticated stellar template corrections due to our limited S/N. All line ratios fall in the AGN regime in the diagnostic diagrams, suggesting that the NLR extends out to at least 3'' radius from the center (Fig. 4.18, *second right panel from top*). The line ratios have rather high values on the x-axis, most probably due to the underestimated H α line flux.

Due to the remaining underlying absorption lines in the central spectra (Fig. 4.10, *second panel from top on the left*), we cannot measure the temperature. Only emission-line fluxes from the strongest lines [O II], H β , [O III], [O I], H α , [N II], and [S II] can be derived (Table 4.7).

The reddening determined from the continuum slope relative to the template shows a similar distribution as the reddening distribution using the Balmer decrement with the highest reddening value in the center and a slow decrease to the outer parts (Fig. 4.13, *bottom left and right panel*). However, the absolute values differ significantly: The reddening of the continuum slope shows negative values, implying that the template is redder than the inner spectra, due to the presence of young stars (Cid Fernandes et al., 1998). Moreover, the covered reddening scatter is small ($\Delta E_{B-V} \sim 0.07$ mag), while a ~ 10 times higher range is obtained using the H α /H β ratio ($\Delta E_{B-V} \sim 0.6$ mag). These differences can be explained first by the relative reddening value that was obtained in case of the continuum slope, i.e. both outer template and central spectra suffer similar dust extinction which do not reflect in the derived value. Second, dust may be intrinsic to the NLR. We used the reddening determined by the emission-line ratio for correction.

The surface-brightness distributions of H α , [O III], and continuum peak at the center and decrease with distance (Fig. 4.24, *bottom right panel*).

The electron density also reaches the highest value in the center of $n_e \sim 1420 \pm 70$ cm $^{-3}$ and decreases outwards (using a temperature of $T_e = 10000$ K for correction; Fig. 4.26, *bottom right panel*).

The ionization parameter peaks in the photometrical center [$U_{\log(n_e)=3} \sim (2.76 \pm 0.1) \cdot 10^{-3}$] and decreases to $U_{\log(n_e)=3} \sim 1.1 \cdot 10^{-3}$ in the outer parts (Fig. 4.28, *bottom right panel*). The observed decrease of ionization parameter has already been suggested by Fraquelli et al. (2000) based on the increase of the [O II]/[O III] ratio, at least in the central $r \sim 5''$ (their Fig. 11).

Along the observed p.a. of 163° (i.e. close to the photometrical major axis of p.a. = 167° ; RC3), the velocity curves derived from the peak wavelength of [N II] (which is in contrast to H α and H β unaffected by underlying absorption lines) and the peak wavelength of the Ca II K absorption line are quasi identical (Fig. 4.30, *bottom right panel*). The central velocity is $v_{\text{hel}} \sim 4870 \pm 20 \text{ km s}^{-1}$. The maximum velocity range in the inner $4''$ is $\Delta v \sim 190 \text{ km s}^{-1}$ with blueshifted velocities towards the south–east. Our results are comparable to that of Fraquelli et al. (2000) and can be interpreted as circular motion in the plane of the galaxy, with the south–east side approaching. However, the center and the region $1''$ north–west show gaseous and stellar velocities which are by $v_{\text{hel}} \sim 50 \text{ km s}^{-1}$ redshifted compared to what would be expected by interpolating the outer stellar velocity curve. This can be interpreted as either inflow, possibly fueling the AGN or indicates an outflow away from our line–of–sight triggered by the interaction with the radio jet as the position coincides with extended radio emission (Nagar et al., 1999).

MCG –6–30–15

Literature data

The E/S0 galaxy MCG –6–30–15 hosts an X–ray bright AGN of Seyfert 1.2 type (NED) and has been the subject to intense spectroscopic studies in the X–ray band [e.g. Iwasawa et al. (1996)].

A multiwavelength study has been performed by Reynolds et al. (1997): In the optical, an extracted host galaxy spectrum with Balmer and Ca II absorption features is subtracted to gain the absorption–line free AGN spectra. The nuclear spectrum reveals a strong non–stellar continuum, broad Balmer lines, and narrow permitted and forbidden lines. High–excitation forbidden lines (e.g. [Fe X], [Fe XI] $\lambda 7892 \text{ \AA}$, and [Fe XIV] $\lambda 5303 \text{ \AA}$) are clearly displayed. A significant amount of dust extinction is deduced from optical line and continuum emission, lying in the range $E_{(B-V)} = 0.6\text{--}1.1 \text{ mag}$. Due to the absence of cold (neutral) absorption in the X–ray spectra, Reynolds et al. (1997) postulate that the dust resides in the so–called warm absorber, i.e. ionized gas that absorbs X–rays produced in the accretion disk of the AGN. The coronal–line region may also arise in the outer warm absorber.

VLA observations at both 3.6 and 20 cm show that MCG –6–30–15 is an unresolved radio source (Nagar et al., 1999).

HST continuum images and color maps from Ferruit et al. (2000) show a dust lane south of the nucleus, running roughly parallel to the photometric major axis of the galaxy (p.a. $\sim 115^\circ$; $i \sim 60^\circ$). The south–west side of the galaxy is found to be systematically redder than the north–east side, with the central regions redder than the outer ones. The [O III] image shows emission extending in the direction of the galaxy major axis. It is included in the study of Schmitt et al. (2003a) and presented here in Figure 4.1 (*lower left panel*) with the slit position of our observation overlayed (p.a. = 115°), tracing the direction of the maximum extent in [O III]. The emission is extended by $1''.5 \times 3''.9$.

Bonatto et al. (2000) use UV spectra to determine the stellar population. An old bulge population is dominating the stellar contribution, with indications of previous bursts of star formation.

Dust location and composition of the dust in the MCG-6-30-15 warm absorber has been investigated by Ballantyne et al. (2003). They argue that the dust lane crossing the galaxy just below the nucleus seen in HST images is producing the reddening of the nuclear emission. The dust in the ISM of the host galaxy is proposed to be the location of the warm absorber, at a distance of hundreds of pc from the nucleus.

Comparison with our results

The VLT long-slit spectra of MCG-6-30-15 allow us to trace [O III] emission out to a distance of $\pm 12''$ from the optical nucleus, i.e. six times larger than the [O III] extension seen in the HST image of Schmitt et al. (2003a). We confirm the existence of high-excitation forbidden lines in the central spectra as reported by Reynolds et al. (1997).

MCG-6-30-15 is the only Seyfert-1 galaxy in our sample in which we were not able to disentangle the broad and narrow Balmer emission lines. This is first due to the classification as Sy1.2 whereas the other Seyfert-1 galaxies (apart from Fairall 51) can be classified as either Sy1.5 or Sy1.9, i.e. a clear separation of the narrow emission line superimposed on the broad one is visible. Second, it is also due to the lower resolution of our VLT/FORS1 spectra while all other type 1s were observed with the higher spectral resolution of the NTT/EMMI. Thus, we cannot determine the central emission line fluxes relative to $H\beta$. Moreover, it was difficult to disentangle the [O III] $\lambda 4363 \text{ \AA}$ emission line from the broad $H\gamma$ and we therefore do not measure the temperature.

MCG-6-30-15 is also the only Seyfert-1 galaxy for which we applied a stellar template subtraction. This was both necessary as strong Balmer and Ca II H&K absorption lines were seen in the NLR spectra (Fig. 4.5, *lower right panel*) and possible given the high sensitivity VLT data allowing us to derive an emission-line free template spectrum in the outer parts. The template was determined at a distance of $12''$ north-west of the nucleus as average over a spatial region of $2''$ and median-filtered along the spectral axis over three pixels to increase the S/N (Table 4.6). A reddening correction was applied to fit the slope of the stellar template to each spectrum of the NLR (Fig. 4.14, *top left panel*). The continuum gets steadily redder towards the nucleus where it reaches the highest reddening value of $E_{B-V} \sim 0.3 \pm 0.02 \text{ mag}$. In the outer parts, the reddening is at a minimum of $E_{B-V} \sim 0.02\text{--}0.04 \text{ mag}$.

This amount of dust extinction is significantly lower than what has been determined by Reynolds et al. (1997). They were also not able to disentangle the broad and narrow emission lines in their low resolution spectra and use instead the total Balmer decrement. They derive a range of $E_{B-V} \sim 0.6\text{--}1 \text{ mag}$. The difference may arise from either additional reddening of the BLR only [as Reynolds et al. (1997) use the total Balmer decrement] or is due to the fact that our reddening value is a value relative to the stellar template and simply reflects the differences of dust extinction between the NLR and the template. If the extinction is at least partially due to dust in the ISM of the host galaxy as proposed by Ballantyne et al. (2003), both the stellar template and the central continuum suffer the same extinction which will then not reflect in the reddening determined by the fitting of the stellar template to the continuum slope of the NLR spectra.

As the broad Balmer lines are limited to the central $2\text{--}3''$ (Table 4.14; Section 4.4.10), we are able to measure the narrow line fluxes in the outer regions to a distance of $\pm 4''$.

We find that the line ratios are typical for AGNs when inserting them in the diagnostic diagrams. Given the broad emission lines, it is reasonable to believe that the central values also lie in the AGN regime and that the NLR extends out to at least $4''$ distance from the nucleus.

The surface-brightness distribution has been determined for the [O III] emission line and the continuum and is presented in Figure 4.25 (*top left panel*). It peaks at the photometrical nucleus and slowly decreases outwards. The HST [O III] surface-brightness distribution is also centrally peaked and smoothly declines with distance from the center.

The central electron density is the lowest electron density observed in the nuclear spectra of our sample ($n_e \sim 300 \pm 40 \text{ cm}^{-3}$ using a temperature of $T_e = 10000 \text{ K}$ for correction; Table 4.9; Fig. 4.27, *top left panel*), even when using the average temperature of the four Seyfert 1s in our sample ($T_{e,\text{ave}} = 33600 \text{ K}$) for correction which leads to $n_e \sim 550 \pm 40 \text{ cm}^{-3}$. It remains at the same level $1''.5$ south-west of the center and decreases in the outer regions to the low-density limit at $\pm 4''$ north-west and south-east of the nucleus.

We used the reddening determined from the continuum slope variation relative to the stellar template to correct the observed [O II]/[O III] ratio throughout the whole NLR. The thereby derived ionization parameter may have a greater uncertainty than using the reddening within the NLR as measured from the Balmer decrement: In those objects in which we measured the reddening from both the continuum slope and the narrow $\text{H}\alpha/\text{H}\beta$ value, we observe differences in the reddening distributions (Figs. 4.12 and 4.13) and, moreover, a smaller reddening of the continuum is observed. Thus, for MCG-6-30-15, the absolute ionization parameter values may be overestimated due to a correction by too low reddening values, but we consider the deduced general behavior as reliable: We have shown exemplarily for NGC 1386 that the general distribution of the ionization parameter does not change significantly using either reddening values for correction (Fig. 4.28, *both upper panels*). The resulting ionization parameter peaks at the optical nucleus [$U_{\log(n_e)=3} \sim (2.95 \pm 0.04) \cdot 10^{-3}$] and decreases to $U_{\log(n_e)=3} \sim (0.05 - 0.07) \cdot 10^{-3}$ (Fig. 4.29, *top left panel*).

We trace the gaseous velocity field using the peak wavelength of the [O III] line and the stellar one from the Ca II K absorption along the photometric major axis (Fig. 4.31, *top left panel*). The [O III] velocity of the photometrical center is $v_{\text{hel}} \sim 2375 \pm 20 \text{ km s}^{-1}$, the stellar one slightly lower with $v_{\text{hel}} \sim 2330 \pm 20 \text{ km s}^{-1}$. The velocities scatter within the NLR with a maximum amplitude of $\Delta v \sim 80 \text{ km s}^{-1}$. The stellar velocity field shows a rather flat distribution within the errors and no clear sign of rotation, possible due to the classification of the host galaxy as E/S0.

Fairall 51

Literature data

The Seyfert-1 galaxy Fairall 51 is known for its high polarization, noticed already by Martin et al. (1983), Thompson & Martin (1988), and Brindle et al. (1990). As Fairall 51 is a radio-quiet object, synchrotron emission can be neglected as contribution to the polarization spectrum. The high polarization indicates that a substantial fraction of the observed light is scattered by dust or free electrons in the system.

In his spectroscopic variability studies of Seyfert galaxies, Winkler (1992) states that the broad lines of Fairall 51 were slightly brighter in August 1990 than three years earlier.

Fairall 51 is listed as barred spiral in RC3 [(R'₂)SB(rs)b]. The bar extends to about 12'' on both sides of the nucleus in north-south direction (West et al., 1978). However, Malkan et al. (1998) give Sa from their HST images. The inclination is $i \sim 64^\circ$ (RC3).

Schmid et al. (2001) investigated the origin of the polarization and the geometry of the system using VLT spectropolarimetry. While the AGN continuum and the broad lines reveal a practically identical amount of intrinsic polarization (5% in the red up to 13% in the UV), the narrow lines are unpolarized or show only little intrinsic polarization. The spectrum is much redder in total flux than in polarized flux. These Seyfert 2-like polarization characteristics indicate that the nucleus is partially obscured with the scattering region located far from the BLR and the continuum source. This specific geometry allows to study the BLR both directly and via scattering. From the indistinguishable line profiles in polarized and total light, Schmid et al. (2001) conclude that the velocity field of the BLR is spherically symmetric. The polarization issue is discussed in detail in Section 4.4.10.

Schmitt et al. (2003a) presented HST [O III] emission-line images of Fairall 51. The image is presented in Figure 4.2 (*upper left panel*) with the p.a. of our NTT observations overlaid (p.a. = 160°). The emission is extended by 2''65 along the host galaxy major axis (p.a. = 162°; RC3).

Comparison with our results

Fairall 51 is the object with the strongest iron emission lines relative to H β seen in the nuclear spectrum in our sample: Compared to the average values determined from the four other Seyfert-1 galaxies from Table 4.8, the [Fe VII] $\lambda 5721 \text{ \AA}$ /H β flux ratio is more than twice as high in Fairall 51, the [Fe VII] $\lambda 6087 \text{ \AA}$ /H β flux ratio is roughly three times as high, and the [Fe X] $\lambda 6375 \text{ \AA}$ /H β flux ratio is \sim four times higher than the average value ([Fe VII] $\lambda 5721 \text{ \AA}$ /H $\beta_{\text{ave},4\text{Sy}1\text{s}} \sim 0.15 \pm 0.05$ versus 0.34; [Fe VII] $\lambda 6087 \text{ \AA}$ /H $\beta_{\text{ave},4\text{Sy}1\text{s}} \sim 0.18 \pm 0.05$ versus 0.49; [Fe X] $\lambda 6375 \text{ \AA}$ /H $\beta_{\text{ave},4\text{Sy}1\text{s}} \sim 0.11 \pm 0.05$ versus 0.43). The electron temperature determined in the central spectrum is $T_e \sim 22200 \pm 400 \text{ K}$.

We detect [O III] emission (S/N > 3) out to a distance of 9'' from the nucleus (Table 4.10), i.e. three times larger than the maximum extension of the HST [O III] image from Schmitt et al. (2003a). Emission-line ratios out to $\sim 8''$ indicate ionization by the central AGN source, although the outer 6-7'' north-west of the nucleus (marked as E/F in the diagnostic diagram) show line ratios at the border between those typical for AGNs and those expected for LINERs (Fig. 4.18, *from top third left panel*). Possibly, this change indicates that the influence of circumnuclear H II regions begins to be comparable to the AGN ionization and may be the dominating ionization source further out. However, we are limited by the S/N to measure such a transition. We therefore classify the inner 14'' as NLR (Table 4.10).

The reddening in the NLR is highest $\sim 1''$ north-west of the nucleus and decreases rather smoothly towards the outer parts with the exception of a low reddening value at 1'' south-east of the center and an exceptional high value at $\sim 5''$ north-west. It ranges from $E_{B-V} \sim 0.01 \text{ mag}$ to 0.8 mag (Fig. 4.14, *top right panel*).

The reddening of the central BLR, deduced from the broad H α /H β ratio of ~ 4.4 , is comparable to the central NLR reddening ($E_{(B-V),\text{broad}} \sim 0.45 \text{ mag}$). It indicates that the dust is either associated with the NLR or has an external origin such as the host galaxy.

In the same region where we find line ratios approaching that expected for LINERs, we observe an enhanced surface brightness in the [O III] and H α emission as well as the continuum (Fig. 4.25, *top right panel*). Apart from this secondary peak at 6'' north-west and a tertiary peak observed to the south-east at a comparable distance ($\sim 7''$), the surface brightness is decreasing smoothly with distance from the nucleus in all line and continuum fluxes. Even with the ten times higher spatial resolution of the HST [O III] image, the [O III] surface-brightness distribution do not reveal any subpeaks, but is confined to the central 3''.

The electron-density distribution peaks at the center ($n_e \sim 1430 \pm 40 \text{ cm}^{-3}$) and decreases outwards with two smaller peaks symmetrically around the nucleus at a distance of $\sim 5''$ ($n_e \sim 750 \text{ cm}^{-3}$ to the south-east and $n_e \sim 580 \text{ cm}^{-3}$ to the north-west). Further out, it reaches the low density limit. The two density peaks on both sides of the nucleus roughly coincide with the enhanced surface brightness and the north-western region in which line ratios close to LINER ones are observed (Fig. 4.27, *top right panel*).

The ionization parameter in Fairall 51 is centrally peaked, decreasing rapidly towards the outer NLR ($U_{\log(n_e)=3} \sim 9.3 \cdot 10^{-3}$ to $U_{\log(n_e)=3} \sim 0.7 \cdot 10^{-3}$). It reveals a small secondary peak at $\sim 6''$ north-west of the nucleus (Fig. 4.29, *top right panel*).

Is the match of the increased electron density, ionization parameter, surface brightness as well as the line ratios close to LINER type at 5–6'' to the north-west of the nucleus pure coincidence or does it hint e.g. shocks occurring at these distances? Unfortunately, there is no published information on the radio source in Fairall 51 allowing to discuss a possible jet-NLR interaction. Alternatively, the bar (p.a. $\sim 180^\circ$) may influence the NLR, resulting in the observed properties on both sides of the center (p.a._{obs} $\sim 160^\circ$).

The velocity field was derived from the peak wavelength of the narrow H α emission line only, as the [N II] line is difficult to disentangle in the central parts. It shows a steep central increase from blueshifted velocities at 2'' south-east of the centrum towards redshifted velocities at 2'' north-west of the nucleus with a range of $\Delta v \sim 180 \text{ km s}^{-1}$ (Fig. 4.31, *top right panel*). Beyond a radius of 2'', the velocities approaches again the central value ($v_{\text{hel}} \sim 4230 \pm 20 \text{ km s}^{-1}$) and the curve flattens, especially in the north-western region. The velocities of the central arcseconds may be influenced by the bar potential. We do not trace the stellar velocity curve as the Ca II K absorption line is too noisy for an accurate fit.

The existence of broad extended H α emission seen out to $\sim 6''$ from the nucleus (Table 4.14; Fig. 4.32) is discussed in Section 4.4.10, focussing on the polarized emission observed by various authors. In the central spectra, the broad emission lines in both H α and H β clearly dominate the profile, confirming the classification of Fairall 51 as pure Seyfert-1 galaxy.

NGC 6860

Literature data

The luminous infrared galaxy NGC 6860 shows a composite nature of a Seyfert-1 nucleus embedded in a dusty star formation environment (Lípari et al., 1993). While NED classify NGC 6860 as Seyfert 1, Cid Fernandes et al. (1998) and Lípari et al. (1993) find emission lines typical for a Seyfert 1.5.

Lípari et al. (1993) studied NGC 6860 in detail, presenting optical imaging as well as optical and near-infrared spectroscopy. Based on broad-band images of the host galaxy

which show various morphological details such as a compact nucleus, two weak spiral arms, a bar, a bulge, an inner ring and possibly an outer ring, they classify NGC 6860 as (R')SB(r')b; NED gives (R')SB(r)ab. The p.a. of the photometric major axis is 34° , the inclination $i = 61^\circ$ (RC3). The $H\alpha + [N II]$ image shows a bright emission-line region associated with the AGN activity and a circumnuclear ring of star formation with clear signs of young stars in the spectrum. The $[O III]$ image reveals emission extended by $10''$ in east-west direction, perpendicular to the direction of the bar (p.a._{bar} $\sim 13^\circ$). Lípári et al. (1993) use templates from Bica (1988) to fit the stellar population, finding that an S3 template represents the nuclear stellar population, while the rather young population of an S6 template fits the inner star formation ring. The bar reveals a typical spectrum of an old stellar population. A high electron temperature ($T_e \sim 35000$ K) is observed in the nuclear region. NGC 6860 is classified as a typical intermediate case between AGN activity completely dominating the energy input and starburst galaxy where the ionizing continuum is spread over a much larger star-forming region (Lípári et al., 1993). This is strengthened by line ratios in diagnostic diagrams which locate the galaxy in a transitional zone between areas occupied by AGNs and H II regions. Along the bar, the velocity curves from both stellar absorption lines as well as emission lines are typical for purely circular motion, implying a central of $\sim 1.5 \cdot 10^{11} M_\odot$ within a radius of $35''$. Systematic deviations of such a smooth velocity curve are seen in the innermost $5''$ from emission lines. Lípári et al. (1993) interpret these deviations as gas inflow, possibly fueling the Seyfert nucleus.

Cid Fernandes et al. (1998) performed stellar population modeling with the result that the stellar population derived from absorption lines is typical to an S2 template in the central region. The continuum ratios show a gradient decreasing from S4 in the inner $5''$ radius to S5 further out. A featureless continuum can be seen in the nucleus.

Near-infrared imaging reveals an asymmetrical bar along p.a. $\sim 10^\circ$ which is more extended to the north than to the south. There is evidence for a secondary smaller inner bar. Spiral arms detach from the southern end of the outer bar and at the west end of the inner bar (Márquez et al., 1999).

The HST $[O III]$ image from Schmitt et al. (2003a) is elongated in east-west direction by $\sim 4''.5$ and in perpendicular direction by $2''.4$.

Márquez et al. (2004) also presented the gas kinematics of NGC 6860, concluding that the p.a. of the photometric major axis is in close agreement with the kinematical major axis. Along the major axis, gas rotation is observed with a velocity range of ± 200 km s^{-1} . Along different position angles, the velocity field is more complex, probably due to the presence of the bar.

Comparison with our results

The p.a. of the long slit used in our NTT observations traces the maximum extent of the $[O III]$ emission seen in the HST image of Schmitt et al. (2003a) (p.a. = 85° ; Fig. 4.2, *upper right panel*). Besides MCG-05-13-017, NGC 6860 is the other Seyfert-1 galaxy in our sample which shows, in all three diagnostic diagrams, a clear transition between central line ratios falling in the AGN regime and outer ones typical for H II regions (Fig. 4.16, *left panels*). While we detect $[O III]$ emission at a $S/N > 3$ out to a distance of $r \sim 10''$ in east-west direction, comparable to the maximum extension of the $[O III]$ groundbased image of Lípári et al. (1993), the emission beyond $5''$ can be attributed to circumnuclear star forming regions (Table 4.10).

Our results confirm the classification of NGC 6860 as an intermediate case between AGN activity and starburst galaxy (Lípari et al., 1993). While Lípari et al. (1993) find line ratios in the transitional zone between Seyfert galaxies and H II regions, we are able to trace the radial varying ratios and determine the radius where the transition takes place in all three diagnostic diagrams. Showing that the transition occurs at the same distance in the second diagnostic diagram is essential to exclude spatial variations of physical parameters resulting in a transition of line ratios from the AGN to the H II-region regime despite an intrinsic AGN photoionizing source (Section 4.4.4). Thus, we can determine the NLR size of NGC 6860 to a radius of $r \sim 5''$ (observed along a p.a. of 85°), i.e. the AGN radiation field dominates over the stellar one in the inner $10''$. The maximum [O III] extent we observe is four times larger than what is observed in the HST [O III] image by Schmitt et al. (2003a) ($d \sim 20''$ versus $d \sim 5''$).

In the center, we find a high electron temperature of $T_e \sim 36325 \pm 250$ K, in agreement with the results of Lípari et al. (1993) (Table 4.9).

The reddening values vary rather randomly between $E_{B-V} \sim 0.1$ mag and 0.6 mag with a central value of $E_{B-V} \sim 0.31 \pm 0.02$ mag. Moreover, there is no significant difference between the reddening in the NLR and that in the surrounding H II regions (Fig. 4.14, *middle left panel*). The BLR shows a reddening comparable to that of the NLR (in the central $2''$: $H\alpha_{\text{broad}}/H\beta_{\text{broad}} \sim 5.5$, $E_{B-V} \sim 0.6$ mag). As in Fairall 51, it indicates dust either within the NLR or dust in the host galaxy.

The surface-brightness distributions of line emission and continuum show a general decrease with distance from the center (Fig. 4.25, *middle left panel*). While the [O III] surface brightness exceeds that of H α in the central $\sim 10''$, i.e. in the NLR, the H α surface brightness is higher in the outer region, as is expected from our diagnostic diagrams. The continuum surface brightness smoothly decreases with radius. A secondary peak in the H α surface-brightness distribution is seen $\sim 7''$ east of the nucleus and may be attributed to a region of enhanced star formation. The [O III] surface-brightness distribution of the HST image extends out only to $\sim 3''$ from the nucleus and shows a subpeak at $\sim 1''$ east of the center. This peak is smoothed out in our ten times lower spectral resolution.

The electron density is highest at the center ($n_e \sim 1015 \pm 50$ cm $^{-3}$), decreases with radius towards the low density limit and shows two subpeaks at $\sim 3''$ west and $\sim 6''$ east of the nucleus (Fig. 4.27, *middle left panel*). While the eastern subpeak lies within the NLR, the western one falls just outside.

The ionization parameter in NGC 6860 is generally decreasing with distance from the nucleus ($U_{\log(n_e)=3} \sim (2.73 \pm 0.04) \cdot 10^{-3}$ to $U_{\log(n_e)=3} \sim 0.23 \cdot 10^{-3}$; Fig. 4.29, *middle left panel*). However, it reveals a secondary peak at $\sim 2''$ west of the nucleus ($U_{\log(n_e)=3} \sim 1.7 \cdot 10^{-3}$).

The velocity measured along p.a. = 85° using the average value of the H α and [N II] peak wavelengths reveals an ‘‘S’’ like structure (Fig. 4.31, *middle left panel*). The central velocity is $v_{\text{hel}} \sim 4400 \pm 20$ km s $^{-1}$. The largest velocity range is observed in the central $4''$ ($\Delta v \sim 265$ km s $^{-1}$) with a blueshifted velocity of $v_{\text{hel}} \sim 4285$ km s $^{-1}$ to the east and a redshifted one of $v_{\text{hel}} \sim 4550$ km s $^{-1}$ to the west. Further out, the velocities get again closer to the central value and the curve seems to flatten beyond the NLR in the east. Lípari et al. (1993) already discussed deviations from a smooth rotational model in the central $5''$ and speculate that these deviations are consistent with gas inflow along the bar, fueling the AGN. Our gaseous velocity curve is comparable to the H α velocity distribution along p.a. = 64° observed by Márquez et al. (2004), i.e. at a p.a. which

crosses the bar and where they report a steeper velocity gradient than expected from a simple rotation model.

At p.a. = 124° , they observe a similar asymmetric S-like feature close to the nucleus. The residuals in the inner $\pm 4''$ are attributed to the presence of the inner bar.

As the narrow components in both H α and H β which are superimposed on the broad components are clearly visible in our central spectra, we agree with Lípari et al. (1993) to classify NGC 6860 as Sy1.5.

We find broad extended H α emission out to a distance of $r \sim 4\text{--}5''$ from the center (Table 4.14; Fig 4.34) and discuss the origin in Section 4.4.10.

Mrk 915

Literature data

Mrk 915 is a highly-inclined ($i \sim 80^\circ$) Seyfert-1 galaxy with a companion at $126''$ to the south-east (Keel, 1996). Goodrich (1995) observes flux changes in the broad H α line which has almost disappeared in 1993 compared to spectra obtained nine years earlier (their Fig. 3). If this change can be explained by an increase in reddening, then $\Delta E_{(B-V)} \geq 0.53$ mag. From these observations and from the evidence of short-term spectral changes in several other Seyferts, they conclude that the dusty clouds have high transverse velocities and must thus be close to, but outside of, the bulk of the BLR itself.

A groundbased H α + [N II] image were taken by Colbert et al. (1996), showing extended emission along the major axis (p.a. $\sim 168^\circ$) out to a radius of $15''$ in south-eastern direction. Along a p.a. of 5° , the H α + [N II] emission extends out to $\sim 10''$. Keel (1996) gives a photometric major axis of 166° and shows a rotation curve which covers a range of $\Delta v \sim 410$ km s $^{-1}$.

The radio emission shows an unresolved nuclear structure with a faint tail of emission to the south-west (Schmitt et al., 2001). Mrk 915 lack clear evidence for intrinsic polarization (Smith et al., 2002).

The HST [O III] image of Schmitt et al. (2003a) reveals irregular emission with a major extent of $4''.1$ along p.a. = 5° and $2''.6$ in the perpendicular direction.

Comparison with our results

The long slit of our NTT spectroscopy was placed along the major [O III] extension seen in the HST image of Schmitt et al. (2003a) (Fig. 4.2, *lower left panel*). As the spectra taken in the blue wavelength range were corrupted due to instrumental problems, we did not derive the ionization parameter and the temperature.

We detect [O III] emission at a S/N ≥ 3 out to a radius of $r \sim 12''$, i.e. three times further out than the HST [O III] image (Table 4.10). The [O III] extension obtained from our spectra is comparable to the $r \sim 10''$ extension seen in the groundbased H α + [N II] image at a p.a. of 5° [Colbert et al. (1996), see their Fig. 2h].

Emission-line ratios at S/N > 3 were traced out to a distance of $r \sim 6''$ from the nucleus. Within this region, all ratios are typical for AGN ionization and we thus classify the emitting region as NLR (Table 4.10; Fig. 4.18, *third right panel from top*).

The reddening distribution within the NLR varies and ranges from $E_{B-V} \sim 0.2$ mag at $\sim 6''$ north to ~ 0.8 mag at $1''$ north of the nucleus (Fig. 4.14, *middle right panel*). The nucleus itself shows a slightly lower reddening with $E_{B-V} \sim 0.66$ mag. Calculating the reddening of the BLR in the central $2''$ yields a reddening value comparable to that of the

NLR, indicating that there is no significant dust amount between the broad and narrow Balmer lines ($H\alpha_{\text{broad}}/H\beta_{\text{broad}} \sim 5$; $E_{B-V,\text{broad}} \sim 0.5$ mag).

The surface–brightness distribution of the [O III] and $H\alpha$ emission lines as well as that of the continuum is decreasing with radius (Fig. 4.25, *middle right panel*) with the surface brightness of the emission lines decreasing steeper than that of the continuum. The [O III] surface–brightness distribution determined from the HST image is confined to the central $\sim 4''$ and shows substructure such as a bright shoulder $\sim 1''$ to the north and a secondary peak at $\sim 1''$ to the south of the nucleus. Although this substructure is smoothed out in the lower resolution of our spectra, it reflects in a discontinuity in the surface–brightness distribution of both the [O III] and $H\alpha$ emission: While at $1''$ to the north and south, the surface brightness is only slightly lower than the central one, it falls off significantly at $2''$ north and south.

The electron density is highest at the center ($n_e \sim 570 \pm 35 \text{ cm}^{-3}$ using a temperature of $T_e = 10000 \text{ K}$ for correction). A comparable high density is also observed at $1''$ south of the nucleus ($n_e \sim 565 \text{ cm}^{-3}$). In general, the electron density decreases with distance from the nucleus down to the low density limit in the outer parts (Fig. 4.27, *middle right panel*). Note that the [S II] $\lambda 6716 \text{ \AA}$ emission line is slightly truncated by telluric absorption bands and the absolute density value has to be taken with some caution. However, we consider the slope as reliable.

While the velocity curve derived from Keel (1996) along the photometric major axis (p.a. = 166°) shows clear sign of rotation, with a total velocity range of $\Delta v \sim 410 \text{ km s}^{-1}$ in the central $20''$, the velocity curve obtained from our spectroscopic data along a p.a. of $\sim 5^\circ$ does not reveal the same smooth rotational pattern (Fig. 4.31, *middle right panel*). We observe a velocity range of $\Delta v \sim 220 \text{ km s}^{-1}$ in the central $12''$ which is comparable to the velocity range covered at a p.a. of 166° in the same region [Keel (1996): $\Delta v \sim 250 \text{ km s}^{-1}$; their Fig. 2]. The central velocity is $v_{\text{hel}} \sim 7240 \pm 20 \text{ km s}^{-1}$. We cannot trace the stellar velocity curve from the Ca II K absorption line as it is not covered by our spectral range.

The broad $H\alpha$ emission we find in our nuclear spectra observed in September 2004 is comparable to that seen by Goodrich (1995) in 1984, i.e. it is significantly higher than that observed in 1993, confirming the periodical change of the broad flux during ~ 9 – 10 years suggested by Goodrich (1995) ($F_{H\alpha,1984} = 637 \cdot 10^{-15} \text{ erg s}^{-1} \text{ cm}^{-2}$, $F_{H\alpha,1993} \leq 223 \cdot 10^{-15} \text{ erg s}^{-1} \text{ cm}^{-2}$, $F_{H\alpha,2004} = 649 \cdot 10^{-15} \text{ erg s}^{-1} \text{ cm}^{-2}$).

The detection of broad extended $H\alpha$ emission out to a distance of ~ 4 – $5''$ from the nucleus in Mrk 915 (Table 4.14; Fig. 4.36) is discussed in Section 4.4.10.

As both the broad and the superimposed narrow components in $H\alpha$ and $H\beta$ can be easily recognized in the nuclear spectra, we classify Mrk 915 as Seyfert–1.5 galaxy rather than Sy1. This classification may also be time–dependent, due to the significant periodic changes in the broad $H\alpha$ flux. However, it seems that we did observe in a phase in which the broad $H\alpha$ flux is already strong. If we can nevertheless classify Mrk 915 as Sy1.5 in such a phase, it is implausible that Mrk 915 resembles a Sy1 galaxy in another phase.

NGC 526a

Literature data

NGC 526a is the brighter member of a strongly interacting pair of galaxies; the fainter one is NGC 526b at a distance of $\sim 35''$ to the south-east. The morphological classification of NGC 526a is S0pec (NED). It has an inclination of $i \sim 55^\circ$, with the photometric major axis running along p.a. = 112° .

The Seyfert type is discussed controversially: Mulchaey et al. (1996a) and Whittle (1992) list NGC 526a as Sy2, while NED and RC3 classify it as Sy1.5. Winkler (1992) discuss the presence of broad $H\alpha$ and the absence of broad $H\beta$, suggesting a classification of Sy1.9. They report a low value of the narrow $H\alpha/H\beta$ ratio (~ 3) indicating that the NLR is essentially unreddened while the BLR suffers significant obscuration ($H\alpha/H\beta \geq 10$).

NGC 526a is one of the brightest extragalactic X-ray sources and has been observed in both soft and hard X-rays by various authors [see e.g. Polletta et al. (1996)].

Groundbased emission-line images in [O III] and $H\alpha + [N II]$ are presented by Mulchaey et al. (1996a). The images reveal extended line emission out to $r \sim 10''$ in north-west/south-east direction (a p.a. of 123° is used for long-slit spectroscopy; Fig. 4.2, *lower right panel*), in approximately the direction of the companion galaxy. Excitation maps show evidence of a bi-conical shape of the highest excitation gas. In the color map, the nucleus is red.

Nagar et al. (1999) studied the radio emission of NGC 526a. While at 20 cm, it is a triple radio source elongated in north-west/south-east direction corresponding to the extension of [O III] (Mulchaey et al., 1996a), only the central source is seen at 3.6 cm.

The stellar population synthesis performed by Cid Fernandes et al. (1998) indicates an S3-S4 template derived from the equivalent width of absorption lines, while at $7''$ from the nucleus, the width are typical for an S4-S5 template.

Comparison with our results

We detect extended [O III] emission at a $S/N > 3$ out to a radius of $\sim 20''$ (~ 7240 pc) from the nucleus (Table 4.10), i.e. twice as far as seen in the groundbased emission-line image of Mulchaey et al. (1996a). The line ratios needed for diagnostics and the derivation of physical parameters were determined out to $9''$ (~ 3260 pc) to the north-west and south-east from the nucleus. All emission-line ratios within this region indicate AGN ionization (Table 4.10; Fig. 4.18, *bottom panel*). The central temperature is $T_e \sim 23330 \pm 1700$ K.

Our spectra do not show signs of broad $H\beta$ emission but a broad $H\alpha$ component is clearly visible in the central $2''$ (Table 4.14). Thus, we agree with Winkler (1992) in classifying NGC 526a as Sy1.9.

The reddening is low throughout the whole NLR ($E_{B-V} \sim 0.06-0.4$ mag), with the highest values in the center and $\sim 5.5''$ south-east of the nucleus (Fig. 4.14, *bottom left panel*). The central (narrow) $H\alpha/H\beta$ ratio of ~ 4.1 is slightly higher than the value reported by Winkler (1992) (~ 3) but significantly lower than the reddening of the BLR: We tried to fit any spurious underlying broad $H\beta$ flux and find, in agreement with Winkler (1992), a high reddening of the BLR with $H\alpha/H\beta \geq 10$, corresponding to $E_{B-V, \text{broad}} \geq 1.26$ mag.

The surface–brightness distributions of NGC 526a are rather smooth, decreasing with distance from the nucleus and showing a secondary peak at $\sim 7''$ north–west of the nucleus in both the [O III] and H α emission lines (Fig. 4.25, *bottom left panel*). The electron density is highest at the nucleus ($n_e \sim 835 \pm 70 \text{ cm}^{-3}$) and decreases outwards to the low density limit (Fig. 4.27, *bottom left panel*). Note that the [S II] $\lambda 6731 \text{ \AA}$ emission line is slightly truncated by telluric absorption bands and the absolute density value has to be taken with some caution, but we consider the slope as reliable.

The ionization parameter is also decreasing with radius [$U_{\log(n_e)=3} \sim (2.89 \pm 0.05) \cdot 10^{-3}$ to $U_{\log(n_e)=3} \sim 0.55 \cdot 10^{-3}$] (Fig. 4.29, *middle right panel*).

Although we observe roughly along the photometric major axis (p.a.m.a. $\sim 112^\circ$ compared to p.a.[OIII] $\sim 123^\circ$), the gaseous velocity curve of NGC 526a does not show signs of rotation (Fig. 4.31, *bottom left panel*). As the galaxy is classified as S0pec in NED, the lack of clear rotational velocities is not surprising. There is a significant drop in velocities $\sim 5\text{--}6''$ north–west of the nucleus, coinciding with the secondary peak seen in the surface–brightness distributions. It is possible that a radio jet interacts with the NLR, resulting in outflowing gas clouds: The p.a. of the extended radio emission at 20 cm observed by Nagar et al. (1999) coincides with the p.a. of the major NLR extension.

The central velocity, determined from the average peak wavelength of H α and [N II], is $v_{\text{hel}} \sim 5640 \pm 20 \text{ km s}^{-1}$. Throughout the NLR, the maximum amplitude of the velocity field is $\Delta v \sim 280 \text{ km s}^{-1}$. We do not trace the stellar velocity curve from the Ca II K absorption line as it is too noisy in most of the spectra.

MCG–05–13–017

Literature data

According to Mulchaey et al. (1996a), the Seyfert–1.5 galaxy MCG–05–13–017 is a strongly perturbed galaxy, showing extended [O III] emission out to a radius of $\sim 11''$ to the south–east around an emission component concentrated in the nucleus. The [O III] emission extends roughly along the host galaxy major axis (p.a. = 160° with $i = 54^\circ$; RC3). The groundbased H α image reveals more symmetrically distributed emission, with the strongest off–nuclear emission within the [O III] extension. From the excitation map, Mulchaey et al. (1996a) concludes that not all of the gas within the south–eastern extension is of high excitation. The host galaxy is classified as S0/a in NED.

The HST image reveals homogeneously distributed [O III] emission around the nucleus (Schmitt et al., 2003a). The total [O III] extension of $\sim 2''$ along p.a. = 140° and $\sim 1''.5$ perpendicular is by a factor of ~ 10 smaller than the one seen in the groundbased image, possibly due to the short exposures of the HST snapshot survey.

The radio emission is unresolved (Schmitt et al., 2001).

Rodríguez–Ardila et al. (2000) study the nuclear spectra of MCG–05–13–017, finding that 44% of the continuum at 5870 \AA is of stellar origin. They derive an electron density of 1000 cm^{-3} .

The absorption line widths and continuum ratios determined by Cid Fernandes et al. (1998) show a strong dilution by a featureless continuum in the nuclear region, while an S5 template is determined at $5''$ and further out.

Tsvetanov & Petrosian (1995) classify 38 H II regions in their groundbased H α + [N II] image of MCG–05–13–017. These 38 regions are distributed in a cloud around the nucleus with distances between $3\text{--}18''$ from the nucleus.

The most extensive spectroscopic study of the extended NLR of MCG-05-13-017 has been performed by Fraquelli et al. (2000). To derive absorption-line free nuclear spectra, a stellar population template was extracted from averaged off-nuclear spectra. After subtracting the template, a featureless continuum remained. Emission-line fluxes were measured along p.a. = 158° out to 17'' from the nucleus. The [O II]/[O III] ratio increases with distance to the nucleus, indicating a decreasing ionization parameter. The gas and stellar kinematics are similar and consistent with circular rotation (along p.a. = 158°) with the south-east side approaching.

Comparing these results with groundbased images of Mulchaey et al. (1996a), Fraquelli et al. (2000) suggest that the nuclear continuum ionizes the gas in the disk along p.a. = 158°, giving rise to the cone-shaped region observed in [O III].

Comparison with our results

We observed along a p.a. of 140° to trace the major [O III] extension seen in the HST image (Fig. 4.3; *upper left panel*). We detect [O III] emission with a S/N > 3 out to a radius of 17'' from the photometrical center (Table 4.10). This is significantly larger than the $d \sim 2''$ total extension seen in the HST snapshot image and also larger than what has been determined from the groundbased image of Mulchaey et al. (1996a) ($r \sim 11''$). The excitation map of Mulchaey et al. (1996a) already indicate that not all of the gas is of high excitation and the diagnostic diagrams in our study can confirm this finding (Fig. 4.16, *all three right panels*). Moreover, we can show that only the central $\pm 3''$ show line ratios typical for AGN ionized gas (marked with 0, A/a, B/b, C/c, respectively in Fig. 4.16) and that the spectra out to $r \sim 11''$ north-west and out to $r \sim 6''$ south-east have line ratios falling in the regime covered by H II regions (D/d to F/k). The outer line ratios coincide with the position of H II regions defined by Tsvetanov & Petrosian (1995): Along the p.a. of 140° as used in our long-slit observations, H II regions start at a distance of 4'' from the nucleus and extend out to 11''. While Fraquelli et al. (2000) attribute emission out to $\sim 17''$ from the nucleus to the extended NLR, we can show that only the central $\pm 3''$ are gas ionized by the central AGN.

This transition cannot be explained by variations of physical parameters such as ionization parameter, electron density or metallicity (Section 4.4.4). We interpret it as real border between the NLR, i.e. the central AGN-photoionized region and surrounding H II regions. The broad emission is confined to the central 2-3'' (Section 4.4.10).

MCG-05-13-017 is the object with the highest central electron temperature in our sample ($T_e \sim 52500 \pm 3000$ K: Table 4.9). The ionization parameter is also high in the center [$U_{\log(n_e)=3} \sim (4.28 \pm 0.1) \cdot 10^{-3}$]. These values reflect in high flux ratios of high-excitation lines (Table 4.8). The nuclear spectrum shows strong [Ne III] $\lambda 3869$ Å emission, even exceeding that of [O II] $\lambda 3727$ Å; it is the highest flux ratio [Ne III]/H β ($F_{\text{dered}} = 3.43$) observed in our sample. Also the ratios [O III] $\lambda 5007$ Å/H β ($F_{\text{dered}} = 16.3$; $R_{\text{dered}} = [\text{O III}] \lambda 4959 \text{ \AA} + 5007 \text{ \AA} / \text{H}\beta \sim 21.7$) and [O I] $\lambda 6300$ Å/H β ($F_{\text{dered}} = 0.79$) are the highest ones of our sample. Additionally, strong coronal lines are observed.

The reddening determined from the Balmer decrement is high at the center ($E_{B-V} \sim 0.46 \pm 0.03$ mag) and decreases with distance to the south-east side where it reaches a minimum value of $E_{B-V} \sim 0.03$ mag. Towards the north-west, it is variable with $E_{B-V} \sim 0.08$ –0.7 mag (Fig. 4.14, *bottom right panel*), in agreement with the results of Fraquelli et al. (2000).

The broad Balmer decrement $H\alpha_{\text{broad}}/H\beta_{\text{broad}}$ of 5.7 indicates a slightly higher reddening of the BLR with respect to the central NLR ($E_{B-V,\text{broad}} \sim 0.7$ mag), possibly due to dust in between the two regions.

The surface-brightness distributions peak in the photometrical center. The emission lines show a difference between the NLR, where the [O III] surface brightness exceeds that of $H\alpha$, and the outer H II region where $H\alpha$ is brighter (Fig. 4.25, *bottom right panel*). At $\sim 8''$ north-west of the center, a secondary peak is seen in both [O III] and $H\alpha$. The continuum surface brightness smoothly decreases with distance from the center. The [O III] surface-brightness distribution determined from the HST image is confined to the central $\sim 2''$ and does not show any substructure.

The electron density is highest in the center ($n_e \sim 2460 \pm 55 \text{ cm}^{-3}$; Table 4.9). This value is roughly 2.5 times higher than the value reported by Rodríguez-Ardila et al. (2000) which is approximately the factor that we took into account when correcting with the observed central temperature of $T_e \sim 52500 \text{ K}$ ¹⁵. The electron density decreases constantly to the outer edge of the NLR where it reaches a minimum of $n_e \sim 55 - 60 \text{ cm}^{-3}$. In the H II regions at both sides of the nucleus, it varies between $n_e \sim 110 - 650 \text{ cm}^{-3}$ and finally reaches the low density limit (Fig. 4.27, *bottom right panel*).

The ionization parameter is peaked in the nucleus ($U_{\log(n_e)=3} \sim (4.28 \pm 0.1) \cdot 10^{-3}$) and rapidly decreases within the NLR down to a value of $U_{\log(n_e)=3} \sim 0.65 \cdot 10^{-3}$ (Fig. 4.29, *lower panel*). It stays low in the H II regions, especially on the north-west side of the nucleus. Our observations confirm the results of Fraquelli et al. (2000) who already suggest that the ionization parameter is decreasing, based on the increased [O II]/[O III] ratio (observed along a slightly different p.a. of $\sim 20^\circ$).

The gas in MCG -05-13-017 along p.a. = 140° follows a smooth velocity distribution characteristic for rotational motion in the plane of the galaxy (photometric major axis = 160° as given in RC3). The velocity field traced by the average of the peak wavelengths of $H\alpha$ and [N II] is shown in Figure 4.31 (*bottom right panel*). The stellar velocities measured from the Ca II K absorption line are distributed similarly, suggesting that gaseous and stellar kinematics are comparable. The velocity of the photometrical center is $v_{\text{hel}} \sim 3780 \pm 20 \text{ km s}^{-1}$ and roughly coinciding with the kinematical center, defined by taking the symmetry center of the outer portions of the velocity curve ($v_{\text{hel}} \sim 3785 \text{ km s}^{-1}$). The maximum amplitude is $\Delta v \sim 220 \text{ km s}^{-1}$.

Though the natural explanation of the observed velocity field is rotation in an inclined emission-line disk in the center, it is not unambiguous: An alternative is outflowing gas with the south-eastern side approaching. However, in that case it is surprising that the kinematical major axis and the bipolar flow are aligned as indicated by the similarity between gaseous and stellar velocities. Interestingly, the velocity curve is steepest within the NLR and flattens in the H II region, favoring an outflow scenario in which the NLR gas is driven outwards by e.g. radiation pressure or jet interaction. However, no clear sign of a radio jet is seen in the radio map which shows only unresolved emission (Schmitt et al., 2001).

If the rotational interpretation of the velocity field applies, we can calculate the rotational velocity and central mass: Taking into account the offset between observed p.a. and photometric major axis of $\theta = 20^\circ$ and an inclination of $i \sim 54^\circ$ (RC3), this translates to a total rotational velocity difference of $\Delta v_{\text{rot}} \sim 320 \text{ km s}^{-1}$, similar to what

¹⁵ $n_e(\text{T}) = n_e(\text{obs}) \cdot \sqrt{\text{T}/10000}$

has been derived by Fraquelli et al. (2000). The rotational velocity can be used to estimate the enclosed mass. Within $R \sim 5''$ (1215 pc), we estimate a central mass of $M \sim 4.3 \pm 0.5 \cdot 10^9 M_{\odot}$ (see Appendix C for details).

4.5 Conclusions

We study high-sensitivity spatially-resolved spectra along the extended [O III] emission of 12 Seyfert galaxies (6 Sy1s, 6 Sy2s) obtained with the VLT and the NTT. To derive the pure emission-line fluxes, we successfully use the galaxy itself as stellar template to subtract the underlying absorption lines in six out of 12 objects.

The nuclear spectra reveal the typical strong NLR emission from oxygen at different ionization states, lines from ionized nitrogen and sulfur, as well as Balmer lines. In most objects, high-excitation iron lines are additionally seen in the central spectra, originating from the powerful and hard ionization source in the center. High-ionization emission lines as well as those with high critical densities tend to be stronger in Seyfert-1 galaxies. We determine the electron temperature and ionization parameter in the optical nucleus and find that they are in general higher in type-1 Seyferts than in type 2s.

Applying diagnostic diagrams to our spatially-resolved spectra, we observe a transition of emission-line ratios from the central AGN region to H II region in four Seyfert galaxies (the Sy2s NGC 1386 and NGC 5643 as well as the Sy1s NGC 6860 and MCG-05-13-017). This transition occurs at a distance of several arcseconds on both sides of the optical nucleus and is observed in all three diagnostic diagrams, i.e. including the second diagnostic diagram involving the [O I] emission line. The most probable explanation for this transition is that the stellar ionization field starts to dominate that of the AGN. We can exclude other effects such as the variation of physical parameters from CLOUDY photoionization modeling. The second diagnostic diagram ([O III]/H β versus [O I]/H α) was essential to reach this conclusion as our photoionization calculations show that there are means to reach the H II-region regime with an AGN as ionizing source in the [N II] and [S II] diagrams. We are thus able to determine the radius of the NLR in these four objects to 300–1200 pc independent of sensitivity and excluding [O III] contamination from circumnuclear starbursts. In former spectroscopic studies, the observed [O III] has often been attributed to the extended NLR. We can show that at least part of this “extended NLR” emission is actually powered by H II regions and that only the central few arcseconds are indeed gas photoionized by the AGN.

In the other eight objects, no such transition is observed but the line ratios fall in the AGN regime in all three diagnostic diagrams. Thus, the determined NLR size is a lower limit, limited by either the S/N of our data or the lack of a strong surrounding stellar ionization field.

We derive physical parameters of the NLR such as reddening, surface brightness, electron density, and ionization parameter as a function of distance from the nucleus. The differences between the reddening distributions determined from the continuum slope and the Balmer decrement argue in favor of locally varying dust intrinsic to the NLR. Both electron density and ionization parameter decrease with radius. In general, the decrease is faster in Seyfert-1 galaxies than in type 2s. This trend can be explained in the framework of the unified model, and we discuss the dependency of observed radial distributions on viewing angle.

The decreasing electron density argues against a simple Strömgen behavior of the NLR gas which has been suggested by the NLR size–luminosity relation with a slope of 0.33. The decreasing ionization parameter in the individual objects do not rule out a common effective ionization parameter in AGNs as suggested by a slope of 0.5 of the NLR size–luminosity relation. These results are in agreement with the predictions of our theoretical model developed in Chapter 3.

We discuss the results on an object–by–object basis, led by a detailed case study of the prototypical nearby Seyfert–2 galaxy NGC 1386. In individual objects, substructures are seen in both the ionization parameter and electron density and can often be interpreted as signs of shocks from the interaction of a radio jet and the NLR gas.

In several objects (7 out of 12), the gaseous velocity distribution is characteristic for rotational motion in an (inclined) emission–line disk in the center. However, this interpretation is not unambiguous. Alternatives are for example outflowing gas from jet/NLR interactions, inflowing gas fueling the AGN, gas moving along elliptical streamlines in a barred potential or a rotating gas ring. These scenarios or a superposition of them may also explain deviations from a smooth rotational model. For those objects where we can trace the stellar and the gaseous velocity field, both are in general similar to each other. For the objects which show a transition from the central NLR to surrounding H II regions, the gaseous velocity curve does not show a different behavior in these two regimes. It indicates that the NLR does not consist of a gas component intrinsically different from that of the normal ISM with its own kinematic, but is gas in the galactic disk photoionized by the AGN. These results suggest that the torus axis is not aligned with the galaxy disk; rather, the ionization cone seem to lie in the disk.

We find evidence for extended broad H α lines in three of our six Seyfert–1 galaxies (Fairall 51, NGC 6860, Mrk 915). We discuss possible explanations for this observational result and exclude an instrumental or seeing effect. We favor scattering of BLR emission as the most probable scenario. It is supported by strong polarization seen in one of the objects (Fairall 51). Subsequent polarization measurements of the other two objects are needed to scrutinize this explanation.

Applying the methods presented here to a larger sample of Seyfert galaxies will help to verify the NLR size–luminosity relation. Our results have shown that although [O III] imaging is less time intensive than the spectroscopic method, it often yields an either too small NLR size in case of low sensitivity or a too large NLR size in case of circumnuclear H II regions contributing to the [O III] emission. Using the new 3D spectroscopic techniques (e.g. VLT/VIMOS¹⁶) has the advantage that one can determine the NLR size in all directions from the center, not only in the major [O III] extension as in our case. It is a worthwhile investigation to extend this approach to the luminous cousins of Seyferts, to quasars (type 1 and type 2). We successfully applied for observing time at the VLT with both long–slit spectroscopy (FORS1¹⁷) and 3D spectroscopy (VIMOS¹⁸) and hope to be able to study the NLR of quasars with these methods. Nevertheless, one has to keep in mind that this definition of the NLR size may not be unambiguous as it depends on the distribution of young stars surrounding the NLR.

¹⁶ Visible MultiObject Spectrograph

¹⁷ PI: Marcus Albrecht, 075.B–0298, 9 h service mode (A priority), partly carried out in April 2005, the rest to be carried out in September 2005

¹⁸ PI: Marcus Albrecht, 076.B–0770, 12 h service mode (A priority) to be carried out in March 2006

Conclusions

5.1 Summary

We use the NLR size and luminosity determined from HST narrow-band images of Seyferts and their luminous counterparts, quasars, to study the size–luminosity relation for type–1 and type–2 AGNs. We find that the NLR radius of type–1 objects increases with roughly the square root of the [O III] luminosity, a behavior which can be explained if, on average, all AGNs have the same ionization parameter, density, and ionizing spectral energy distribution. Type–2 objects show a flatter slope of ~ 0.33 , expected for NLR gas distributed with constant density in a sphere (Strömgren law). Comparable relations persist when using groundbased data instead, although they show significantly larger sizes due to the higher sensitivity than the HST snapshot survey. We develop a model to probe whether the different observed slopes for type–1 and type–2 AGNs can be explained by a dependency on viewing angle in the framework of the unified scheme. When assuming the concept of a receding torus, the model is indeed able to reproduce the observed slopes of the NLR size–luminosity relation, with the intrinsic NLR size scaling with the square root of the AGN luminosity.

In addition to the NLR size–luminosity relation, we find that the BLR and the NLR sizes are related. Such a correlation can in principle be used to estimate black hole masses directly from the NLR size, avoiding the time–consuming derivation of the BLR size via reverberation mapping.

The surface–brightness profiles of the NLR are in agreement with the expectation from the unified scheme: The majority of type–1 AGNs reveal profiles typical for halo–like gas distributions while most type–2 AGNs show signs of elongated extended emission. The major part of the total [O III] luminosity is often emitted in an unresolved central source, indicating that the critical factor of the NLR size–luminosity relation is the size and its dependency on sensitivity of the observations.

To look for a definition of the NLR size which is less dependent on sensitivity and stellar contribution, we analyze long–slit spectroscopy of 12 Seyfert galaxies obtained with the NTT/EMMI and the VLT/FORS1. We show that using the galaxy itself as stellar template is in most cases a well suited approach to subtract the underlying absorption lines. Applying diagnostic line–ratio diagrams to our spatially resolved spectra, we find a transition of emission–line ratios from the central AGN–photoionized region

to circumnuclear H II regions in four galaxies. CLOUDY photoionization models show that this transition is due to the stellar ionization field starting to dominate that of the AGN and that it cannot be explained by other effects such as the variation of metallicity, density or ionization parameter. We are thus able to determine the “real” extent of the NLR in these objects. Comparing the sizes to those derived from [O III] images shows the difficulties of determining the NLR size from narrow-band imaging alone: In case of low sensitivity, images may lead to an underestimation of the NLR size; in case of high sensitivity and surrounding H II regions, an apparently larger NLR size is deduced. However, the uncertainty of the NLR size due to different determination methods is small enough to not affect the general slopes of the NLR size–luminosity relation which extends over four orders of magnitudes in luminosity and two orders of magnitudes in size.

We measure the emission–line fluxes and ratios of several lines as a function of distance from the nucleus and derive gas properties such as reddening, electron density, and ionization parameter with unprecedented detail. Both electron density and ionization parameter decrease with distance, indicating that the NLR is photoionized by a central source only. Deviations from this general behavior can be interpreted as signs of shocks from the interaction of a radio jet with the NLR gas. The decrease of electron density shows that a simple Strömgen law cannot be used to explain the NLR size–luminosity relation for type–2 AGNs, in agreement with the results of our model. In several cases, the comparison of gaseous and stellar velocity curves reveals signs of rotational motion. Moreover, for objects with surrounding H II–like emission, we observe no break in velocities from the NLR towards the H II regions. These results suggest that the torus axis is not aligned with the galaxy disk; rather, the ionization cone seem to lie in the disk.

The methods developed and successfully applied here give important insights into the size, structure, and physical properties of the NLR in active galaxies.

5.2 Outlook

Applying these methods to a larger number of objects, especially the recently discovered type–2 quasars, is a worthwhile investigation to study the NLR in these sources. Long–slit spectra of two quasars have already been obtained with VLT/FORS1 and another quasar will be observed in September 2005. Using the new 3D spectroscopic techniques allows to address also the NLR structure of these objects: The presence and opening angle of any putative ionization cone will shed light on the receding–torus concept and probe the extension of the unified model towards higher AGN luminosities. Observing time with VLT/VIMOS has been granted for March 2006.

Studying the NLR of high–z quasars will show whether the NLR size–luminosity relation can be extrapolated towards higher luminosities or whether the NLR gas may escape the system leading to AGNs with weak or no [O III] emission.

Polarization measurement of the three Seyfert–1 galaxies with apparently extended broad lines will probe the proposed scattering scenario.

On a theoretical basis, numerical simulations extend the model developed here to estimate the effects of a disk NLR distribution and a decreasing density on the size–luminosity relation. These simulations have already been started and will enable us to also study the effect of the obscuring torus on the observed [O III] emission. From the simulations, NLR surface–brightness profiles can be created and compared to the observed ones presented in this thesis.

Appendix A

Hubble Constant and World Model

We here summarize how luminosities and linear scales were calculated throughout this thesis. We adopt a Hubble constant of $H_0 = 71 \text{ km s}^{-1} \text{ Mpc}^{-1}$ as well as a homogeneous, isotropic, flat world model, which includes Einstein's cosmological constant Λ in agreement with the recent results of the Wilkinson Microwave Anisotropy Probe (Bennett et al., 2003): $\Omega_{\text{matter}} = 0.27$ and $\Omega_{\Lambda} = 0.73$.

Luminosity distances were calculated using redshifts relative to the 3K microwave background

$$v_{\text{new}} = v + v_{\text{apex}} [\sin b \cdot \sin b_{\text{apex}} + \cos b \cdot \cos b_{\text{apex}} \cdot \cos (l - l_{\text{apex}})] \quad , \quad (\text{A.1})$$

with $v_{\text{apex}} = 371 \text{ km s}^{-1}$, $b_{\text{apex}} = +48.26^\circ$ and $l_{\text{apex}} = 264.14^\circ$ (Fixsen et al., 1996) and $z = z_{3\text{K}} = \frac{v_{\text{new}}}{c}$, using the NED velocity calculator.

For $\Omega_{\text{total}} = \Omega_{\text{matter}} + \Omega_{\Lambda} = 1$, the luminosity distance (in cm) is given as:

$$d_l = (1 + z) \cdot \frac{c}{H_0} \int_1^{z+1} \frac{dz'}{z' \cdot \sqrt{\Omega_{\text{matter}} \cdot z' + \Omega_{\Lambda}/z'^2}} \quad . \quad (\text{A.2})$$

This luminosity distance is used

(i) to calculate the physical extension of a source with the angular diameter θ :

$$R = \frac{\theta \cdot d_l}{(1 + z)^2} \quad , \quad (\text{A.3})$$

(ii) to derive a linear scale which gives the arcseconds corresponding to one parsec in the galaxy:

$$D = 4.848 \cdot 10^{-6} \cdot d_l \quad , \quad (\text{A.4})$$

(iii) to calculate luminosities from measured fluxes:

$$L = 4\pi \cdot d_l^2 \cdot \phi \quad . \quad (\text{A.5})$$

Note that the difference between applying the Hubble law directly ($d = v/H_0$) instead of using the adopted world model lies within the uncertainty of H_0 and v for the Seyfert galaxies. However, for consistency, we use equation A.2 to derive the luminosity distance for all objects (i.e. including the quasars).

Observed Surface–Brightness Profiles

Here, we present the surface–brightness profiles (SBPs) for 58 Seyfert galaxies from Schmitt et al. (2003a) and seven quasars from Bennert et al. (2002). The *left panel* shows a logarithmic plot in $L_{[\text{OIII}]}^{\text{area}}$, while in the *right panel*, $L_{[\text{OIII}]}^{\text{area}}$ is normalized to 1 for comparison. The first 21 Seyfert galaxies are all type 1s, the following 37 type 2s. All Seyferts are plotted with an x–axis covering a range of ± 2000 pc and the quasars with one of ± 6000 pc, for comparison. The data points which fall below the 3σ limit (as given by Schmitt et al. (2003a), their Table 2 and by Bennert et al. (2002), their Table 2) are shown as open symbols. The classification of the SBP type [0, (0), 1, 2] is shown in brackets behind the name of the object (*right panel*). Note that “1” and “2” do not refer to the Seyfert type.

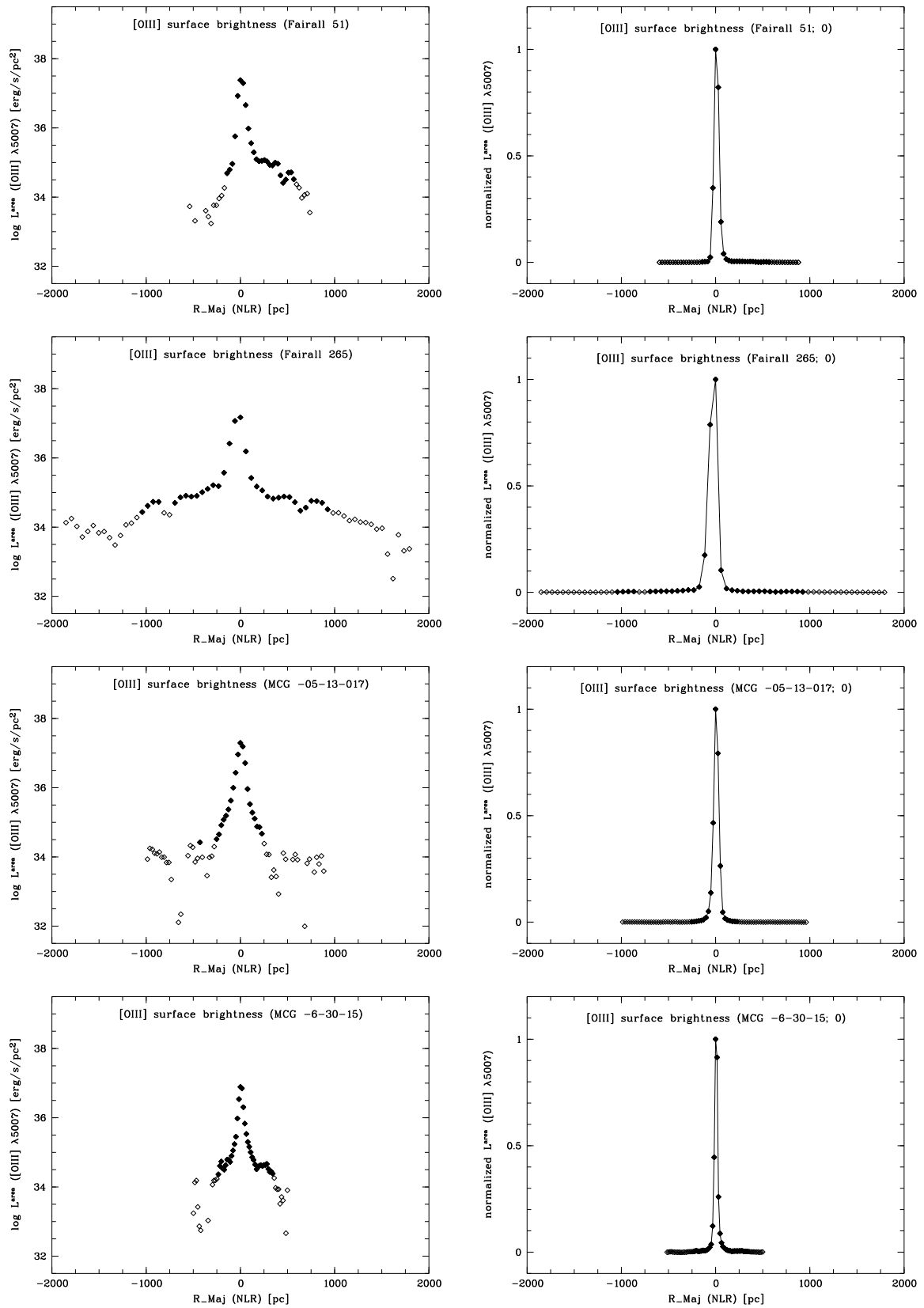
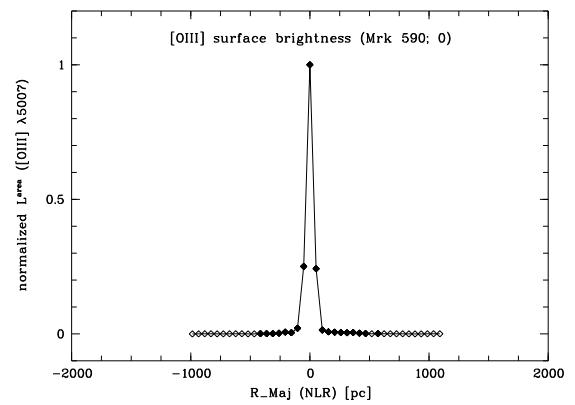
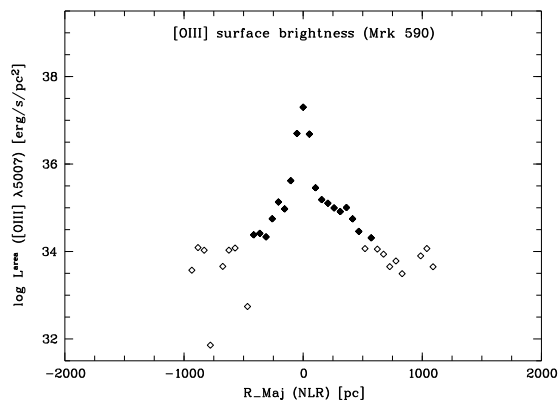
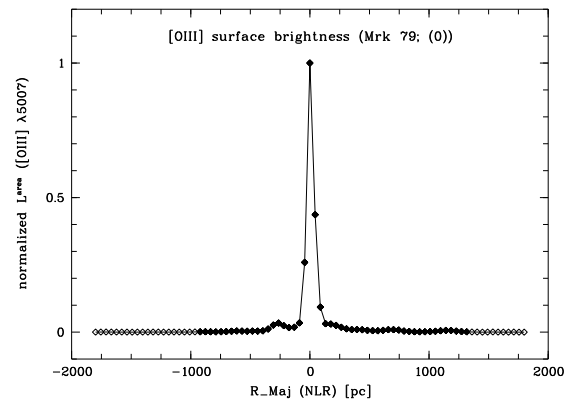
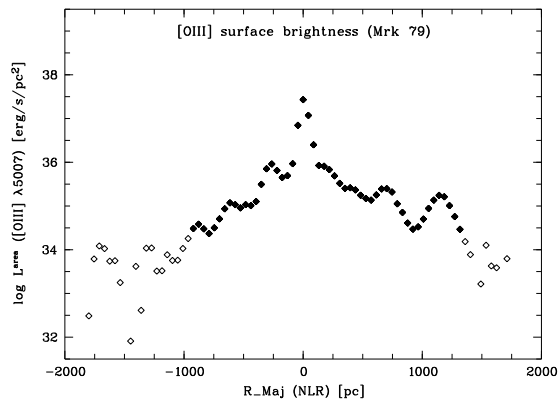
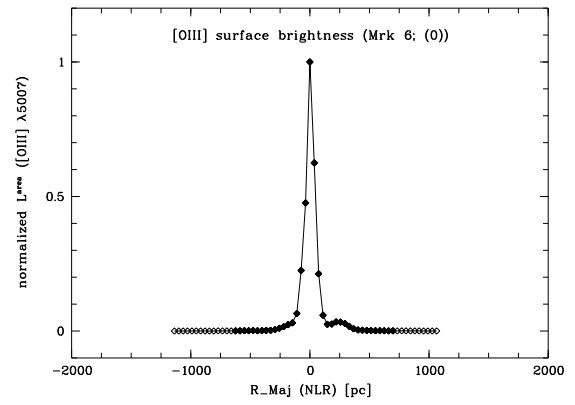
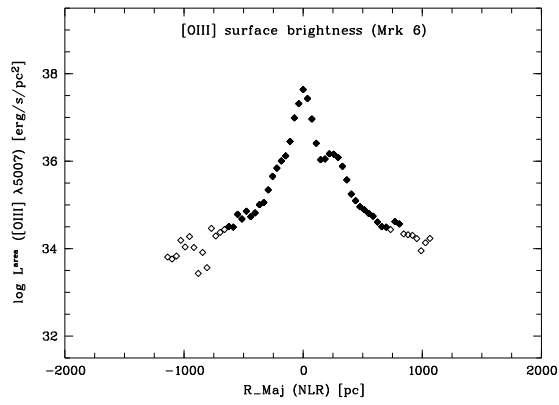
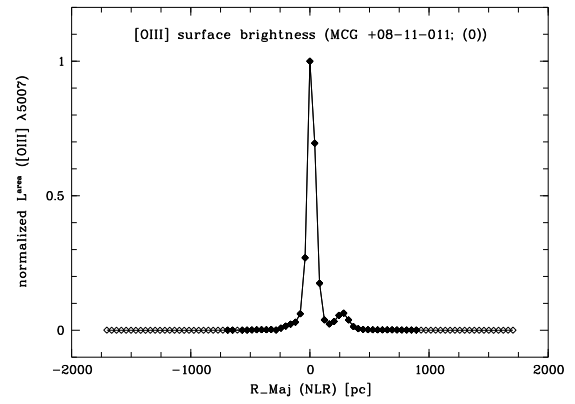
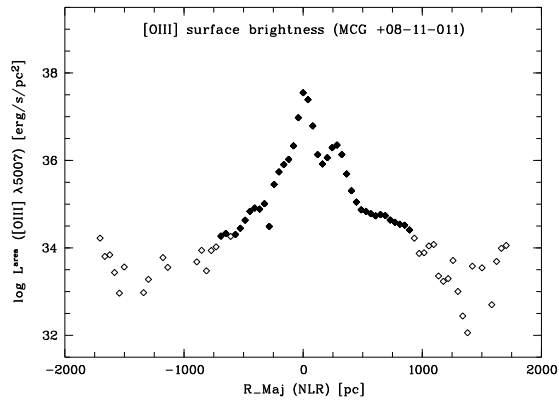
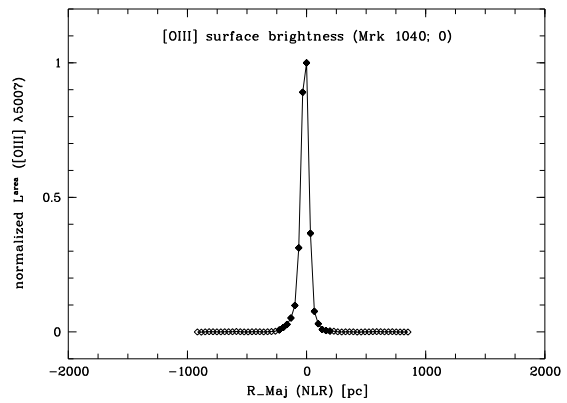
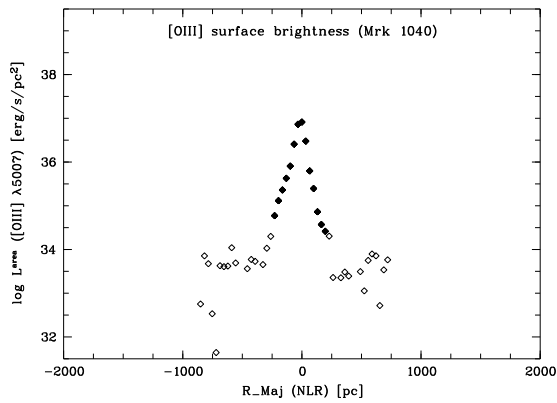
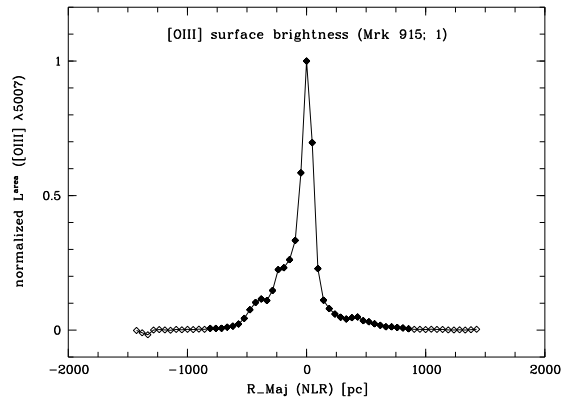
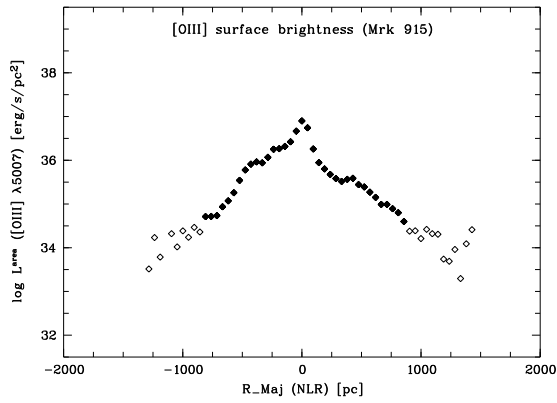
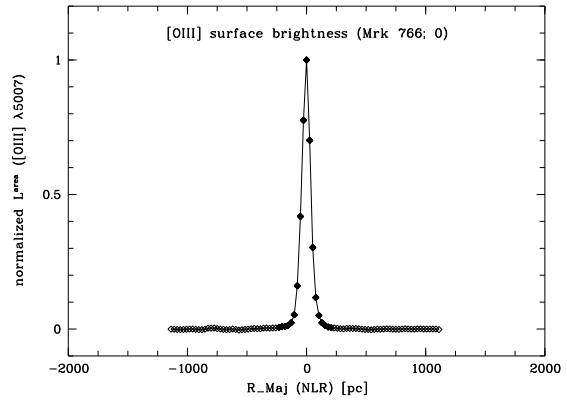
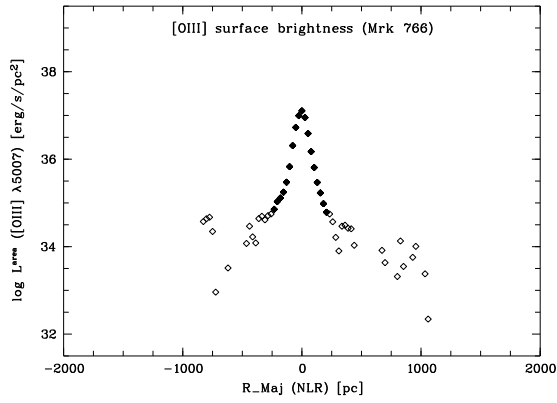
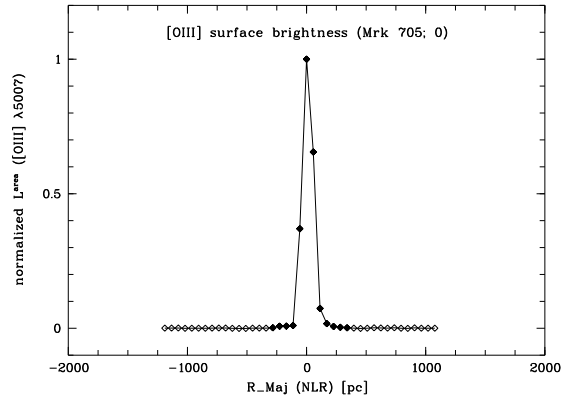
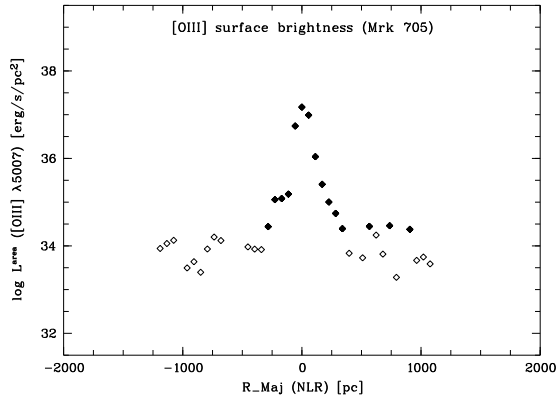
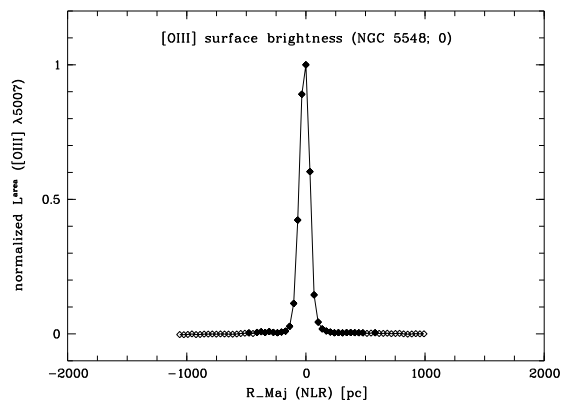
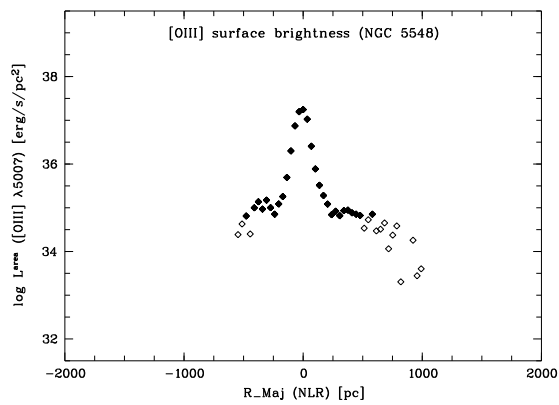
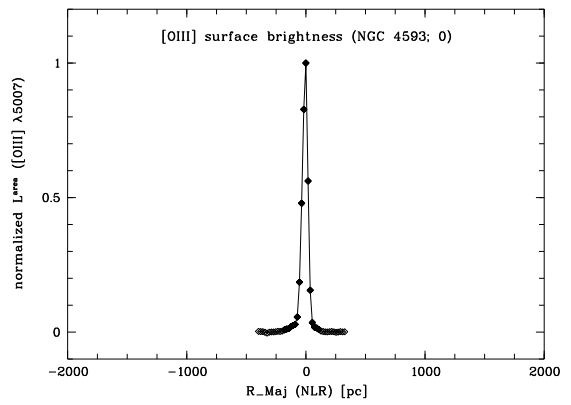
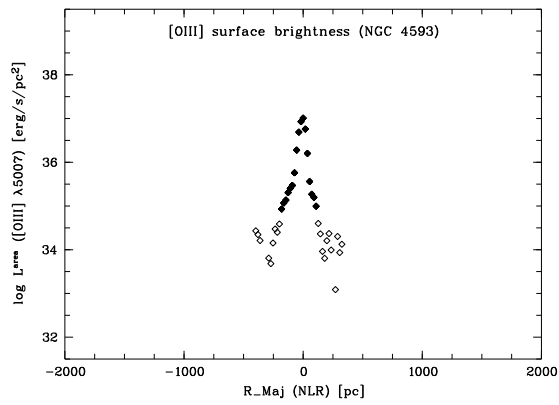
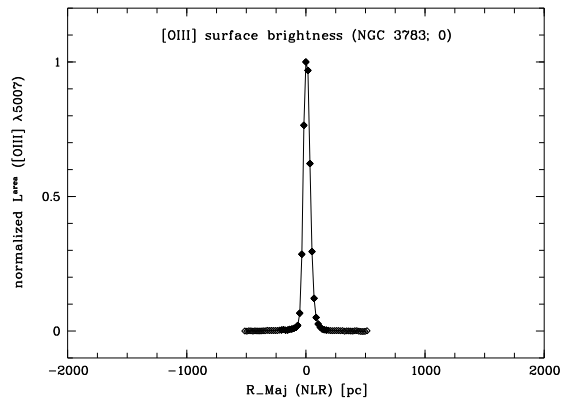
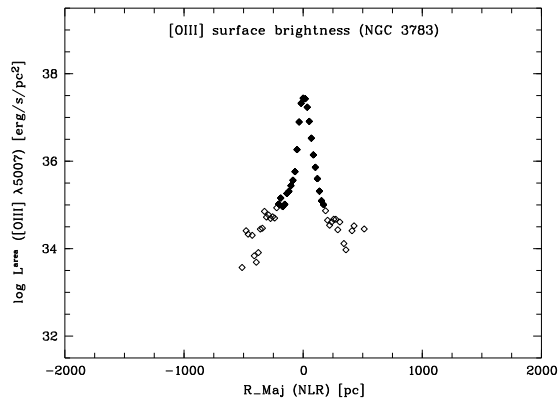
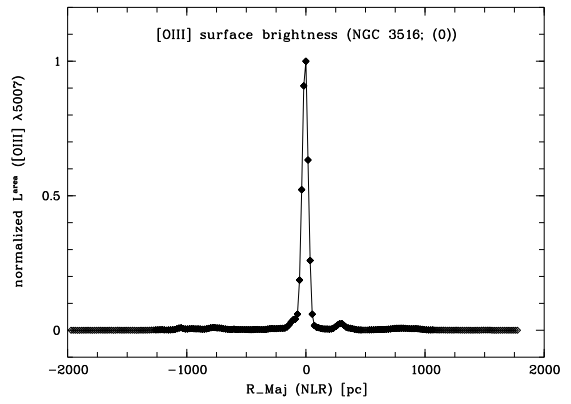
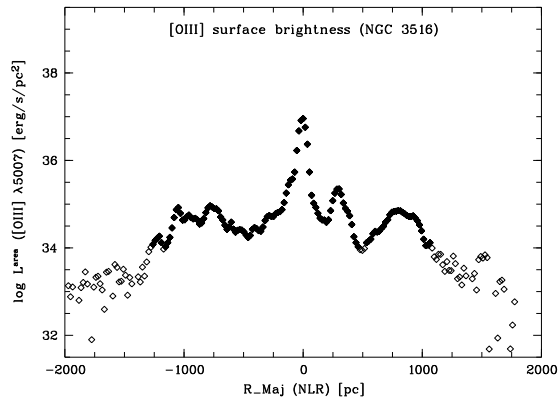
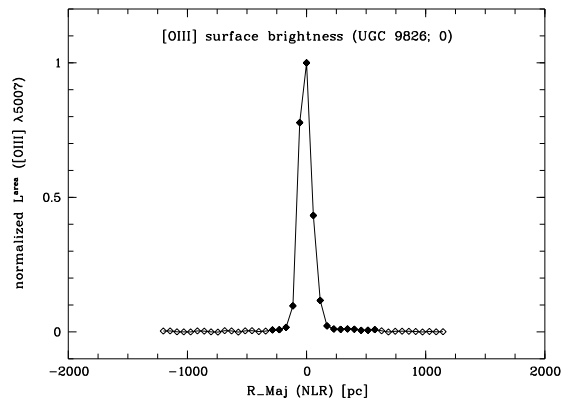
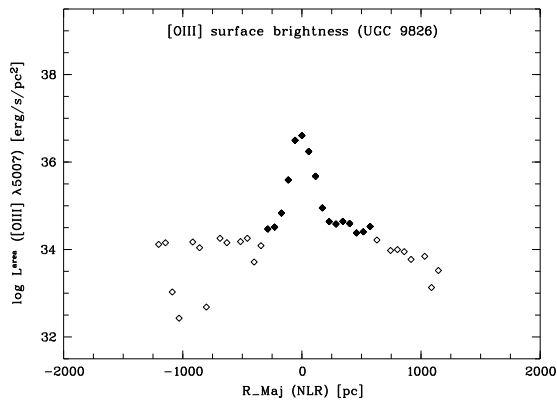
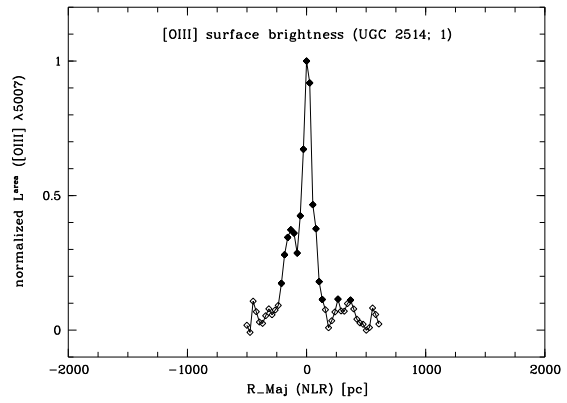
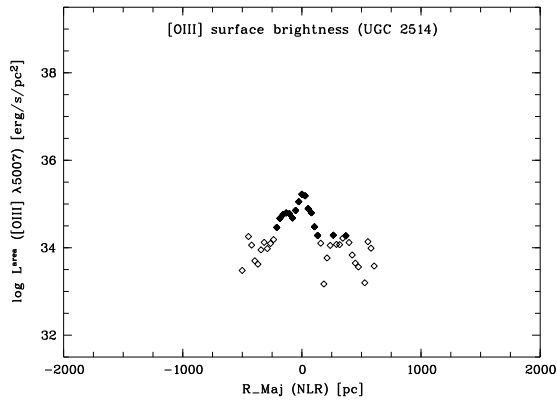
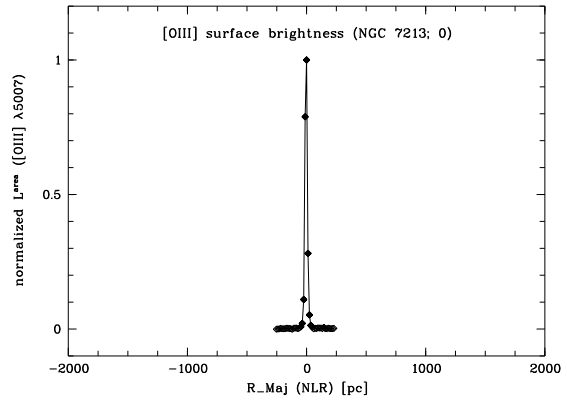
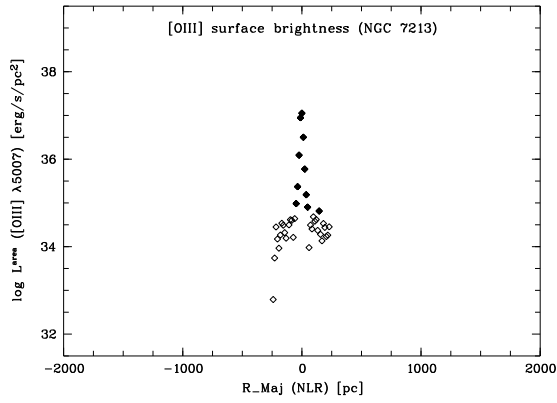
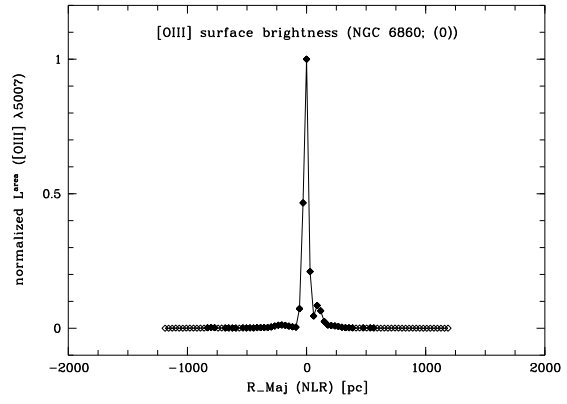
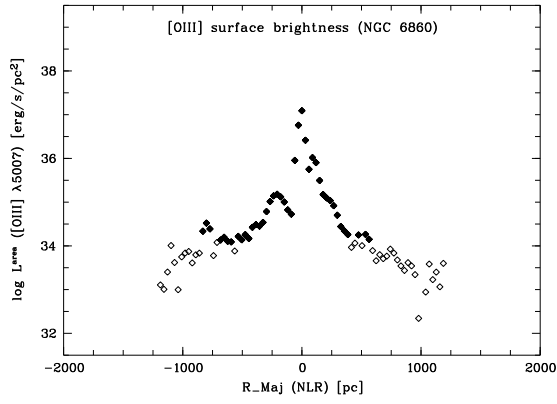


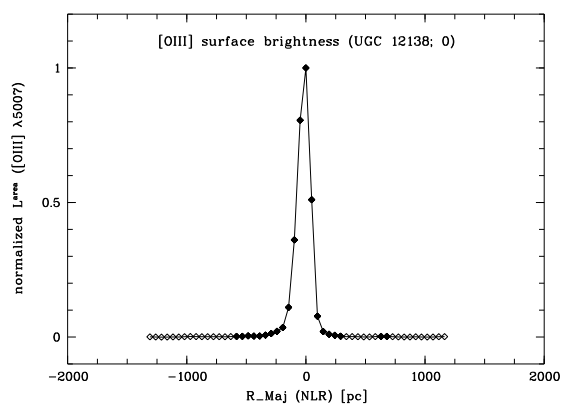
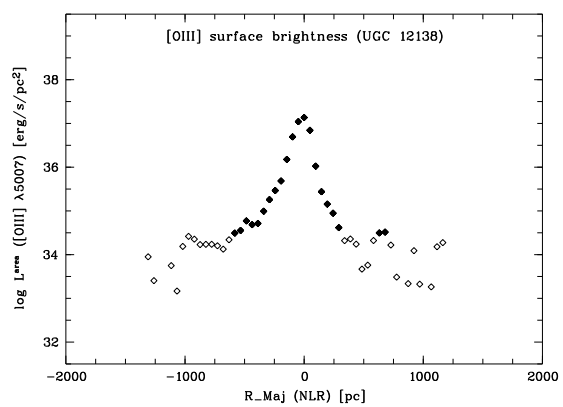
Figure B.1: This Figure and the following 17 show the SBPs of 58 Seyfert galaxies and seven quasars as imaged with the HST. The *left panel* shows a logarithmic plot in $L^{\text{area}}_{[\text{OIII}]}$, while in the *right panel*, $L^{\text{area}}_{[\text{OIII}]}$ is normalized to 1, for comparison. In the *right panel*, the classification of the SBP type [0, (0), 1, 2] is shown in brackets behind the name of the object.

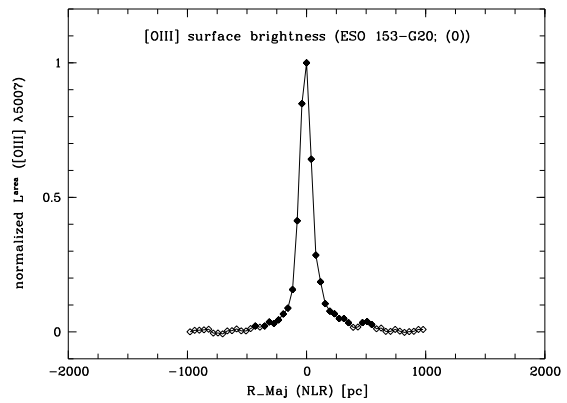
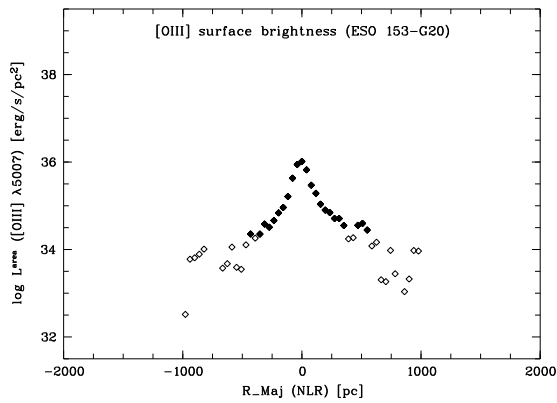
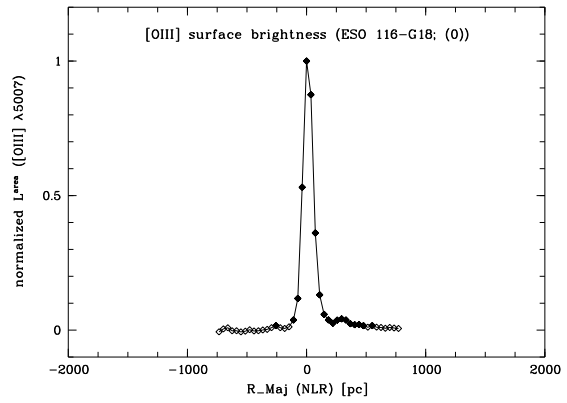
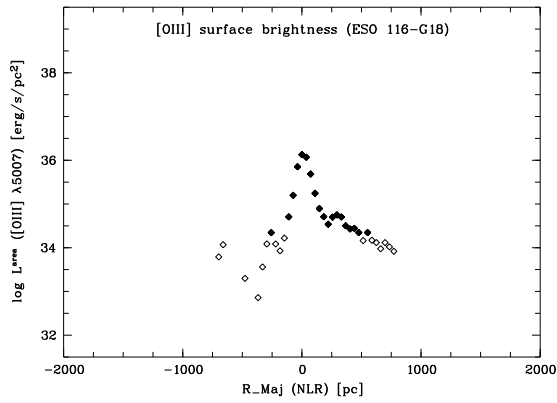
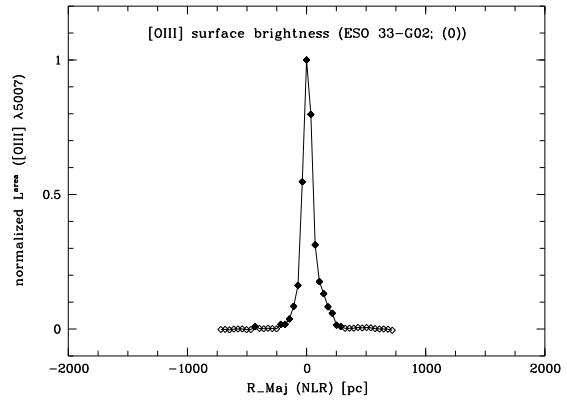
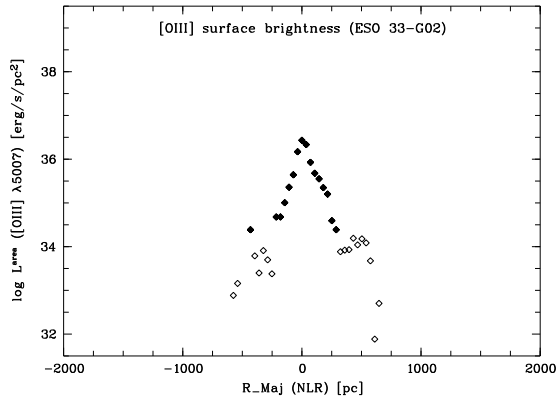
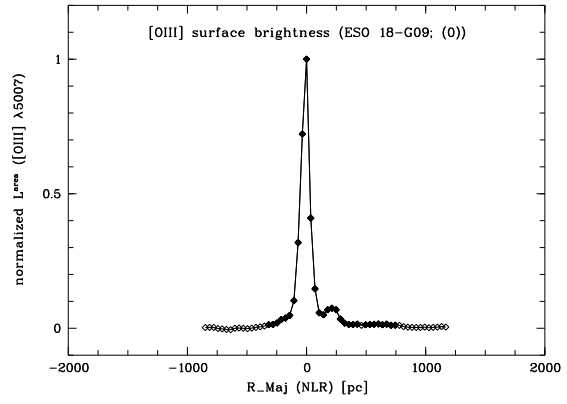
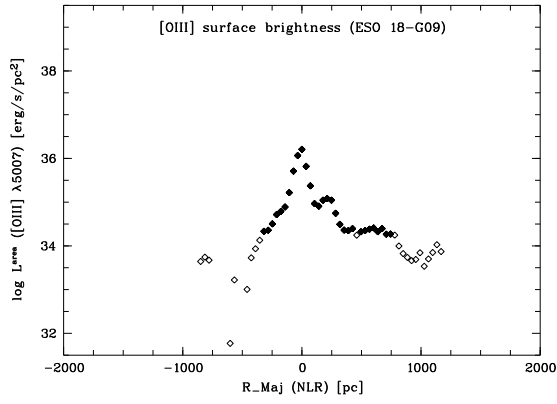


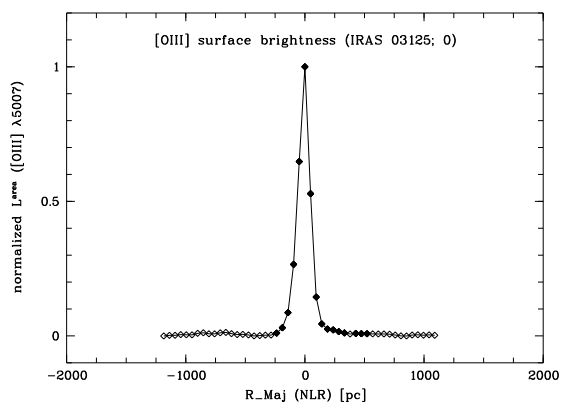
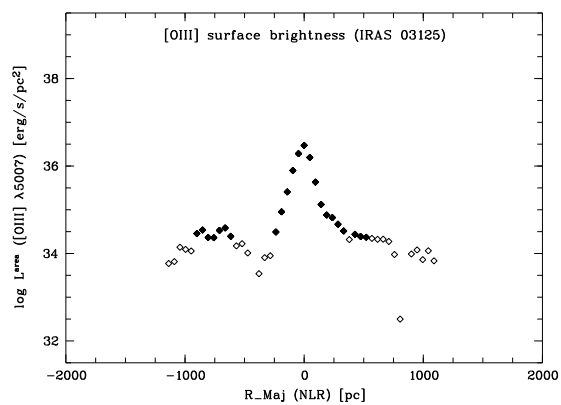
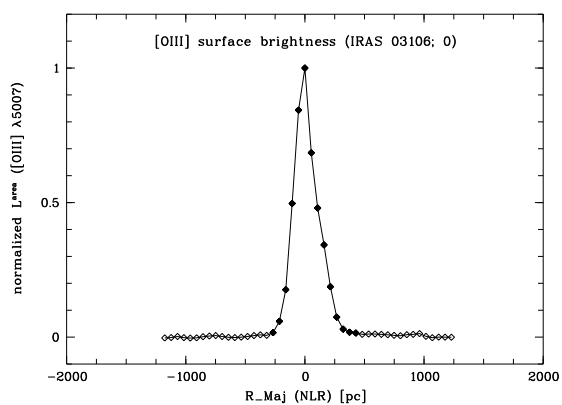
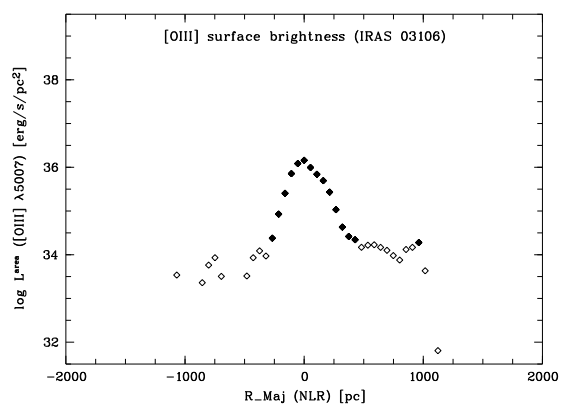
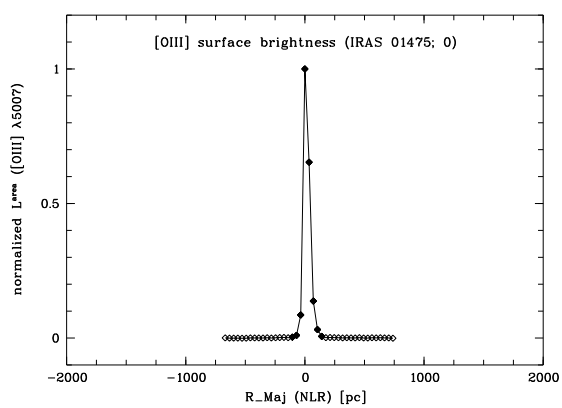
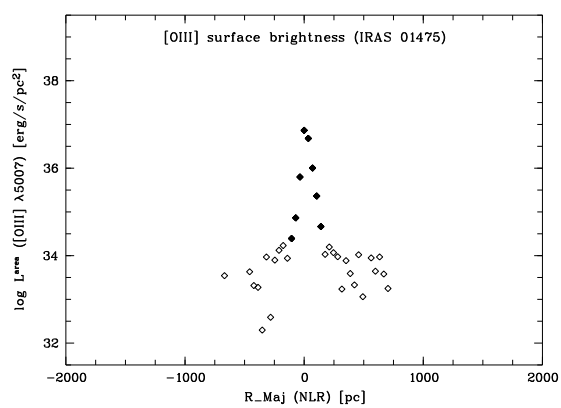
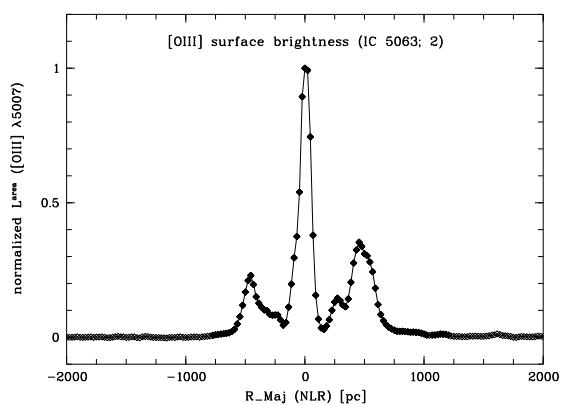
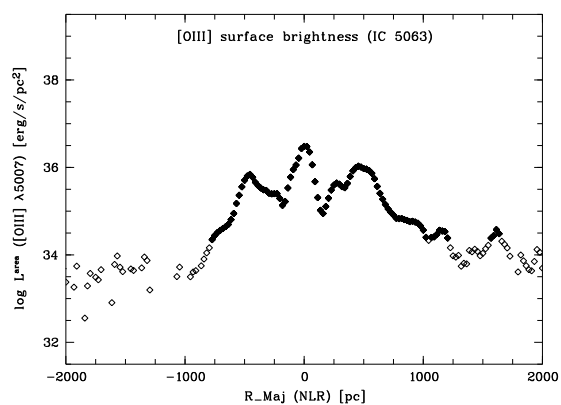


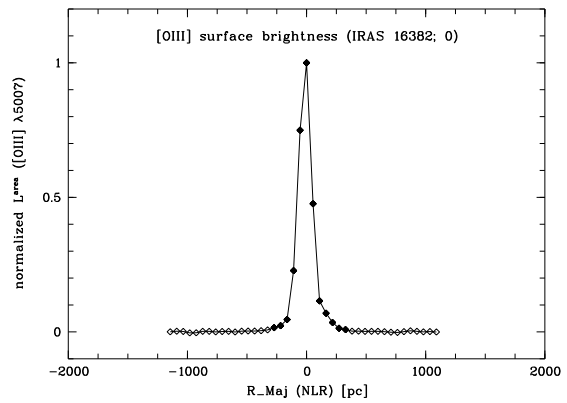
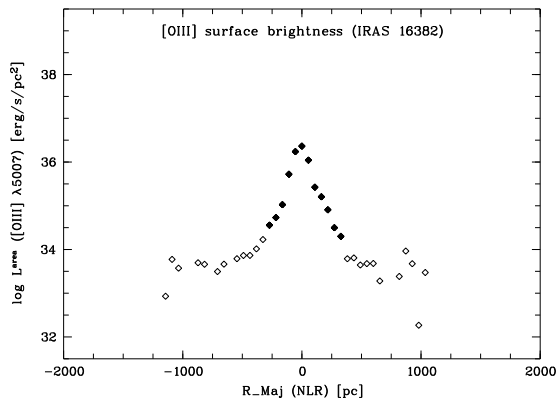
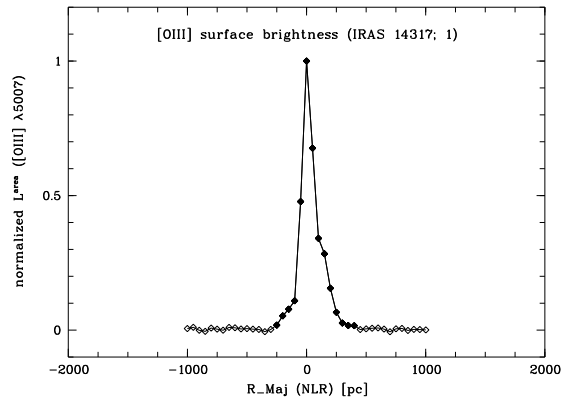
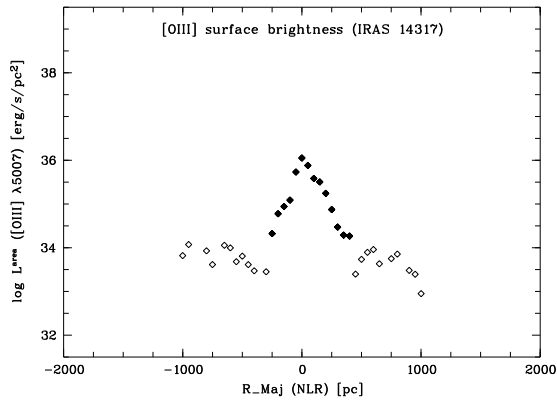
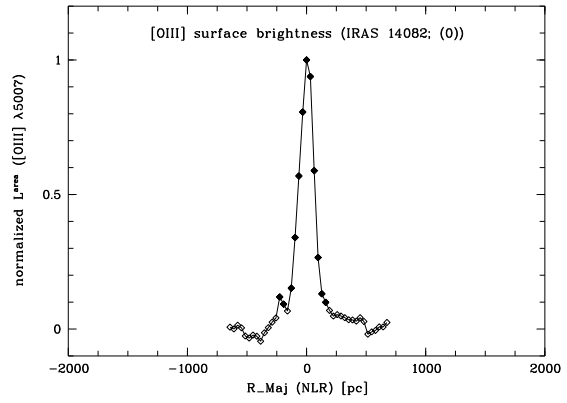
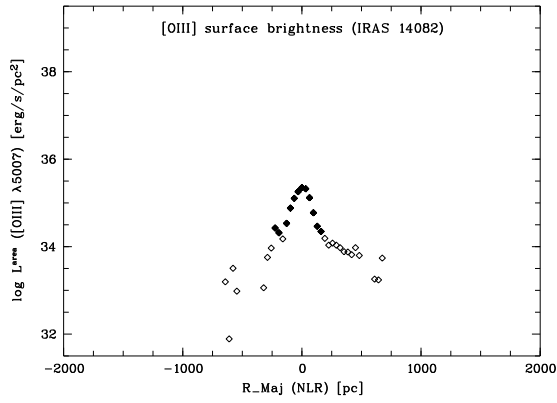
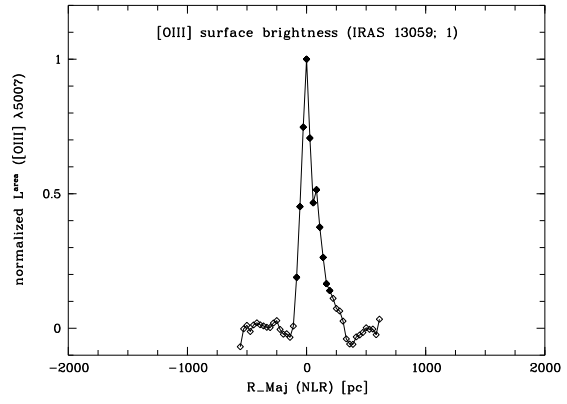
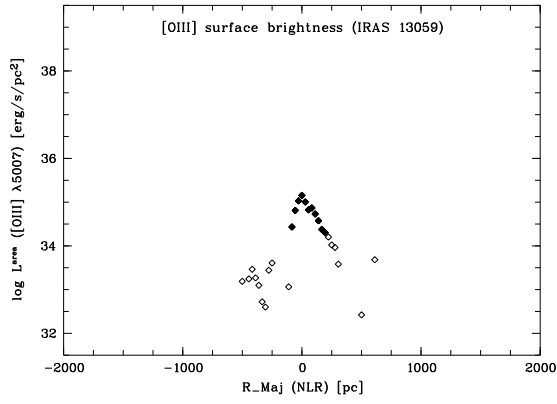


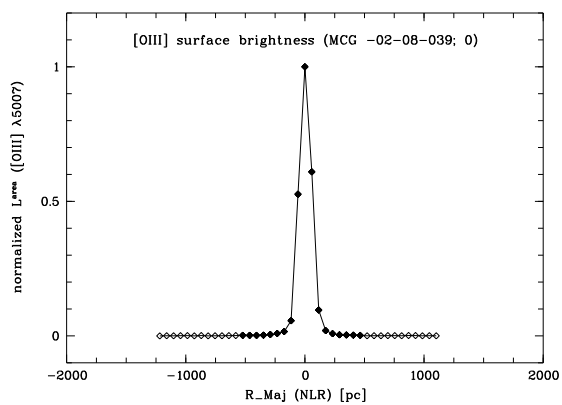
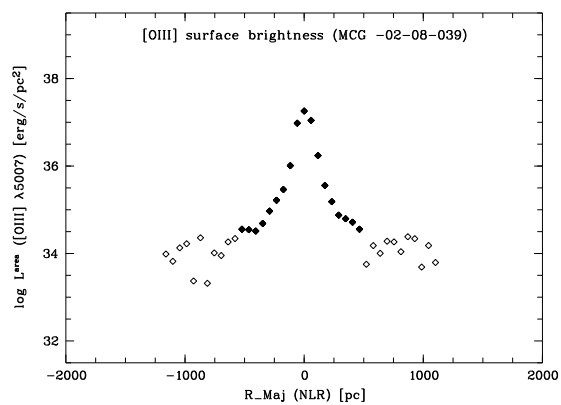
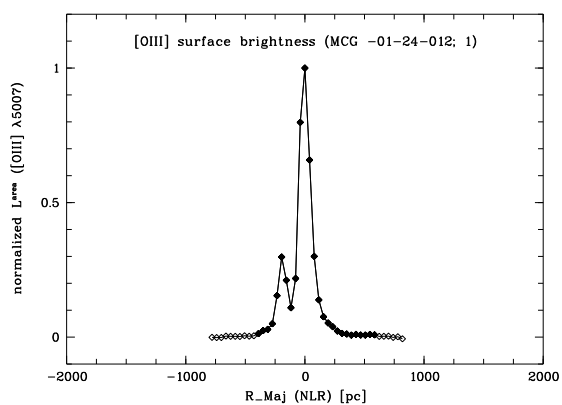
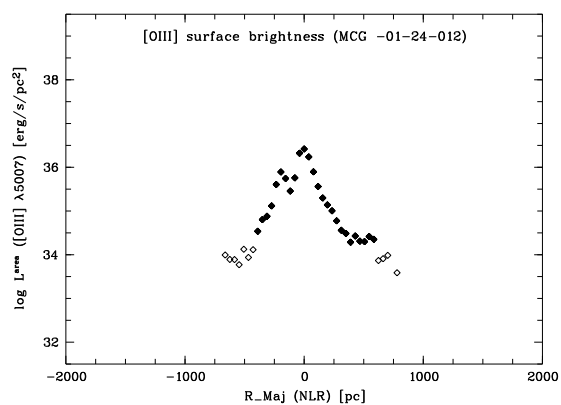
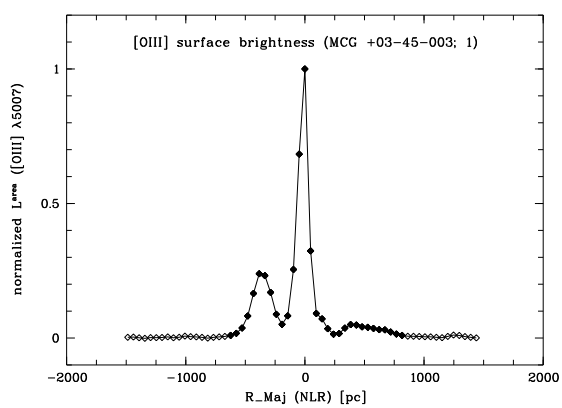
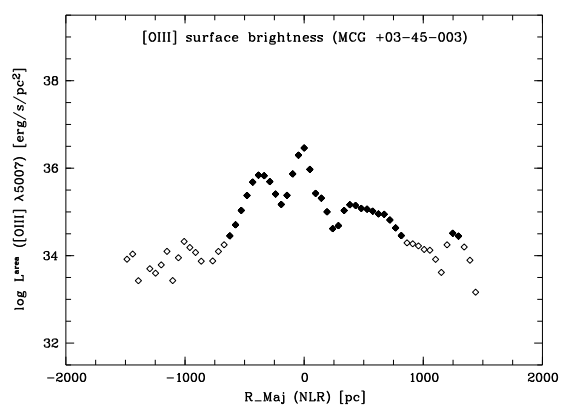
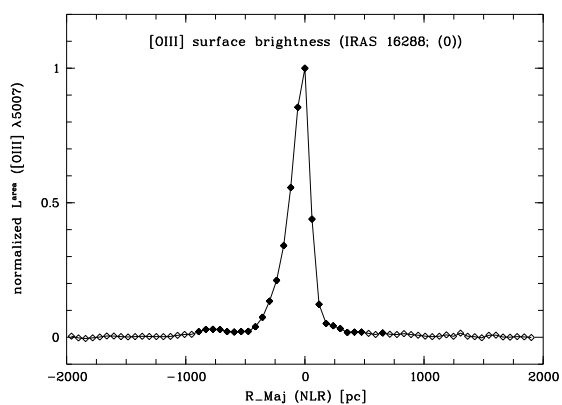
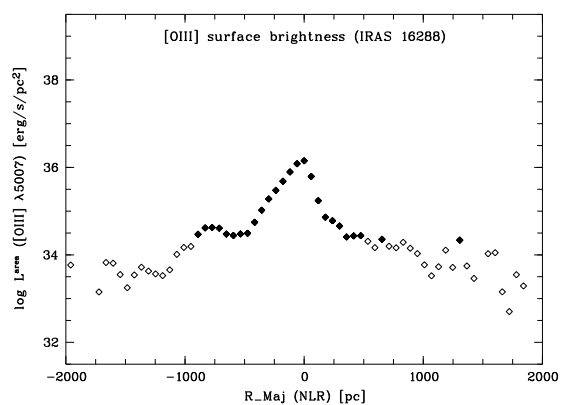


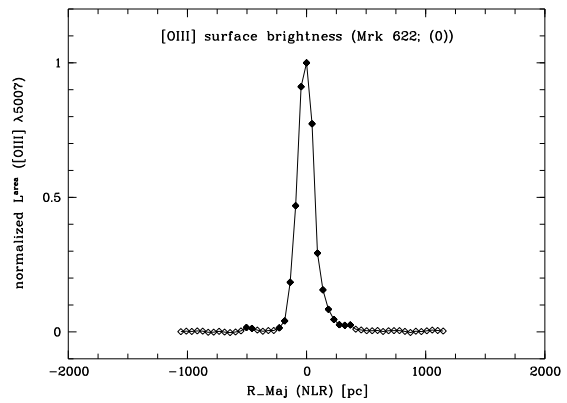
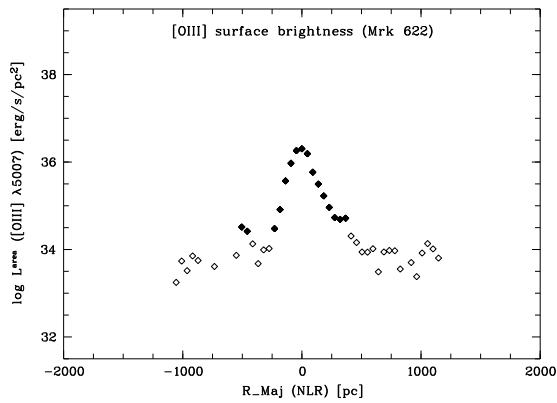
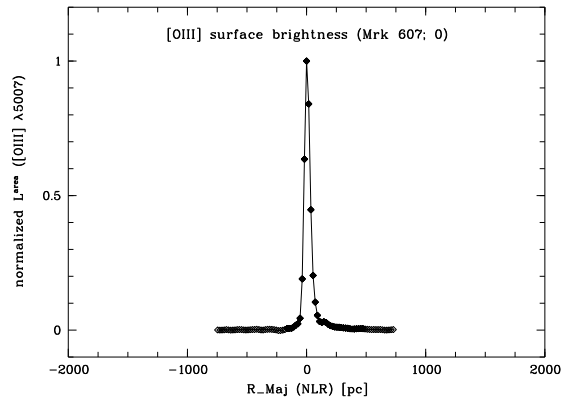
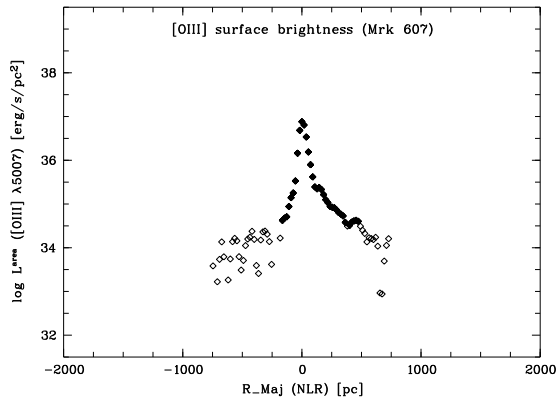
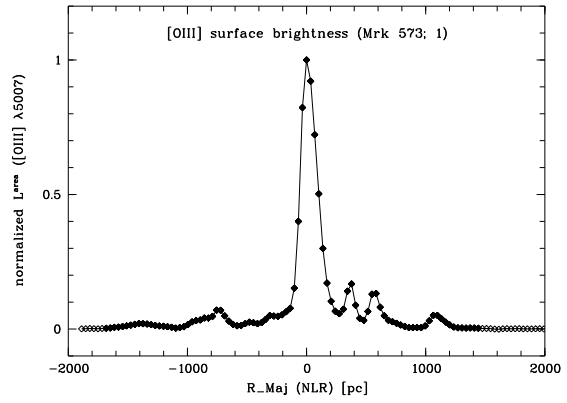
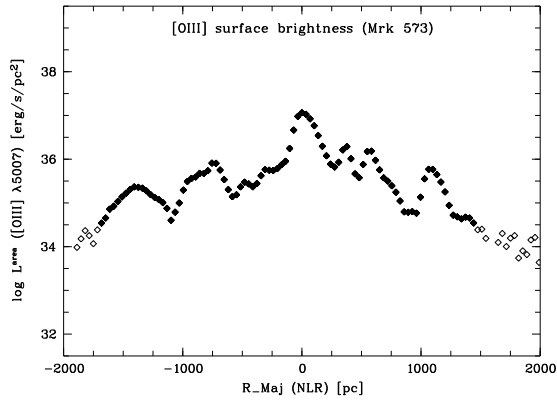
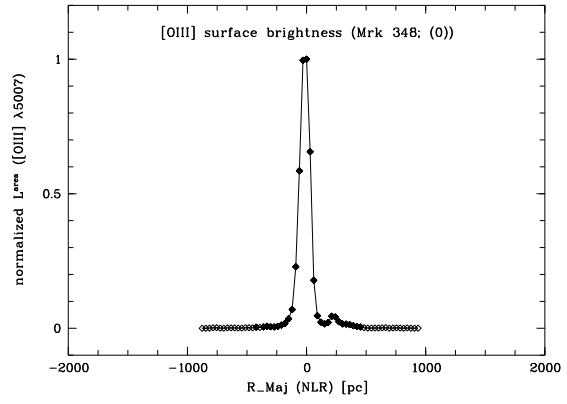
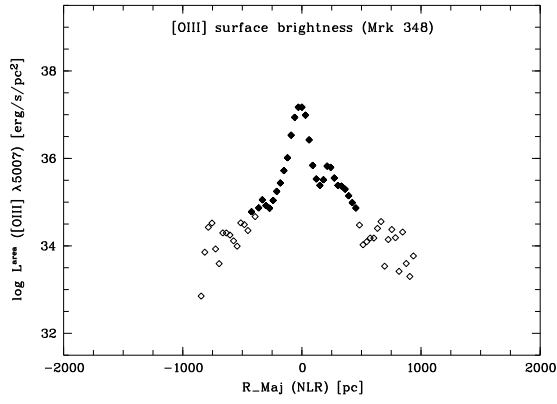


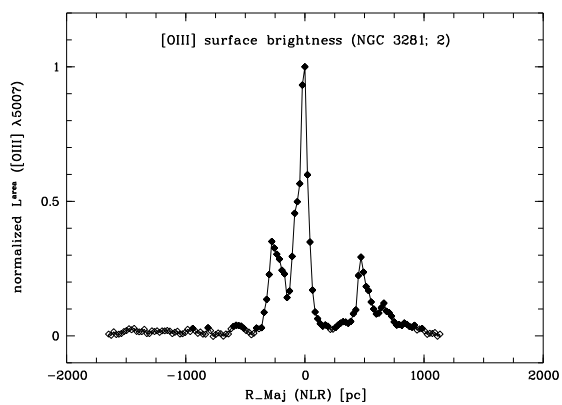
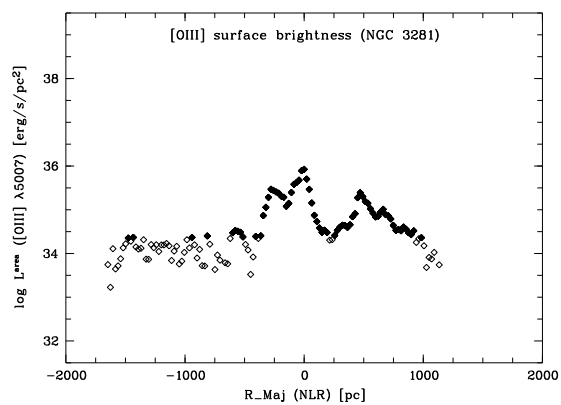
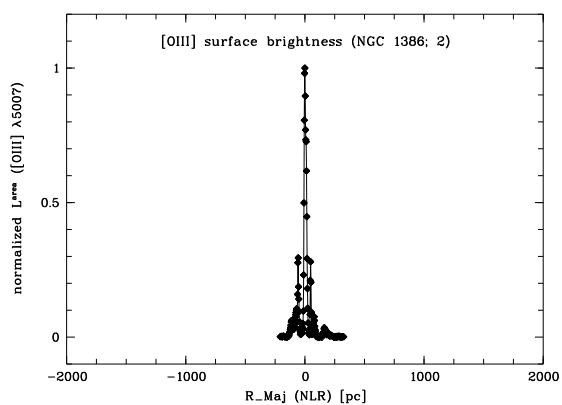
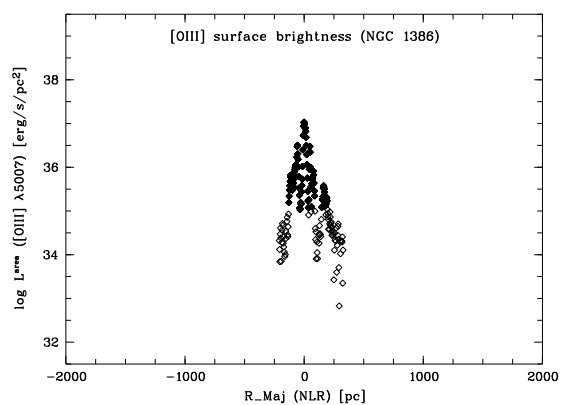
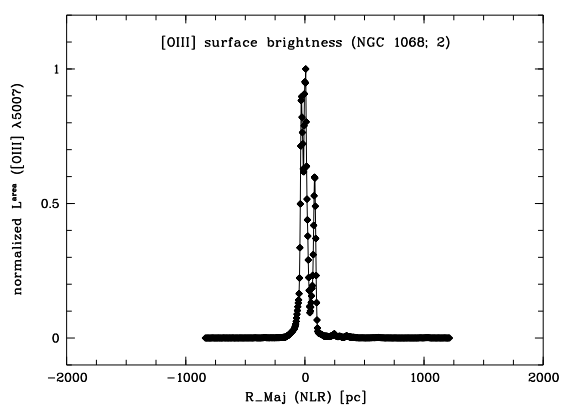
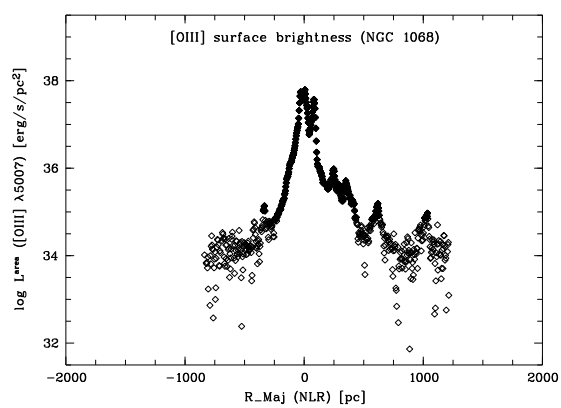
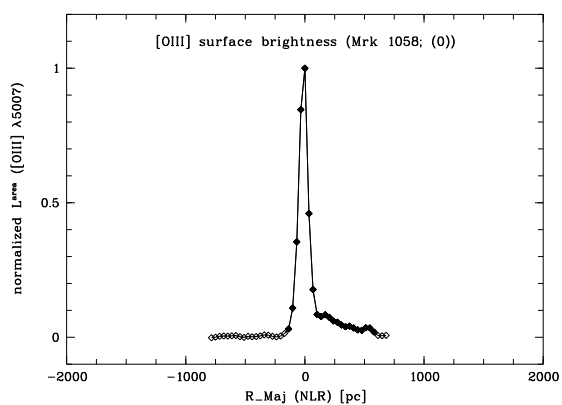
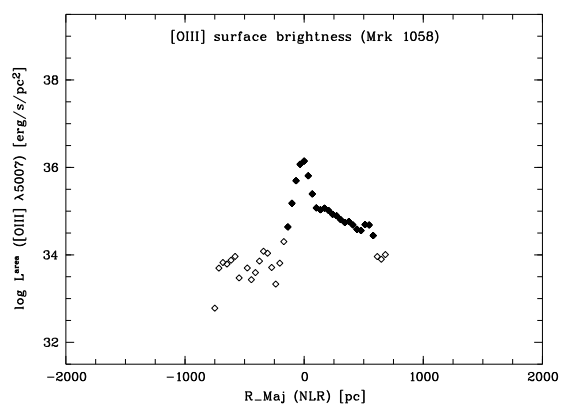


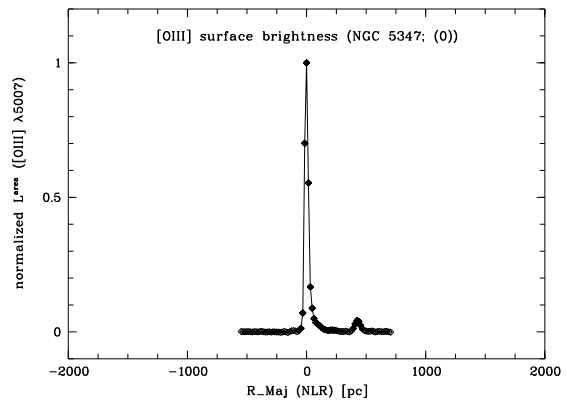
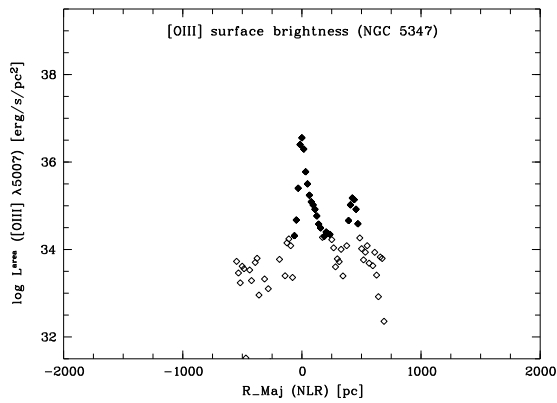
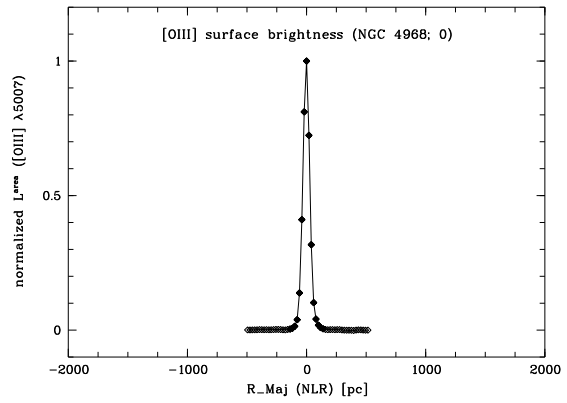
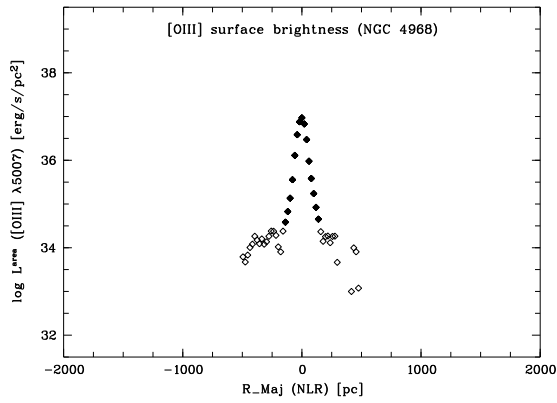
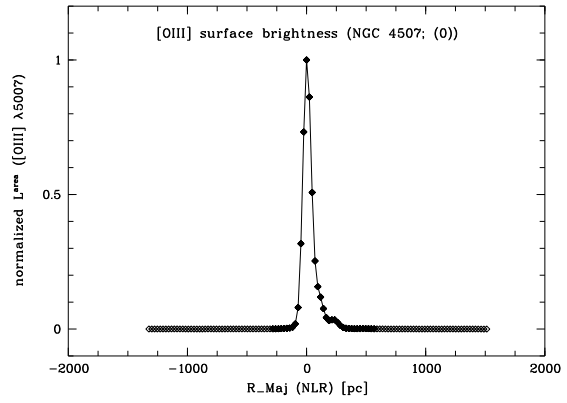
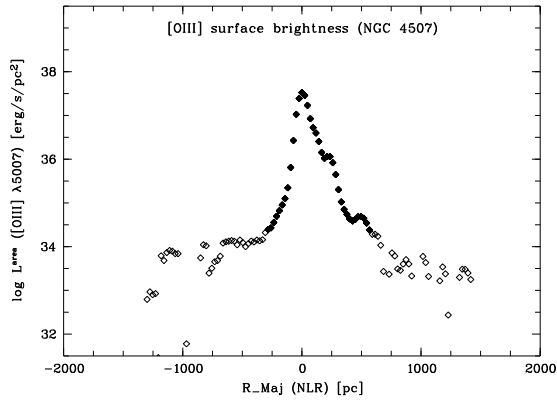
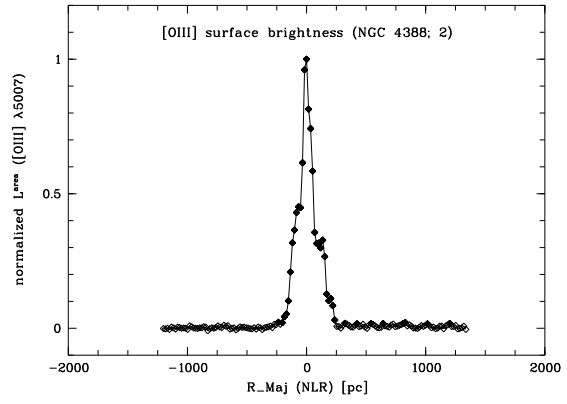
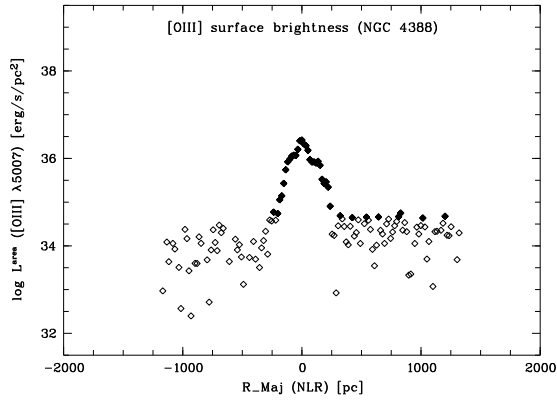


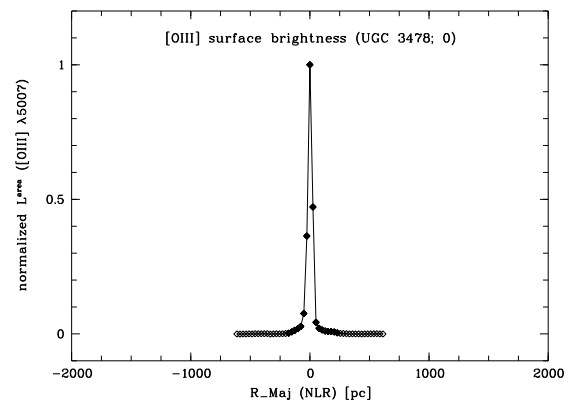
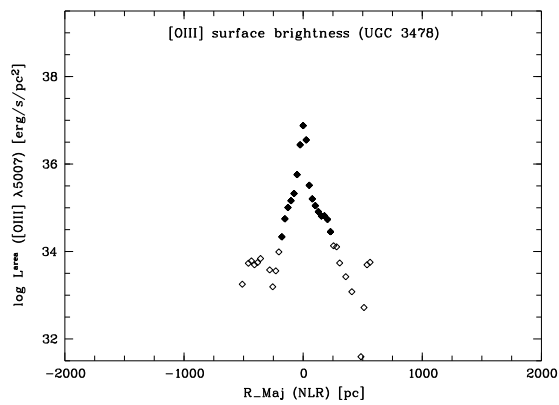
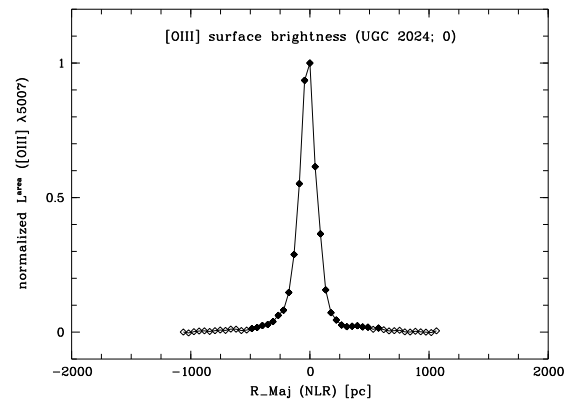
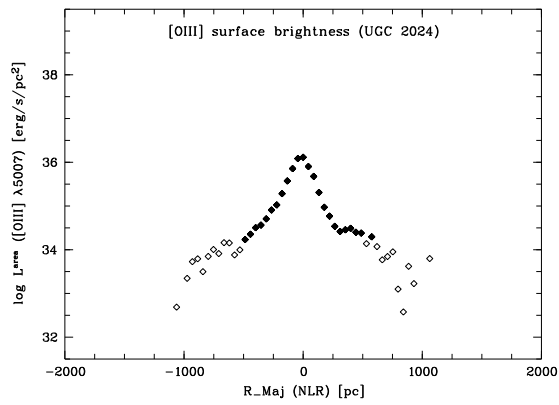
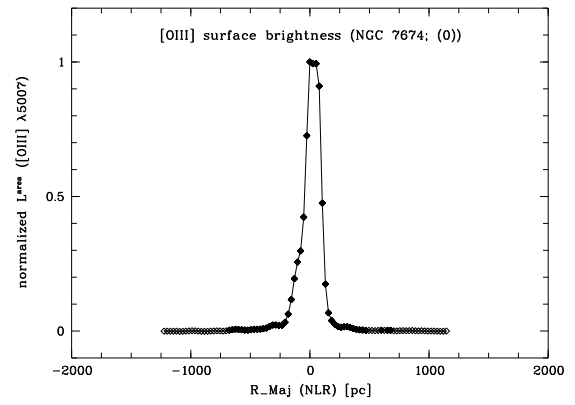
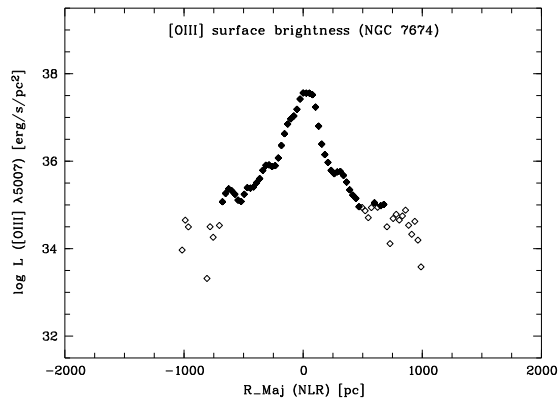
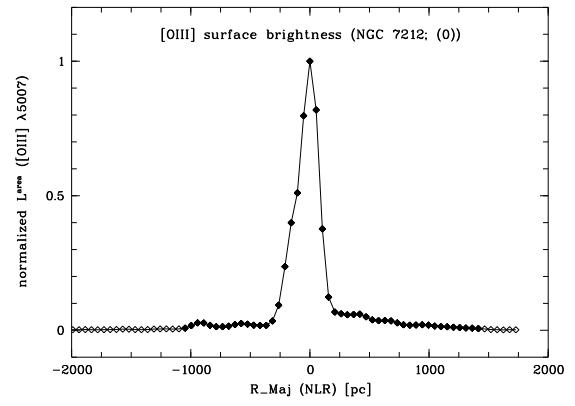
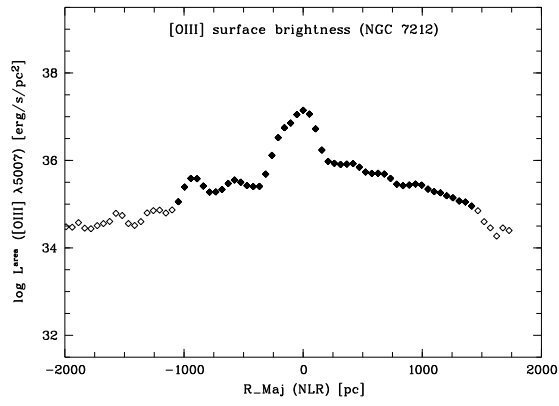


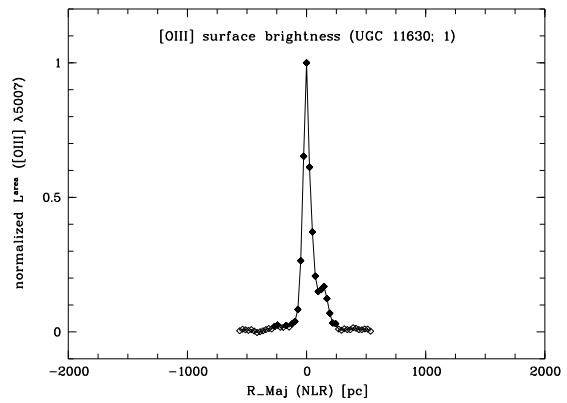
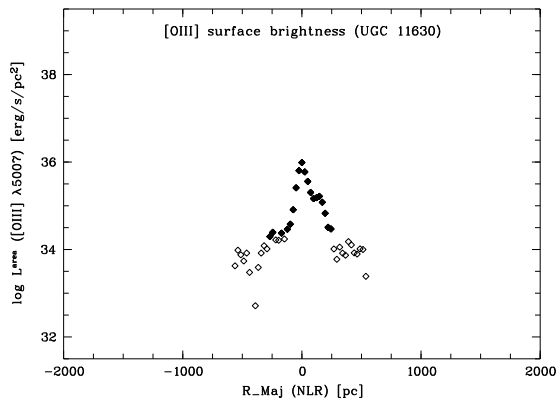
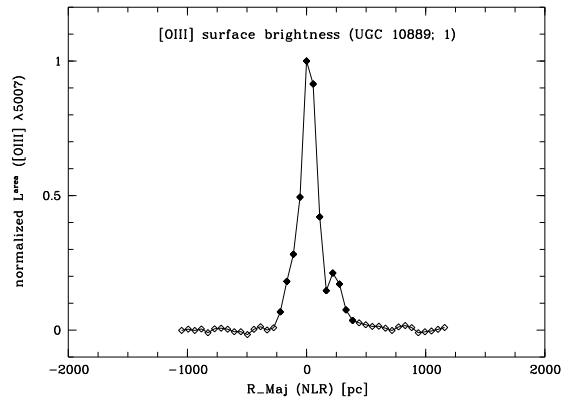
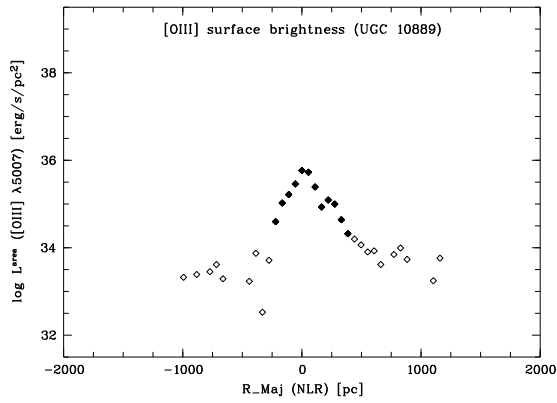
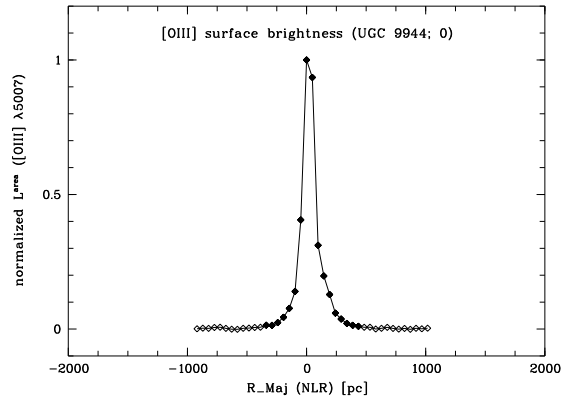
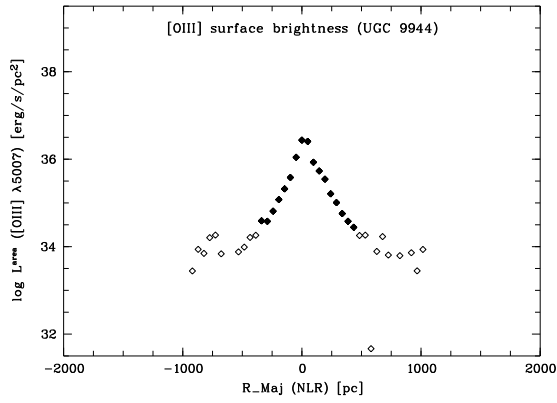
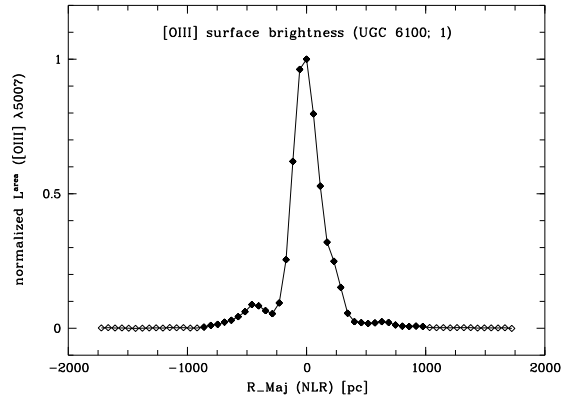
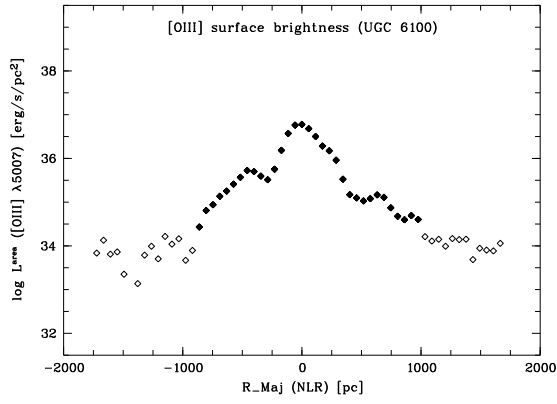


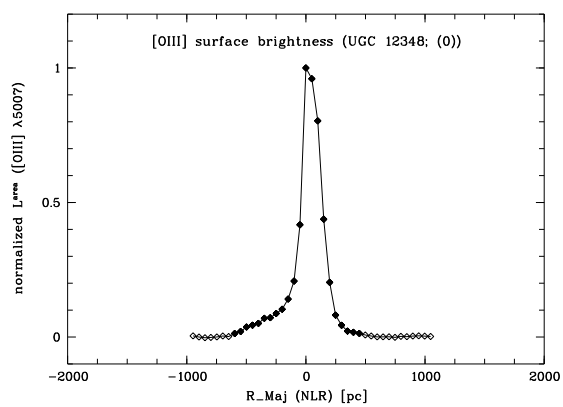
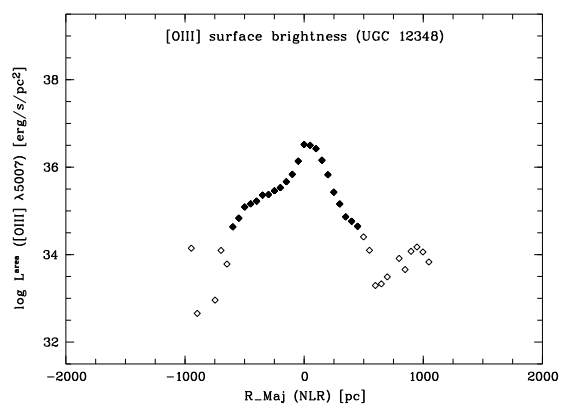


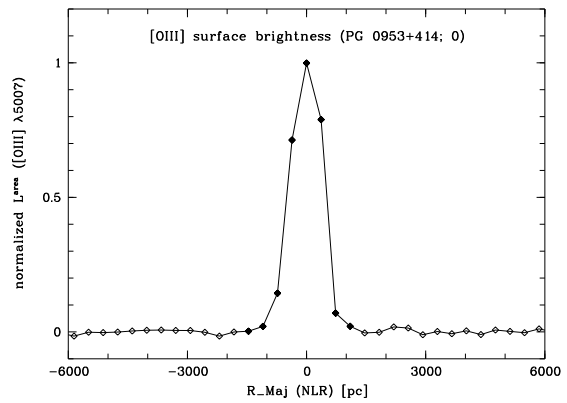
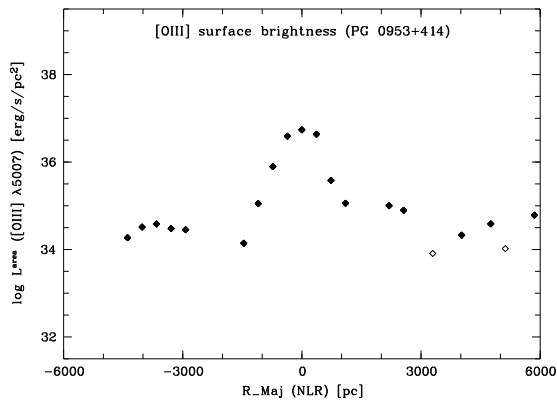
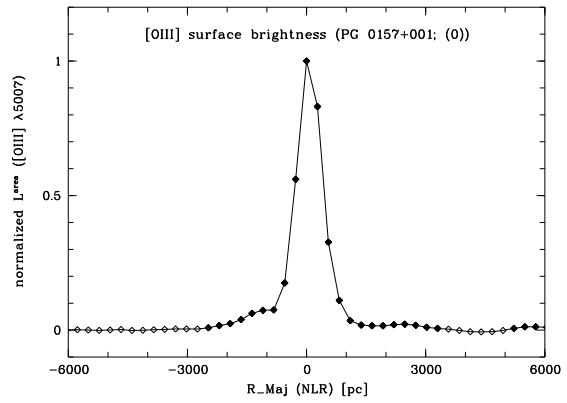
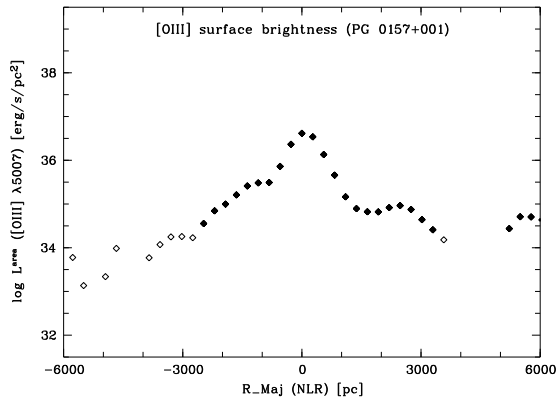
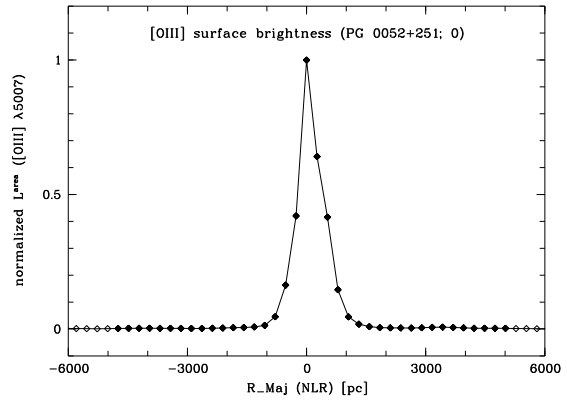
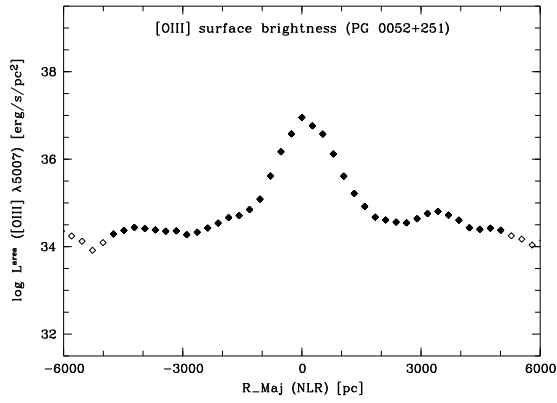
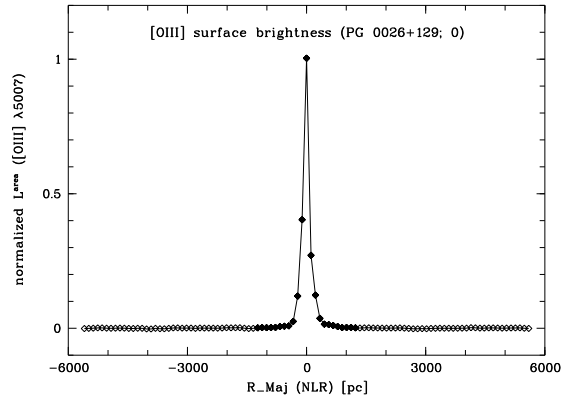
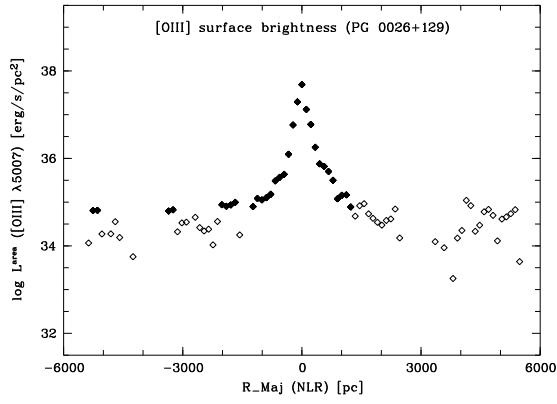


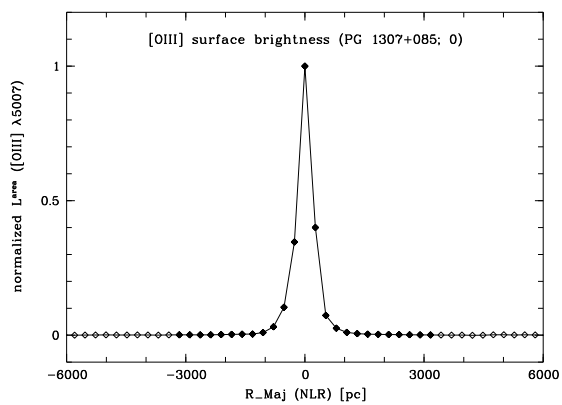
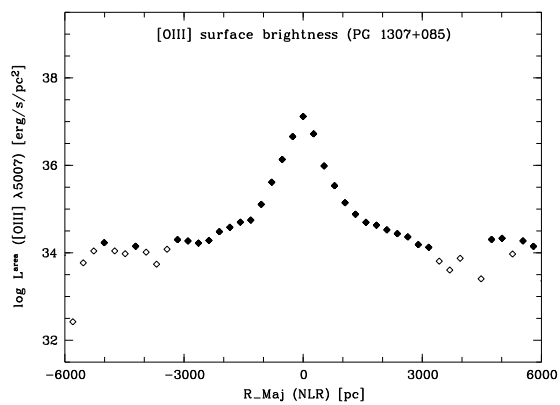
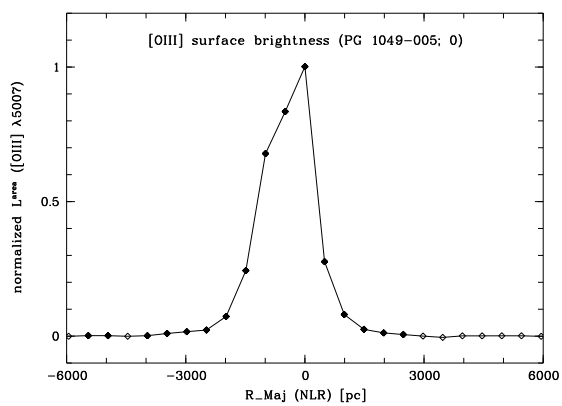
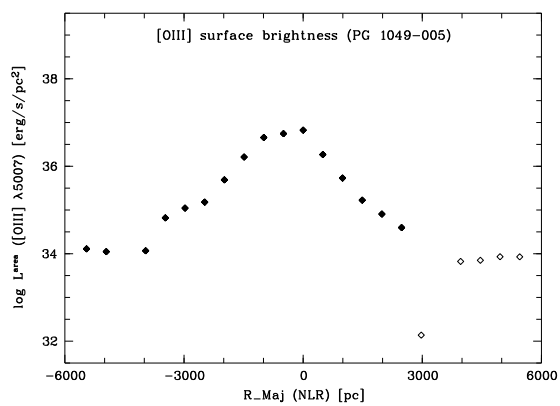
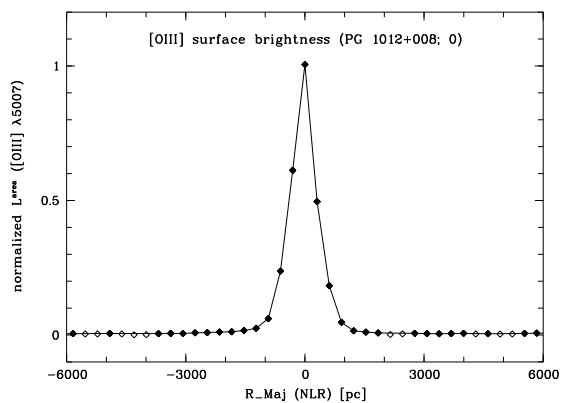
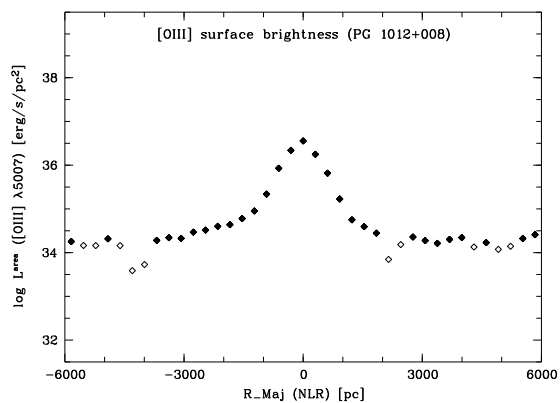












Calculation of Physical Parameters

From the observed emission–line fluxes, ratios, velocities, and FWHMs, we derive several parameters such as reddening, temperature, electron density, ionization parameter, and mass to study the physics of the NLR. We here summarize the derivation of these physical parameters and discuss the assumptions involved.

The spectra cover several emission lines particularly suited for specific diagnoses: $H\alpha$ and $H\beta$ (normalizer, reddening indicator, counter of ionizing photons); $[O\ II]\ \lambda 3727\ \text{\AA}/[O\ III]\ \lambda 5007\ \text{\AA}$ (ionization parameter); $[O\ III]\ \lambda\lambda 4363, 5007\ \text{\AA}$ (temperature sensitive); $[O\ I]\ \lambda 6363\ \text{\AA}$, $[N\ II]\ \lambda 6583\ \text{\AA}$, $[S\ II]\ \lambda\lambda 6716, 6731\ \text{\AA}$ (AGN classifier); $[S\ II]\ \lambda 6716\ \text{\AA} / [S\ II]\ \lambda 6716\ \text{\AA}$ (density).

In Table C.1, we give the central wavelengths of the most important emission lines visible in the spectra as well as the abbreviations used throughout this thesis.

C.1 Reddening

The internal extinction can be derived from the ratio $H\alpha/H\beta$. The observed emission lines originate from recombination of an hydrogen ion and the subsequent down cascade of the electron ($n = 3$ to 2 for $H\alpha$ and $n = 4$ to 2 for $H\beta$, respectively). For a pure recombination and a temperature of 10000 K, this ratio is expected to have the value $H\alpha/H\beta = 2.87$ (case B recombination; Osterbrock (1989), page 80). An observed ratio higher than this value can thus be attributed to reddening from dust. To calculate the reddening E_{B-V} from this ratio, a parameter c is commonly used. It is defined as

$$c = \frac{1}{0.37} \cdot \log \left(\frac{1}{2.87} \cdot \frac{H\alpha}{H\beta} \right) , \quad (C.1)$$

$$E_{B-V} = \frac{2.4}{3.1} \cdot c . \quad (C.2)$$

An extinction correction can then be applied to all observed emission–line fluxes, normalized to the $H\beta$ flux using

$$\frac{I_{\text{line,obs}}}{I_{H\beta,\text{obs}}} = \frac{I_{\text{line,0}}}{I_{H\beta,0}} \cdot 10^{-c[f(\text{line})-f(H\beta)]} . \quad (C.3)$$

The $[f(\text{line}) - f(H\beta)]$ values were taken from Osterbrock (1989) (Table 7.2), interpolating between different values as not all lines are listed in the Table (Table C.3).

Table C.1: Central wavelengths of emission lines

Line	Wavelength (Å)	Line	Wavelength (Å)
[O II] ^a	3727.43	[Fe VII]	5721.11
[Ne III]	3868.76	He I ^b	5875.75
[Ne III]	3967.47	[Fe VII]	6086.92
H ϵ	3970.07	[O I]	6300.32
H δ	4101.74	[O I]	6363.81
H γ	4340.47	[Fe X] ^c	6374.51
[O III]	4363.21	[N II]	6548.06
He II	4685.68	H α	6562.82
H β	4861.33	[N II]	6583.39
[O III]	4958.92	[S II]	6716.42
[O III]	5006.85	[S II]	6730.78

Note. – The restframe wavelengths were taken from Moore (1945) (permitted lines) and Bowen (1960) (forbidden lines).

^a Unresolved pair [O II] $\lambda\lambda$ 3726.05,3728.8 Å

^b Unresolved triplet He I $\lambda\lambda\lambda$ 5875.62,5875.65,5875.99 Å

^c Blended with [O I] λ 6363.81 Å at the given spectral resolution

Table C.2: Ionization potentials and critical densities

Line	Ionization Potential		Critical Density (cm ⁻³)
	Lower (eV)	Upper (eV)	
[O II] λ 3726 Å	13.6	35.1	$1.4 \cdot 10^4$
[O II] λ 3729 Å	13.6	35.1	$3.3 \cdot 10^3$
[Ne III] λ 3869 Å	41.0	63.5	$9.7 \cdot 10^6$
[O III] λ 4363 Å	35.1	54.9	$3.3 \cdot 10^7$
[O III] λ 5007 Å	35.1	54.9	$7.0 \cdot 10^5$
[Fe VII] λ 6087 Å	99.1	125.0	$3.6 \cdot 10^7$
[O I] λ 6300 Å	0.0	13.6	$1.8 \cdot 10^6$
[Fe X] λ 6375 Å	233.6	262.1	$4.8 \cdot 10^9$
[N II] λ 6583 Å	14.5	29.6	$8.7 \cdot 10^4$
[S II] λ 6716 Å	10.4	23.3	$1.5 \cdot 10^3$
[S II] λ 6731 Å	10.4	23.3	$3.9 \cdot 10^3$

Note. – Ionization potentials and critical densities for forbidden emission lines, adopted from Nagao et al. (2001), their Table 6.

Table C.3: Reddening corrections from average interstellar extinction curve

Line	$[f(\text{line}) - f(\text{H}\beta)]$	Line	$[f(\text{line}) - f(\text{H}\beta)]$
[O II] $\lambda 3727 \text{ \AA}$	+0.280	He I $\lambda 5876 \text{ \AA}$	-0.202
[Ne III] $\lambda 3869 \text{ \AA}$	+0.240	[Fe VII] $\lambda 6087 \text{ \AA}$	-0.277
[Ne III] $\lambda 3967 \text{ \AA}$	+0.220	[O I] $\lambda 6300 \text{ \AA}$	-0.323
H ϵ	+0.220	[O I] $\lambda 6364 \text{ \AA}$	-0.335
H δ	+0.190	[Fe X] $\lambda 6375 \text{ \AA}$	-0.337
H γ	+0.130	[N II] $\lambda 6548 \text{ \AA}$	-0.367
[O III] $\lambda 4363 \text{ \AA}$	+0.120	H α	-0.370
He II $\lambda 4686 \text{ \AA}$	+0.040	[N II] $\lambda 6583 \text{ \AA}$	-0.374
[O III] $\lambda 4959 \text{ \AA}$	-0.028	[S II] $\lambda 6716 \text{ \AA}$	-0.388
[O III] $\lambda 5007 \text{ \AA}$	-0.041	[S II] $\lambda 6731 \text{ \AA}$	-0.389
[Fe VII] $\lambda 5721 \text{ \AA}$	-0.197		

Note. – The $[f(\text{line}) - f(\text{H}\beta)]$ value was taken from the average interstellar extinction curve [Osterbrock (1989), Table 7.2] and interpolated if necessary.

The absolute fluxes can be calculated from the absolute H β flux

$$A_{\text{H}\beta} = 2.85 \cdot c, \quad (\text{C.4})$$

$$\text{H}\beta_{\text{abs}} = \text{H}\beta_{\text{obs}} \cdot 10^{0.4A_{\text{H}\beta}}, \quad (\text{C.5})$$

by multiplying the dereddened ratios with $\text{H}\beta_{\text{abs}}$.

Luminosities were calculated from the dereddened fluxes ϕ using the luminosity distance d_l derived from the world model used throughout this thesis (Appendix A).

C.2 Temperature

The temperature can be determined using ions with forbidden emission lines originating from two different upper levels with considerably different excitation energies. If, in the low-density limit, collisional de-excitation can be neglected, the line intensity ratio depends only on the excited level population. This is, due to the different excitation energies, depending on the energy of the colliding electron and thus on the (electron) temperature. An ion having a suited energy-level structure is [O III]. [O III] $\lambda 4363 \text{ \AA}$ comes from the upper ^1S level, while $\lambda 4959 \text{ \AA}$ and $\lambda 5007 \text{ \AA}$ come from the intermediate ^1D level. The relative rates of excitation to the ^1S and ^1D level depend very strongly on T . Inserting numerical values of the collision strengths and transition probabilities, the [O III] ($\lambda 4959 \text{ \AA} + \lambda 5007 \text{ \AA}$) / $\lambda 4363 \text{ \AA}$ intensity ratio as a function of temperature can be approximated as [Osterbrock (1989); page 121]:

$$[\text{O III}] \left(\frac{\lambda 4959 \text{ \AA} + \lambda 5007 \text{ \AA}}{\lambda 4363 \text{ \AA}} \right) \simeq \frac{7.73 \exp [(3.29 \cdot 10^4) / T]}{1 + 4.5 \cdot 10^{-4} (n_e / T^{1/2})}. \quad (\text{C.6})$$

For the low densities generally observed in the NLR ($10^3 \text{ cm}^{-3} < n_e < 10^4 \text{ cm}^{-3}$) and for a typical temperature of 10000 K, the additional addend in the denominator is $0.045 - 0.0045$ and negligible against 1. Thus, the dependency on n_e is negligible and Equation C.6 can be simplified to

$$[\text{O III}] \left(\frac{\lambda 4959 \text{ \AA} + \lambda 5007 \text{ \AA}}{\lambda 4363 \text{ \AA}} \right) = \text{ratio}_{[\text{O III}]} = 7.73 \exp \left[\left(3.29 \cdot 10^4 \right) / T \right] \quad (\text{C.7})$$

$$\Leftrightarrow T = \frac{32900}{\ln \left[1 / 7.73 \cdot \text{ratio}_{[\text{O III}]} \right]} . \quad (\text{C.8})$$

Unfortunately, the $[\text{O III}] \lambda 4363 \text{ \AA}$ emission line is usually very weak in Seyfert spectra. In most of our spectra, it has a S/N ratio > 3 in the central row only.

C.3 Electron Density

The electron density can be measured by observing the effects of collisional de-excitation. Forbidden lines are well suited for this study due to their metastable levels, i.e. the long time electrons stay in the excited level to make a collisional de-excitation possible. The intensity ratio of two lines of the same ion emitted by different levels with nearly the same excitation energy (to be temperature independent) will depend on both the transition probability as well as the rate of collisional de-excitation and thus, on the electron density. Pairs suited for such a study are $[\text{S II}] \lambda \lambda 6716, 6731 \text{ \AA}$ and $[\text{O II}] \lambda \lambda 3729, 3726 \text{ \AA}$. The latter lines are, however, only resolvable at high spectral resolution.

The dependency of electron density on the measured $[\text{S II}]$ intensity ratio is shown in Figure C.1 [*left panel*; Osterbrock (1989), page 134]. The curve has two theoretical limits: In the low density limit, collisional de-excitation is negligible and every excitation results in emission of a photon of either $\lambda 6716 \text{ \AA}$ or $\lambda 6731 \text{ \AA}$ (with the relative excitation rates proportional to their statistical weights). In the case of high density, collisional excitation and de-excitation dominate and set up a Boltzmann population ratio. At the so-called critical density, radiation and collisional de-excitation is comparable (see Table C.2).

Both $[\text{O II}]$ and $[\text{S II}]$ arise in fairly low stages of ionization, in outer parts or in dense parts where recombination depresses the ionization the most. Thus, the densities derived from these regions may not be representative for the entire emission line region.

The density depends on the temperature

$$n_{e,T} = \frac{n_{e,\text{obs}}}{\sqrt{(10000/T)}} . \quad (\text{C.9})$$

We therefore use the observed central temperature for correction.

C.4 Ionization Parameter

The line ratio $[\text{O II}] \lambda 3737 \text{ \AA} / [\text{O III}] \lambda 5007 \text{ \AA}$ can be used to estimate the value of the ionization parameter U [e.g. Penston et al. (1990)]. Komossa & Schulz (1997) have shown that independent of continuum shape and for sufficient low density ($n_H < 10^3 \text{ cm}^{-3}$), this line ratio yields U . It gives a good approximation of the ionization parameter as

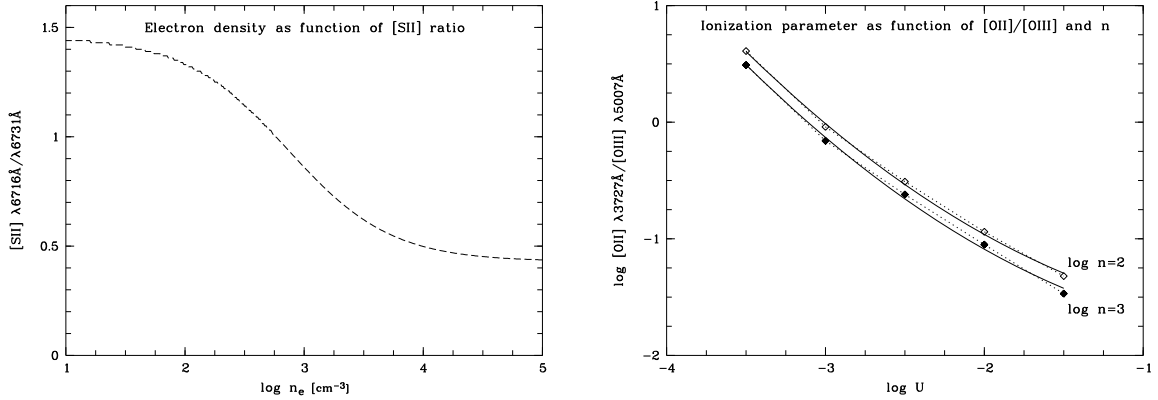


Figure C.1: *Left panel:* Electron density as a function of [S II] ratio, adopted from Osterbrock (1989) (page 134). *Right panel:* Ionization parameter as a function of [O II]/[O III] ratio (Komossa & Schulz, 1997) with fit shown as solid line. The open symbols correspond to $n = 100 \text{ cm}^{-3}$, the filled ones to $n = 1000 \text{ cm}^{-3}$, respectively.

long as there are no strong density inhomogeneities with radius. But even in that case, in which the absolute value of U is overpredicted, the observed slope does not change.

We used the theoretical variations of [O II]/[O III] with U for a continuum shape corresponding to a power law ($\alpha_{\text{uv-x}} = -1.5$) and a density of $\log n = 2 - 3$ from Komossa & Schulz (1997). The latter is a typical value found in our NLR spectra. For our analysis, we applied a linear fit to these data points (Fig. C.1, *right panel*). The fit is very good and can be used to more easily estimate U from the reddening corrected [O II]/[O III] line ratio:

$$\log U_{n_e=100} = -2.294 \cdot \sqrt{(\log [\text{OII}]/[\text{OIII}])_{\text{dered}} + 1.722} , \quad (\text{C.10})$$

$$\log U_{n_e=1000} = -2.284 \cdot \sqrt{(\log [\text{OII}]/[\text{OIII}])_{\text{dered}} + 1.856} . \quad (\text{C.11})$$

The [O II]/[O III] ratio decreases with increased n due to the lower critical density of [O II] compared to [O III]. As we observe an electron density which is not constant with radius but decreasing, we use the two limiting cases of $n = 100 \text{ cm}^{-3}$ and $n = 1000 \text{ cm}^{-3}$ and present the ionization parameter for both cases. The “real” ionization parameter lies in between the two curves, i.e. the slope flattens.

C.5 FWHM

To calculate the observed line width from the FWHM of the Gaussian fit, the instrumental spectral resolution has to be taken into account, as probed using the width of night-sky or wavelength-calibration emission lines which are intrinsically very small.

This $\text{FWHM}_{\text{instr}}$ reflects the effective resolution and must be considered when measuring observed line widths

$$\text{FWHM}_{\text{true}} = \sqrt{\text{FWHM}_{\text{obs}}^2 - \text{FWHM}_{\text{instr}}^2} . \quad (\text{C.12})$$

Often, our observations are limited by the spectral resolution ($\text{FWHM}_{\text{instr}} = 2.65 \text{ \AA pix}^{-1}$ for the VLT data, and $\text{FWHM}_{\text{instr}} = 1.58 \text{ \AA pix}^{-1}$ for the NTT data, respectively).

C.6 Mass

Assuming Keplerian rotation, the central mass can be estimated from the observed velocity curve. The observed velocity amplitude $v_{\max}/2$ has to be corrected for the inclination angle ι of the galaxy and the deviation θ between the photometric major axis and the long-slit position of the observations:

$$v_{\text{rot}} = v_{\text{obs}} \cdot \frac{\sqrt{\cos^2 \iota + \tan^2 \theta}}{\sin \iota \cdot \cos \iota} . \quad (\text{C.13})$$

For a point-like mass or a radial symmetric mass distribution the following equation is valid

$$M = \frac{v_{\text{rot}}^2 \cdot R}{G} . \quad (\text{C.14})$$

If the gravitational field is dominated by the galactic disk, this estimation has to be modified with a factor α which can vary between 0.6 and 1 (Lequeux, 1983). $\alpha = 0.6$ was used to derive a lower limit of the central enclosed mass.

Calculation of Errors

Here, we summarize how the uncertainties of the VLT and NTT long-slit spectroscopic measurements were estimated.

As the uncertainties in flux measurements are mostly caused by uncertainties in the placement of the continuum, we estimate the error as the product of the FWHM of the line and the root-mean square deviation of the continuum flux in a spectral region without emission or absorption lines. Note that we do not take into account uncertainties introduced by the stellar absorption correction and the quality of the Gaussian fits (which was fairly good keeping in mind the low spectral resolution).

To calculate the uncertainties of quantities involving different line fluxes, such as line ratios, we use the error propagation equation [see e.g. Bevington & Robinson (1992), page 43–48]. It approximates the standard deviation σ_x for $x = f(u, v)$:

$$\sigma_x^2 \simeq \sigma_u^2 \left(\frac{\delta x}{\delta u} \right)^2 + \sigma_v^2 \left(\frac{\delta x}{\delta v} \right)^2 + \dots + 2\sigma_{uv}^2 \left(\frac{\delta x}{\delta u} \right) \left(\frac{\delta x}{\delta v} \right) + \dots \quad (\text{D.1})$$

If the fluctuations in the measured quantities u and v are uncorrelated, the third term vanishes. This is a reasonable approximation in our case and we can reduce the equation to

$$\sigma_x^2 \simeq \sigma_u^2 \left(\frac{\delta x}{\delta u} \right)^2 + \sigma_v^2 \left(\frac{\delta x}{\delta v} \right)^2 + \dots \quad (\text{D.2})$$

In Table D.1, we summarize the equations of the uncertainties for the different measurements. A detailed description on how we derived the physical parameters is given in Appendix C.

Table D.1: Error propagation

Value	x	σ_x
Sum/Difference	$u \pm v$	$\sqrt{\sigma_u^2 \pm \sigma_v^2}$
Factor	$a \cdot u$	$a \cdot \sigma_u$
Product	$u \cdot v$	$x \cdot \sqrt{\left(\frac{\sigma_u}{u}\right)^2 + \left(\frac{\sigma_v}{v}\right)^2}$
Logarithm	$\log u$	$\frac{1}{\ln 10 \cdot u} \cdot \sigma_u$
Fraction (Flux Ratio)	$\frac{u}{v}$	$x \cdot \sqrt{\left(\frac{\sigma_u}{u}\right)^2 + \left(\frac{\sigma_v}{v}\right)^2}$
Diagnostic Diagram	$\log\left(\frac{u}{v}\right)$	$\frac{1}{\ln 10} \cdot \sqrt{\left(\frac{\sigma_u}{u}\right)^2 + \left(\frac{\sigma_v}{v}\right)^2}$
Diagnostic Diagram	$\log\left(\frac{u+v}{z}\right)$	$\frac{1}{\ln 10} \cdot \sqrt{\left(\frac{\sigma_u}{u+v}\right)^2 + \left(\frac{\sigma_v}{u+v}\right)^2 + \left(\frac{\sigma_z}{z}\right)^2}$
Reddening E_{B-V}^a	$\frac{2.4}{3.1 \cdot 0.37} \cdot \log\left(\frac{u}{3.1 \cdot v}\right)$	$\frac{2.4}{3.1 \cdot 0.37 \cdot \ln 10} \cdot \sqrt{\left(\frac{\sigma_u}{u}\right)^2 + \left(\frac{\sigma_v}{v}\right)^2}$
Reddening Corrected Flux Ratio ^b	$\frac{u}{v} \left(10^{\frac{a}{0.37} \cdot \log\left(\frac{y}{3.1 \cdot z}\right)}\right)^{-1}$	$x \cdot \sqrt{\left(\frac{\sigma_u}{u}\right)^2 + \left(\frac{\sigma_v}{v}\right)^2 + \left(\frac{a}{0.37}\right)^2 \left(\frac{\sigma_y}{y}\right)^2 + \left(\frac{a}{0.37}\right)^2 \left(\frac{\sigma_z}{z}\right)^2}$
Electron Temperature T_e^c	$\frac{32900}{\ln\left(\frac{u+v}{7.3 \cdot z}\right)}$	$\frac{x^2}{32900} \cdot \sqrt{\left(\frac{\sigma_u}{u+v}\right)^2 + \left(\frac{\sigma_v}{u+v}\right)^2 + \left(\frac{\sigma_z}{z}\right)^2}$
Logarithm of Ionization Parameter U^d	$-\sqrt{\frac{\log\left(\frac{u}{v}\right) + a}{b}}$	$\frac{1}{2 \cdot x \cdot b \cdot \ln 10} \cdot \sqrt{\left(\frac{\sigma_u}{u}\right)^2 + \left(\frac{\sigma_v}{v}\right)^2}$

Note. – The uncertainties σ_x of the values x were calculated using the error propagation equation (Eq. D.2).

^a With u = flux (H α) and v = flux (H β) (Eqs. C.1 and C.2)

^b With $\frac{u}{v}$ observed ratio, $a = [f(\text{line}) - f(\text{H}\beta)]$, $\frac{y}{z}$ = flux ratio H α /H β (Eq. C.3)

^c With u , v , and z = reddening corrected [O III] $\lambda\lambda 4959, 5007, 4363$ Å to H β fluxes (Eq. C.7)

^d With u and v = reddening corrected [O II] $\lambda 3727$ Å and [O III] $\lambda 5007$ Å to H β fluxes; $a = 1.7229$, $b = 0.190059$ for $n_e = 100$; $a = 1.85582$, $b = 0.191677$ for $n_e = 1000$, respectively (Eq. C.10)

Bibliography

- Antonucci, R. R. J. 1983, *Nature*, 303, 158
- Antonucci, R. R. J., & Miller, J. S. 1985, *ApJ*, 297, 621
- Antonucci, R. R. J. 1993, *ARA&A*, 31, 473
- Antonucci, R. R. J. 2001, in: *Astrophysical Spectropolarimetry*, ed. Trujillo–Bueno, J., Moreno–Insertis, F., & Sanchez, F., 151, Cambridge University Press, Cambridge
- Arshakian, T. G. 2005, *A&A*, 436, 817
- Baldwin, J. A., Phillips, M. M., & Terlevich, R. 1981, *PASP*, 93, 5
- Ballantyne, D. R., Weingartner, J. C., & Murray, N. 2003, *A&A*, 409, 503
- Barth, A. J. 2004, *Proceedings of IAU Symposium*, 222, 3, Cambridge University Press, Cambridge
- Bennert, N., Falcke, H., Schulz, H., Wilson, A. S., & Wills, B. J. 2002, *ApJ*, 574, L105
- Bennert, N., Schulz, H., & Henkel, H. 2004a, *A&A*, 419, 127
- Bennert, N., Falcke, H., Shchekinov, Y., & Wilson, A. S. 2004b, *Proceedings of IAU Symposium*, 222, 307, Cambridge University Press, Cambridge
- Bennert, N., Jungwiert, B., Komossa, S., Haas, M., & Chini, R. 2005, *A&A*, submitted
- Bennett, C. L., Halpern, M., Hinshaw, G., et al. 2003, *ApJS*, 148, 1
- Bergeron, J., Durret, F., & Boksenberg, A. 1983, *A&A*, 127, 322
- Bevington, P. R., & Robinson, D. K. 1992, *Data reduction and error analysis for the physical sciences*, Second Edition, McGraw–Hill Book Company, New York
- Bica, E., & Alloin, D. 1986, *A&A*, 166, 83
- Bica, E. 1988, *A&A*, 195, 76
- Boller, T., Brandt, W. N., & Fink, H. 1996, *A&A*, 305, 53
- Bonatto, C., Bica, E., Pastoriza, M. G., & Alloin, D. 2000, *A&A*, 355, 112

- Boroson, T. A., & Green, R. F. 1992, *ApJS*, 80, 109
- Bowen, I. S. 1960, *ApJ* 132, 1
- Braatz, J. A., Wilson, A. S., & Henkel, C. 1997, *ApJS*, 110, 321
- Brindle, C., Hough, J. H., Bailey, J. A., et al. 1990, *MNRAS*, 244, 577
- Buta, R., & Combes, F. 1996, *Fundamentals of Cosmic Physics*, 17, 95
- Canalizo, G., & Stockton, A. 2001, *ApJ*, 555, 719
- Canalizo, G., Max, C., Antonucci, R. R. J., et al. 2004, *astro-ph/0406669*
- Cao, X. 2005, *ApJ*, 619, 86
- Capetti, A., Axon, D. J., Macchetto, F., Sparks, W. B., & Boksenberg, A. 1996, *ApJ*, 469, 554
- Cid Fernandes, R., Storchi-Bergmann, T., & Schmitt, H. R. 1998, *MNRAS*, 297, 579
- Cid Fernandes, R., Heckman, T. M., Schmitt, H. R., González Delgado, R. M., & Storchi-Bergmann, T. 2001, *ApJ*, 558, 81
- Cohen, R. D. 1983, *ApJ*, 273, 489
- Colbert, E. J. M., Baum, S. A., Gallimore, J. F., et al. 1996, *ApJS*, 105, 75
- Colina, L., Sparks, W. B., & Macchetto, F. 1991, *ApJ*, 370, 102
- Combes, F. 2004, *Proceedings of IAU Symposium*, 222, 383, Cambridge University Press, Cambridge
- Crenshaw, D. M., Kraemer, S. B., Hutchings, J. B., et al. 2000, *AJ*, 120, 1731
- Croom, S. M., Rhoads, K., Corbett, E. A., et al. 2002, *MNRAS*, 337, 275
- De Robertis, M. M., Yee, H. K. C., & Hayhoe, K. 1998, *ApJ*, 496, 93
- De Vaucouleurs, G., De Vaucouleurs, A., Corwin, H. G., et al. 1991, *Third Reference Catalog of Bright Galaxies, Vol. III*, Springer Verlag, New York (RC3)
- Dopita, M. A., & Sutherland, R. S. 1996, *ApJS*, 102, 161
- Dopita, M. A., Groves, B. A., Sutherland, R. S., Binette, L., & Cecil, G. 2002, *ApJ*, 572, 753
- Draine, B. T. 2003, *ARA&A*, 41, 241
- Durret, F., & Bergeron, J. 1988, *A&AS*, 75, 273
- Durret, F., & Warin, F. 1990, *A&A*, 238, 15
- Eckart, A., & Genzel, R. 1996, *Nature*, 383, 415

- Emsellem, E. 2004, *Proceedings of IAU Symposium*, 222, 419, Cambridge University Press, Cambridge
- Evans, I., Koratkar, A., Allen, M., Dopita, M., & Tsvetanov, Z. I. 1999, *ApJ*, 521, 531
- Falcke, H., Malkan, M. A., & Biermann, P. L. 1995, *A&A*, 298, 375
- Falcke, H., Wilson, A. S., & Simpson, C. 1998, *ApJ*, 502, 199
- Ferland G. J., & Osterbrock, D. E. 1986, *ApJ*, 300, 658
- Ferland G. J., Korista K. T., Verner D. A., et al. 1998, *PASP*, 110, 761
- Ferrarese, L., & Merrit, D. 2000, *ApJ*, 539, L9
- Ferruit, P., Wilson, A. S., & Mulchaey, J. 2000, *ApJS*, 128, 139
- Filippenko, A. V. 1982, *PASP*, 94, 715
- Filippenko, A. V., & Terlevich, R. 1992, *ApJ*, 397, L79
- Fixsen, D. J., Cheng, E. S., Gales, J. M., et al. 1996, *ApJ*, 473, 576
- Fraquelli, H. A., Storchi-Bergmann, T., & Binnette, L. 2000, *ApJ*, 532, 867
- Fraquelli, H. A., Storchi-Bergmann, T., & Levenson, N. A. 2003, *MNRAS*, 341, 449
- Gebhardt, K., Bender, R., Bower, G., et al. 2000, *ApJ*, 539, L13
- Ghez, A., Klein, B., Morris, M., & Becklin, E. 1998, *ApJ*, 509, 678
- González Delgado, R. M., Heckman, T., & Leitherer, C. 2001, *ApJ*, 546, 845
- Goodrich, R. W. 1995, *ApJ*, 440, 141
- Greenhill, L. J., Jiang, D. R., Moran, J. M., et al. 1995, *ApJ*, 440, 619
- Greenhill, L. J., Kondratko, P. T., Lovell, J. E. J., et al. 2003, *ApJ*, 582, L11
- Grimes, J. A., Rawlings, S., & Willott, C. J. 2004, *MNRAS*, 349, 503
- Haas, M., Müller, S. A. H., Bertoldi, F., et al. 2004, *A&A*, 424, 531
- Heckman, T. M., & Balick, B. 1979, *A&A*, 79, 350
- Heckman, T. M. 1980, *A&A*, 87, 152
- Heckman, T. M., Bothun, G. D., Balick, B., Smith, E. P. 1984, *AJ*, 89, 958
- Heckman, T. M., Armus, L., & Miley, G. K. 1987, *AJ*, 93, 276
- Hernquist, L., & Mihos, J. C. 1995, *ApJ*, 448, 41
- Hill, G. J., Goodrich, R. W., & DePoy, D. L. 1996, *ApJ*, 462, 163
- Ho, L. C. 2001, *ASP Conference Series*, 284, 13

- Ho, L. C., Terashima, Y., & Okajima, T. 2003, *ApJ*, 587, L35
- Hutchings, J. B., Janson, T., & Neff, S. G. 1989, *ApJ*, 342, 660
- Inglis, M., Hough, J. H., Axon, D. J., Bailey, J., & Ward, M. J. 1993, *MNRAS*, 263, 895
- Iwasawa, K., Fabian, A. C., Reynolds, C. S., et al. 1996, *MNRAS*, 282, 1038
- Kaspi, S., Smith, P. S., Netzer, H., et al. 2000, *ApJ*, 533, 631
- Keel, W. C. 1996, *AJ*, 111, 2
- Kellermann, K. I., Sramek, R., Schmidt, M., Shaffer, D. B. & Green, R. 1989, *AJ*, 98, 1195
- Kewley, L. J., Dopita, M. A., Sutherland, R. S., Heisler, C. A., & Trevena, J. 2001, *ApJ*, 556, 121
- Khachikian, E. Y., & Weedman, D. W. 1974, *ApJ*, 192, 581
- Kinney, A. L., Schmitt, H. R., Clarke, C. J., et al. 2000, *ApJ*, 537, 152
- Komossa, S., & Schulz, H. 1997, *A&A*, 323, 31
- Kormendy, J., & Richstone, D. 1995, *ARA&A*, 33, 581
- Kulkarni, V. P., Calzetti, D., Bergeron, L., et al. 1998, *ApJ*, 492, L121
- Laine, S., Shlosman, I., Knapen, J. H., & Peletier, R. F. 2002, *ApJ*, 567, 97
- Laor, A. 2003, *ApJ*, 590, 86
- Lawrence, A. 1991, *MNRAS*, 252, 586
- Leipski, C., & Bennert, N. 2005, *A&A*, submitted
- Leipski, C., Falcke, H., Bennert, N., Hüttemeister, S., & Wilson, A. S. 2005, in preparation
- Lequeux, J. 1983, *A&A*, 125, 394
- Lípari, S., Tsvetanov, Z., & Macchetto, F. 1993, *ApJ*, 405, 186
- Lutz, D., Maiolino, R., Moorwood, A. F. M., et al. 2002, *A&A*, 396, 439
- Malkan, M. A. 1984, *ApJ*, 287, 555
- Malkan, M. A., Gorjian, V., & Tam, R. 1998, *ApJS*, 117, 2588
- van der Marel, R. P. 1999, *ASP Conference Series*, 182, 65
- Márquez, I., Durret, F., González Delgado, R. M., et al. 1999, *A&AS*, 140, 1
- Márquez, I., Durret, F., Masegosa, J., et al. 2004, *A&A*, 416, 475
- Martin, P. G., Thompson, I. B., Maza, J., & Angel, J. R. P. 1983, *ApJ*, 266, 470

- Martini, P., & Schneider, D. P. 2003a, *ApJ*, 597, 109
- Marziani, P., Sulentic, J. W., Zamanov, R., et al. 2003b, *ApJS*, 145, 199
- Mauder, W., Appenzeller, I., Hofmann, K.-H., et al. 1992, *A&A*, 264, 9
- McLure, R. J., & Jarvis, M. J. 2002, *MNRAS*, 337, 109
- Miller, J. S., & Goodrich, R. W. 1990, *ApJ*, 355, 456
- Minezaki, T., Yoshii, Y., Kobayashi, Y., et al. 2004, *ApJ*, 600, L35
- Merritt, D., & Ferrarese, L. 2001, *MNRAS*, 320, L30
- Moore, C.E. 1945, *A multiplet table of astrophysical interest*, Princeton, New Jersey
- Moran, E. C., Barth, A. J., Kay, L. E., & Filippenko, A. V. 2000, *ApJ*, 540, L73
- Morganti, R., Osterloo, T., & Tsvetanov, Z. I. 1998, *AJ*, 115, 915
- Morse, J. A., Raymond, J. C., & Wilson, A. S. 1996, *PASP*, 108, 426
- Morris, S., Ward, M., Whittle, M., Wilson, A. S., & Taylor, K. 1985, *MNRAS*, 216, 193
- Mulchaey, J. S., Koratkar, A., Ward, M. J., et al. 1994, *ApJ*, 436, 586
- Mulchaey, J. S., Wilson, A. S., & Tsvetanov, Z. I. 1996a, *ApJS*, 102, 309
- Mulchaey, J. S., Wilson, A. S., & Tsvetanov, Z. I. 1996b, *ApJ*, 467, 197
- Mulchaey, J. S., & Regan, M. W. 1997, *ApJ*, 482, L135
- Murayama, T., & Taniguchi, Y. 1998a, *ApJ*, 497, L9
- Murayama, T., & Taniguchi, Y. 1998b, *ApJ*, 503, L115
- Myoshi, M., Moran, J. M., Hernstein, J., et al. 1995, *Nature*, 373, 127
- Nagao, T., Murayama, T., & Taniguchi, Y. 2000, *AJ*, 119, 2605
- Nagao, T., Murayama, T., & Taniguchi, Y. 2001, *PASJ*, 53, 629
- Nagar, N. M., Wilson, A. S., Mulchaey, J. S., & Gallimore, J. F. 1999, *ApJS*, 120, 209
- Netzer, H. 1990, in: *Active Galactic Nuclei*, ed. Courvoisier, T. J.-L., & Mayor, M., 57, Springer Verlag, Berlin
- Netzer, H., & Laor, A. 1993, *ApJ*, 404, L51
- Netzer, H., Shemmer, O., Maiolino, R., et al. 2004, *ApJ*, 614, 558
- Oknyanskij, V. L., & Horne, K. 2001, *ASP Conference Series*, 224, 149
- Osterbrock, D. E. 1978, *Lick Obs. Bull.*, 775
- Osterbrock, D. E., & Pogge, R. W. 1985, *ApJ*, 297, 166

- Osterbrock, D. E. 1989, *Astrophysics of Gaseous Nebulae and Active Galactic Nuclei*, University Science Books, Mill Valley
- Penston, M. V., Robinson, A., Alloin, D., et al. 1990, *A&A*, 236, 53
- Peterson, B. M. 1993, *PASP*, 105, 247
- Peterson, B. M. 2003, *An introduction to active galactic nuclei*, Cambridge University Press, Cambridge
- Pogge, R. W. 1988, *ApJ*, 328, 519
- Pogge, R. W. 1989, *ApJ*, 345, 730
- Polletta, M., Bassani, L., Malaguti, G., Palumbo, G. G. C., & Caroli, E. 1996, *ApJS*, 106, 399
- Pounds, K. A., Done, C., & Osborne, J. P. 1995, *MNRAS*, 277, L5
- Quillen, A. C., Alonso-Herrero, A., Rieke, M. J., et al. 1999a, *ApJ*, 525, 685
- Quillen, A. C., Alonso-Herrero, A., Rieke, M. J., et al. 1999b, *ApJ*, 527, 696
- Raimann, D., Storchi-Bergmann, T., González Delgado, R. M., et al. 2003, *MNRAS*, 339, 772
- Regan, M. W., & Mulchaey, J. S. 1999, *AJ*, 117, 2676
- Reif, K., Mebold, U., Goss, W., van Woerden, H., & Siegman, B. 1982, *A&AS*, 50, 451
- Reynolds, C. S., Ward, M. J., Fabian, A. C., & Celotti, A. 1997, *MNRAS*, 291, 403
- Ricotti, M., & Ostriker, J. P. 2003, *astro-ph/0311003*
- Rodríguez-Ardila, A., Pastoriza, M. G., & Donzelli, C. J. 2000, *ApJS*, 126, 63
- Röttgering, H., Jaffe, W., Meisenheimer, K., et al. 2005, *astro-ph/0507236*
- Rossa, J., Dietrich, M., & Wagner, J. S. 2000, *A&A*, 362, 501
- Rousset, A. 1992, PhD Thesis, Université Jean Monnet de Saint-Etienne
- Ruiz, J. R., Crenshaw, D. M., Kraemer, S. B., et al. 2001, *AJ*, 122, 2961
- Ryder, S. D., & Dopita, M. A. 1993, *ApJS*, 88, 415
- Savage, B. D., & Mathis, J. S. 1979, *ARA&A*, 17, 73
- Schiano, A.V.R. 1986, *ApJ*, 302, 81
- Schlegel, D. J., Finkbeiner, D. P., & Davis, M. 1998, *ApJ*, 500, 525
- Schmid, H. M., Appenzeller, I., Camenzind, M., et al. 2001, *A&A*, 372, 59
- Schmidt, M., & Green, R. F. 1983, *ApJ*, 269, 352

- Schmitt, H. R., Storchi–Bergmann, T., & Baldwin, J. A. 1994, *ApJ*, 423, 237
- Schmitt, H. R., & Kinney, A. L. 1996, *ApJ*, 463, 498
- Schmitt, H. R. 1998, *ApJ*, 506, 647
- Schmitt, H. R., Ulvestad, J. S., Antonucci, R. R. J., & Kinney, A. L. 2001, *ApJS*, 132, 199
- Schmitt, H. R., Donley, J. L., Antonucci, R. R. J., Hutchings, J. B., & Kinney, A. L. 2003a, *ApJS*, 148, 327
- Schmitt, H. R., Donley, J. L., Antonucci, R. R. J., et al. 2003b, *ApJS*, 597, 768
- Schmitt, H. R. 2004, *Proceedings of IAU Symposium*, 222, 395, Cambridge University Press, Cambridge
- Schulz, H. 1988, *A&A*, 203, 233
- Schulz, H., Mücke, A., Boer, B., Dresen, M., & Schmidt–Kaler, T. 1995, *A&AS*, 109, 523
- Schulz, H., & Henkel, C. 2003, *A&A*, 400, 41
- Seyfert, C. K. 1943, *ApJ*, 97, 28
- Shields, G. A., Gebhardt, K., Salviander, S., et al. 2003, *ApJ*, 583, 124
- Shlosman, I., Begelman, M. C., & Frank, J. 1990, *Nature*, 345, 679
- Shuder, J. M., & Osterbrock, D. E. 1981, *ApJ*, 250, 55
- Simkin, S. M., Su, H. J., & Schwarz, M. P. 1980, *ApJ*, 237, 404
- Simpson, C., Wilson, A. S., Bower, G., et al. 1997, *ApJ*, 474, 121
- Simpson, C. 1998, *MNRAS*, 297, L39
- Simpson, C., Rawlings, S., & Lacy, M. 1999, *MNRAS*, 306, 828
- Simpson, C. 2005, *MNRAS*, 360, 565
- Smith, E. P., Heckman, T. M., Bothun, G. D., Romanishin, W., & Balick, B. 1986, *ApJ*, 306, 64
- Smith, J. E., Young, S., Robinson, A., et al. 2002, *MNRAS*, 335, 773
- Smith, J. E., Robinson, A., Alexander, D. M., et al. 2004, *MNRAS*, 350, 140
- Stasinska, G. 1984, *A&AS*, 55, 15
- Storchi–Bergmann, T., Mulchaey, J. S., & Wilson, A. S. 1992a, *ApJ*, 395, L73
- Storchi–Bergmann, T., Wilson, A. S., & Baldwin, J. A. 1992b, *ApJ*, 396, 45
- Storchi–Bergmann, T., Raimann, D., Bica, E. L. D., & Fraquelli, H. A. 2000, *ApJ*, 544, 747

- Tadhunter, C., & Tsvetanov, Z. I. 1989, *Nature*, 341, 422
- Taniguchi, Y., & Wada, K. 1996, *ApJ*, 469, 581
- Terlevich, R., Tenorio-Tagle, G., Franco, J., & Melnick, J. 1992, *MNRAS*, 255, 713
- Thompson, I. B., & Martin, P. G. 1988, *ApJ*, 330, 121
- Tran, H. D., Miller, J. S., & Kay, L. E. 1992, *ApJ*, 397, 452
- Tran, H. D. 1995, *ApJ*, 440, 578
- Tran, H. D. 2003, *ApJ*, 583, 632
- Tsvetanov, Z. I., & Petrosian, A. R. 1995, *ApJS*, 101, 287
- Tüg, H. 1997, *ESO Messenger*, 11, 7
- Ulvestad, J. S., & Wilson, A. S. 1984, *ApJ*, 278, 544
- Unger, S. W., Pedlar, A., Axon, D. J., et al. 1987, *MNRAS*, 228, 671
- Urry, C. M., & Padovani, P. 1995, *PASP*, 107, 803
- Veilleux, S. 1990, *PASP*, 102, 494
- Véron-Cetty, M.-P., Véron, P., & Gonçalves, A. C. 2001a, *A&A*, 372, 730
- Véron-Cetty, M.-P., & Véron, P. 2001b, *A&A*, 374, 92
- Véron-Cetty, M.-P., & Véron, P. 2003, *A&A*, 412, 399
- Véron-Cetty, M.-P., Joly, M., & Véron, P. 2004, *A&A*, 417, 515
- Vignali, C., & Comastri, A. 2002, *A&A*, 381, 834
- Vrtilek, J. M., & Carleton, N. P. 1985, *ApJ*, 294, 106
- Wagner, S. J., & Appenzeller, I. 1989, *A&A*, 225, L13
- Wandel, A., Peterson, B. M., & Malkan, M. A. 1999, *ApJ*, 526, 579
- Wasilewski, A. J. 1981, *PASP*, 93, 560
- Weaver, K. A., Wilson, A. S., & Baldwin, J. A. 1991, *ApJ*, 366, 50
- West, R. M., Danks, A. C. & Alcaïno, G. 1978, *A&A*, 65, 151
- Whittle, M. 1982, PhD Thesis, Cambridge University
- Whittle, M. 1985, *MNRAS*, 213, 1
- Whittle, M. 1992, *ApJS*, 79, 49
- Willot, C. J., Rawlings, S., Blundell, K. M., & Lacy, M. 2000, *MNRAS*, 316, 449

Wilson, A. S., & Tsvetanov, Z. I. 1994, *AJ*, 107, 1227

Winkler, H. 1992, *MNRAS*, 257, 677

Zakamska, N. L., Strauss, M. A., Krolik, J. H., et al. 2003, *AJ*, 126, 2125

Zubko, V. G., & Laor, A. 2000, *ApJS*, 128, 245

Acknowledgements

This research has made use of several astronomical databases: the NASA's Astrophysics Data System (ADS) Bibliographic Services, the NASA/IPAC Extragalactic Database (NED), operated by the Jet Propulsion Laboratory, California Institute of Technology, under contract with the National Aeronautics and Space Administration, as well as the Online Digitized Sky Surveys (DSS1 & 2) server at the ESO/ST-ECF Archive produced by the Space Telescope Science Institute through its Guide Star Survey group.

The allocation of the required observing time for this project by the time allocation committee of the European Southern Observatory (ESO) is gratefully acknowledged.

I thank the "Studienstiftung des Deutschen Volkes" for financial and idealistic support. Sincere thanks are especially given to Prof. Dr. Wolf-Ekkehard Kalisch and Prof. Dr. Hans-Ottmar Weyand for their encouraging advice.

The financial support of the "Astronomische Gesellschaft" and the "Ruth und Gert Massenbergs-Stiftung" enabled me to attend the AG meetings in Germany, the conference in Gramado (Brazil) as well as the upcoming conference in Leiden (The Netherlands). I thank the Institute for Pure and Applied Mathematics (IPAM) for their financial support allowing me to attend the workshop on "Transfer Phenomena".

I am very grateful to my supervisors Prof. Dr. Rolf Chini and Dr. Martin Haas for providing me the opportunity to continue my thesis on this most fascinating topic of contemporary astrophysics. Their support by scientific, personal, and financial means has been of great value.

I am deeply indebted to Prof. Dr. Heino Falcke, Dr. Bruno Jungwiert, and Dr. Stefanie Komossa for their very valuable advice, persistent encouragement, and many ideas helping to improve this PhD thesis. I thank Dr. Bruno Jungwiert and Dr. Pierre Ferruit for their hospitality. I am much obliged to Dr. Pierre Ferruit for providing and helping me with the "fit/spec" line-fitting tool and for stimulating discussions. I thank Prof. Dr. Yuri Shchekinov and Prof. Dr. Andrew Wilson for their interesting ideas on the modeling issue. Dr. Christian Henkel wrote encouraging emails in hard times and supported my crazy idea resulting in the allocation of 100 hours of Effelsberg observing time for my postdoc position.

Prof. Dr. Gary Ferland provided CLOUDY and Dr. Henrique Schmitt was so kind to send me the continuum-subtracted HST [O III] images. Prof. Dr. Gabriela Canalizo was very hospitable during my short visit in Pasadena and Riverside. By offering me a postdoc position at the University of California in Riverside starting in November 2005, she made me finish my PhD thesis after less than three years of studies.

I would like to express my gratitude to Daniel Brown and Christian Leipski for having been such pleasant room mates who were always in the mood for inspiring discussions on all of our three thesis topics, for their great ability to think in three dimensions, for helping me to improve my repartee, and for creating a joyful atmosphere.

During the last few weeks before finishing my thesis, they provided tremendous help by checking and correcting the text, equations, tables, and figures. I thank Christian Leipski for providing the NTT spectra of NGC 5643.

Thanks are due to the members of the Astronomical Institute of the Ruhr–University Bochum for their hospitality and help during the last couple of years and especially to the “Team Chini” for creating such a familiar atmosphere. I give special thanks to my colleagues and friends Dr. Marcus Albrecht, Katrin Brede, Daniel Brown, Janine van Eymeren, Dr. Martin Haas, Vera Hoffmeister, Thomas Jürges, Volker Knierim, Christian Leipski, Dr. Sven Müller, Dr. Markus Nielbock, Dominik Rosenbaum, Claus Michael Scheyda, and Clemens Trachternach for joint proposals, shared lunch breaks, philosophical discussions, soccer games, and much more. I really appreciated and needed the computer skills of Thomas Jürges, Dr. Sven Müller, and Claus Michael Scheyda.

I am much obliged to the former AIRUB members Dr. Michael Pohlen, Dr. Linda Schmidtbreick, Dr. Claus Tappert, and Dr. Ralf Vanscheidt for encouraging me in my studies, their stimulating discussions, and joyfull e-mails on various topics. I look up to them as astronomers and friends.

I thank the staff of the Hoher List Observatory and especially Dr. Klaus Reif and Prof. Dr. Seggewiss for their generous allocation of observing time. I appreciated the more than one dozen pleasant weeks I spent with various participants at the observatory during my studies, the fruitful discussions during long clear or foggy nights, and the inspiring hikes through the beautiful landscape of the “Vulkan Eifel”. I especially thank the “September 2003 Hoher List participants” and my “first” students for being such a loyal team and making me realize the deep pleasure of teaching.

The members of the “Initiativkreis Horizontastronomie im Ruhrgebiet e.V.” are thanked for our combined efforts in promoting astronomical knowledge to the public. I especially thank Dr. Burkard Steinrücken for his ironical and striking comments providing insights in his interesting view of life.

I thank my sister Nadine Bennert for the sportive and yet relaxing lunch breaks at the “Kemnader Stausee” which helped me to clear my mind and get concentrated again on my PhD studies.

Last but not least, there are not enough words to describe my gratitude to my beloved family Carmen, Wilfried & Nadine Bennert, and my beloved friends Christian Leipski, Renate Dylla, Olessia Brandstätter, Klaus Rösler, and Manuel Landers. They kept me grounded and helped me to get focussed again on the important things in life. I am grateful for their patience, trust, deeply touching conversations, encouraging words, and supporting love during all the good and bad times I lived through while writing this thesis.

Curriculum Vitae

Personal data

Date of birth: April 26th 1977

Place of birth: Bochum, NRW, Germany

Nationality: German

Education

June 1996

Abitur (Highschool Diploma; Schiller–Gymnasium Witten, Germany)

Oct 1996 – Sep 1999

Undergraduate student of physics, mathematics, astronomy, and biology at the Ruhr–University Bochum (RUB)

Oct 1999

Pre–degree (Vordiplom; B.Sc.) in physics (RUB)

Oct 1999 – Sep 2001

Graduate student of physics (astrophysics/zoology as major/minor subject)

Sep 2001 – Nov 2002

Diplom student (Master’s student) working on Active Galactic Nuclei

Nov 2002

Diplom (Master’s degree) in physics (RUB)

Title of thesis: “Analyse von ionisiertem Gas um Aktive Galaktische Kerne” (Analysis of ionized gas around Active Galactic Nuclei)

Advisors: Prof. Dr. R. Chini, Prof. Dr. H. Schulz

Dec 2002 – present

PhD student (Astronomical Institute of the Ruhr–University Bochum)

Title of thesis: “The Narrow–Line Region of Active Galaxies”

Advisors: Prof. Dr. H. Schulz¹, Prof. Dr. R. Chini, PD Dr. M. Haas

PhD scholarship granted by Studienstiftung des Deutschen Volkes (German National Academic Foundation)

¹ Deceased August 2003